UNIVERSITÀ DEGLI STUDI DI MODENA E REGGIO EMILIA

Dottorato di Ricerca in Models and Methods for Material and Environmental Sciences

Ciclo XXXVII

Development of hybrid bio-materials for theranostic applications

Candidata: Dott.ssa Debora Carrozza

Relatore (Tutor): Prof. Gianluca Malavasi

Eventuale Correlatore (Co-Tutor): Prof. Erika Ferrari

Coordinatore del Corso di Dottorato: Prof. Stefano Lugli

Preface

In recent years, the field of bio-materials for theranostic applications has witnessed remarkable progress, driven by the need for more efficient and versatile systems that can simultaneously perform therapeutic and diagnostic functions. This thesis focuses on the development of Large Pore Mesoporous Silica (LPMS) materials, specifically designed to overcome the limitations of classical Mesoporous Silica (MS). While traditional MS materials are hindered by smaller pore sizes that can cause pore-blocking and limit the loading capacity for large therapeutic molecules, LPMS structures, with their significantly larger pores, offer a solution by enabling efficient loading, stabilization, and controlled release of bioactive agents.

This work is part of a broader effort to explore the potential of LPMS for pharmaceutical applications, particularly in the delivery of larger bioactive molecules, such as peptides, which play a vital role in modern medicine. The need for materials that can encapsulate and protect such therapeutic molecules while ensuring their gradual release within the body is paramount. The research presented here addresses this challenge by investigating LPMS structures synthesized using advanced techniques, such as hydrothermal and microwave-assisted processes. The goal is to optimize these materials for better performance in drug delivery, bioactivity, and mechanical stability, ultimately contributing to the development of next-generation bio-materials.

During my doctoral journey, I was involved in the publication "Curcumin-Based β-Diketo Ligands for Ga^{3+}: Thermodynamic Investigation of Potential Metal-Based Drugs", published in Pharmaceuticals. This work focused on designing curcumin-based β-diketo ligands with gallium ions, exploring their thermodynamic properties and potential use in anticancer therapies. Our study highlighted the formation of stable complexes with enhanced bioavailability and improved therapeutic efficacy, particularly in colon cancer cell models.

Additionally, I have had the opportunity to contribute to several research studies that were crucial to shaping this thesis. One of the key projects I worked on was the study titled "Alginate Beads Containing Cerium-Doped Mesoporous Glass and Curcumin: Delivery and Stabilization of Therapeutics", published in the International Journal of Molecular Sciences. In this project, we explored the development of bioactive glass systems doped with cerium and loaded with curcumin, focusing on their ability to deliver and stabilize curcumin in targeted therapeutic applications. The study demonstrated the effectiveness of alginate beads containing cerium-

doped mesoporous glasses in promoting a controlled curcumin release, thereby achieving a synergistic antioxidant effect.

Moreover, I contributed to the research titled "Assessing Mn as an Antioxidant Agent in Bioactive Glasses by Quantification," which evaluated the role of manganese in bioactive glasses. This study aimed at quantifying the antioxidant activity of manganese-doped bioactive glasses and their potential application in reducing oxidative stress, making them highly relevant for biomedical applications, such as tissue regeneration.

These research projects provided me with invaluable experience and insights into the synthesis, characterization, and functionalization of bioactive materials. They have profoundly shaped my understanding of how these materials can be tailored for specific therapeutic and diagnostic purposes. The research presented in this thesis is not only a culmination of my efforts but also a reflection of the interdisciplinary collaboration that has been instrumental throughout this journey.

Index

Abstract - Italian

La sintesi di silice mesoporosa a pori larghi (LPMS) offre un approccio promettente per ospitare e stabilizzare molecole bioattive con applicazioni farmaceutiche, essenziale per mantenere la loro attività biologica. A differenza della silice mesoporosa classica (MS), che presenta limitazioni dovute alle ridotte dimensioni dei pori (2–5 nm) che possono causare ostruzione dei pori e insufficiente capacità di caricamento, le strutture LPMS presentano pori significativamente più grandi (20–60 nm e 200–600 nm). Questi pori più grandi consentono un caricamento più efficiente, la stabilizzazione e il rilascio controllato di molecole bioattive.

Le LPMS sono sintetizzate utilizzando una soluzione acquosa acida di Tetraetil-Ortosilicato con agenti formanti pori (Pluronic F127® e mesitilene), attraverso reazioni idrotermiche e assistite da microonde. Ottimizzazioni nel tempo di reazione e nell'uso di tensioattivi sono state effettuate per migliorare le proprietà del materiale. Studi di caricamento con Nisina, un peptide antibatterico policiclico con dimensioni di 4–6 nm, hanno dimostrato un'efficienza di caricamento significativamente più elevata (LE%) per le LPMS rispetto alle MS, come confermato da analisi UV-Vis, Analisi Elementare e Termogravimetrica. Gli studi sul rilascio in fluido corporeo simulato (SBF) hanno evidenziato un profilo di rilascio controllato per le LPMS su scale temporali estese, con la Microscopia a Scansione Elettronica (SEM) che ha confermato la conservazione dell'integrità strutturale e della resistenza meccanica dopo i test di rilascio.

Inoltre, le LPMS sono state ulteriormente funzionalizzate incorporando ioni come Ca^{2+} e Ga^{3+}, noti per le loro proprietà bioattive, antibatteriche e anticancro. Queste LPMS modificate hanno dimostrato proprietà di caricamento e rilascio superiori, in particolare in termini di rilascio di Ca^{2+} e Ga^{3+} in SBF, come mostrato dalla spettroscopia a emissione ottica con plasma accoppiato induttivamente (ICP-OES). Il comportamento bioattivo di queste strutture è stato confermato tramite Spettroscopia Infrarossa a trasformata di Fourier (FT-IR), SEM-EDS e Diffrazione a Raggi-X su polveri (XRPD). Questi risultati indicano che le LPMS non solo offrono migliori caratteristiche di caricamento e rilascio per le molecole bioattive rispetto alla MS classica, ma presentano anche proprietà bioattive, rendendole candidate promettenti per applicazioni nella rigenerazione ossea e in altri campi biomedici.

Abstract - English

The synthesis of large pore mesoporous silica (LPMS) offers a promising approach for accommodating and stabilizing bioactive molecules with pharmaceutical applications, which is crucial for maintaining their biological activity. Unlike classical mesoporous silica (MS), which suffers from limitations due to smaller pore sizes (2–5 nm) that can lead to pore blocking and insufficient loading capacity, LPMS structures feature significantly larger pores (20–60 nm and 200–600 nm). These larger pores enable more efficient loading, stabilization, and controlled release of bioactive molecules.

LPMSs are synthesized using an acidic water solution of tetraethyl orthosilicate with pore-forming agents (Pluronic F127® and mesitylene), through hydrothermal and microwave-assisted reactions. Reaction time and surfactant use have been optimized to enhance the material properties. Loading studies using Nisin, a polycyclic antibacterial peptide with dimensions of 4–6 nm, demonstrated a significantly higher loading efficiency (LE%) for LPMSs compared to MS, as confirmed by UV-Vis, Elemental Analysis, and thermogravimetric analysis. Release studies in Simulated Body Fluid (SBF) highlighted a controlled release profile for LPMSs over extended time scales, with Scanning Electron Microscopy (SEM) confirming the preservation of structural integrity and mechanical strength after the release tests.

Moreover, LPMSs were further functionalized by incorporating ions such as Ca^{2+} and Ga^{3+}, known for their bioactive, antibacterial, and anticancer properties. These modified LPMSs demonstrated superior loading and release properties, particularly in terms of Ca^{2+} and Ga^{3+} release in SBF, as shown by inductively coupled plasma—optical emission spectroscopy (ICP-OES). The bioactive behavior of these structures was confirmed through Fourier-transform infrared spectroscopy (FT-IR), SEM-EDS, and X-Ray Powder Diffraction (XRPD). These results indicate that LPMSs not only provide better loading and release characteristics for bioactive molecules compared to classical MS but also exhibit bioactive properties, making them promising candidates for applications in bone tissue regeneration and other biomedical fields.

Abbreviations

AMPs	Antimicrobial Peptides
A_p	Pore Area
BET	Brunauer, Emmet and Teller
BG	Bioactive Glass
BJH	Barrett-Joyner-Halenda
CA	Calcite
CLSM	Confocal Laser Scanning Microscopy
DTG	Thermo Gravimetric Derivative Graph
EA	Elemental Analysis
ECM	Extracellular Matrix
EISA	Evaporation-Induced Self Assembly
FT-IR	Fourier-Transform Infrared Spectroscopy
HA	Hydroxyapatite
HCA	Hydroxycarbonate
HIF-1α	Hypoxia-inducible factor
ICP-OES	Inductively Coupled Plasma—Optical Emission Spectroscopy
IUPAC	International Union of Pure and Applied Chemistry
LC	Loading Capacity
LE	Loading Efficiency
LPMS	Large Pores Mesoporous Silica
MBG	Mesoporous Bioactive Glass
Me	Metal

MMS	Matrix Metalloproteinase
MS	Mesoporous Silica
MWs	Microwaves
PDB	Protein Data Bank
PEO	Poly(Ethylene oxide)
PPO	Poly(Propylene Oxide)
ROS	Reactive Oxygen Species
SSA	Specific Surface Area
SBF	Simulated Body Fluid
SEM-EDS	Scanning Electron Microscopy with Energy-Dispersive X-Ray Spectroscopy
SEM-FEG	Scanning Electron Microscopy with Field Emission Gun
SI	International Sistem of Units
SMM	Silica Mesoporous Materials
SOD	Superoxide Dismutase
TEOS	Tetraethyl Orthosilicate
TG-DTA	Thermogravimetric Analysis - Differential Thermal Analysis
TMB	1,2,3-Trimethylbenzene
TRIS	Tris(hydroxymethyl)aminomethane
UV-VIS	Ultraviolet-Visible Spectroscopy
VMD	Visual Molecular Dynamics
Vp	Intrusion Volume
WMS	Without Mesopores Silica
XRDP	X-Ray Powder Diffraction
XRF	X-Ray Fluorescence Spectroscopy

Chapter 1: Introduction.

1.1 Biomaterials

The term "biomaterials" refers to materials utilized in the medical field for structural applications. These substances are instrumental in the creation of devices designed to either replace or enhance the function of a particular part of the body in a manner that is both safe and reliable (1). Their composition can range from synthetic to natural origin, and they are carefully engineered to interact seamlessly with bodily tissues, blood, and other biological fluids. Importantly, biomaterials are intended for a variety of uses, including prosthetic, diagnostic, therapeutic, and storage applications, all while ensuring they do not adversely impact the living organism (2).

The history of biomaterials spans approximately 60-70 years, marking a significant milestone in the progression of medical science. Since the advent of medical devices in the late 1940s and early 1950s, the field of biomaterials has experienced exponential growth, revolutionizing the landscape of healthcare. Today, these materials and the devices crafted from them are indispensable components of various medical procedures, ranging from cardiovascular and orthopedic surgeries to dental and ophthalmologic interventions, as well as reconstructive surgeries. Additionally, biomaterials play crucial roles in other medical interventions such as surgical sutures, bioadhesives, and controlled drug release devices (3).

In the realm of medical applications, biomaterials are classified into distinct categories to cater to specific needs (Figure 1) (4). These categories include:

- Ceramics biomaterials: HA is widely used in bone grafts and dental implants due to their biocompatibility and similarity to natural bone mineral;
- Metals and alloys biomaterials: Titanium alloys are commonly used in orthopedic implants like hip and knee replacements and dental implants because of their excellent strength, corrosion resistance, and biocompatibility;
- Polymer biomaterials: Polylactic Acid is a biodegradable polymer used in sutures, drug delivery systems, and scaffolds for tissue engineering;

- Composite biomaterials: Carbon Fiber-Reinforced Polymers are used in prosthetics and orthopedic implants, combining the strength and stiffness of carbon fibers with the lightweight properties of polymers.

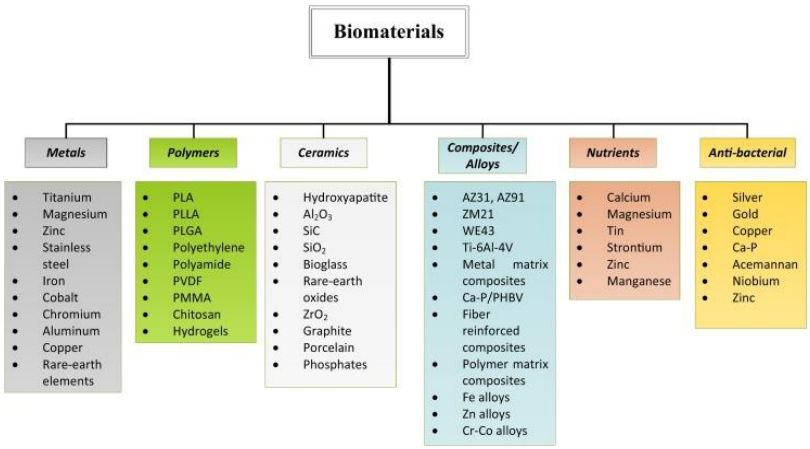

Figure 1. Classification of Biomaterials used for implant applications.

Each category serves a unique purpose and possesses its own set of properties, making them suitable for diverse medical applications. This classification system underscores the versatility and adaptability of biomaterials in addressing various healthcare challenges and advancing medical technology (Figure 2) (5).

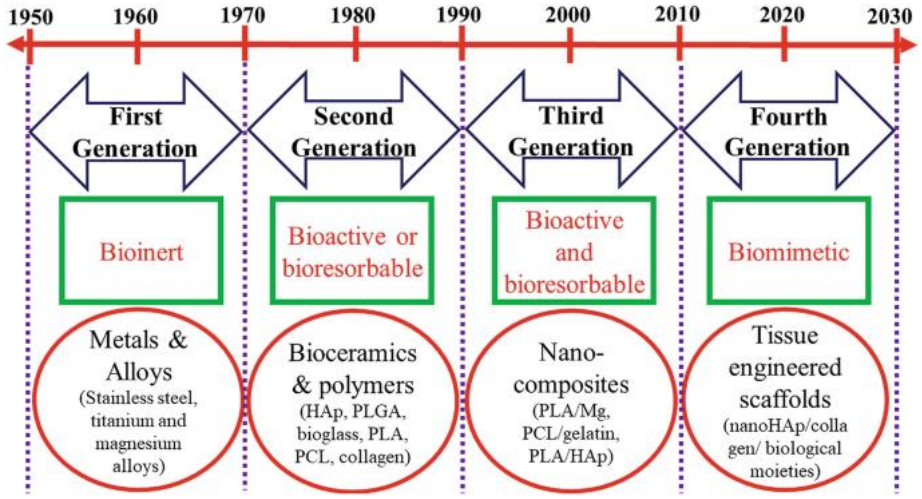

Figure 2. Evolution of biomaterials in bone regeneration and repair. .

Early biomaterials, known as the *first generation*, aimed to find the right mix of properties to match the tissues they were replacing. They were chosen because they didn't cause much of a reaction from the body, meaning they were considered safe and compatible. This was crucial for their success in medical applications.

The next step, the *second generation* of biomaterials, built upon these early successes. They were designed to interact with tissues in a controlled way to produce specific therapeutic effects. In the 1980s, these materials, known as bioactive, found applications in orthopedic and dental surgeries, as well as in controlled drug release devices like the Norplant contraceptive (6). Additionally, this era saw the development of resorbable biomaterials, which could break down over time without causing harm, eliminating the need for a long-term foreign presence in the body.

Looking ahead, the *third generation* of biomaterials aims to go even further. They seek to actively support and stimulate the regeneration of functional tissue. This is a significant advancement, considering that throughout history, the ability to regenerate lost tissues and organs has been limited (7). With the strides made in tissue engineering and regenerative medicine, the possibility of replacing damaged tissues with living tissue is becoming more attainable. One example of this is the use of Bioglass® and its gene activation properties to promote tissue regeneration and repair.

In the end, electroactive biomaterials, including piezoelectric ones, have garnered significant attention in tissue engineering due to their capacity to offer inherent electrical stimulation (8). Biomaterials capable of replicating the electrical properties and microenvironments found in living organisms are referred to as "*4th Generation Biomaterials*" (9).

Biomaterials are at the forefront of the rapidly advancing field of tissue engineering and regenerative medicine. Tissue engineering involves using living cells to help create or repair tissues, offering promising therapeutic and diagnostic benefits. This interdisciplinary approach, merging biomedical and engineering sciences, holds great potential for improving healthcare outcomes in the future (3).

1.2 Bioceramics

Over the past four decades, there has been a notable revolution in the application of ceramics to enhance quality of life. This transformation involves the innovative use of specially designed ceramics for repairing and reconstructing damaged parts of the body, a field known as bioceramics (10).

Bioceramics encompass various types, including single crystals like sapphire, polycrystalline forms such as alumina or hydroxyapatite (HA), glass compositions like Bio-glass®, glass-ceramics

such as Ceravital® or A/W glass-ceramic, and composites like stainless-steel-fiber-reinforced Bio-glass® or polyethylene-hydroxyapatite. They are among the most widely used biomaterials due to their favourable physical properties such as hardness, strength, and their ability to interact well with biological tissues, known as biocompatibility. These materials also exhibit biofunctionality, bioactivity, and reabsorption capability.

Bioceramics find numerous applications in medical procedures, including hip and knee replacements, dental implants, tendon, and ligament repairs, treatments for periodontal disease, maxillofacial reconstruction, jaw augmentation and stabilization, spinal fusion, and bone fillers following tumour surgery. For successful clinical outcomes, bioceramic materials must possess hardness and Young's modulus similar to the tissues they replace.

The response of tissues to implants varies depending on the material's properties. Toxic materials lead to tissue death, while non-toxic, biologically inactive materials result in the formation of a fibrous tissue layer. Non-toxic, bioactive materials form a bond with surrounding tissues, while those that dissolve are gradually replaced by host tissues. It is important to clarify that toxicity refers to the cell response and viability when in contact with a material, while bioactivity is related to the ability of the material to form an HA layer upon contact with an aqueous solution.

Bioceramics can be classified based on how they attach to tissues, with the attachment mechanism directly influencing tissue response at the implant interface (1).

Nearly inert, microporous bioceramics promote tissue ingrowth into surface pores or throughout the implant, enhancing stability. However, excessive micromovement at the interface can cause tissue damage and inflammation. Coating porous metals with bioactive ceramics like HA can mitigate potential problems and accelerate bone formation. While bioactive materials elicit a specific biological response, they can weaken the material's strength if the porosity is too high (11).

The expansion of the interface area between the implant and surrounding tissues results in heightened resistance to movement within the tissue. This interaction is facilitated by living tissue within the pores of the implant. It's crucial for these pores to exceed diameters of 100 to 150 μm, as this allows for adequate blood supply to the ingrown connective tissue, ensuring tissue viability and health. When micromovement occurs at the interface of a porous implant, it can lead to tissue damage, compromised blood supply, tissue death, inflammation, and ultimately,

destabilization of the interface. In cases where the material is metallic, the significant increase in surface area can promote corrosion of the implant, leading to the release of metal ions into surrounding tissues, which may result in various medical complications (12,13).

To mitigate these potential issues, one effective strategy involves utilizing a bioactive ceramic material such as HA as a coating on the porous metal (14). A bioactive material elicits a specific biological response at the material-tissue interface, resulting in the formation of a bond between the tissues and the material. This concept was first demonstrated in 1969 (15). The HA coating also accelerates bone formation within the pores. However, the presence of large pores required for bone growth can weaken the overall strength of the material. Consequently, this approach to enhancing interfacial stability is best suited for use as porous coatings or unloaded space fillers in tissues.

The concept of bioactive materials lies between resorbable and bioinert materials and encompasses bioactive glass as well (16). Additionally, there exist bioceramics designed to degrade gradually over time and be replaced by natural host tissue, known as resorbable bioceramics (17–19). This aligns with the body's natural ability to repair and replace tissues through a continuous turnover of cell populations throughout life.

1.3 Hierarchical structure of bones

Its structural organization is optimized at three levels (Figure 3): macrostructure, microstructure, and nanostructure (20,21). At the macrostructure level, it is divided into trabecular (also known as cancellous or spongy) bone and cortical (compact) bone. Trabecular bone constitutes about 20% of the total skeletal system. It is highly porous and has a sponge-like structure with branching rods or plates of varying sizes called trabeculae. Cortical bone makes up about 80% of the skeletal system, being almost solid and much less porous (approximately 10%) compared to cancellous bone.

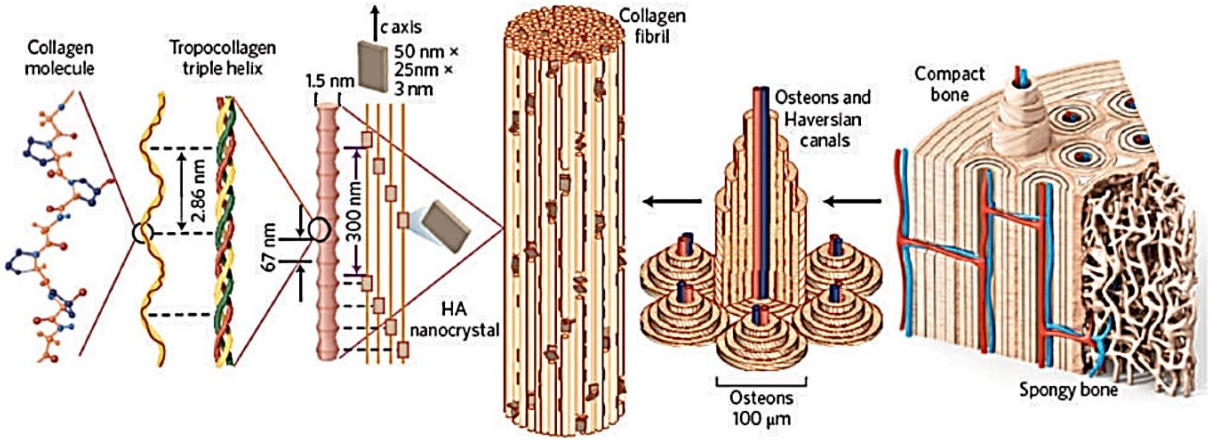

Figure 3. Scheme showing the hierarchical organization of bone from the macro - to the nanoscale (22).

The microstructure includes haversian systems, osteons, single trabeculae, and lamellae. In mature compact bone, the haversian system or osteon consists of concentric rings of lamellae surrounding a canal known as the Haversian canal. The osteon resembles a cylinder about 200-250 µm in diameter, running roughly parallel to the long axis of the bone (23). These canals encircle blood vessels and nerve cells throughout the bone, communicating with osteocytes through canaliculi. Bone lamellae are 3-7 µm thick, although the arrangement of the substances within the lamellae is not well defined (24).

The nanostructure of bone comprises the Extracellular Matrix (ECM), which is divided into organic (25-30%) and inorganic (65-70%) components. The organic matrix primarily consists of type I collagen (95%), with the remaining portion made up of proteoglycans and non-collagenous proteins such as osteocalcin, osteonectin, and osteopontin. The inorganic matrix mainly includes calcium and phosphate in the form of HCA nanocrystals. These HCA crystals are arranged within the collagen fibrils and are calcium-deficient by 5-10%. The crystals typically measure 50x25 nm in length and width, with a thickness of 2-3 nm. Additionally, bone apatite contains elements such as carbonate, potassium, sodium, chlorine, and magnesium (25), and lacks a well-defined crystallographic order. The ECM, which constitutes the bulk of the bone, provides rigidity and strength while maintaining some elasticity (26).

Bone architecture is shaped by mechanical stresses (27), leading to anisotropic properties, meaning the bone exhibits different characteristics depending on the direction of the load. Bone is deposited in areas subjected to stress and resorbed where stress is minimal (28).

Bone formation, maintenance, and resorption are managed by three cell types: osteoblasts, osteoclasts, and osteocytes. Throughout an individual's life, bone remodeling involves the

resorption of old bone and the formation of new bone. Osteoclasts play a key role in resorbing bone matrix by creating a low pH environment and secreting Matrix Metalloproteinases (MMPs) (29). Degradation products are then processed by osteoclasts and macrophages (30). The resorbed areas are subsequently filled with new bone matrix produced by osteoblasts. Osteoblasts and osteoclasts typically function in proximity during active bone remodeling. A disruption in this coupling can lead to weak bone structures and diseases such as osteoporosis. Some osteoblasts become trapped within the matrix during bone formation and differentiate into osteocytes, which comprise 90-95 % of all bone cells (31,32). These osteocytes communicate with other bone cells through canaliculi and are believed to sense mechanical loads on the bone (33,34), contributing to bone resorption (35).

1.4 Bioactive glasses

In 1969, Professor Larry Hench at Gainesville University in Florida discovered and patented bioactive glasses, marking a significant milestone in biomaterials research. The first composition he tested and patented was 45S5 Bioglass®, with a theoretical weight composition (%) as follows: SiO_2 (45%), Na_2O (24.5%), CaO (24.5%), and P_2O_5 (6%) (36). This composition has been clinically used since 1985 and is renowned as the first synthetic material capable of bonding to living tissues (37).

Professor Hench's discovery of the 45S5 Bioglass composition was described as the result of several fortuitous events. These included a chance conversation with an Army officer in the early 1960s during the Vietnam War, an award of funding by the Army medical branch despite his lack of a medical degree, and the fortunate selection of the right composition in the Na_2O–CaO–P_2O_5–SiO_2 phase diagram during his research (Figure 4, (36)).

Zone A is called the bioactivity zone: chemical bonds at the glass/bone interface are created in less than 30 days. Zone B (bio-inertia zone) is marked by a too low reactivity leading to the formation of a fibrous capsule that inhibits the bond between the bone and the glass. Zone C, the resorbability zone (too high reactivity), leads to total resorption of the bioglass in less than 30 days. Zone D does not lead to homogeneous glasses (devitrification or phase separation). The results of this work show that the critical characteristic for the rate of bioactivity is a silicate SiO_2 content that must be maintained below 60% of the weight.

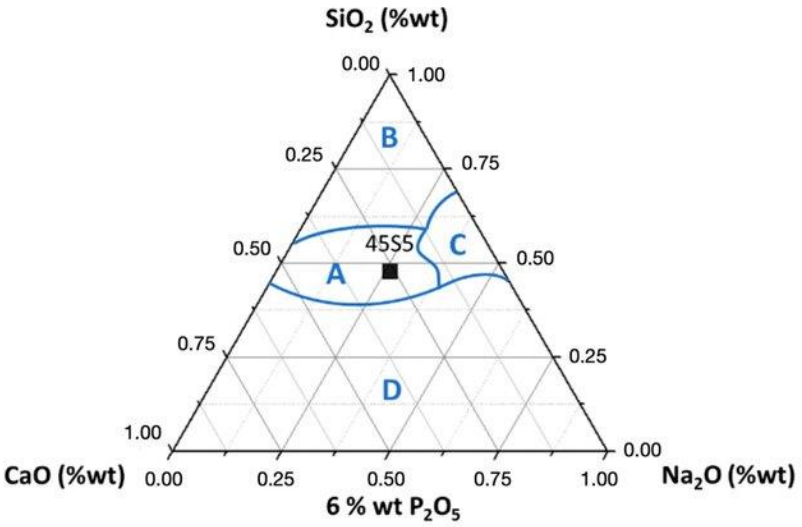

Figure 4. Hench diagram and bioactivity index in the SiO_2-Na_2O-CaO system and 6% P_2O_5. 45S5 refers to the composition of bioglass according to Hench's description.

Driven by the potential of man-made materials to aid in organ regeneration and replacement, Professor Hench continued to explore innovative applications of biomaterials. As evidenced by his presentations at events like the 2014 ACerS Bioceramics meeting, he envisioned materials not only improving the quality of life for the aged or injured by facilitating the repair or replacement of bones and teeth but also by enabling the regeneration of organs such as kidneys and tissues like urethra, trachea, and cartilage.

Bioactive glasses can be produced through methods like melting or the sol-gel process. These glasses exhibit bioactive properties because, in specific compositions, they can bond to connective tissues and bones through the formation of a biologically active hydroxyapatite-like layer ($Ca_5(PO_4)_3OH$) on their surface. This layer, akin to the main constituent of bones, fosters interaction with living tissues, thereby stimulating bone-rebuilding mechanisms involving osteoblast and osteoclast cells.

1.4.1 Bioactivity in Bioactive Glasses

The inorganic component of human bone is a type of calcium phosphate called hydroxycarbonate/hydroxyapatite (HCA/HA). When bioactive glasses are implanted in the body, they form an HCA/HA layer on their surface upon contact with biological fluids, initiating a series of surface chemical reactions. This layer formation is crucial for the material to bond with living bone.

Materials that can develop an Apatite phase on their surfaces when soaked in simulated body fluid exhibit bioactive behavior under in vivo conditions (Figure 5).

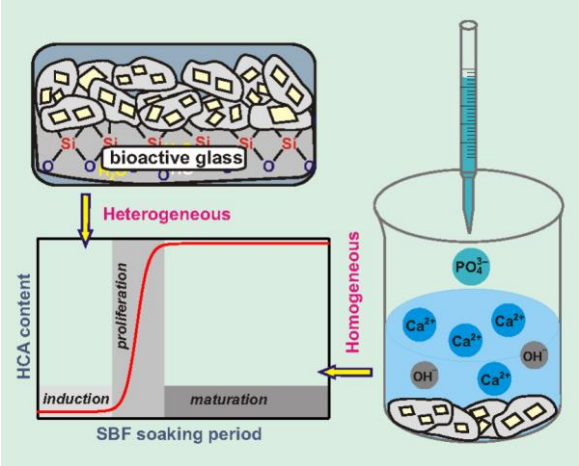

Figure 5. Illustration of apatite formation in two distinct contexts: on the right) Homogeneous nucleation by precipitation, where an aqueous solution comprising phosphate ions is added to a Ca^{2+} bearing solution. On top) Heterogeneous nucleation at the surface of a bioactive glass on its exposure either to a body fluid in vivo, or a simulated body fluid in vitro. The pale yellow and gray colors of the calcium phosphate particles depict the crystalline core of HCA, coated by an ACP surface layer, respectively (38).

The overall surface reaction that leads to the formation of a bone tissue-material bond can be divided into two sections.

The first section involves reactions on the implant side of the interface. Hench proposed a mechanism for the generation of the hydroxyapatite layer on bioactive glasses (Figure 6) (39), involving five stages:

1. Rapid exchange of alkali and alkaline earth ions (Na^+ and Ca^{2+}) with H^+ ions from the soaking solution;
2. Dissolution of the silica matrix of the glass into H_4SiO_4 form, through the rupture of siloxane bonds (Si-O-Si) and formation of silanol groups (Si-OH);
3. Condensation and polymerization of ortho-silicic acid to form a hydrated silica gel on the glass surface;
4. Formation of an amorphous Ca-P rich layer, facilitated by the silica gel layer which aids the migration of Ca^{2+} and PO_4^{3-} ions toward the glass surface;
5. Crystallization of the Ca-P rich layer, incorporating additional ions from the solution (OH^-, F^-, CO_3^{2-}), with the type of apatite formed depending on the incorporated ions.

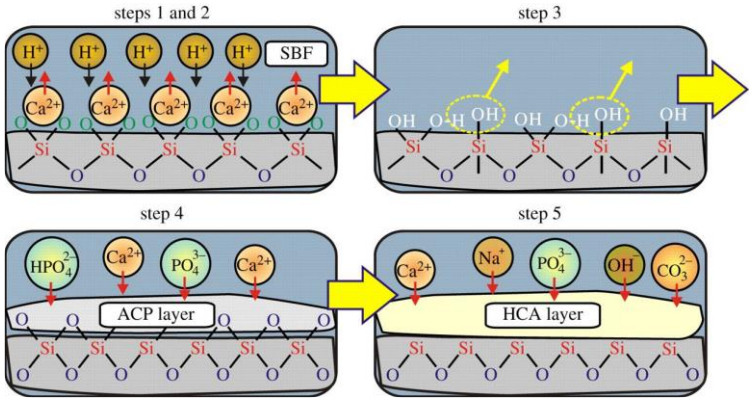

Figure 6. Schematic illustration of the reaction sequence leading to HCA formation according to Hench and co-workers in mesoporous bioactive glasses (39).

The second section involves a series of reactions leading to tissue bonding, which are less defined and not fully understood. These events include:

6. Adsorption of biological entities onto the HCA layer;
7. Macrophage action;
8. Stem cell bonding;
9. Osteoblast differentiation and proliferation;
10. Bone matrix generation;
11. Matrix crystallization and bone growth.

The first five reaction stages can occur without the presence of tissues and can be performed in distilled water, tris-buffer solution, or simulated body fluids. Analyzing bioactivity in vitro before in vivo studies is important because in vivo studies are costly, require animal sacrifices, and are not easily reproducible. Thus, in vitro, bioactive studies are frequently used in the development of new bioactive glasses to predict their behavior inside the human body (40).

Different methods are adopted to study the in vitro bioactive response of bioceramics, including static, dynamic, and differential methods. The static method involves soaking the biomaterial in a solution that is not changed throughout the experiment. The dynamic method periodically replaces the soaking solution with a fresh solution. In the differential method, the biomaterial is continuously in contact with a new solution by recirculating it. Although no method is proven to best simulate the in vivo situation, the static method quickly induces saturation of the solution, leading to rapid apatite precipitation and a pH increase (41,42).

In vitro, bioactivity of Bioglass® was initially performed in a TRIS-buffered (Tris(hydroxymethyl)aminomethane) solution, which only contains ions dissolved from the soaked materials. In 1990, Kokubo introduced Simulated Body Fluid (SBF) to analyze the bioactivity of different materials (43). SBF is an aproteic and acellular solution that mimics the ion concentration and pH of human plasma (see Table 1).

Table 1. SBF composition compared to human blood plasm (mM).

	Na^+	K^+	Mg^{2+}	Ca^{2+}	Cl^-	HCO_3^-	HPO_4^{2-}	SO_4^{2-}	pH
SBF	142.0	5.0	1.5	2.5	147.8	4.2	1.0	0.5	7.40
Plasm	142.0	5.0	1.5	2.5	103.0	27.0	1.0	0.5	7.20/7.40

Bioactivity is a surface phenomenon, so any factor increasing the specific surface area of bioactive glasses accelerates their bioactive response. High porosity favours rapid and extensive initial cation exchange, speeding up the chemical reactivity of the glass. Among different bioceramics, sol-gel bioactive glass (BG) and mesoporous bioactive glass (MBG) have emerged as highly bioactive due to their excellent textural properties and biocompatibility. However, their textural properties result in different in vitro bioactive responses (Figure 7).

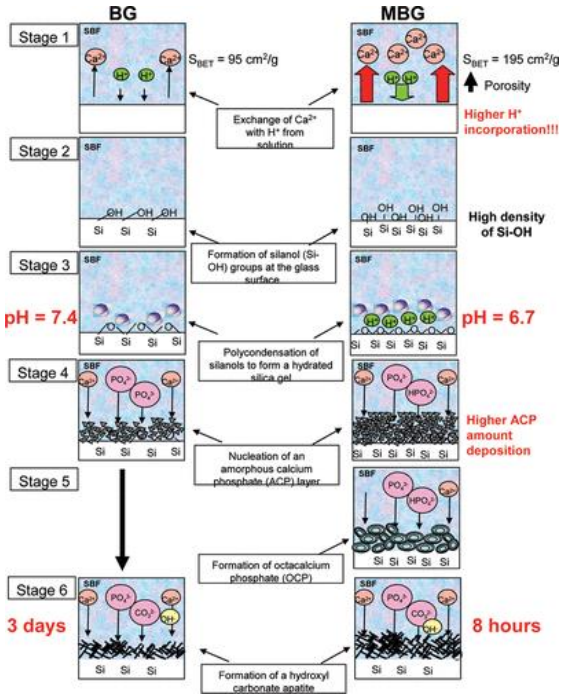

Figure 7. Bioactive mechanism in simulated body fluid of conventional sol-gel glasses (proposed by Hench in 1970) versus bioactive mechanism of mesoporous bioactive glasses proposed in this manuscript (44).

In BG, the textural properties are influenced by chemical composition, with mesopores formed by the random distribution of CaO aggregates within the SiO_2 network during drying and calcination (45). The incorporation of surfactants during MBG synthesis leads to highly ordered mesoporous structures with enhanced textural properties. This facilitates a quicker and better in vitro bioactive response, reducing HCA/HA formation time from a few days (~3 days in BG) to a few hours (~8 hours in MBG).

Researchers are focusing on modifying the composition of bioactive glass by adding or substituting oxides to introduce specific properties. For instance, substituting strontium oxide for calcium oxide in bioactive glasses improves bone bonding and stimulates osteoblast activity, with anabolic and anti-catabolic effects (46). Copper promotes angiogenesis markers, while scaffolds containing zinc increase osteogenesis markers and provide higher antibacterial capacity against methicillin-resistant Staphylococcus aureus bacteria than un-doped glass (47).

1.4.2 Mesoporous Bioactive Glass (MBG)

In 1991, scientists from Mobil Oil Corporation discovered Silica Mesoporous Materials (SMM), a breakthrough recognized for its potential applications in host-guest systems (48–50). SMMs are characterized by their ordered porous structure of SiO_2, high surface area, high pore volume, and regularly ordered pore arrangements. These pores, with sizes ranging from 2 to 50 nm, can be controlled and modified using various synthetic strategies.

The synthesis of SiO_2-CaO-P_2O_5 mesoporous bioactive glasses (MBGs) involves the addition of a non-ionic surfactant as a structure-directing agent in the conventional sol-gel glass synthesis process, utilizing the Evaporation-Induced Self-Assembly (EISA) method (Figure 8) (51). This process, based on sol-gel chemistry, starts with the hydrolysis of silica precursors in organic solvents, which act as the reaction medium. A catalyst is added to accelerate hydrolysis, and a surfactant (usually Pluronic P123®) is dispersed in the solvent to form a supramolecular structure that interacts with the silica. As the solvent evaporates, the surfactant concentration increases, leading to micelle formation once the critical micelle concentration is exceeded. The co-self-assembly of these micelles and silica results in the formation of a mesophase. After gelling, drying, and surfactant calcination, MBG is obtained.

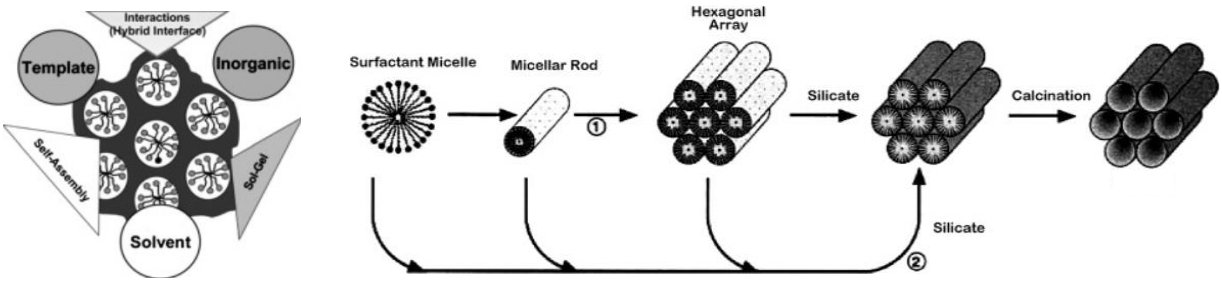

Figure 8. Schematic representation of mesopores formation during the EISA process (52).

MBGs display superior bioactivity compared to conventional sol-gel glasses due to their exceptional textural properties, such as high surface area, pore volume, and uniform pore size. The presence of silanol groups in the mesopore walls allows the incorporation of various biologically important species, enabling controlled release and making them suitable for drug delivery systems.

The formation of the ordered mesoporous arrangement in MBGs is influenced by factors such as the nature and concentration of the surfactant, solvent, pH, and temperature (53–55). The final mesoporous structure is determined by the presence of calcium, phosphorus, and the solvent evaporation temperature. Calcium oxide acts as a network modifier, disrupting the silica network connectivity. Increasing the Ca^{2+} content raises the inorganic/organic volume ratio of the micelles, resulting in a hexagonal phase instead of a cubic one (56). Conversely, the presence of P_2O_5 decreases this ratio because calcium forms amorphous calcium phosphate crystals, leading to a cubic structure (57). Additionally, solvent evaporation temperature significantly affects the final mesostructure, with a transition from a 3D bicontinuous cubic structure to a 2D hexagonal structure as the temperature decreases (57,58).

Silica (SiO_2) is a versatile material with a wide range of structural forms, from crystalline to amorphous. Its structure is based on the SiO_4^{4-} tetrahedron, where a central silicon atom is covalently bonded to four oxygen atoms. These tetrahedra connect by sharing oxygen atoms, forming highly ordered or disordered networks. In crystalline forms such as quartz, cristobalite, and tridymite, the tetrahedra are arranged in a repeating lattice where each oxygen bridges two silicon atoms, creating a fully connected three-dimensional network. In amorphous silica, such as glass or fused silica, the SiO_4 tetrahedra remains connected but lacks long-range periodicity, resulting in a disordered structure. The addition of network modifiers, such as alkali or alkaline earth ions, can disrupt the silica network by breaking Si-O-Si bonds and creating non-bridging

oxygens, significantly altering the material's thermal, mechanical, and optical properties. This adaptability and chemical stability make silica essential in various applications, including construction, electronics, and biomaterials.

In silica-based glasses, Ca functions as a network modifier, significantly impacting the structure and bioactivity of the glass (59) (Figure 9). Due to its ionic radius of 0.99 Å, Ca^{2+} does not directly integrate into the silica network but instead disrupts Si–O–Si bonds, creating non-bridging oxygens that reduce the network's connectivity (60). This structural modification makes the glass more reactive, facilitating ion exchange and dissolution when immersed in aqueous environments. Calcium typically exists in a coordinated environment with oxygen, forming Ca–O bonds that stabilize the disrupted glass network. Its role is critical in the bioactivity of glasses, as calcium ions released from the glass surface interact with phosphate ions in physiological fluids to form calcium phosphate clusters, which later grow into HA. This HA layer is essential for bonding with bone tissue, making calcium crucial for applications like bone regeneration. The presence of calcium also enhances the solubility of the glass, allowing for controlled ion release that supports the formation of HA and promotes bioactivity. Moreover, calcium's network-modifying effect can influence the glass's mechanical and thermal properties by lowering the glass transition temperature and facilitating crystallization under certain conditions (61). Thus, calcium's interaction within silica-based structures not only enables the formation of biologically active surfaces but also contributes to the glass's overall reactivity and performance in biomedical applications.

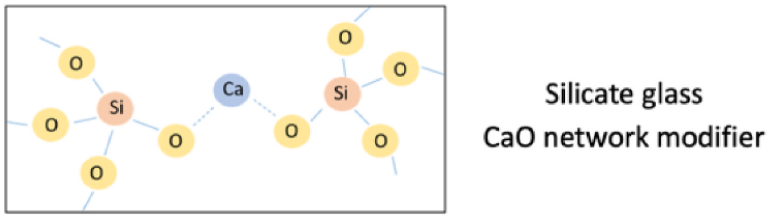

Figure 9. Effect of Ca in the silicate glass structure (60).

1.4.3 Sol-gel Bioactive glasses

Hench bioactive glasses, traditionally produced via the classical melting method, have seen increased interest in Sol-gel synthesis since the 1990s (62). The Sol-gel method, especially for the ternary SiO_2-CaO-P_2O_5 system, has shown faster hydroxyapatite (HA) deposition compared to melt-derived glasses (63).

In the Sol-gel synthesis (64), alkoxide precursors undergo hydrolysis, catalyzed by acids or bases, forming silanol (SiOH) groups. Concurrently, the condensation of silanol-silanol and/or silanol-ester takes place. The resulting sol is then transferred to petri dishes for casting. Continued polycondensation forms interconnected silica nanoparticles during gelation, increasing the viscosity and leading to gel formation. Catalysts may be added to expedite this process.

The aging step involves water byproducts from condensation remaining in the gel pores, allowing localized solution and reprecipitation to increase density and strength. This step is performed at elevated temperatures for several hours or days. During drying, pore water is removed, leaving behind pores with diameters of 1-20 nm. This is conducted at temperatures between 60-130°C. Thermal stabilization involves thermal treatment at 500-700°C to enhance density, strength, and hardness.

Sol-gel glasses are purer and more homogeneous in composition compared to melt-derived glasses. They can form HA with up to 90% silica content, compared to 60% for melt-derived glasses. Sol-gel glasses also have higher porosity and surface area (200-650 m^2/g) compared to melt-derived glasses (1-2 m^2/g). The porous nature of sol-gel glasses allows for the formation of a hydrated layer, maintaining biological activity and facilitating integration with host tissue without residual particles.

In conclusion, Sol-gel bioactive glasses offer significant advantages over traditional melt-derived glasses, particularly in their structural and biological properties, making them highly suitable for medical applications such as bone regeneration (65).

1.5 Antitumoral effect of Gallium (III) compounds

There is an ongoing need to create new medications for cancer treatment. Gallium Nitrate, a type of Group IIIa metal salt, has been shown to inhibit tumor cell growth both in laboratory settings and in living organisms. It has demonstrated efficacy against non-Hodgkin's lymphoma and bladder cancer in clinical studies. Gallium can mimic iron, disrupting iron-dependent processes and tumor cell proliferation. Unlike traditional chemotherapy drugs, gallium nitrate does not cause myelosuppression or cross-resistance, making it a viable option when other treatments fail or when blood counts are low. Due to its potential, newer gallium-based compounds are currently in various stages of preclinical (66).

The chemical and biological properties that make Ga^{3+} a useful analog for Fe^{3+} in biological systems, particularly in cancer treatment are listed below (67):

- Chemical Properties:
    - *Charge and Size*: Both Ga^{3+} and Fe^{3+} have a +3 oxidation state and similar ionic radii (0.620 Å for Ga^{3+} and 0.645 Å for Fe^{3+}), allowing gallium to mimic iron in various biological processes.
    - *Coordination Chemistry*: Ga^{3+} and Fe^{3+} share similar coordination chemistry, forming complexes with similar geometries (tetrahedral ionic radius is 0.47 Å for Ga^{3+} and 0.49 Å for Fe^{3+}). This allows gallium to interact with iron-binding proteins and enzymes like iron.
- Biological Competition (68,69):
    - *Transferrin Binding*: Both Ga and Fe can bind to transferrin, a plasma protein that transports iron in the blood. Ga competes with Fe for binding to transferrin, which can disrupt iron transport and metabolism in cells, particularly in rapidly dividing cancer cells that have a high demand for iron. Ga^{3+}-loaded silica structures could target transferrin receptors on tumor cells, enhancing the specificity of drug delivery to cancerous tissues.
    - *Ferritin Interaction*: Gallium can also bind to ferritin, an iron storage protein, further interfering with iron storage and release, which may contribute to its anticancer effects. Incorporating Ga^{3+} into biomaterials could inhibit ferritin's function, impairing iron homeostasis within tumor cells and promoting their death.
- Iron-Dependent Processes:
    - Enzyme Inhibition: Gallium (III) can inhibit iron-dependent enzymes that are critical for DNA synthesis and cell proliferation, such as ribonucleotide reductase. By substituting for iron in these enzymes, gallium disrupts their function, leading to impaired DNA synthesis and reduced tumor growth. Ga^{3+}-functionalized biomaterials could inhibit tumor cell proliferation by blocking key iron-dependent enzymes, making them effective in cancer therapy.

- *Iron Metabolism Disruption*: By mimicking iron, gallium disrupts normal iron metabolism in cancer cells. Since cancer cells require high levels of iron for rapid proliferation, this disruption can lead to cellular stress and apoptosis.

- Lack of Redox Activity:

  - *Stable Oxidation State*: Unlike iron, which can undergo redox cycling between Fe(II) and Fe(III), gallium remains in the Ga(III) oxidation state. This stability means gallium does not participate in redox reactions that generate harmful free radicals, potentially reducing toxicity compared to iron. Ga^{3+}-loaded LPMS materials could enhance anticancer activity by reducing oxidative stress in tumor cells, promoting their apoptosis.

The similarities between Gallium (III) and Iron (III) allow Ga to effectively interfere with iron-dependent processes in cancer cells, making it a valuable therapeutic agent. Its ability to mimic iron and disrupt key cellular functions, combined with its stable oxidation state, underpins its potential as an anticancer agent.

In tumors, iron also stabilizes the hypoxia-inducible factor (HIF-1α), which regulates angiogenesis (the formation of new blood vessels) and the tumor's resistance to chemotherapy. By interfering with the iron-dependent stabilization of HIF-1α, Ga^{3+} inhibits angiogenesis and reduces the tumor's ability to form new blood vessels, thereby limiting nutrient and oxygen supply to the tumor. This makes tumor cells more susceptible to treatments.

In summary, the similarity between Ga^{3+} and Fe^{3+} allows Ga^{3+} to target and disrupt key iron-dependent mechanisms that are vital for tumor growth, DNA replication, and resistance to therapy. By substituting for iron in these processes, Ga^{3+} effectively blocks tumor proliferation, reduces oxidative stress, and inhibits angiogenesis, thereby making it a promising candidate for cancer therapy.

Typical compounds containing Gallium that are used as anticancer agents include:

- *Gallium Nitrate ($Ga(NO_3)_3$)* (70)*:* This is one of the most studied and used gallium compounds in cancer treatment. It has shown efficacy in treating various types of cancers, particularly non-Hodgkin's lymphoma and bladder cancer. Gallium nitrate works by disrupting iron metabolism in cancer cells, inhibiting cell growth, and inducing apoptosis;

- *Gallium Citrate ($Ga(C_6H_5O_7)$)* (71)*:* Gallium citrate is often used in diagnostic imaging to detect tumors due to its ability to localize in areas of high metabolic activity, such as cancerous tissues. Its role in therapy is less prominent, but it can still contribute to anticancer effects through similar mechanisms as gallium nitrate;

- *Gallium Maltolate ($Ga(C_6H_6O_5)_3$)* (72)*:* This is an orally active gallium compound with promising anticancer properties. It has been studied for its potential to treat various cancers, including prostate cancer and multiple myeloma. Gallium maltolate works by disrupting iron-dependent pathways, inhibiting tumor cell proliferation, and inducing apoptosis;

- *Gallium Chloride ($GaCl_3$)* (71)*:* Gallium chloride is another compound that has been investigated for its anticancer properties. Like other gallium compounds, it interferes with iron metabolism and has shown activity against certain types of cancer cells.

These Gallium compounds exploit the ability of Gallium to mimic iron and disrupt iron-dependent processes in cancer cells, leading to inhibited growth and increased cell death.

In silica-based glasses, Ga plays a dual role, acting both as a network former and network modifier in the glass structure, due to its ability to adopt tetrahedral (CN = 4, where CN is the coordination number) and octahedral (CN = 6) coordination geometry toward the oxygen

atom (73,74) (Figure 10).

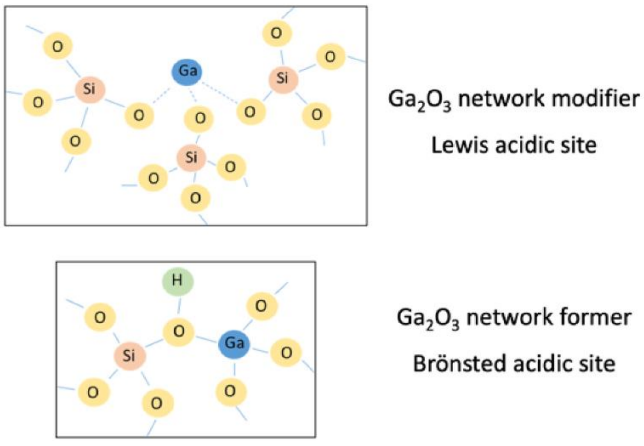

Figure 10. Effect of Ga in the silicate glass structure (60).

When Ga^{3+} ions are incorporated into the silica network in small to moderate amounts, they typically function as network modifiers, breaking Si–O–Si bonds and creating non-bridging oxygens. This disruption weakens the overall silica network, making the glass structure more

open and influencing its physical and chemical properties, such as solubility, ion release, and bioactivity (75). The ionic radius of Ga^{3+} (0.62 Å) is much smaller than that of Ca^{2+} ions, which have a radius of 0.99 Å. This size difference allows Ga^{3+} to substitute for Ca^{2+} more easily within the glass matrix, particularly in calcium phosphate-related regions, which can significantly hinder the formation of HA on the glass surface during exposure to SBF (76).

At higher concentrations, gallium can act as an intermediate oxide, forming more stable Ga–O bonds that can integrate into the glass network itself. In this case, gallium often forms tetrahedral units (GaO_4), which contribute to the glass structure by participating in the silica framework. This integration affects the network's connectivity and rigidity, enhancing the glass's chemical durability and thermal stability (77). However, higher Gallium content also increases the release of Ga^{3+} ions into solution, especially during immersion in biological fluids or water. This release can have important biological implications, as Gallium ions are known for their antimicrobial, anti-inflammatory, and anticancer properties. The controlled release of Ga^{3+} can therefore enhance the therapeutic potential of bioactive glasses, making them suitable for applications like bone regeneration, where controlled bioactivity, antibacterial effects, and ion-mediated healing processes are critical. Additionally, Gallium's ability to interfere with calcium phosphate cluster growth directly impacts the material's ability to bond with bone and form HA, further modifying the bioactive behavior of the glass (60).

1.6 Mechanism of synthesis of Mesoporous silica

The synthesis of these mesoporous materials can be tailored by adjusting the surfactant used as a template, as well as its concentration (78). Other factors, such as temperature, synthesis duration, reagent types, and their molar ratios, also influence the size, shape, and other characteristics of the final product.

These materials feature large surface areas and pore sizes ranging from 2 nm to 50 nm, classifying them as mesoporous materials according to the IUPAC definition (79).

1.6.1 Sol-Gel EISA Process

The Sol-Gel process is a widely utilized wet chemical technique in materials science and ceramic engineering, often referred to as the chemical solution deposition method. In this process, a colloidal suspension, known as a sol, is first prepared to facilitate the growth of an inorganic

network. This sol undergoes gelation, transforming into a gel, which forms a continuous network within a liquid phase. The starting materials, typically metal or metalloid compounds surrounded by reactive ligands, are processed to form a dispersible oxide that creates the sol when exposed to water or a dilute acid. As the liquid is removed from the sol, a gel is produced, and the transition from sol to gel allows for control over particle size and shape. Calcining the gel results in the formation of metal oxides. The sol-gel chemistry primarily involves hydrolysis followed by the condensation of metal alkoxides, leading to the production of oxides or mixed oxides with varying stoichiometries (80). This technique is now extensively used to synthesize mesoporous materials with various morphologies. During the process, templates such as cationic surfactants, triblock copolymers, or small organic molecules can act as structure-directing agents to achieve the desired mesoporous structure (81).

1.6.2 Microwave-assisted synthesis of Silica Mesoporous Materials

Microwaves are electromagnetic waves with frequencies ranging from 300 MHz to 300 GHz, corresponding to wavelengths between 1 m and 1 mm. Despite the relatively low energy in this range, microwaves are widely used for transmitting information and generating heat. The process of microwave heating has been extensively explored by several researchers (82,83). When polar or charged, molecules are exposed to this type of electromagnetic radiation, they attempt to align with the oscillating electromagnetic field. This movement leads to molecular agitation, which in turn dissipates the radiation's energy and raises the temperature of the material.

Numerous susceptor materials have been developed to efficiently convert microwaves into heat, and advances in composite materials have resulted in improved properties, such as increased resistance to oxidation (84,85). The interaction of microwaves with matter creates a reversed temperature gradient compared to conventional heating methods (86). In traditional heating techniques, such as oil baths, heating mantles, or heat blocks, heat is transferred through the surface of the material via convection, causing the outer parts of the container to become significantly hotter than the interior. This can result in uneven heating, leading to the decomposition of the product or reagents, the formation of unwanted by-products, and lower yields, necessitating more extensive purification processes.

In contrast, microwaves penetrate non-metallic materials to a depth that depends on their dielectric properties, enabling more uniform heating from within.

Numerous benefits of microwave heating have been reported, including faster reaction times, higher yields, and selective heating (87). These advantages have spurred the development of microwave-based technologies across a wide range of fields, such as food processing (88), water treatment (89), drying (90), and chemical synthesis (91). These advancements are supported by ongoing research into specialized microwave devices tailored to the needs of each application.

In chemical synthesis, microwaves have been employed not only for organic reactions (92) but also in the production of inorganic materials (93). Materials such as metal oxides, metallic nanomaterials, Metal-Organic Frameworks (94), polymers (95), and graphene-based materials have been synthesized using microwave-assisted techniques (96). While there have been several reviews on the synthesis of microporous and mesoporous materials, including silica, via microwave irradiation, no comprehensive reviews focusing exclusively on silica synthesis using microwave energy have been published. This review aims to provide a detailed overview of the synthesis of mesoporous and non-porous silica materials using microwave-assisted methods over the past decade and highlights their various applications.

Mesoporous materials can also be utilized to store substances within their pores, acting as carriers that protect their cargo from harsh environments. This property is particularly useful for applications in sensing and drug delivery. Due to the uniform heating provided by microwave processing, materials produced through this method have been applied in drug delivery systems, where small particle sizes with narrow distributions are often critical (97).

In experiments where different microwave power levels (ranging from 100 to 450 W) were applied, it was observed that higher power resulted in smaller, more crystalline particles. At 450 W for 1 hour, spherical particles with sizes between 30 and 45 nm and smooth surfaces were produced, along with solids displaying high crystallinity and surface areas of 817 m^2/g. Conversely, lower power levels, such as 100 W, resulted in irregular particles with rough surfaces, while powers of 500 W led to disordered structures. The materials were then evaluated for their ability to adsorb and release ibuprofen.

The MW-assisted synthesis of silica gels offers not only the clear advantage of reducing the synthesis time, but also the possibility of using moderate operating conditions of temperature and pressure.

The hypothesis concerning the impact of microwave heating on the reactions involved in the synthesis and its beneficial effect on the final polymeric network structure has been confirmed in several studies (98). Microwave-assisted synthesis accelerated the reaction kinetics, significantly speeding up the formation of silica structure. However, its role becomes particularly critical during crosslinking reactions, leading to a polymeric network that differs from those produced by conventional methods (99). This unique effect, for example, which has not been observed in other materials like resorcinol-formaldehyde gels, may be attributed to certain functional groups in silica intermediates that absorb microwaves (100).

Microwave heating has been shown to offer a fast and straightforward approach to producing silica structures (98). The resulting materials exhibit greater microporosity, narrower mesopores, and larger surface areas compared to those made using traditional techniques. Furthermore, the same properties typically associated with silica structures can be achieved using this method, but with significant time savings (101,102).

1.7 Mechanism of pores blocking in Mesoporous Silica structures

Pore blocking in mesoporous silica is a significant issue that can limit its effectiveness in applications such as catalysis, drug delivery, adsorption, and sensing. Mesoporous silica materials are characterized by their highly ordered structure and uniform pore sizes, making them ideal for the controlled transport of molecules through their channels (103). However, over time or under certain conditions, these pores can become blocked, reducing their accessibility and impairing performance. Several factors contribute to this phenomenon, which may arise during the synthesis, functionalization, or operational phases of the material's lifecycle (104):

- *Agglomeration of Particles:* Over time, mesoporous silica particles may agglomerate, especially in liquid environments, which leads to pore blockages (105);
- *Adsorption of Molecules:* Large molecules or contaminants may adsorb onto the pore walls and block the entry of smaller molecules, hindering the material's intended use (106);
- *Precipitation of Insoluble Materials:* In certain applications, materials like salts or other compounds can precipitate inside the pores, reducing pore accessibility (107);

- *Excess Functionalization:* Over-functionalization of the pore surfaces (e.g., with organic groups for specific reactivity) can cause pore narrowing or complete blocking (108);
- *Unreacted Precursors:* During synthesis, incomplete removal of surfactants or templates used to create the pores can lead to partial blocking (109).

Strategies to prevent or address pore blocking are several and can be generically resumed as follows:

- *Optimizing Synthesis Procedures* (110)*:* one of the primary causes of pore blocking is the incomplete removal of templates or surfactants used during the synthesis of mesoporous silica. These surfactants, such as Cetyltrimethylammonium Bromide, are necessary for directing the formation of the ordered pore structure, but if not completely removed after synthesis, they can obstruct the pores. To avoid this, optimized template removal methods, such as calcination or solvent extraction, should be employed. In some cases, employing milder conditions like supercritical CO_2 extraction or extended solvent washes can ensure complete removal without damaging the pore structure. Additionally, precise control of the reaction conditions, such as temperature, pH, and the concentration of reagents, is critical to ensuring a uniform pore network that is free of defects or blockages;
- *Controlling Functionalization of Pore Walls* (111): functionalizing the surface of mesoporous silica with organic or inorganic groups is often necessary to tailor the material for specific applications, such as drug delivery or catalysis. However, over-functionalization can lead to pore narrowing or complete blocking. For instance, excessive attachment of large functional groups (e.g., amines or thiols) can restrict pore diameters, limiting the diffusion of guest molecules. To prevent this, functionalization should be carefully controlled to avoid covering too much of the pore surface while still achieving the desired chemical properties. Techniques like selective functionalization, where only the external surfaces or specific regions of the pore network are modified, can also help in retaining pore accessibility while incorporating reactive sites;
- *Preventing Agglomeration and Maintaining Dispersion* (112)*:* mesoporous silica particles tend to agglomerate in colloidal suspensions due to van der Waals forces and other

interparticle interactions. Agglomeration can lead to the obstruction of pore entrances, reducing the material's surface area and blocking molecular access to the interior pores. This issue is particularly problematic in drug delivery systems and liquid-phase catalysis, where good dispersion is crucial. To mitigate this, additives such as surfactants, polymers, or electrostatic stabilizers can be introduced to keep the particles dispersed. Surface modification strategies, such as grafting hydrophilic or hydrophobic groups onto the particles, can also help control the particle interactions and prevent aggregation in different environments;

- *Regeneration and Cleaning of Pores* (113)*:* Over time, mesoporous silica may become fouled with adsorbed species, including organic molecules, biomolecules, or reaction by-products, leading to pore blocking. Regular regeneration procedures, such as washing with appropriate solvents or using ultrasonic baths, can help remove these contaminants and restore pore accessibility. In some cases, more aggressive treatments like thermal regeneration (calcination) may be necessary to burn off organic matter that has accumulated in the pores. However, thermal treatments should be used with caution, as high temperatures may cause pore collapse or structural degradation. Chemical treatments, such as exposure to oxidizing agents (e.g., Hydrogen Peroxide) or acid washes, can also effectively clear organic blockages while preserving the integrity of the mesoporous structure;

- *Tailoring Surface Chemistry to Prevent Fouling* (114): in applications where pore blocking is caused by the adsorption of unwanted molecules or fouling agents, modifying the surface chemistry of the mesoporous silica can be an effective strategy. The interactions between the material and certain fouling agents can be minimized by introducing hydrophilic, hydrophobic, or zwitterionic groups onto the pore surfaces. For example, hydrophilic modifications can help reduce the adsorption of proteins in biological applications, while hydrophobic modifications might repel organic contaminants in chemical processes. Additionally, using self-cleaning surface coatings or antifouling layers on the external surfaces can further prevent clogging, especially in environments with a high concentration of potential blocking agents;

By employing these strategies, ranging from synthesis optimization and controlled functionalization to regeneration techniques and surface modifications, the occurrence of pore

blocking in mesoporous silica can be minimized, allowing the material to retain its high performance across a wide range of applications. These approaches ensure that the pores remain accessible for molecular transport, adsorption, or catalytic processes, thereby enhancing the material's utility and longevity.

1.8 Classification of pores

The proposed pore classification system offers a more structured and detailed framework, aligning with the International Sistem of Units (SI) (115) and covering a broad range of pore sizes from nanometers to millimeters. This new classification seeks to standardize pore size terminology across various scientific fields, improving clarity and consistency (116).

The classification of pore sizes recommended by International Union of Pure and Applied Chemistry (IUPAC) is as follow (115):

- Micropore: <2 nm;
- Mesopore: 2-50 nm;
- Macropore: >50 nm.

The three main pore size ranges proposed with the new classification are (Figure 11) (116):

- Nanopore: 0.1-100 nm;
- Micropore: 0.1-100 μm;
- Millipore: 0.1-100 mm.

The nanopores category is further divided into three subcategories: sub-nanopores (0.1 to 1 nm), inter-nanopores (1 to 10 nm), and super-nanopores (10 to 100 nm). These pores are at the atomic or molecular scale, which is critical in nanotechnology, molecular sieving, and certain types of filtrations and catalysis. The nanopore category in this classification is broader than in the traditional IUPAC system (117), which typically considers pores below 2 nm as micropores.

Moving up in size, micropores' subcategories are sub-micropores (0.1 to 1 μm), inter-micropores (1 to 10 μm), and super-micropores (10 to 100 μm). This classification is significantly different from the IUPAC definition, where micropores refer to pores less than 2 nm. In this new system, micropores encompass a much larger range, making the term more intuitive and consistent with

its common usage in other scientific contexts. Micropores in this range are particularly important in materials like porous ceramics, catalysts, and adsorbents, where pore size influences the material's reactivity and filtration capabilities.

The largest category, millipores, is subdivided into sub-millipores (0.1 to 1 mm), inter-millipores (1 to 10 mm), and super-millipores (10 to 100 mm). These pores are large enough to be seen with the naked eye and are relevant in the study of macroporous structures such as foams, sponges, and certain biological tissues. The inclusion of this category allows for a comprehensive classification system that spans from the nanoscale to structures visible to the naked eye.

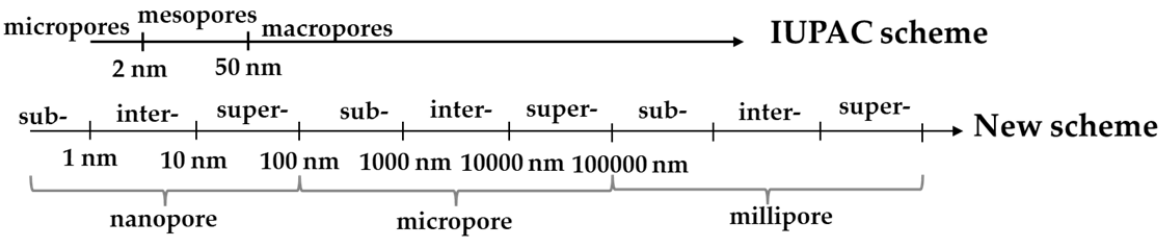

Figure 11. Pores classification due to dimension according to the IUPAC scheme and a new scheme proposed by T. J. Mays et al. *(116)*.

This new classification system is designed to replace the traditional IUPAC classification, which has been criticized for its narrow and sometimes confusing definitions, especially the use of "micropores" to describe very small pores (less than 2 nm). By aligning with SI units and expanding the range of each category, this new system aims to be more intuitive and applicable across different scientific and engineering disciplines.

The new classification provides a more comprehensive and consistent framework for discussing pore sizes, facilitating better communication and comparison of materials across various fields. It covers nine orders of magnitude, from 0.1 nanometres to 100 millimeters, making it applicable to various materials and applications, from nanotechnology and filtration to construction materials and biological tissues.

1.8.1 Mechanism of pores formation in Silica structures

The synthesis parameters of mesoporous silica have been widely investigated to control both the specific surface area and the morphology. Such control is especially important in emerging applications such as thermal insulation, catalysis, sensing, filtering, or drug delivery systems. The template-directed synthesis method has been the most common approach for the preparation of

porous materials with controlled structural features. The template is generally an ionic or non-ionic surfactant, which self-assembles in solution to form ordered structures (118).

A common class of templates is Pluronics. They are amphiphilic non-ionic triblock copolymers composed of a central hydrophobic Poly(Propylene Oxide) (PPO) core flanked by hydrophilic Poly(Ethylene oxide) (PEO) chains with a general PEOn-PPOm-PEOn structure (Figure 12), where n and m denominate the average number of PEO and PPO units in the block copolymer (119).

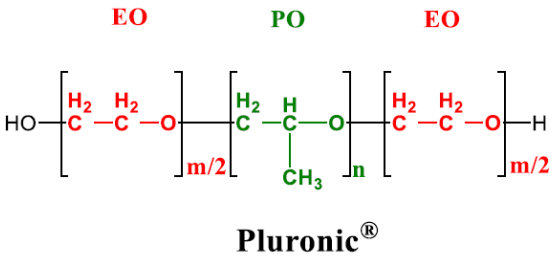

Figure 12. General structure of Pluronic *(119)*.

In the case of Silica structures, and in particular in the Sol-Gel EISA process, well know template is Pluronic P123® (Figures 13 and 14). With the idea to increase pores dimensions in Silica structure, surfactants with longer PEO chains can be used, such as Pluronic F127®. In this way, thanks to the formation of bigger micelles due to the bigger dimensions of the polymer, bigger holes can be obtained (120,121).

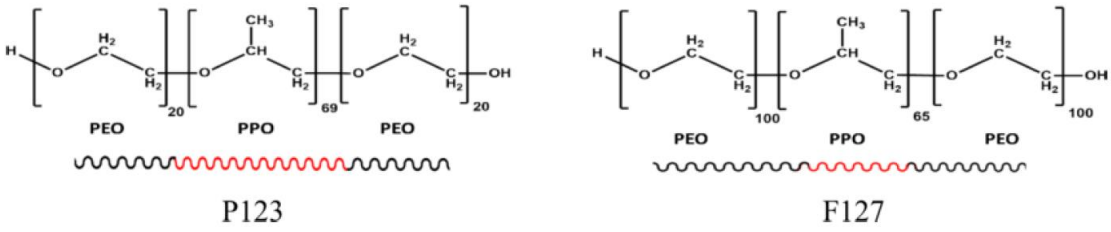

Figure 13. Structure of Pluronic P123® and Pluronic F127®.

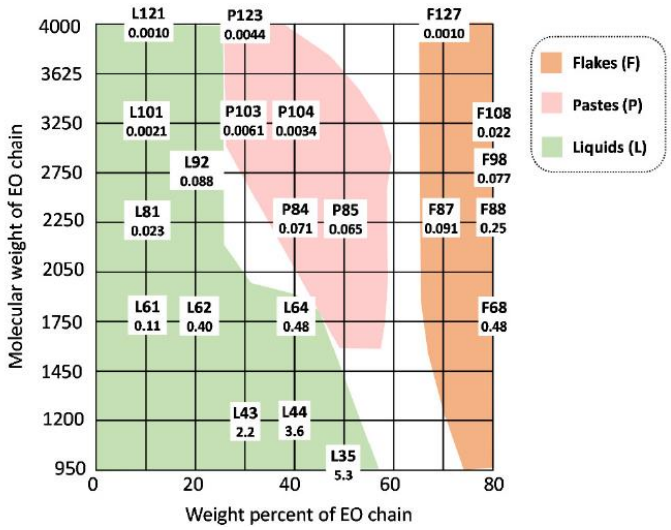

Figure 14. Templates available. In the figure the position of each compound depends on PEO and PPO length. Grid including CMC values at 37 °C (122).

Templates are essential in the synthesis of porous materials, particularly for creating well-defined pore structures. They guide the formation of pores, dictating the size, shape, and connectivity of the resulting material. Templates, often surfactants, self-assemble into ordered structures like micelles, around which the material polymerizes. As the material forms, it solidifies around these structures, creating a porous network that remains after the template is removed.

The size and shape of the pores are controlled by the characteristics of the template and the conditions under which the synthesis occurs, such as temperature and pH. By adjusting these parameters, scientists can tailor the pore structure to specific needs, such as drug delivery or catalysis. The choice of template, whether soft, like surfactants, or hard, like solid colloidal crystals, determines the pore size and arrangement. For instance, soft templates typically produce mesoporous structures, while hard templates can create larger macropores.

After the porous material is formed, the template is removed to leave behind the empty pores. This is typically done through processes like calcination, where the material is heated to burn off the template, or solvent extraction, where the template is dissolved away. The removal method depends on the nature of the template and the desired properties of the final material.

The role of templates extends to influencing the material's structural stability and mechanical properties. The ordered pore structure provided by templating not only offers high surface area but also contributes to the material's mechanical stability, which is important in applications requiring the material to withstand pressure or stress.

In drug delivery, the controlled release of drugs is facilitated by the porous structure created by templates, where the pore size and surface chemistry can be tailored to release therapeutic agents at specific rates.

Porosity can also be influenced by the use of non-polar species, such as Trimethylbenzene; it is capable of entering the hydrophobic core of micelles, causing them to "swell," which allows for the creation of larger pores (123,124).

Chapter 2: Aim.

In the current state of the art MS materials typically feature pore sizes ranging from 2 to 5 nm, which are suitable for small molecules but pose limitations when it comes to loading and delivering larger bioactive agents, such as peptides or proteins. These limitations stem from pore-blocking and restricted loading capacity, which hinder the efficient use of MS in drug delivery systems for larger therapeutic molecules.

In this research, LPMS materials have been developed with significantly larger pores, ranging from 20 to 60 nm and up to 200 to 600 nm - representing an increase in pore size by 4 to 100 times compared to traditional MS. This substantial increase in pore size enables LPMS to better accommodate larger molecules, reduce pore-blocking issues, and improve the loading efficiency for larger bioactive agents. Using advanced synthesis techniques such as hydrothermal and microwave-assisted methods, along with optimized surfactants like Pluronic F127® and mesitylene, your LPMS materials show loading efficiencies that are 3 to 5 times higher than MS, along with enhanced mechanical stability and more controlled release profiles, increasing releasing time up to 2 times passing from MSs to LPMSs structures. These improvements make LPMS highly promising for pharmaceutical and biomedical applications, particularly for the controlled delivery of macromolecular therapeutics.

The synthesis of LPMS structures described in this work, enhances the accommodation, stabilization, and release of bioactive molecules for pharmaceutical applications.

Key objectives include:

- **Synthesis Optimization:** To create LPMS structures with optimized synthesis parameters, including surfactant type and reaction time, using an acidic water solution of tetraethyl orthosilicate (TEOS) and pore agents such as Pluronic® F127 and mesitylene, facilitated by hydrothermal and microwave-assisted methods;
- **Loading Efficiency:** To evaluate the loading capacity of LPMS for bioactive molecules, using Nisin, a polycyclic antibacterial peptide, as a model compound. This involves assessing loading efficiency (LE%) and comparing it with that of classical MS;
- **Structural Characterization:** To characterize the pore structures of LPMS and MS using techniques like N_2 adsorption/desorption and mercury porosimetry, ensuring that LPMS has large pores that can accommodate larger molecules without significant pore blocking;

- **Release Dynamics:** To investigate the release profiles of Nisin from LPMS and MS in SBF, assessing the controlled release capabilities of LPMS compared to MS;
- **Mechanical Strength:** To evaluate the mechanical stability of LPMS structures after prolonged exposure to SBF, ensuring that the LPMS maintains its integrity and strength during and after drug release. Structures' integrity has been demonstrated visually using CSLM;
- **Bioactivity Enhancement:** To explore the incorporation of bioactive ions, such as Ca^{2+} and Ga^{3+}, into LPMS to enhance its potential for bone tissue regeneration and its antibacterial and anticancer properties. This involves studying the release of these ions and confirming their bioactivity using various analytical techniques, like FT-IR, ICP-OES and XRDP;
- **Comparative Analysis:** To compare the performance of LPMS with classical MS in terms of loading efficiency, release profiles, structural integrity, and bioactivity, establishing the advantages of LPMS for pharmaceutical and biomedical applications.

By achieving these objectives, the study aims to demonstrate that LPMS structures offer superior performance in drug loading and release, with potential applications in drug delivery systems and bioactive materials for tissue regeneration.

Chapter 3: Large Pores Mesoporous Silica (LPMS) - New Candidate for Delivery of Big Therapeutics Molecules.

3.1 Introduction

In the current landscape of scientific research, addressing immunoresistance to viruses, bacteria, and fungi is crucial. Antimicrobial peptides (AMPs) have emerged as promising alternatives to traditional antibiotics (125,126), particularly in combating multidrug-resistant infections (126,127). These peptides, with both antimicrobial and anticancer properties, represent a potential new avenue for therapeutic development (128). It has been demonstrated that naturally occurring or synthetic AMPs can be a new functional class of antibiotics (129,130).

Peptides have emerged as promising antimicrobial agents due to their ability to effectively target and kill a wide range of pathogens, including bacteria, fungi, and viruses. AMPs are naturally occurring molecules that serve as part of the innate immune system, providing the first line of defense against infections (131–133). Their primary mode of action is disrupting microbial cell membranes, leading to cell death. This mechanism is less prone to inducing resistance compared to conventional antibiotics, making peptides attractive in the fight against drug-resistant pathogens (134).

Key advantages of using peptides as antimicrobials include:

- *Broad-Spectrum Activity:* Peptides can target a wide range of microorganisms, including Gram-positive and Gram-negative bacteria, fungi, and some viruses (135);
- *Low Resistance Development:* The membrane-disrupting action of AMPs is a physical mechanism, making it harder for bacteria to develop resistance compared to traditional antibiotics that target specific enzymes or pathways (136);
- *Structural Diversity:* Peptides have diverse structures (e.g., α-helices, β-sheets), allowing for customization to target specific pathogens or types of microbial membranes (137);
- *Immunomodulatory Properties:* Some peptides, like human defensins and cathelicidins, not only kill pathogens but also modulate the immune response, bridging innate and adaptive immunity (138).

Despite their potential, challenges like susceptibility to degradation by proteases (enzymes that catalyze the breakdown of proteins by hydrolyzing the peptide bonds between amino acids),

toxicity at high concentrations, short half-lives, and costly production need to be addressed. To overcome these issues, researchers are developing synthetic peptide analogs, known as peptidomimetics, which mimic the structure and function of AMPs but are more stable and resistant to degradation (139).

Peptides are promising as next-generation antimicrobials, particularly in combating multidrug-resistant infections, though further research is needed to address their limitations for widespread clinical use.

However, the effective administration and controlled release of AMPs are challenging due to their susceptibility to peptidase degradation in biological fluids. This degradation leads to reduced stability and a short half-life in the bloodstream (140,141), limiting their clinical efficacy. Enhancing the bioavailability and stability of these peptide drugs is therefore essential for their successful therapeutic application (142).

The action mechanism of different types of antibiotics is shown in Figure 15.

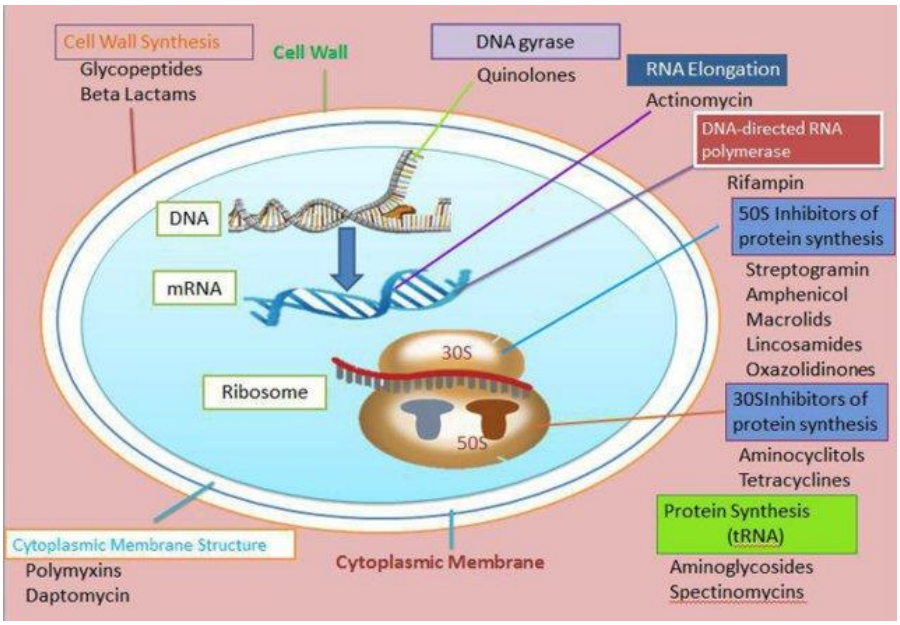

Figure 15. The mechanism of action of different types of antibiotics. Antibacterial action generally falls within one out of four mechanisms, three of which involve the inhibition or regulation of enzymes involved in cell wall biosynthesis, nucleic acid metabolism and repair, or protein synthesis, respectively. The fourth mechanism involves the disruption of membrane structure. Many of these cellular functions targeted by antibiotics are most active in multiplying cells.

Nisin (Figure 16) was selected for our study due to its dimensions (18.37x49.14 Å) and pharmacological activity. The molecular visualization in Figure 1 w6as generated using the Visual Molecular Dynamics (VMD, version 1.9.4a53) software (143). The structural data used for

the visualization was obtained from the Protein Data Bank (PDB), specifically the PDB ID: 1WCO (144). VMD, a widely used tool for molecular modeling, provided the graphical rendering, while the atomic coordinates for the structure were derived from the cited PDB entry. The original publication associated with the PDB ID can be referenced for more information on the structure.

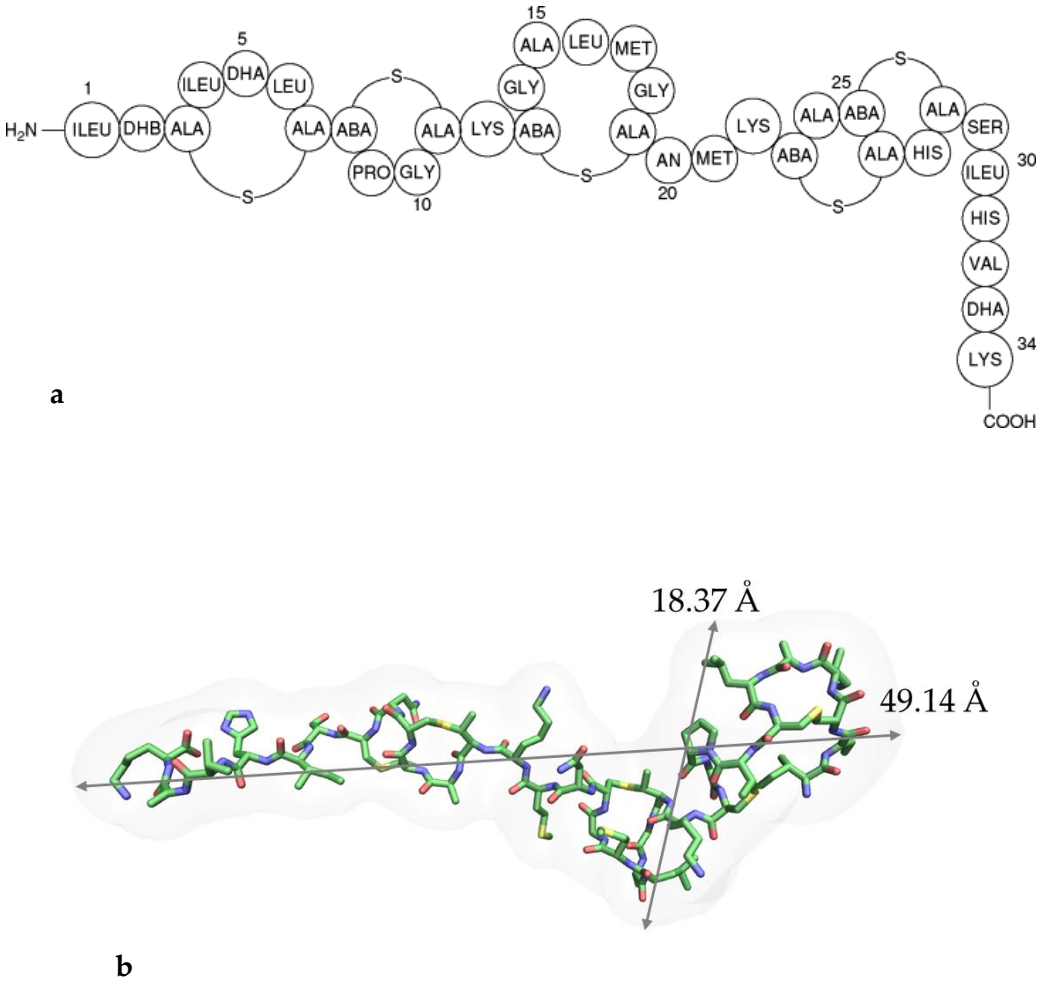

Figure 16. a) The structure of nisin A. ABA, aminobutyric acid; DHA, dehydroalanine; DHB, dehydrobutyrine (β-methyldehydroalanine); ALA-S-ALA, lanthionine; ABA-S-ALA, β-methyllanthionine. **b)** 3-Dimentional structure of Nisin.

Nisin, a polycyclic antimicrobial peptide from the Lantibiotic family - a class of polycyclic peptide antibiotics that contain the characteristic thioether amino acids lanthionine or methyllanthionine, as well as the unsaturated amino acids dehydroalanine, and 2-aminoisobutyric acid. They belong to ribosomally synthesized and post-translationally modified peptides - and are increasingly recognized for their therapeutic potential, especially in addressing the urgent need for novel antimicrobials amidst rising antibiotic resistance (145). Its mode of action is particularly noteworthy due to its dual mechanism: Nisin binds to lipid II, a precursor involved in bacterial

cell wall synthesis, which consists of a lipid carrier attached to a disaccharide-pentapeptide, and serves as a substrate for enzymes that build peptidoglycan, thereby blocking cell wall construction. Simultaneously, it forms pores in the bacterial membrane, leading to leakage of vital cellular components and ultimately causing bacterial cell death. This dual activity is especially effective against Gram-positive bacteria, including multi-drug-resistant strains like *Methicillin-Resistant Staphylococcus Aureus* and *Clostridium Difficile*, which are major culprits in hospital-acquired infections (146). Nisin's low potential for resistance development further enhances its appeal, particularly as resistance to conventional antibiotics continues to surge globally.

From a clinical perspective, Nisin is being explored for various applications. In the realm of skin and soft tissue infections, it has shown promise in treating chronic wounds, diabetic foot ulcers, and burns (147). These infections, which are often complicated by biofilms and antibiotic-resistant bacteria, present significant challenges in clinical management. Nisin, when formulated into topical gels, ointments, or wound dressings, has demonstrated efficacy in reducing bacterial load and facilitating faster wound healing. Another important area of application is oral healthcare (148). Nisin is already an active ingredient in some over-the-counter products, such as lozenges, mouthwashes, and toothpaste, aimed at controlling oral pathogens associated with plaque formation, gingivitis, and periodontal disease. Its ability to combat *Streptococcus mutans* and other oral pathogens without causing major disruptions to the natural oral microbiome is one of its key advantages in this field (149).

Moreover, Nisin's potential extends to gastrointestinal infections, particularly those involving *Clostridium difficile* (150). Its selective activity against pathogenic bacteria, while sparing beneficial gut flora, makes it a promising adjunct in the treatment of conditions like *C. difficile*-associated diarrhea, a serious complication often seen in hospitalized patients after prolonged antibiotic use. Additionally, Nisin's role as a biofilm disruptor is under active investigation (151). Biofilms, which are protective matrices formed by bacterial communities, contribute to chronic and recurrent infections, particularly in cases involving medical implants, catheters, and other indwelling devices. Nisin’s ability to break down biofilms could open new avenues for preventing and treating these persistent infections, which are notoriously difficult to eradicate with traditional antibiotics.

Despite these promising applications, Nisin's clinical use faces several challenges, particularly regarding its stability and bioavailability. Peptides like Nisin are susceptible to degradation by

proteolytic enzymes in the body, limiting their efficacy when administered systemically or orally (152). However, advances in drug delivery technologies, such as encapsulation in liposomes, nanoparticles, or hydrogels, are being explored to enhance Nisin's stability and ensure targeted release at the site of infection (153). These innovative formulations may increase its therapeutic potential, particularly for systemic infections or gastrointestinal applications.

Combination therapies also represent an exciting frontier for Nisin. Studies have shown that when used alongside traditional antibiotics, Nisin can enhance the overall antimicrobial effect, often achieving synergy (154). This is particularly important in the fight against antibiotic-resistant infections, where using Nisin could lower the required dosage of conventional antibiotics, reducing the risk of side effects and slowing the development of resistance. In addition to its antimicrobial properties, Nisin has been identified for its potential anti-cancer activity. Preliminary research indicates that Nisin can induce apoptosis (programmed cell death) in certain cancer cells, particularly in head and neck squamous cell carcinoma (155–158). While this area of research is still in its early stages, it opens the possibility of Nisin being used as a therapeutic agent in oncology.

Regulatory approval for Nisin's therapeutic use is still in progress. It is currently approved by the U.S. Food and Drug Administration as a food preservative and is categorized as Generally Recognized As Safe. Although it is already included in some consumer health products, such as oral care solutions, its widespread clinical application in the treatment of infections or as part of cancer therapy is still under investigation. Early-phase clinical trials have shown encouraging results, particularly in topical and oral applications, but large-scale clinical trials are needed to establish its efficacy and safety in broader medical contexts. Additionally, the cost and scalability of producing peptides like Nisin for pharmaceutical use are concerns that need to be addressed. Peptide-based drugs are generally more expensive to manufacture than small-molecule antibiotics, which could limit their widespread adoption unless more cost-effective production methods are developed.

In conclusion, Nisin represents a promising antimicrobial agent with a broad range of potential clinical applications, particularly against antibiotic-resistant Gram-positive bacteria. Its dual mechanism of action, low resistance development, and potential use in combination therapies make it a valuable candidate in the fight against resistant infections. Furthermore, its emerging roles in biofilm disruption and cancer treatment open exciting new avenues for research.

However, its clinical utility will depend on overcoming challenges related to stability, bioavailability, and production costs, as well as the outcomes of ongoing clinical trials.

To address these challenges, this study focuses on developing a scaffold capable of accommodating and protecting these large molecules to maintain their biological activity. LPMS particles are proposed as innovative supports for this purpose (159). The larger pore sizes of LPMS, comparable to the dimensions of peptides, allow for the internal loading of bioactive molecules, providing both stabilization and protection from enzymatic degradation. In contrast, classical mesoporous silica (MS) with smaller pores (2–5 nm) (160) is inadequate for this task, as its pores are too small to effectively encapsulate large peptides, resulting in only external loading.

The synthesis of mesoporous silica involves the use of TEOS as a silica precursor, with the pore size being adjustable through the selection and quantity of pore-forming agents. By optimizing these parameters, larger pores can be achieved, making LPMS more suitable for peptide encapsulation.

Additionally, the study explores the development of smart materials by coating silica particles with responsive layers that can release the drug in response to environmental changes, such as those occurring in tumor tissues (161,162).

This research aimed to establish a new synthesis method for producing LPMS particles with large pore sizes. The synthesis process was optimized by adjusting the type and quantity of surfactants and reaction times (123). Peptide loading was then tested on both LPMS and MS for comparison. Results from surface area analysis, thermogravimetric analysis, UV-Vis spectroscopy, and elemental analysis showed that LPMS achieved higher peptide encapsulation and a more controlled, prolonged release than MS. SEM-FEG imaging confirmed the improved mechanical resistance and strength of LPMS structures post-release. In contrast, MS did not perform as well, indicating that LPMS is a more effective candidate for delivering large therapeutic molecules.

3.2 Materials and Methods

General procedures

All the chemicals and solvents were purchased with the highest purity grade available and used without further purification unless otherwise specified. To synthesize LPMSs, hydrothermal

treatments were performed with Microwaves (MWs), using FlexiWAVE (Milestone S.r.l., Sorisole, Italy) 230 V.

The FlexiWAVE from Milestone S.r.l. is a highly versatile microwave synthesis platform designed for various chemical reactions, including classic glassware synthesis, high-pressure reactions, and solid-phase synthesis. It is powered by two 950-watt magnetrons, offering a total power output of 1900 watts. This allows for rapid heating and enhanced reaction control, reducing reaction times from hours to minutes.

Key benefits include improved product yields, minimal by-product formation, and reduced contamination. The system also supports high-temperature reactions up to 300°C. ideal for both organic and inorganic synthesis across various research applications. The FlexiWAVE is equipped with advanced sensors for precise temperature control and offer.

Synthesis of LPMSs

The synthesis of LPMS was adapted based on earlier studies (123,124). It is important to notice that this specific reaction for LPMS production and obtaining was not present in the literature and has been completely optimized in terms of way of synthesis, reaction time, type of Pluronic, ratio TEOS:Surfactant, and presence of adjuvant.

In general, tetraethyl orthosilicate (TEOS) is used as the silica precursor, with a Pluronic surfactant serving as the pore-forming agent, and 1,2,3-Trimethylbenzene (TMB) acting as an adjuvant to the surfactant (163,164).

For this study, LPMS synthesis began with an acidic water solution (1.7 % w/w HCl) containing TEOS ($Si(OC_2H_5)_4$, Sigma Aldrich, 98%) , Pluronic® surfactant P123 (PEG-PPG-PEG, Sigma Aldrich, 100%) or F127 ($(C_3H_6O{\cdot}C_2H_4O)x$, Bioreagent, 100%), and TMB ($C_6H_3(CH_3)_3$, Sigma Aldrich, 97%). The solution underwent hydrothermal treatment using MWs heating, initially at 80 °C for 6 hours, followed by a second thermal treatment at 160 °C for 12 hours. The MWs power was adjusted by the instrument to maintain the desired solution temperature.

The general procedure is schematically reported in Figure 17.

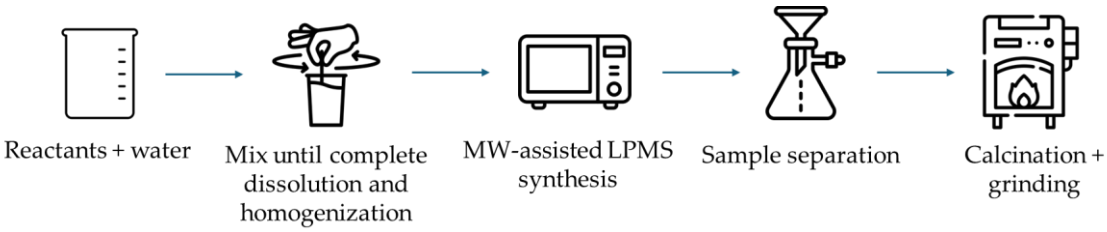

Figure 17. general procedure for LPMS' synthesis.

To optimize the synthesis, various molar ratios of TEOS to Pluronic were tested, along with different reaction times. Additionally, experiments were conducted both with and without TMB to assess its impact on pore size. The different synthesis conditions and their corresponding samples are detailed in Table 2, with samples labelled as LPMS_n_TMB_yh, where "n" indicates the synthesis sequence, "TMB" specifies whether the adjuvant was used, and "y" denotes the reaction time if it deviated from the standard 18 hours (with the ratio of the thermal treatments at 80 °C and 160 °C being consistent across variations).

Table 2. Synthesis conducted.

Sample	Type of Surfactant	Reaction Time (h)	Mass ratio TEOS:Surfactant	Surfac-tant (g)	TEOS (g)	TMB (mL)	HCl 1.7 % w/w (mL)
LPMS_1_TMB	P123	18	1.7	3.4	2.0	0.52	140
LPMS_2_TMB	P123	18	1.7	3.4	2.0	0.26	140
LPMS_1	P123	18	1.7	3.4	2.0	-	140
LPMS_2	P123	18	1.7	3.4	2.0	-	140
LPMS_1_TMB_2h	P123	2	1.7	3.4	2.0	0.52	140
LPMS_1_TMB_4h	P123	4	1.7	3.4	2.0	0.52	140
LPMS_1_TMB_6h	P123	6	1.7	3.4	2.0	0.52	140
LPMS_1_TMB_8h	P123	8	1.7	3.4	2.0	0.52	140
LPMS_3_TMB_8h	P123	8	1.0	2.0	2.0	0.52	140
LPMS_4_TMB_8h	P123	8	1.4	2.8	2.0	0.52	140
LPMS_5_TMB_8h	P123	8	2.0	4.0	2.0	0.52	140
LPMS_6_TMB	P123	18	2.0	4.0	2.0	0.52	140
LPMS_7_TMB_18h	F127	18	2.0	4.0	2.0	0.52	140
LPMS_8_TMB_8h	F127	8	2.0	4.0	2.0	0.52	140
LPMS_9_TMB_8h	F127	8	1.7	3.4	2.0	0.52	140
LPMS_10_TMB_8h	F127	8	1.4	2.0	2.0	0.52	140
LPMS_11_TMB_8h	F127	8	1.0	2.8	2.0	0.52	140

After thermal treatment, synthesis solutions were filtered, and solids collected were dried overnight at 60 °C and then calcined at 2 °C/min up to 700 °C for 3 h, under an air atmosphere to remove the surfactant as well as to stabilize the resultant mesoporous glasses. After quenching in air, the LPMSs were gently milled in an agate mortar and sieved at a mean dimension lower than 355 μm.

Loading tests

Loading tests were conducted using a molecule capable of differentiating between the pore sizes of LPMS and MS. Nisin, an antimicrobial and biocompatible peptide (165–167), was selected for this purpose.

Nisin was sourced with a purity of over 900 IU/mg.

Various concentrations of Nisin loading solutions were prepared, ranging from 0.5 to 20 mg per mL of deionized water. To perform the loading tests, 125 mg of each sample was soaked in 5 mL of the Nisin solution in a thermos-shaker set at 25 °C and 120 rpm for 24 hours. Following the soaking period, the solutions were centrifuged, and the solid samples were collected, washed, and then dried overnight at 70 °C to remove any remaining water.

Elemental analysis was conducted on the dried solids to determine the Nisin content. Additionally, the Nisin concentration in the solutions was measured spectrophotometrically before and after the loading process. This quantification was carried out using a calibration curve, which was established with Nisin concentrations ranging from 0.2 to 1 mg/mL in deionized water.

Nisin Release in SBF

Release tests for Nisin were conducted using the dried solid samples immediately after drying and again after a few weeks to assess the stability of Nisin over time (168). The dried solids were stored in anhydrous and dark conditions, and both sets of release tests yielded consistent results.

For the release tests, 50 mg of the sample was immersed in 5 mL of SBF at 37 °C in a thermos-shaker set to 120 rpm. The release was monitored at various time intervals, ranging from 0.5 to 96 hours. After each interval, the mixture was centrifuged, and the supernatant was collected for spectrophotometric analysis to determine the amount of Nisin released. The spectrophotometric measurements were carried out using a Nisin calibration curve with concentrations between 0.05 and 0.25 mg/mL in SBF. After each measurement, fresh SBF was added to the solid sample, and the process was repeated until complete Nisin release was achieved.

To verify the stability of Nisin in SBF, additional experiments were conducted where Nisin was soaked for extended periods. UV-Vis spectroscopy was used to quantify Nisin, confirming its stability over the time intervals tested in the release experiments.

Physical-Chemical Characterization of Powders

a. Scanning Electron Microscopy with Field Emission Gun (SEM-FEG)

The morphology of the unaltered powdery samples, of the loaded powdery samples, and of samples after soaking in SBF was examined by Scanning Electron Microscopy with Field Emission Gun (SEM-FEG) using a SEM Nova NanoSEM 450 (FEI Company, Milan, Italy) microscope operating at 15 kV.

b. Textural Characterization of Powders

To evaluate the loading behavior of LPMSs, the surface areas were determined by N_2 adsorption/desorption isotherms carried out at T~77 K using ChemiSorb 2750—Micromeritics (Alfatest S.r.l., Rome, Italy). Adsorption data were processed by the standard Brunauer, Emmet and Teller (BET) method (169) to determine the Specific Surface Area (SSA_{BET}). The total pore area and the intrusion volume were determined with a mercury porosimeter, using AutoPore IV 9500 (Micrometrics Instrument Corporation, Alfatest S.r.l., Rome, Italy) operating at a Mercury filling pressure of 1.51 psi.

The pore size can be determined from the pressure value of the liquid through the Washburn equation (Equation (1)), which describes its capillary flow within them.

$$L = \sqrt{\frac{\gamma r t \cos\theta}{2\eta}} \quad (1)$$

where L is the penetration length, γ is the surface tension, r is the pore radius, θ is the contact angle between the penetrating liquid and pore walls, t is the penetration time and η is the dynamic viscosity.

c. UV-VIS Spectroscopy

To evaluate the amount of Nisin loaded inside the structures and the amount released after soaking with SBF, UV-VIS spectra were acquired. UV-visible spectra were recorded using a JASKO V-570 UV/Vis/NIR (JASCO Europe S.r.l., Cremella, Italy) (spectrophotometer at 298 K in the 190–400 nm spectral range employing quartz cells (1 cm optical path).

Nisin quantification was performed at 277 nm.

d. Elemental Analysis (EA)

EA was performed to confirm data collected with UV-VIS spectra, evaluate the amount of Nisin loaded inside the structures and evaluate its stability, using Thermo Scientific™ FLASH 2000 CHNS Anal (Thermo Fischer Scientific Inc., Milan, Italy).

A process blank was prepared and analyzed for all samples, and the results show this taken into consideration.

e. Thermogravimetric Analysis (TG-DTA)

To confirm the presence of stable Nisin onto the structures, TG analyses were performed using a Seiko SSC 5200 in a temperature range between 25 °C and 1000 °C with a heating rate of 1 °C/min.

f. Confocal Laser Scanning Microscopy (CLSM)

A confocal microscope was used to evaluate the presence of Nisin on the surface of powdery samples loaded with Nisin. Nisin fluorescence was obtained using an exciting wavelength of 405 nm and registering the emission in the range 470–580 nm, using Leica TCS SP8 (Leica Biosystems, Milan, Italy).

3.3 Results and Discussion

LPMSs' Morphology Characterization with SEM-FEG

To determine the optimal reaction time and adjuvant quantity, SEM-FEG was used to characterize the samples.

The study began by using a fixed surfactant, specifically P123®, to synthesize MS (170,171). The analysis focused on how the presence and amount of adjuvant affected the structure. For instance, in the sample LPMS_1_TMB_18h, where the adjuvant quantity was double that in LPMS_2_TMB_18h, there was a noticeable difference in the openness of the structure (Figure 15). In contrast, samples LPMS_1_18h and LPMS_2_18h, which were synthesized without any adjuvant, exhibited more compact structures. Based on these observations, the inclusion of an adjuvant was deemed essential, leading to the selection of a 1:3.85 mass ratio of TMB to TEOS.

With the ratio of TEOS to surfactant fixed at 1.7:1 and TEOS to TMB at 3.85:1, as used in LPMS_1_TMB_18h, the reaction time was varied to find the most effective duration (Figure 18). SEM-FEG images revealed that reducing the reaction time from 18 hours to shorter intervals (as low as 2 hours) resulted in increasingly non-homogeneous surface structures. The optimal reaction time was thus confirmed to be 18 hours.

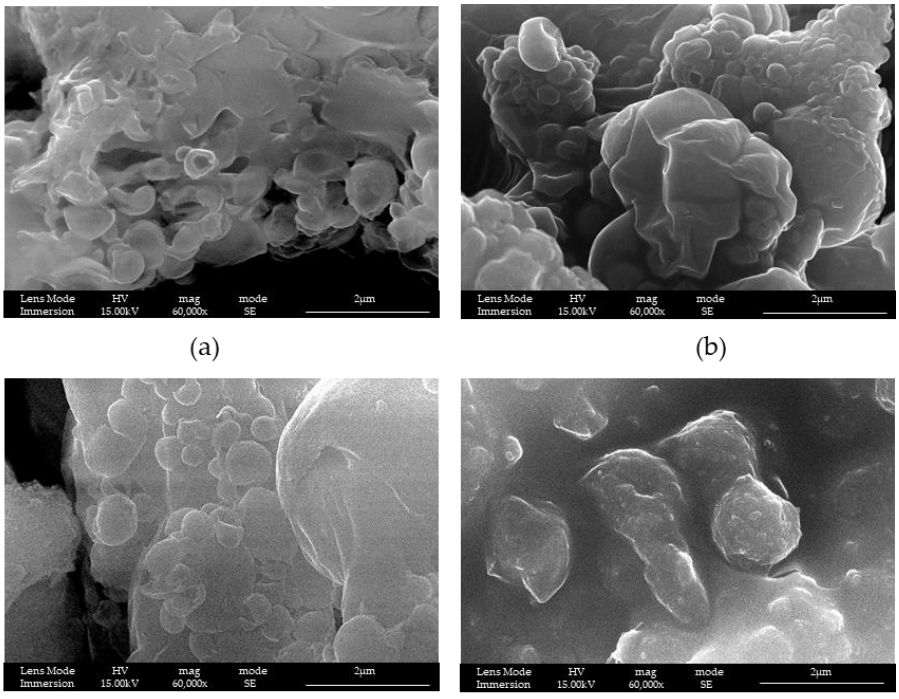

Figure 18. SEM-FEG images of samples (**a**) LPMS_1_TMB_18h, (**b**) LPMS_2_TMB_18h, (**c**) LPMS_1_18h and (**d**) LPMS_2_18h.

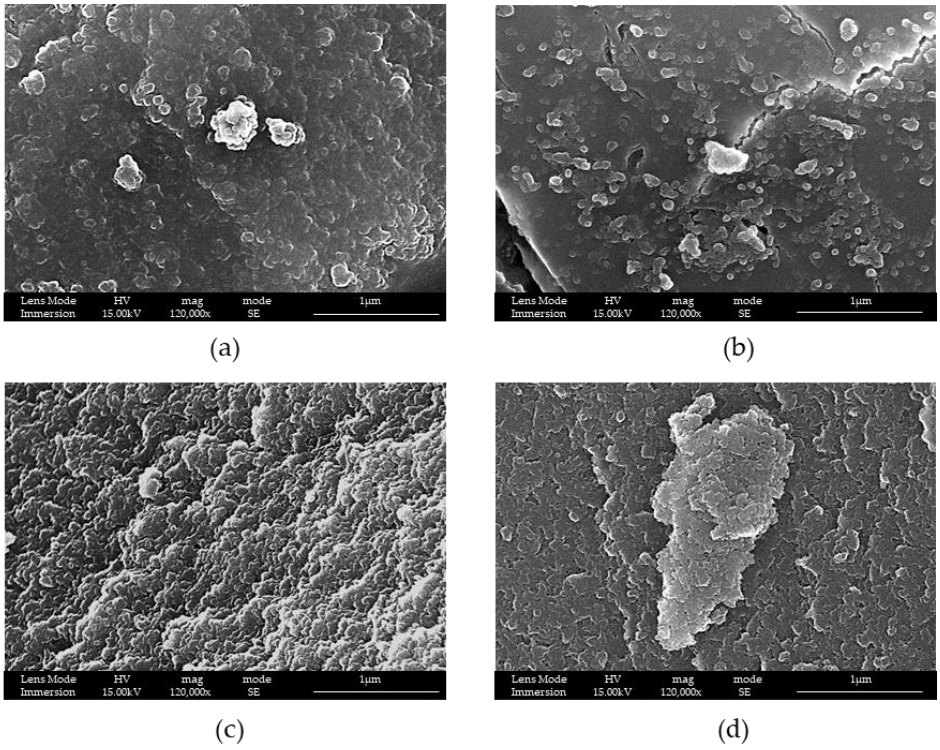

Figure 19. SEM-FEG images of samples (**a**) LPMS_1_2h, (**b**) LPMS_1_4h, (**c**) LPMS_1_6h, and (**d**) LPMS_1_8h.

Figures 18 and 19 demonstrate that increasing the reaction time leads to better aggregation of silica nanoparticles. At 2 hours, the nanoparticles are more dispersed, whereas at 18 hours, the structures appear more sintered and consolidated.

To explore potential improvements in the structure, further experiments were conducted by fixing the reaction time at 8 hours and varying the TEOS:Surfactant mass ratio from 1.0:1.0 to 1.0:2.0. As shown in Figure 20, increasing the amount of surfactant resulted in larger pore sizes, which was the desired outcome. Consequently, the TEOS:Surfactant mass ratio was established at 1:2 for subsequent experiments.

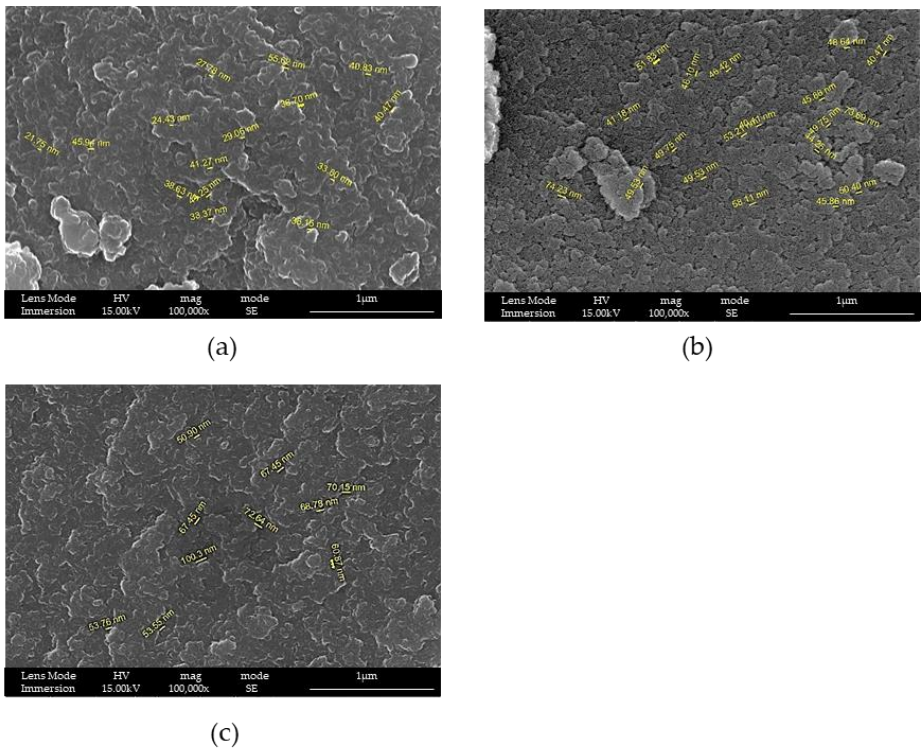

Figure 20. SEM-FEG images of samples (**a**) LPMS_3_8h ratio by mass 1:1, (**b**) LPMS_4_8h ratio by mass 1:1.4 and (**c**) LPMS_5_8h ratio by mass 1:2. SEM images report the cavity dimensions measured with specific SEM-FEG software tool.

While 18 hours of microwave treatment appeared optimal for achieving the desired structure, we also conducted studies on samples subjected to an 8 hour thermal treatment for comparison.

At this stage, a new surfactant, Pluronic® F127, was tested due to its polyethylene oxide chain being five times longer than that of P123 (172). Based on previous findings, a new synthesis protocol was developed: LPMS_7_TMB_18h, which used a TEOS:Surfactant mass ratio of 1:2 and a TEOS:TMB mass ratio of 3.85:1, with an 18 hour reaction time.

Figure 21 illustrates the differences between LPMS_7_TMB_18h and a similar synthesis, LPMS_6_TMB_18h, where the only variable was the surfactant—P123® was used in the latter case.

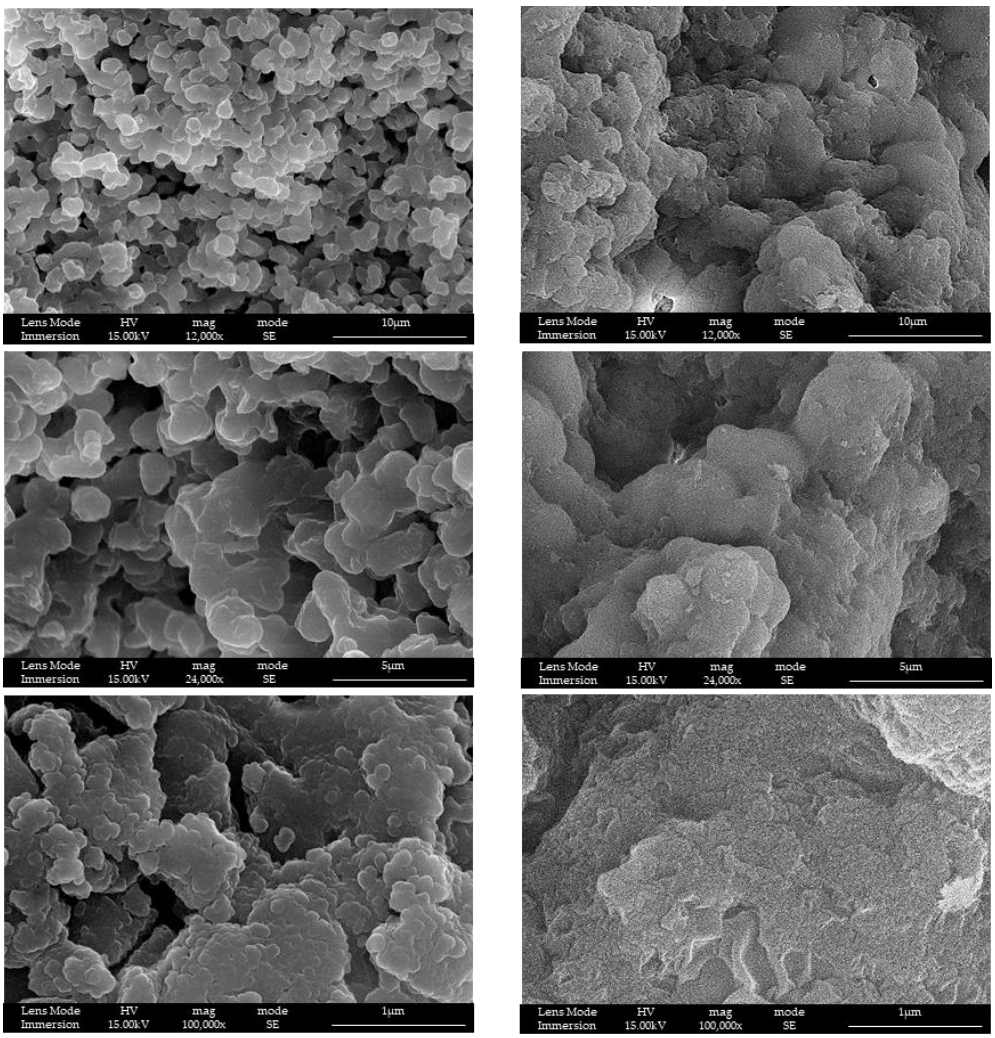

Figure 21. SEM-FEG images of (**a**) LPMS_7_TMB_18h and (**b**) LPMS_6_TMB_18h at different magnifications. The difference between samples stays in surfactant: LPMS_7_TMB_18h is synthesized using F127 and LPMS_6_TMB_18h using P123.

Using F127® as the surfactant significantly improved the morphology of the silica structures, resulting in well-sintered nanoparticles, a more open structure, and larger mesopores. This made F127® the preferred surfactant for our purposes, and it was selected for further experiments.

Subsequent studies were conducted using F127® with an 8 hours reaction time, exploring different TEOS:Surfactant mass ratios, as shown in Figure 22. The results indicated that altering the TEOS:Surfactant ratio with F127® also led to a more open structure. The 1:2 ratio emerged as the most effective.

At this stage, a preliminary analysis was performed to estimate pore sizes and correlate these dimensions with the amount of surfactant used (173). This analysis considered reactions conducted over 8 hours with TEOS:Surfactant mass ratios of 1:2.0, 1:1.7, 1:1.4, and 1:1.0. Both

surfactants, F127® and P123®, were included in the study, and the results are summarized in Table 3.

Table 3. Pores' dimensions obtained for samples.

	Pores Dimensions [1] (nm)	
m TEOS: m Surfactant	**Pluronic® F172**	**Pluronic® P123**
1:2.0	89,7	76,8
1:1.7	64,2	55,1
1:1.4	61,3	43,6
1:1.0	43,5	37,1

[1] Pores' dimensions were calculated as the average of 30 measures collected with the length tool of SEM-FEG software.

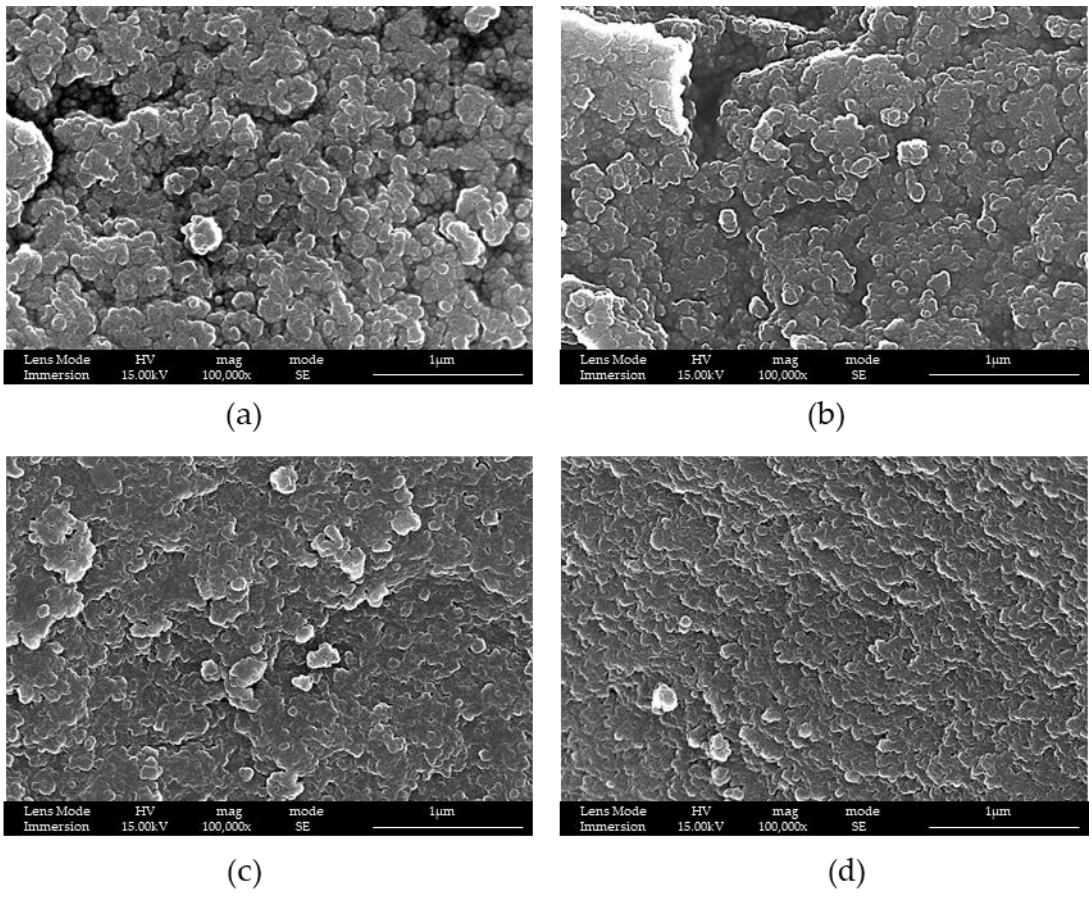

Figure 22. SEM-FEG images of samples (a) LPMS_8_TMB, (b) LPMS_9_TMB, (c) LPMS_10_TMB and (d) LPMS_11_TMB. Ratios of TEOS:Surfactant are respectively (a) 1:2, (b) 1:1.7, (c) 1:1.4 and (d) 1:1.0.

The estimation revealed a linear relationship (Figure 23) between pore size and the amount of surfactant used in the synthesis, specifically the mass ratio. Additionally, due to the longer carbon chain of F127®, this surfactant produced larger pores compared to others (174).

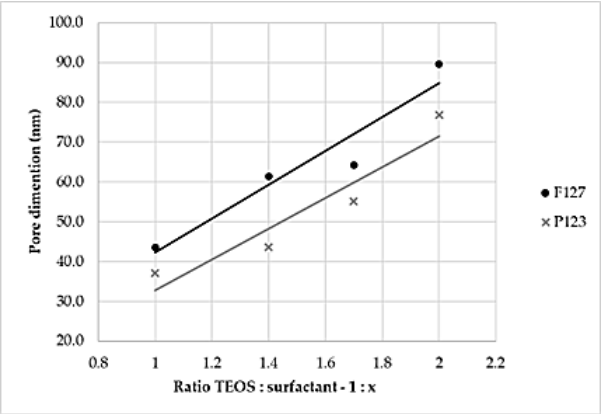

Figure 23. Graph of linear correlation between pores' dimensions (calculated with the length tool of SEM-FEM software ESPRIT 2.1) and ratio of TEOS:Surfactant used for the syntheses.

Based on our findings, a TEOS:Surfactant mass ratio of 1:2.0, using F127® as the surfactant, was determined to be optimal for our purposes. This conclusion was reached through exploratory studies, and the samples selected for further investigation were thoroughly characterized (see Section: Textural Characterization of Powders at page 50, subsection of Section 3.3).

To summarize our key findings:

- The inclusion of an adjuvant, specifically TMB, was essential for achieving larger pores;
- Longer reaction times yielded more compact structures, so samples from both 8-hour and 18-hour reactions were chosen for further analysis;
- F127®, with its larger molecular structure, was the most effective surfactant for creating larger pores;
- A 1:2 TEOS:Surfactant mass ratio consistently produced larger pores, solidifying this as the preferred ratio.

Considering these insights, the samples selected for subsequent studies were LPMS_8_TMB_8h and LPMS_7_TMB_18h.

Additionally, SEM-FEG characterization (Figure 24) was conducted on these structures, which served as references in loading and release tests. Reference structures included classical mesoporous silica (MS) and silica containing only micropores (without mesoporous silica, WMS).

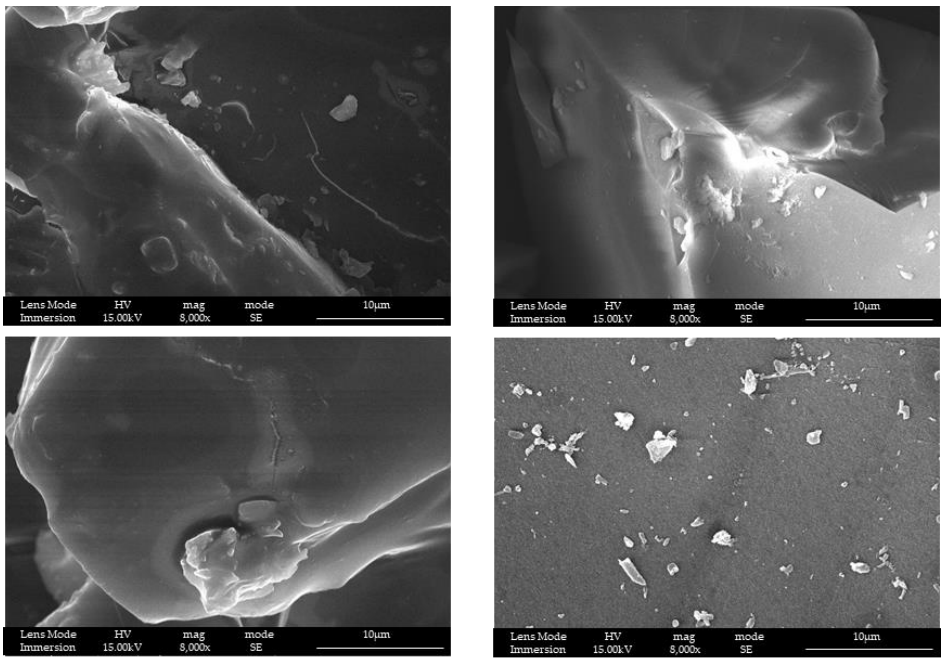

Figure 24. SEM-FEG images of samples (**a**) MS and (**b**) WMS at different magnifications.

It is possible to see, that both structures look compact if compared with the same magnification of LPMS_8_TMB_8h or LPMS_7_TMB_18h, respectively, reported in Figures 18 and 19.

Textural Characterization of Powders

To evaluate and compare the textural properties of the samples, N_2 adsorption/desorption and mercury intrusion measurements were conducted. These analyses provided data on the specific surface area (SSA_{BET}), total pore area (A_P), and total intrusion volume (V_P). The SSA_{BET} was determined using the N_2 adsorption/desorption method, averaging results from three independent measurements. The A_P and V_P values were obtained through mercury intrusion.

Table 4 presents the textural parameters of the samples. The adsorption/desorption isotherms, which were used to calculate surface area values, are shown in Figure 25. A distinct difference in behavior between the MS and LPMS samples is evident from Figure 25. The dashed lines indicate significant intrusion into large pores for LPMSs, a feature not observed in the MS and WMS samples.

Table 4. SSA_{BET}, A_P and V_P of samples subjected to loading and release tests.

Sample	SSA_{BET} (m^2/g)	A_P (m^2/g)	V_P (mL/g)
LPMS_8_TMB_8h	309 ± 15	421	2.36
LPMS_7_TMB_18h	330 ± 17	499	3.57
MS	323 ± 16	289	1.49
WMS	404 ± 21	50	0.78

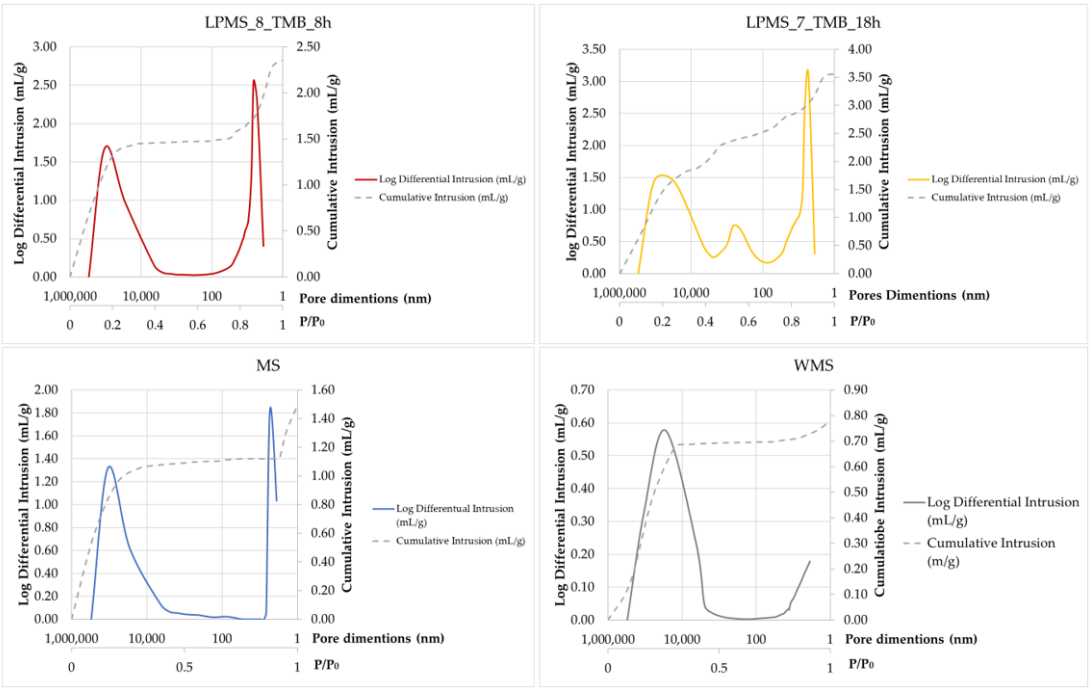

Figure 25. Adsorption/desorption isotherms based on which the surface area values were obtained. From cumulative intrusion (dashed line), it is possible to notice a different behavior between MS and LPMS.

The specific surface area (SSA_{BET}) of the samples studied did not show significant variation among the different types. However, WMS exhibited the highest SSA_{BET} value, likely due to the presence of micropores, which notably contribute to an increased surface area. On the other hand, LPMS_8_TMB_8h and LPMS_7_TMB_18h displayed SSA_{BET} values consistent with those typically observed in classical MS (175). This observation aligns with the other textural parameters, such as total Pore Area (A_P) and total intrusion Volume (V_P), which were considerably higher in LPMS samples compared to other structures (176).

The A_P values were found to be lowest in WMS, which aligns with expectations since this sample only contains micropores, and the porosimeter used is unable to measure such small pore areas. For the MS samples, the SSA_{BET} and A_P values were comparable, whereas LPMS samples

exhibited lower SSA_{BET} compared to A_p. This discrepancy can be attributed to the different measurement techniques: SSA_{BET} was determined through N_2 adsorption/desorption, which primarily measures surface layers, while A_p was measured using mercury intrusion, which is capable of penetrating larger pores that nitrogen cannot, leading to higher A_p values compared to SSA_{BET} (177).

The mercury impregnation method used is limited to detecting pores within the range of 3.5–300 μm. Results from the mercury porosimetry, along with the classification of pore sizes based on the IUPAC standards (178) and a newer classification proposed by T. J. Mays et al. (179), are presented in Figure 26. According to these classifications, supermicropores can be considered as interparticle pores. Pores smaller than 10 μm are categorized into inter-nanopores (1–10 nm), super-nanopores (10–100 nm), and sub-micropores (100–1000 nm). The samples studied exhibit varying pore characteristics, with the type and quantity of pores present in their structures summarized in Table 5. As it is possible to notice from Figure 25, LPMS_8_TMB_8h and LPMS_7_TMB_18h show a high number of pores in the range of 3-10 nm, more than MS's pores amount in the same range. Then, LPMS_8_TMB_8h and LPMS_7_TMB_18h show a big amount of pores in the range 10-30 nm, not shown by MS. Lastly LPMS_7_TMB_18h has pores also in the range 500-600 nm, which no other sample has.

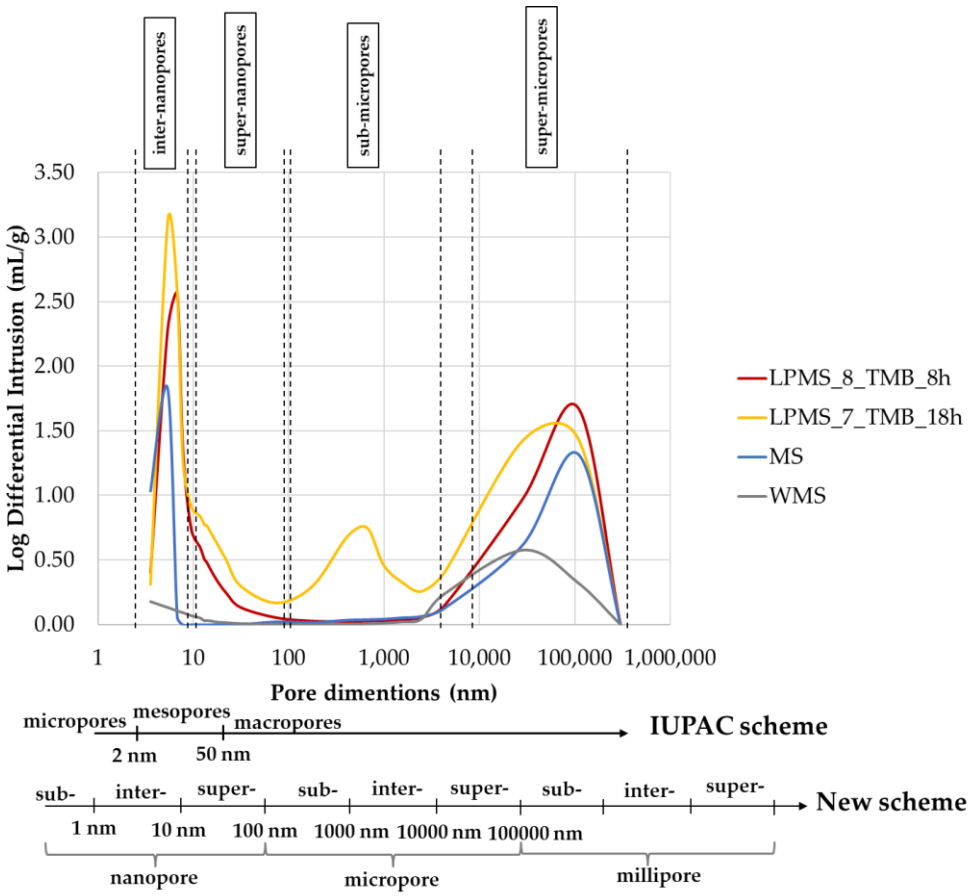

Figure 26. On the top: results obtained with the mercury porosimeter, and a graph of the distribution of pore volume as a function of pore size. In the bottom: pore classification due to dimension according to the IUPAC scheme and a new scheme proposed by T. J. Mays et al. (179).

Table 5. Type and number of pores of samples at a certain range of dimensions.

	3–10 nm	10–30 nm	500–600 nm	10–200 μm
Sample	**Inter-Pore**	**Super-Nanopore**	**Sub-Micropore**	**Super-Micropore**
LPMS_8_TMB_8h	++++	++	-	++++
LPMS_7_TMB_18h	+++++	+++	+++	++++
MS	+++	-	-	++++
WMS	+	-	-	++

* the number of "+" schematically indicates the number of pores at a certain dimension.

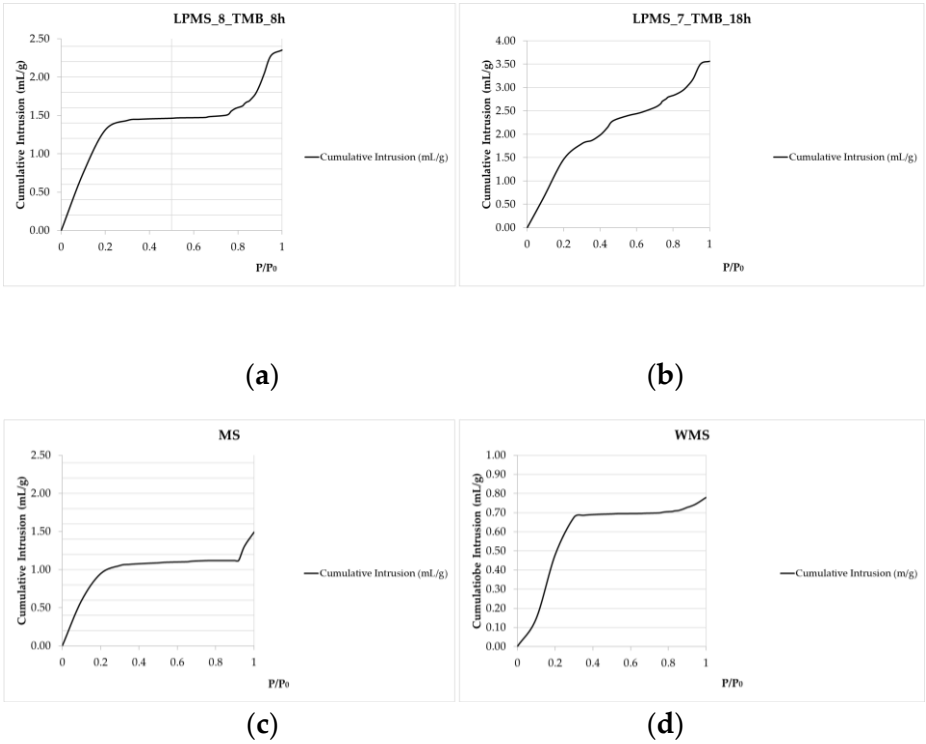

Figure 27. BET surface area analysis results: N_2 adsorption isotherm plots of samples (**a**) LPMS_8_TMB_8h, (**b**) LPMS_7_TMB_18h, (**c**) MS, (**d**) WMS.

In Figure 27 are reported N_2 adsorption isotherm plots of all samples. The different samples can be classified, according to the IUPAC classification of pores (180), into different porous structures:

- LPMS_8_TMB_8h shows the typical adsorption isotherm of type V and VI mesoporous structures;
- LPMS_7_TMB_18h shows the typical shape of type IV, V, and VI, which means that it contains meso- and macroporous structures. It is widely accepted that there is a correlation between the shape of the hysteresis loop and the texture (e.g., pore size distribution, pore geometry, and connectivity) of a mesoporous material.
- MS and WMS show types of isotherms that are characteristic of microporous adsorbents (type I).

Nisin loading tests

The efficiency of the loading of a molecule into a structure can be calculated in different ways, using the following: loading efficiency percentage (LE%), loading percentage (Loading%) or loading capacity percentage (LC%).

The loading efficiency percentage (Equation (2)) considers the only amount of Nisin loaded inside the structure as a function of the initial quantity used for loading (181):

$$LE\% = \frac{Amount\ of\ Nisin\ loaded\ (mg)}{Initial\ amount\ of\ Nisin\ (mg)} \cdot 100 \quad (2)$$

The initial amount of Nisin was determined directly using a spectrophotometric quantification of the concentration of the loading solution; then, the amount of Nisin loaded can be determined as the difference between the initial concentration and the concentration after loading, which is always determined by spectrophotometric measure.

The loading percentage (Equation (3)) considers the amount of Nisin loaded as a function of the total weight of the loaded structure (182):

$$Loading\% = \frac{Amount\ of\ Nisin\ loaded\ (mg)}{Weight\ of\ loaded\ structure\ (silica{+}Nisin)\ (mg)} \cdot 100 \quad (3)$$

Loading% can be also calculated, to compare results, using the EA results as follows (Equation (4)):

$$LE\% = \frac{\%\ C\ determined\ with\ EA}{Theorethical\ \%C} \cdot 100 \quad (4)$$

Finally, the loading capacity percentage was calculated as a function of the amount of Nisin per milligrams of silica (Equation (5)) (183,184):

$$LC\% = \frac{Amount\ of\ Nisin\ loaded\ (mg)}{Silica\ amount\ (mg)} \cdot 100 \quad (5)$$

EA was performed on solids collected after loading and dried overnight. In Table 6, the EA and samples are reported and were labeled as "sample_name_x" in which x indicates the concentration of Nisin (in mg/mL) in the loading solution.

Table 6. Results of EA performed on loaded structures dried overnight at 70 °C.

Sample	%C	%H	%N	%S
LPMS_8_TMB_8h_0.5	0.78	0.36	0.25	0.00
LPMS_8_TMB_8h_1	0.80	0.31	0.26	0.00
LPMS_8_TMB_8h_1.2	1.88	0.58	0.67	0.08
LPMS_8_TMB_8h_1.35	1.96	0.50	0.58	0.00
LPMS_8_TMB_8h_5	7.21	1.30	2.17	0.00
LPMS_8_TMB_8h_10	10.27	1.99	3.36	0.50
LPMS_8_TMB_8h_20	13.05	1.85	4.24	0.64
LPMS_7_TMB_18h_0.5	0.58	0.23	0.22	0.00
LPMS_7_TMB_18h_1	0.97	0.30	0.39	0.00
LPMS_7_TMB_18h_1.2	1.49	0.36	0.52	0.00
LPMS_7_TMB_18h_1.35	1.83	0.48	0.55	0.08
LPMS_7_TMB_18h_5	6.56	1.09	2.20	0.32
LPMS_7_TMB_18h_10	10.99	1.35	3.79	0.00
LPMS_7_TMB_18h_20	11.70	1.60	4.02	0.20
MS_0.5	0.51	0.08	0.15	0.00
MS_1	0.73	0.10	0.22	0.00
MS_1.2	0.92	0.13	0.28	0.00
MS_1.35	1.01	0.15	0.30	0.00
MS_5	4.12	0.83	1.30	0.06
MS_10	6.77	0.89	2.21	0.05
WMS_0.5	0.29	0.32	0.11	0.00
WMS_1	0.39	0.69	0.15	0.00
WMS_1.2	0.54	0.00	0.20	0.00
WMS_1.35	0.46	0.08	0.00	0.00
WMS_5	1.06	0.61	0.38	0.00
WMS_10	7.85	1.14	2.77	0.24
WMS_20	10.09	1.70	3.41	0.43

Elemental analysis (EA) was used to calculate the loading percentage of Nisin and assess its stability within the structures. As shown in Table 5, the loading percentage corresponds well with the concentration of the loading solution - higher concentrations result in higher percentages of each element within the structures.

To investigate the presence of Nisin on the surface of the structures, a plot of %N *vs* %C obtained from EA was created for all samples (Figure 28). The slope of the linear regression from this plot was then compared to the %N *vs* %C ratio calculated for pure Nisin. Based on Nisin's molecular formula ($C_{143}H_{230}N_{42}O_{37}S_7$), the expected %N/%C ratio is 0.343, which closely matches the experimentally obtained ratio of 0.333 from the linear regression. This strong correlation indicates that the Nisin loaded into the structures remain intact.

However, to fully confirm that the Nisin is non-degraded and still present within the structures after several weeks, a UV-Vis spectrophotometric analysis is required. This aspect will be discussed further next Section.

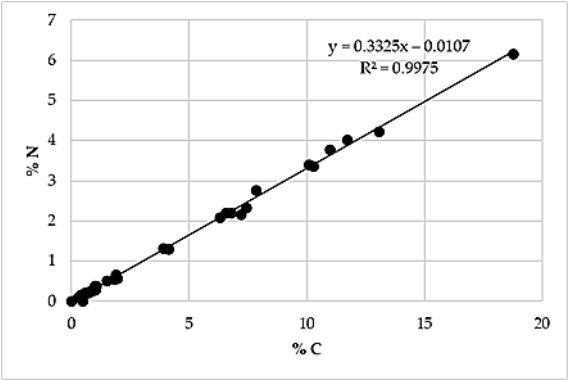

Figure 28. Linear regression was obtained by plotting %N depending on the %C obtained from EA. In the graph, all studied and loaded samples are reported.

When comparing the LE%, LC%, and loading percentage as shown in Table 7 and Figure 29, it's evident that the LE% for LPMS_8_TMB_8h and LPMS_7_TMB_18h remains relatively stable across different loading concentrations, consistently falling within the 50–90% range. In contrast, the LE% for MS is significantly lower, ranging between 20–30%. For WMS, the LE% varies exponentially, indicating a process influenced by precipitation control. Similar trends are observed in the loading percentage.

These differences are primarily due to pore size: LPMSs have much larger cavities that can accommodate more Nisin, resulting in a loading capacity that is three to four times higher than that of traditional structures. In MS and WMS, Nisin tends to remain on the surface, leading to a detected amount that is merely the precipitated Nisin. This surface-level loading leads to faster, less controlled release compared to LPMSs. As for LC%, all samples exhibit the trend where a higher concentration of Nisin in the solution correlates with a greater quantity being trapped or recovered from the surface.

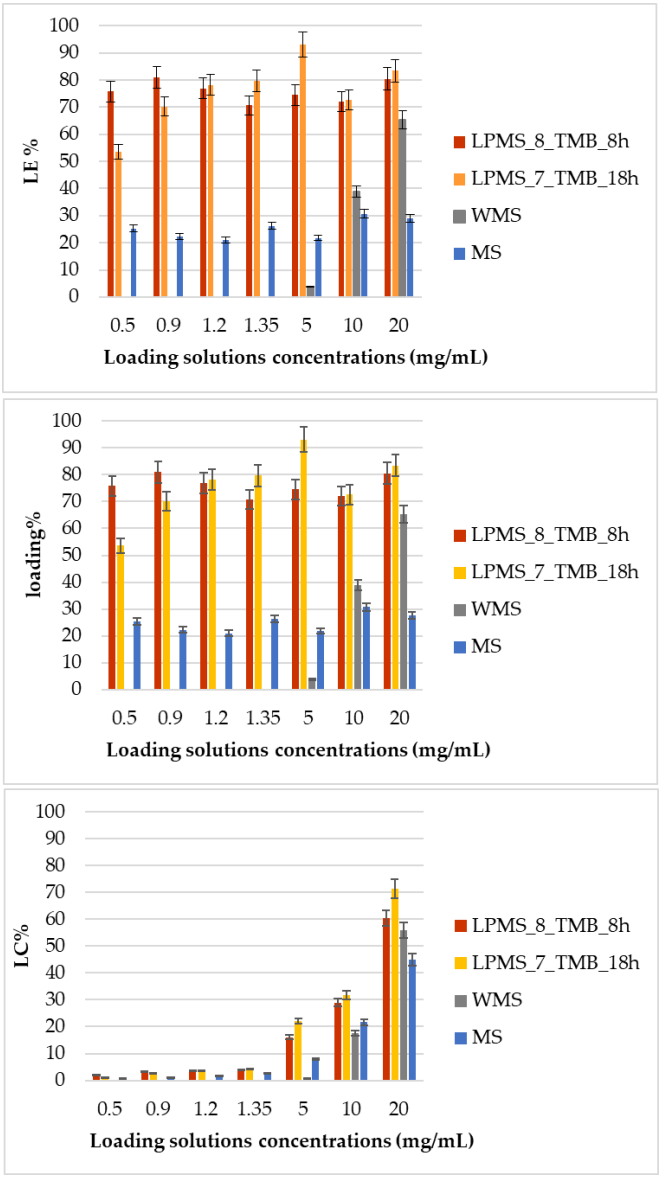

Figure 29. LE%, loading% and LC% of all samples reported in Table 7 are graphed in a bar graph to better understand and compare data collected for LPMSs, MS and WMS.

Table 7. LE%, LC%, loading% and loading% calculated with EA of all samples studied.

Sample	LE%	LC%	Loading%	Loading% Calculated with EA
LPMS_8_TMB_8h_0.5	75.8	1.9	1.8	1.7
LPMS_8_TMB_8h_1	81.0	3.1	3.0	1.7
LPMS_8_TMB_8h_1.2	76.9	3.6	3.5	3.8
LPMS_8_TMB_8h_1.35	70.7	3.8	3.7	4.0
LPMS_8_TMB_8h_5	74.5	16.1	13.8	14.2
LPMS_8_TMB_8h_10	72.1	29.0	26.6	20.2
LPMS_8_TMB_8h_20	80.5	60.4	43.0	25.6
LPMS_7_TMB_18h_0.5	53.6	1.2	1.2	1.3
LPMS_7_TMB_18h_1	70.2	2.5	2.5	2.0
LPMS_7_TMB_18h_1.2	78.2	3.5	3.4	3.0
LPMS_7_TMB_18h_1.35	79.7	4.3	4.1	3.7
LPMS_7_TMB_18h_5	93.1	22.1	18.1	12.9
LPMS_7_TMB_18h_10	72.6	31.8	24.1	21.6
LPMS_7_TMB_18h_20	83.5	71.4	41.7	23.0
MS_0.5	25.3	0.9	0.9	1.0
MS_1	22.2	1.2	1.2	1.5
MS_1.2	21.0	1.6	1.5	1.8
MS_1.35	26.2	2.6	2.5	2.0
MS_5	21.8	7.9	7.3	8.1
MS_10	30.7	21.6	17.8	13.3
MS_20	29.0	45.0	27.6	26.8
WMS_0.5	0.0	0.0	0.0	0.6
WMS_1	0.0	0.0	0.0	0.8
WMS_1.2	0.0	0.0	0.0	1.1
WMS_1.35	0.0	0.0	0.0	0.9
WMS_5	3.8	0.9	0.9	2.1
WMS_10	38.9	17.6	15.0	15.4
WMS_20	65.3	55.9	35.8	19.7

The Loading% values obtained through EA align closely with those calculated using spectrophotometric methods. TGA-DTA was performed on samples with comparable LC% -

specifically, LPMS_8_TMB_8h_1.35, LPMS_7_TMB_18h_1.35, MS_1.35, and WMS_5 - to assess Nisin decomposition within the same mass range.

BET analysis was conducted on all loaded samples to assess the surface area (SSA) behavior of LPMS and MS. The SSA_{BET} values, plotted against LC% (Figure 30), reveal that LPMSs exhibit a smaller reduction in SSA compared to MS. This difference can be attributed to the gradual filling of pores in LPMSs, followed by surface coverage at higher concentrations, leading to a slower decrease in SSA_{BET}. In contrast, MS samples experience more rapid pore-blocking (185,186), a phenomenon commonly observed in mesoporous materials. Additionally, surface analysis highlights the distinct behavior of WMS compared to the other samples.

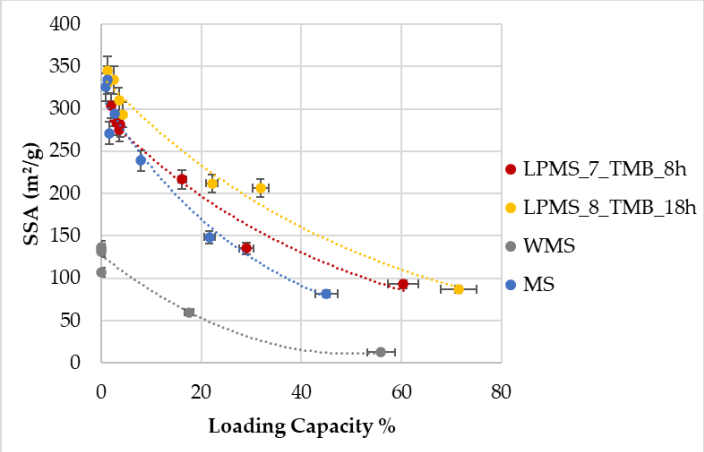

Figure 30. SSA_{BET} determined on unadulterated powders and on loaded powders, plotted as a function of LC%. Data are reported as a mean of three different measures performed on three different amounts of sample.

Thermogravimetric analysis (TG-DTA)

TGA results (Figure 31) corroborate previous findings, with the observed mass loss matching the Nisin content determined by EA and UV-VIS spectroscopy (Table 8). Unprocessed samples were also analyzed as a reference to quantify the mass loss due to Nisin decomposition. The Thermo Gravimetric Derivative Graph (DTG) (Figure 32) indicates a delayed decomposition relative to pure Nisin, likely due to interactions between Nisin and the silica surface. The DTG profiles closely resemble those of pure Nisin, confirming that Nisin remains intact and stable within the structures. The initial peak at 300°C is associated with Nisin pyrolysis (*), while the second peak around 480°C corresponds to peptide structure decomposition (**) (187).

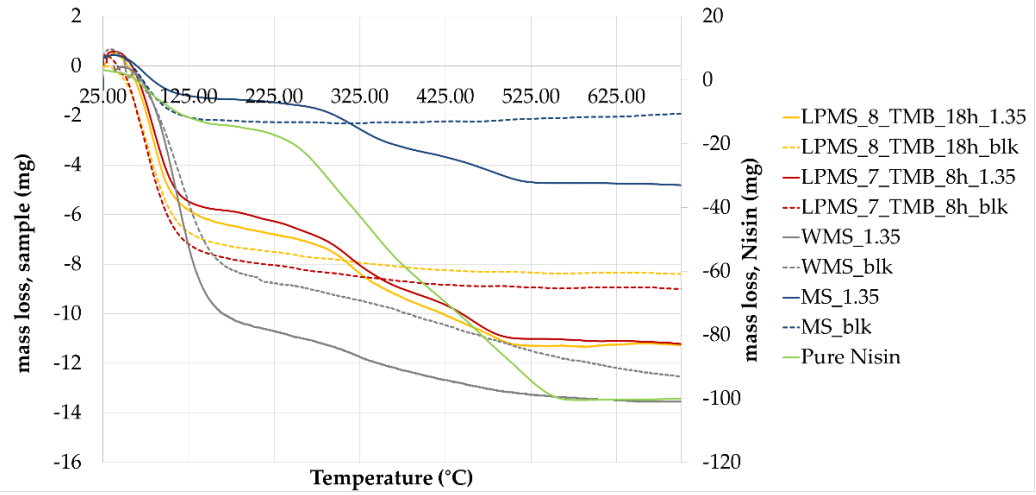

Figure 31. TG graph of loaded samples (full lines) and unprocessed samples (dashed lines). From the differences between curves, it is possible to calculate the loss in mass related to the Nisin content.

Table 8. Total amount of Nisin (calculated as LC%) inside structures determined with different analyses.

	Nisin Content—Different Determination Techniques	
Sample	**UV-Vis**	**TG**
LPMS_8_TMB_8h_1.35	3.8 mg/100 mg	4.2 mg/100 mg
LPMS_7_TMB_18h_1.35	4.3 mg/100 mg	4.7 mg/100 mg
MS_1.35	2.6 mg/100 mg	2.8 mg/100 mg
WMS_5	0.9 mg/100 mg	1.2 mg/100 mg

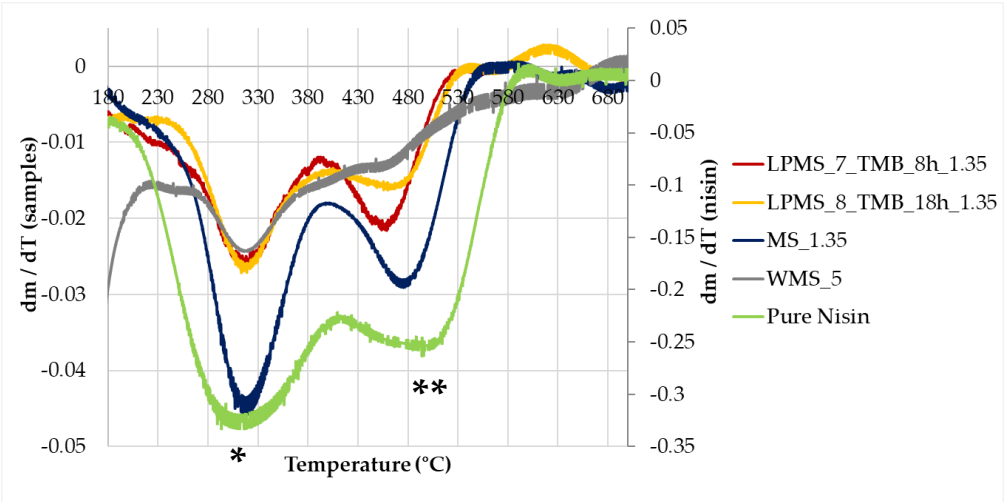

Figure 32. DTG, derivative graph obtained from TG curves. *, peak relative to pyrolisis of Nisin; **, peak relative to the decomposition of Nisin.

Nisin Release Tests

To evaluate Nisin stability, Nisin release tests were performed on loaded structures a few weeks after loadings. The Nisin content obtained spectrophotometrically and with EA is comparable, so can be asserted that Nisin is present and stable.

Nisin release tests were performed for structures with a comparable Loading%, i.e., LPMS_8_TMB_8h_5, LPMS_7_TMB_18h_5, MS_10 and WMS_10, which all have a Loading% of about 15%.

The amount of Nisin released was determined as % of release (Equation (6)):

$$\%\ \text{release} = \frac{Cumulative\ amount\ of\ Nisin\ released\ at\ a\ certain\ time}{Total\ Nisin\ content} \cdot 100 \qquad (6)$$

A controlled release mechanism is achievable with LPMSs, as illustrated in Figure 33. The release duration for LPMSs extends up to 4 days, significantly longer than that of MS, which releases over approximately 1 day, and WMS, which releases within about 1 hour. Compared to MS and previous studies (188), LPMSs demonstrate a much more prolonged release period, lasting four times longer than the approximately 24 hour release observed with MS. This extended release duration makes LPMSs a superior option for sustained delivery applications.

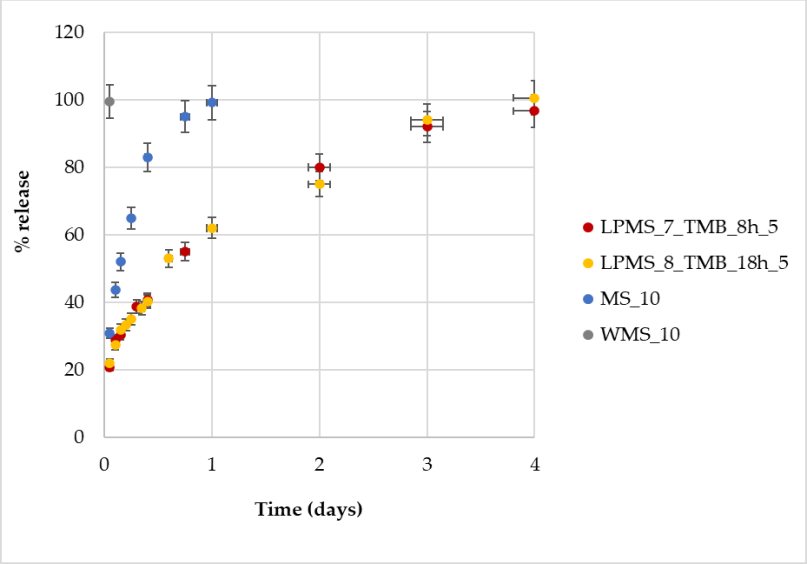

Figure 33. %Release determined with UV-Vis analysis plotted as a function.

Another critical aspect to consider is the mechanical resistance exhibited by LPMS_7_TMB_18h after prolonged exposure to SBF. As shown in Figure 34, SEM-FEG images reveal the structural integrity of unaltered samples, loaded samples, and those that have undergone soaking in SBF. Notably, LPMS_7_TMB_18h retains its structure post-release, indicating strong mechanical

resilience. In contrast, LPMS_8_TMB_8h does not demonstrate the same level of durability, suggesting that a longer thermal treatment is required to enhance structural stability for sustained drug release applications. For MS and WMS, the structural integrity is maintained after 24 hours and 1 hour of release, respectively.

CLSM was employed to visually assess Nisin's loading. Figure 35 presents microscope images of the loaded samples and those post-release, providing a clear visual comparison.

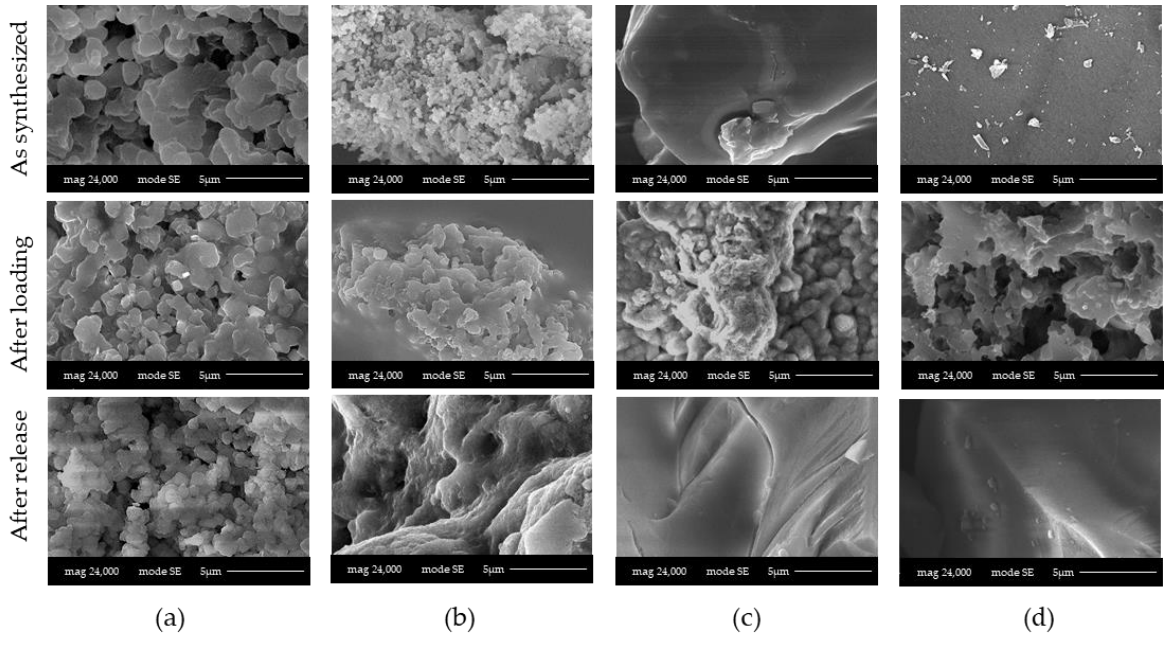

4

Figure 34. SEM-FEG images acquired on samples (**a**) LPMS_7_TMB_18h_5, (**b**) LPMS_8_TMB_8h_5, (**c**) MS_10 and (**d**) WMS_10, studied unaltered, after loading and after release tests in SBF.

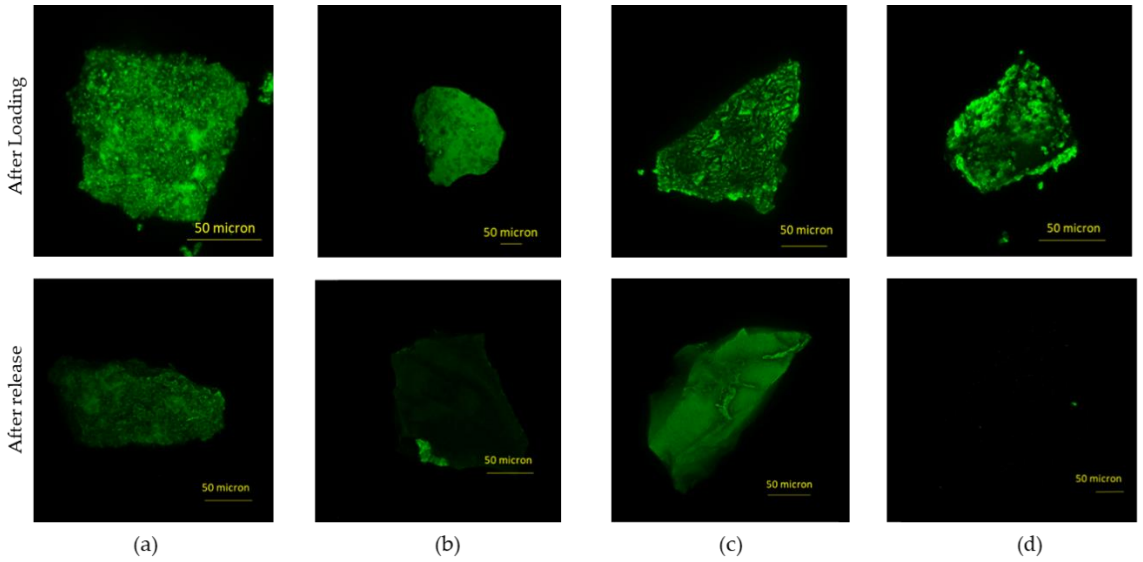

Figure 35. Confocal laser scanning microscopy images acquired on samples (**a**) LPMS_7_TMB_18h_5, (**b**) LPMS_8_TMB_8h_5, (**c**) MS_10 and (**d**) WMS_10 studied when loaded and after release in SBF.

As illustrated by the comparison between the first and second rows in Figure 35, confocal microscopy images provide clear evidence that aligns with the patterns observed in SEM-FEG analysis. The structural integrity of LPMS_8_TMB_18h is well-preserved following the loading process, with Nisin visibly filling the pores, indicating effective internal loading. This sample maintains its porous architecture even after the introduction of the drug, suggesting that the structure is robust enough to support the internal loading of therapeutics without significant alteration.

In contrast, the structure of LPMS_7_TMB_8h appears more compact after the loading process. This compaction is likely due to the filling of superficial cavities with Nisin, which might indicate a higher degree of surface interaction or a less efficient penetration of the drug into deeper pores compared to LPMS_8_TMB_18h. The images suggest that while internal loading occurs, there may also be a substantial amount of Nisin deposited closer to the surface, leading to a denser appearance.

For MS and WMS, the images reveal a marked transformation in surface texture after loading. Originally smooth surfaces become noticeably more irregular and non-homogeneous, which is attributed to the precipitation of Nisin on the surface of the microparticles rather than internal pore filling. This surface deposition is indicative of a less efficient loading mechanism where the drug primarily adheres to the external surface rather than being encapsulated within the material's internal structure.

These findings reinforce the hypothesis that LPMS structures (large-pore mesoporous silica) facilitate in-pore drug loading, providing a more controlled and efficient loading mechanism compared to MS and WMS, where the drug is primarily deposited externally. The visual evidence of pore filling in LPMS samples, as opposed to surface precipitation in MS and WMS, underscores the difference in loading strategies and their implications for drug release profiles.

Furthermore, the images also demonstrate that drug release from these structures is nearly complete. This is indicated by the significant quenching of fluorescence in the samples post-release, which suggests that most, if not all, of the Nisin has been released from the structures. This observation is consistent across different structures but is most pronounced in LPMS samples, indicating that these materials not only effectively load the drug but also release it in a controlled manner over time. The reduced fluorescence signals in the post-release images confirm

that the release mechanism for LPMS is both thorough and efficient, contrasting with the quicker but less controlled release seen in MS and WMS structures.

Chapter 4: Functionalized LPMSs – Comparison of Drug Loading/Release Performance and Bioactivity Relative to Traditional Mesoporous Bioactive Glasses.

4.1 Introduction

In recent years, there has been a growing emphasis on developing structures capable of accommodating large pharmaceutical molecules, such as peptides and proteins, to protect, stabilize, and maintain their biological efficacy. LPMS has emerged as a promising support material due to its ability to meet these requirements effectively (189).

Osteoporosis, which is increasingly prevalent due to the aging population (190), presents significant challenges in treating bone defects. The condition is characterized by reduced bone formation and increased bone resorption, complicating the healing process (191). Given that bone is the second most transplanted tissue, addressing bone diseases is a major concern (192,193). Bone tissue regeneration offers a potential solution by providing materials that not only replace bone temporarily but also stimulate cell growth and differentiation (194).

Mesoporous bioactive glasses have shown considerable potential in bone regeneration due to their excellent textural properties, rapid bioactive response, and biocompatibility (195). These glasses release Si^{4+} ions, which support extracellular events like angiogenesis, and Ca^{2+} ions, which promote cell proliferation and osteogenic activity. They also play a crucial role in gene transfection (196,197).

Recent advances have transformed mesoporous bioactive glasses from basic bioactive materials into sophisticated multitherapy systems for treating various bone-related conditions. This evolution has involved incorporating therapeutic elements such as Cu, Zn, Ga, Sr, Li, and Ce, which enhance bioactivity, biocompatibility, and surface area (194).

In recent years, mesoporous bioactive glasses for clinical applications have evolved from an improved bioactive biomaterial towards a multitherapy system for the treatment of different bone-related pathologies by tuning their composition and functionalizing their surfaces (196).

Traditional treatments for osteoporotic bone defects typically involve bone grafting combined with systemic anti-osteoporosis drugs. However, systemic therapies can face issues like poor availability, liver damage, and osteonecrosis. To address these challenges, bone grafts are

designed to boost osteoblast activity and suppress osteoclast activity, potentially offering more effective solutions for bone regeneration (198,199).

Calcium Silicate ($CaSiO_3$) has been recognized for its beneficial effects on bone regeneration (198,200). When combined with therapeutic metals like Gallium, which can inhibit osteoclast activity and has anticancer properties, the regenerative potential is further enhanced. Gallium has shown promise in boosting osteogenesis and impacting blood clotting. Its ability to mimic iron and disrupt iron-dependent processes in tumor cells adds to its potential as a therapeutic agent (201).

Exploration of Gallium, due to its potential anticancer properties, was prompted by the observation that ^{67}Ga, when administered to rodents with implanted tumors, exhibited a notable concentration within the tumors (66). Consequently, initially, ^{67}Ga was employed as a probe for tumor detection.

The addition of Gallium to bioactive materials has been shown to enhance osteogenesis, affect blood clotting, and exhibit anticancer and antibacterial effects. Incorporating Gallium into biomaterials could significantly improve treatment outcomes for bone-related diseases due to its targeted delivery and effectiveness.

Gallium exhibits the capability to mimic iron and disrupt iron-dependent processes, including proliferation, in tumor cells (202). Gallium can create complexes with proteins and ligands that typically bind Iron, such as transferrin (66). These interactions between Gallium and proteins play a significant role in the potential development of Gallium compounds as therapeutic agents in cancer (203,204). Despite its similarities with iron, Gallium distinguishes itself by not undergoing a trivalent to divalent state transition and being unable to engage in redox reactions.

MS obtained through Sol-Gel EISA processes typically allows only superficial loading and pore blocking (205,206), LPMS offers a better solution. LPMS structures can be engineered to host larger quantities of therapeutic molecules, providing enhanced protection and stability. This makes LPMS an ideal candidate for delivering bioactive agents effectively (120,121).

Sample compositions were chosen considering the biological role of Ga^{3+} and Ca^{2+}.

Adding 1 and 1.6 mol % of Ga had little effect on the material's performance. If a too low Ga^{3+} amount is included in the structure after 30 days of incubation in SBF, the glass surface is not evenly covered with HA, likely due to competition between Ca^{2+} and Ga^{3+} ions (207,208). With an

ionic radius of 0.62 Å, Ga^{3+} is smaller than Ca^{2+} (0.99 Å), making it easier for Ga^{3+} to integrate into calcium phosphate clusters and disrupt their growth (209). The highest Ga ion concentration observed after 30 days in SBF was 6 ppm (208). Larger amounts of Ga (8 and 16 mol %) led to increased Ga^{3+} release from the glass system, so it could easily reach the toxicity level of 14 ppm (210). The glass containing 8 mol % of Ga showed the highest release, with Ga concentrations of 19.5, 26.8, and 37.4 ppm after 1, 7, and 14 days of immersion in ultra-pure water, respectively (211). Taking into account the factors mentioned above, a 5 mol % mol/mol Ga concentration was selected, based on promising outcomes observed in similar compositions reported in other studies. (212–215).

The amount of Ca^{2+} was selected to match the fixed Ga concentration, taking into account data from existing literature. To facilitate a comparison between silica-functionalized structures incorporating either calcium or gallium, the Ca content was also set at 5 % mol/mol. This concentration was chosen not only for comparative purposes but also based on supportive findings from previous studies (211,216–219).

4.2 Materials and Methods

General procedures

The chemicals and solvents, acquired at the highest available purity grade, were employed without additional purification unless explicitly stated. Microwave-assisted hydrothermal treatments using FlexiWAVE (Milestone S.r.l., Sorisole, Italy) at 230 V were conducted to synthesize LPMSs.

Synthesis of Bioactive LPMSs

The synthesis of Functionalized LPMS was adapted from the one reported in Section 3.2. The previous synthesis was modified to achieve the prefixed content in Ca^{2+} and Ga^{3+} due to the high solubility of the salt used. For the reference synthesis, the amount of water was decreased to a third.

All syntheses conducted are reported in Table 9. Samples were named as LPMS_nMe, in which n is the %mol of the Metal (Me) with respect to SiO_2, and Me is replaced with the chemical symbol

of the Metal element added to the silica structure. The amount of $Ca(NO_3)_2 \cdot 4H_2O$ (Sigma Aldrich, 99%) and $Ga(NO_3)_2 \cdot 9H_2O$ (Sigma Aldrich, 99%), reported in Table 1, were optimized to obtain in the synthesized glasses the desired compositions (LPMS_5Ca refers to $100SiO_2$-5CaO, LPMS_5Ga refers to $100SiO_2$-$2.5Ga_2O_3$, and LPMS_5Ca5Ga refers to $100SiO_2$-5CaO-$2.5Ga_2O_3$ in %mol). The final glass composition was checked using X-Ray Fluorescence Spectroscopy (XRF) analysis.

Table 9. Synthesis conducted.

Sample	TEOS (g)	Pluronic® F127 (g)	TMB (mL)	HCl (1.7%) *w*/*w* (mL)	$Ca(NO_3)_2 \cdot 4H_2O$ (g)	$Ga(NO_3)_3 \cdot 9H_2O$ (g)
LPMS_5Ca	2.10	4.20	0.55	40	0.90	\
LPMS_5Ga	2.10	4.20	0.55	40	\	0.93
LPMS_5Ca5Ga	2.10	4.20	0.55	40	0.90	1.05

After the thermal treatment, the synthesis solutions were filtered, and the resulting solids were dried overnight at 60°C. The dried solids were then calcined at a rate of 1.5°C/min, reaching a temperature of 700°C and maintained for 3 hours in an air atmosphere. This calcination process was designed to remove the surfactant and stabilize the mesoporous glasses. Following the calcination, the LPMSs were cooled in air, then finely ground using an agate mortar and sieved to obtain particles with a mean size of less than 355 μm.

Load Tests and Release Tests

Load and release tests were conducted to analyze the behavior of LPMSs both with and without the presence of various metals. These experiments followed the procedures outlined in the previous Section (Section 3.2) and Results are compared to results obtained for LPMSs without metals in the structure (results are reported in Section 3.3).

To quantify the amount of nisin encapsulated within the LPMSs and the quantity released into simulated body fluid (SBF), UV-Vis spectroscopy was used. This technique allowed us to measure the cumulative percentage of nisin released, helping to identify any residual nisin that remained within the porous structures.

UV-Vis spectra were recorded using a JASKO V-570 UV/Vis/NIR spectrophotometer (JASCO Europe S.r.l., Cremella, Italy), operating at 298 K over a wavelength range of 250–400 nm, with quartz cuvettes featuring a 1 cm optical path length. The quantification of nisin was performed by measuring its absorbance at the peak wavelength of 277 nm.

To determine the kinetics of nisin release, the Korsmeyer–Peppas model was applied, described by the equation: $M_t/M_\infty = k - t^n$. In this equation, M_t/M_∞ represents the fraction of nisin released at time t, k is the release rate constant, and n is the release exponent that indicates the release mechanism (220). Nisin release was observed over a period of 4 days, and the Korsmeyer–Peppas model was specifically applied to the linear portion of the release curve where the release rate is significant.

The value of the release exponent, n, was analyzed to determine the release mechanism. If n was found to be less than 0.5, the release process was considered to be under partial diffusion control. If n equaled 0.5, it indicated a release mechanism controlled purely by diffusion. If n equaled 1, it suggested that the release was controlled by the erosion of the delivery system. This analysis provides insights into the mechanisms governing nisin release from the LPMSs and helps in optimizing the delivery system for effective drug release.

Gallium, Calcium, Silica, and Phosphorous Release in SBF

The release of metal ions in SBF was analyzed using ICP-OES. For the experiment, 100 mg of dried solid samples were immersed in 20 mL of SBF. Supernatants were collected, diluted, and acidified at intervals of 1, 3, 7, and 14 days to quantify the release of gallium, calcium, silica, and phosphorus. Separate solutions were prepared for each time point based on established protocols in the literature (221–224). Detecting the maximum concentration of leached inorganic ions near the implanted material is crucial for achieving the desired biological effects, such as antitumor activity. The analysis was conducted using an ICP-OES DA 4500 Perkin Elmer, Perkin Elmer Optima 4200 DV (Perkin Elmer, Milan, Italy).

Bioactivity Evaluation after Soaking with SBF

To assess the bioactivity of the samples, a measured quantity of the powdered sample was immersed in SBF for periods of 1, 3, 7, and 14 days. The formation of a HA layer was monitored

by analysing the characteristic peaks in the IR spectra. These spectra were recorded in the 4000–400 cm^{-1} range using an FT-IR VERTEX 70 (Bruker, Milan, Italy). Additionally, X-Ray Powder Diffraction (XRDP) was employed to verify the presence of an HA layer on the surface of the solid after SBF exposure. The diffraction spectra were collected over a 2θ range of 10–60°, using Cu Kα radiation with a wavelength of 1.5418 Å, at 40 kV and 40 mA, with a maximum power of 2.2 kW, on an X'Pert PRO (Panalytical, Malvern, UK).

Physical-Chemical Characterization of Powders

a. X-ray Fluorescence Spectroscopy (XRF)

The determination and the control of the composition of powdery samples synthesized were conducted through XRF analysis using an X Philips PW 1480 (Panalytical, Lissone, Italy).

b. Scanning Electron Microscopy with Field Emission Gun (SEM-FEG)

The morphology of the original powdered samples was analyzed to confirm the presence of a significant porous structure, in line with previous studies. Additionally, SEM images were taken of both the loaded powdered samples and those immersed in SBF, using a Nova NanoSEM 450 microscope (FEI Company, Milan, Italy) operating at 15 kV.

c. Textural Properties

To thoroughly evaluate the surface properties of LPMSs, a detailed analysis was conducted using N_2 adsorption/desorption isotherms at a low temperature of approximately 77 K. This was achieved using a TriStar II 3020 Micromeritics instrument (Alfatest S.r.l., Rome, Italy). The SSA_{BET} was determined by analyzing the adsorption data with the Brunauer, Emmett, and Teller (BET) method (225).

To further explore the pore structure, the pore size distribution was calculated from the adsorption branch of the isotherm using the Barrett-Joyner-Halenda (BJH) method (226), which provides insights into the mesoporous range of the material. This analysis helps in understanding the distribution of pore sizes within the sample.

In addition to these measurements, the total pore area and intrusion volume were assessed using a Hg intrusion porosimeter. This was carried out with an AutoPore IV 9500 instrument (Micromeritics Instrument Corporation, Alfatest S.r.l., Rome, Italy), operating at a Hg pressure of

1.51 psi. This technique allows for a detailed evaluation of the pore structure, including the measurement of pores that might not be accessible by gas adsorption techniques alone. This comprehensive analysis ensures a complete characterization of the LPMSs' surface and pore properties.

d. Thermogravimetric Analysis (TG-DTA)

To confirm the stability of nisin within the structures and evaluate any specific interactions between nisin and the silica surface, a TG analysis was performed. These analyses were conducted using a Seiko SSC 5200 instrument (Seiko Instrument Inc., Chiba, Japan) over a temperature range from 25°C to 650°C, with a controlled heating rate of 1°C/min.

e. Confocal Laser Scanning Microscopy (CLSM)

A confocal microscope was used to evaluate the presence of Nisin on the surface of the loaded powdery samples. Fluorescence from Nisin was induced using an excitation wavelength of 405 nm, and the emitted light was captured within the 470–580 nm range. Imaging was conducted with a Leica TCS SP8 microscope (Leica Biosystems, Milan, Italy).

4.3 Results and Discussion

Bioactive LPMSs' Morphology Characterization with SEM-FEG

The LPMS structures, synthesized according to the previously outlined procedures, were examined using SEM-FEG to assess their morphological characteristics. This analysis was crucial for verifying the impact of compositional changes and variations in water content on the morphology of the LPMS structures, in comparison to the Results reported in Section 3.3.

The SEM-FEG imaging revealed that, despite modifications in composition and water content, the LPMSs structures consistently exhibited large pores, as shown in Figure 36. These observations confirm that the fundamental pore structure was maintained even with the adjustments in synthesis parameters.

For comparative analysis, we evaluated a reference structure, MS, which was synthesized using the Sol-Gel EISA process (227). The MS structures were produced with the same calcium and gallium compositions as the LPMSs. The MS structures were designated as LPMSs and included

variants such as MS_5Ga, MS_5Ca, and MS_5Ca5Ga. The surface morphology of these MS structures is detailed in Figure 37, providing a baseline for comparison with the LPMS structures.

This comparative analysis allowed for an assessment of how the structural modifications influenced the pore characteristics and overall morphology of the LPMS structures relative to the MS reference structures.

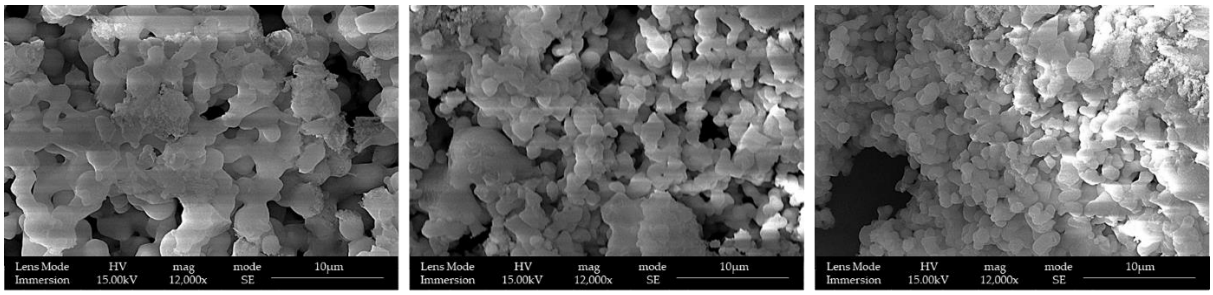

(a) **(b)** **(c)**

Figure 36. SEM-FEG images of (**a**) LPMS_5Ga, (**b**) LPMS_5Ca, and (**c**) LPMS_5Ca5Ga.

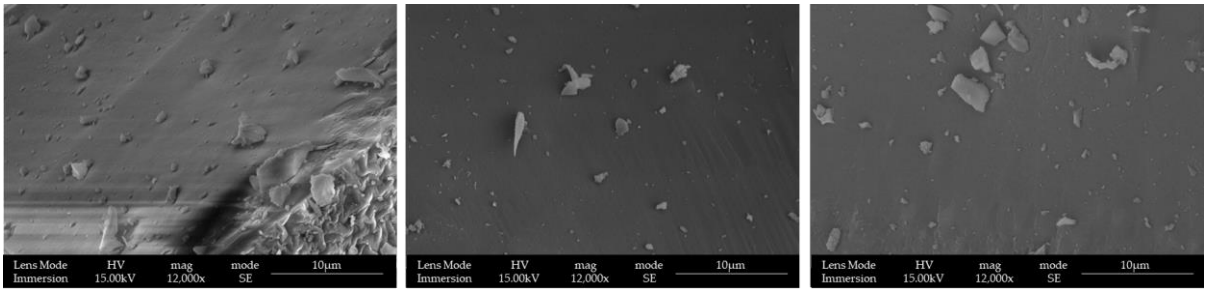

(a) **(b)** **(c)**

Figure 37. SEM-FEG images of (**a**) MS_5Ga, (**b**) MS_5Ca, and (**c**) MS_5Ca5Ga.

Textural Characterization of Powders

Through SSA_{BET} and Hg porosimeter, it is possible to demonstrate the difference in textural properties (i.e., pores dimensions) between LPMSs and MSs (see Table 10 and Figure 38, respectively).

Table 10. SSA_{BET} and Total Pores Area determined respectively with N_2 adsorption/desorption and Hg-Porosimetry.

Sample	SSA_{BET} N_2 ads./des. (m^2/g)	Pore Size N_2 ads./des. (nm)	Pore Volume N_2 ads./des. (cm^3/g)	Total Pores Area Hg-Porosimentry (m^2/g)
LPMS_5Ca	323 ± 16	16.3	1.56	392
LPMS_5Ga	324 ±15	19.2	1.77	376
LPMS_5Ca5Ga	283 ± 13	19.1	1.56	344
MS_5Ca	306 ± 12	4.0	0.31	73
MS_5Ga	417 ± 20	3.0	0.23	53
MS_5Ca5Ga	252 ±12	4.8	0.29	179

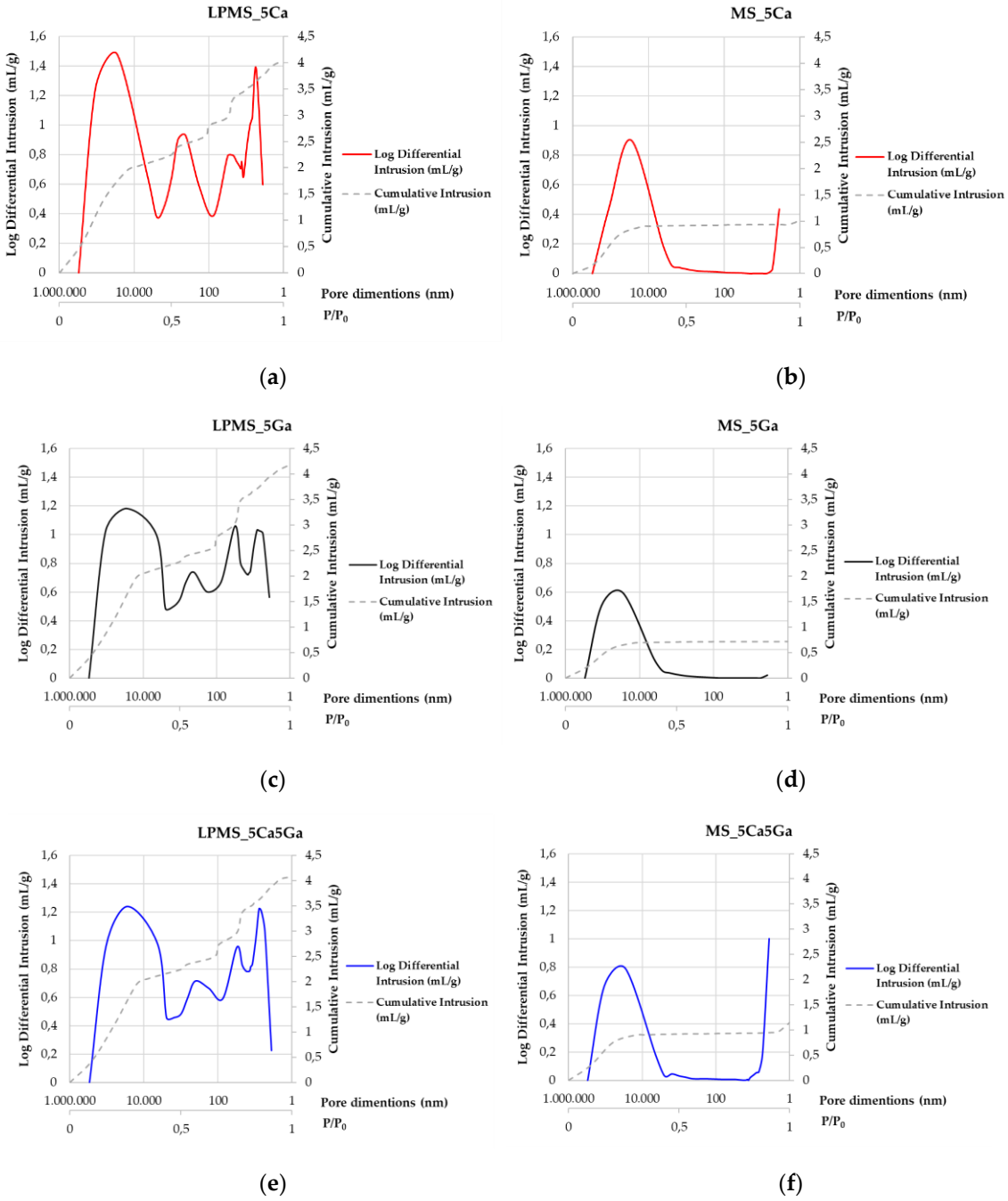

Figure 38. Log Differential Intrusion and Cumulative Intrusion evaluated with Hg-Porosimeter of all samples. In order: (**a**) LPMS_5Ca, (**b**) MS_5Ca, (**c**) LPMS_5Ga, (**d**) MS_5Ga, (**e**) LPMS_5Ca5Ga and (**f**) MS_5Ca5Ga.

Table 11. Type and number of pores of samples at a certain range of dimensions.

	3–10 nm	10–30 nm	500–600 nm	10–200 μm
Sample	**Inter-Pore**	**Super-Nanopore**	**Sub-Micropore**	**Super-Micropore**
LPMS_5Ca	+++++	++	+++	++++
LPMS_5Ga	++++	++++	++	++++
LPMS_5Ca5Ga	+++++	++++	++	++++
MS_5Ca	++	-	-	+++
MS_5Ga	+	-	-	+++
MS_5Ca5Ga	++++	-	-	+++

* the number of "+" schematically indicates the number of pores at a certain dimension.

According to the data presented in Table 10, there is no notable difference in the SSA between the LPMS and MS samples. The SSA for LPMS samples ranges from 283 to 324 m^2/g, whereas for MS samples, it ranges from 252 to 417 m^2/g. These results are consistent with findings in the literature, which report an SSA of approximately 400 m^2/g for comparable bioactive glasses (228).

Further analysis using N_2 adsorption/desorption techniques (Figure 39) reveals that LPMS samples have a significantly higher pore volume compared to MS samples, with LPMS exhibiting a pore volume approximately five times greater than that of MS samples for the same amount of material. This substantial difference is attributed to the LPMS's structure, which contains more extensive cavities and larger pores. In contrast, classical mesoporous bioactive glasses typically achieve a maximum pore volume of around 0.4 cm^3/g, while the LPMS samples show a pore volume in the range of 1.56 to 1.77 cm^3/g.

These observations are corroborated by total pore area measurements obtained via mercury intrusion (refer to Table 9). The total pore area for LPMS samples ranges from 392 to 344 m^2/g, while for MS samples, it is significantly lower, between 179 and 53 m^2/g. The mercury intrusion technique is effective for measuring larger pores, specifically those greater than 3.5 nm in diameter (229). Since MS samples have a substantial number of pores smaller than this size, mercury intrusion is unable to fully penetrate these smaller pores, which does not affect nitrogen adsorption.

Figure 38 illustrates that LPMS samples exhibit mesopores in two distinct size ranges: 20–60 nm and 200–600 nm. In contrast, MS samples predominantly show mesopores within the 2–5 nm range. Based on previous research (180,230), the LPMS pores can be classified as Super-

Nanopores and Super-Micropores. Additionally, Figure 39 indicates that all synthesized structures feature Type IV pores, as classified by the IUPAC (231–233).

It is widely accepted that there is a correlation between the shape of the hysteresis loop and the texture (e.g., pore size distribution, pore geometry, and connectivity) of a mesoporous material. All synthesized structures show type H_1 hysteresis, associated with porous materials consisting of well-defined cylindrical-like pore channels or agglomerates of approximately uniform spheres (234).

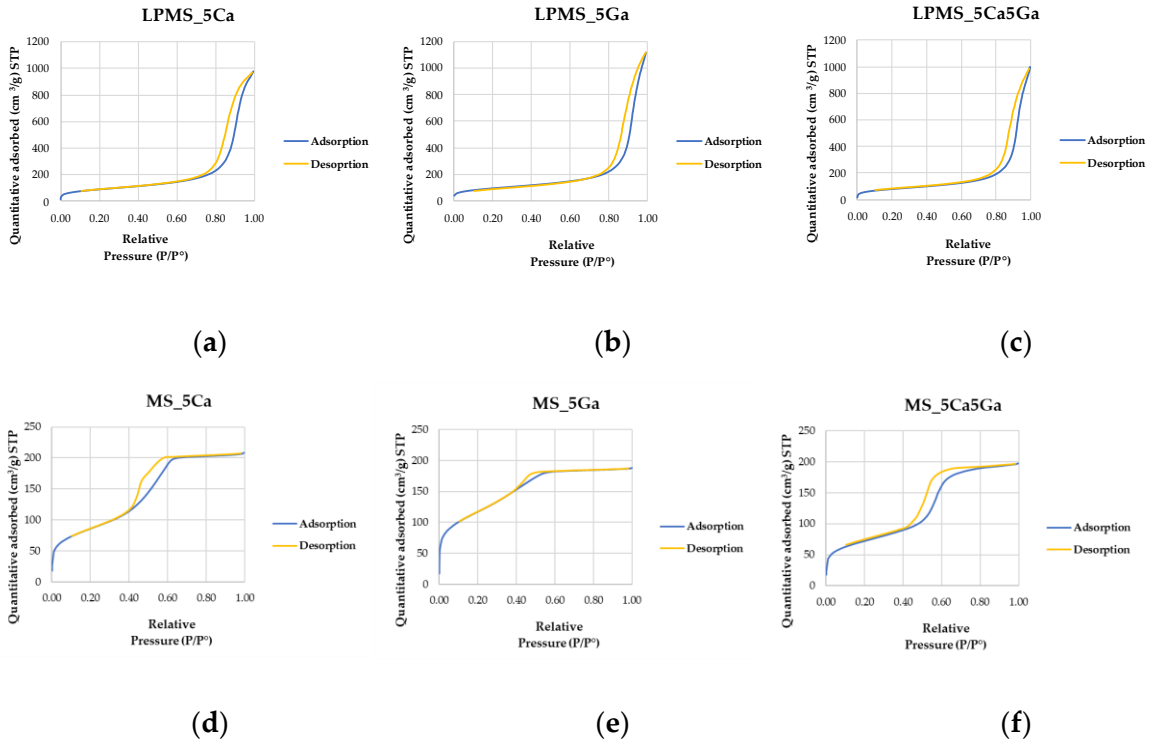

Figure 39. BET surface area analysis results: N_2 adsorption-desorption isotherm plots of samples (**a**) LPMS_5ca, (**b**) LPMS_5Ga, (**c**) LPMS_5Ca5Ga, (**d**) MS_5Ca, (**e**) MS_5Ga, (**f**) MS_5Ca5Ga.

Nisin Loading Tests

The effectiveness of incorporating a molecule into a structure can be assessed using various metrics, including loading efficiency percentage (LE%), loading percentage (Loading%), and loading capacity percentage (LC%). The calculations of these parameters have been performed following the Equations from 2 to 5, reported in Section 3.3.

These parameters are used to quantify how much of the active molecule has been successfully integrated into the structure relative to different benchmarks. Specifically, LE% reflects the efficiency of loading the molecule into the structure, Loading% represents the proportion of the

molecule loaded compared to the total amount introduced, and LC% indicates the capacity of the structure to hold the molecule.

EA was performed on the samples collected after the loading process. The samples were dried overnight to ensure accurate measurements. Table 12 presents the calculated values for LE%, LC, Loading%, and Loading% based on the results of the EA. The samples are labeled as "sample_name_x," where "x" denotes the concentration of nisin (in mg/mL) in the solution used for loading. This nomenclature helps in identifying the specific loading conditions applied to each sample and allows for a comparison of loading efficiencies across different concentrations.

Table 12. Comparison between LE%, LC%, loading% and loading% calculated with EA of all samples studied.

Sample	LE%	LC%	Loading%	Loading% with EA
LPMS_5Ca_5	26.4	8.0	7.4	8.9
LPMS_5Ga_5	27.6	8.4	7.7	9.4
LPMS_5Ca5Ga_5	23.4	7.1	6.6	7.3
MS_5Ca_5	8.1	2.8	2.7	3.6
MS_5Ga_5	12.4	4.1	3.9	3.8
MS_5Ca5Ga_5	13.1	4.3	5.1	4.8
MS_5Ca_10	29.8	9.6	8.7	9.4
MS_5Ga_10	20.5	6.4	6.0	7.5
MS_5Ca5Ga_10	17.3	10.3	9.3	9.0

Table 10 indicates that MS samples only show comparable loading efficiency to LPMS samples when the nisin solution concentration is doubled. This pattern is due to the inherent differences in pore characteristics between LPMS and MS structures. LPMS structures have a higher pore capacity, allowing for more effective loading of the nisin molecule. In contrast, MS samples, with their limited pore capacity, experience only partial filling or blocking of the pores, rather than achieving substantial loading (220,235).

The loading capacity percentage (LC%) for MS samples in contact with a 5 mg/mL nisin solution is approximately three times lower than that for LPMS samples. This disparity is clearly shown in Table S1 in the Supplementary Materials. The lower LC% for MS samples can be attributed to their smaller pore volume and pore size compared to LPMS samples. LPMS structures possess larger and more numerous pores, which contribute to their enhanced ability to accommodate and

retain the nisin molecules effectively. Conversely, the smaller pore volume and size of MS samples limit their capacity to hold the nisin, resulting in a lower LC%.

Nisin Release Tests

The calculations of this parameter have been performed following Equation 6, reported in Section 3.3.

The Release Tests illustrated in Figure 40 reveal that LPMS structures exhibit superior performance compared to MS structures. When evaluating the release of an identical amount of nisin, LPMS samples achieve a significantly prolonged release time compared to MS samples. Specifically, LPMS structures release the same quantity of nisin over a period that is between two and eighty times longer than that observed for MS structures.

This elongated release duration for LPMSs indicates a more controlled and sustained release mechanism. The prolonged release is attributed to the unique properties of LPMS structures, which support a gradual and steady release of the nisin, as opposed to the more rapid release observed with MS structures. This behavior underscores the enhanced ability of LPMSs to maintain therapeutic levels of nisin for extended periods, offering potential advantages for applications requiring sustained drug delivery.

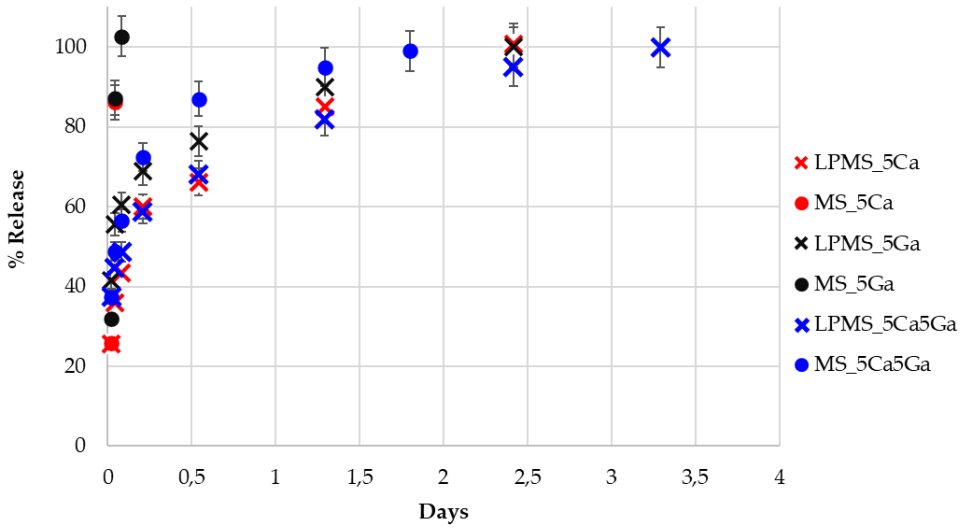

Figure 40. Release tests of LPMSs and MSs. The %Release determined with UV-Vis analysis plotted as a function of time.

The data presented in Figure 40 align with findings reported in Chapter 3, where LPMS structures composed only of SiO_2 demonstrated a release period of 4 days. This is twice as long as the 2-day release period observed for MS structures.

Both Ca and Ga in the LPMS structures also influence the release dynamics. Specifically, when both metals are included, the release time generally decreases, indicating a synergistic effect on the release behavior.

The Korsmeyer-Peppas model values for the release exponent (n) (236) are detailed in Figure 41. For all LPMS samples and the MS_5Ca5Ga sample, the n value is approximately 0.2, suggesting that nisin release is predominantly controlled by partial diffusion. In contrast, MS_5Ca and MS_5Ga samples show an n value of around 0.9, indicating that erosion primarily governs their release. Regarding MS_5Ca5Ga, probably due to the presence of both metals and their synergistic effect and the interaction with Nisin present on the surface, the release is longer and the release is partially governed by diffusion.

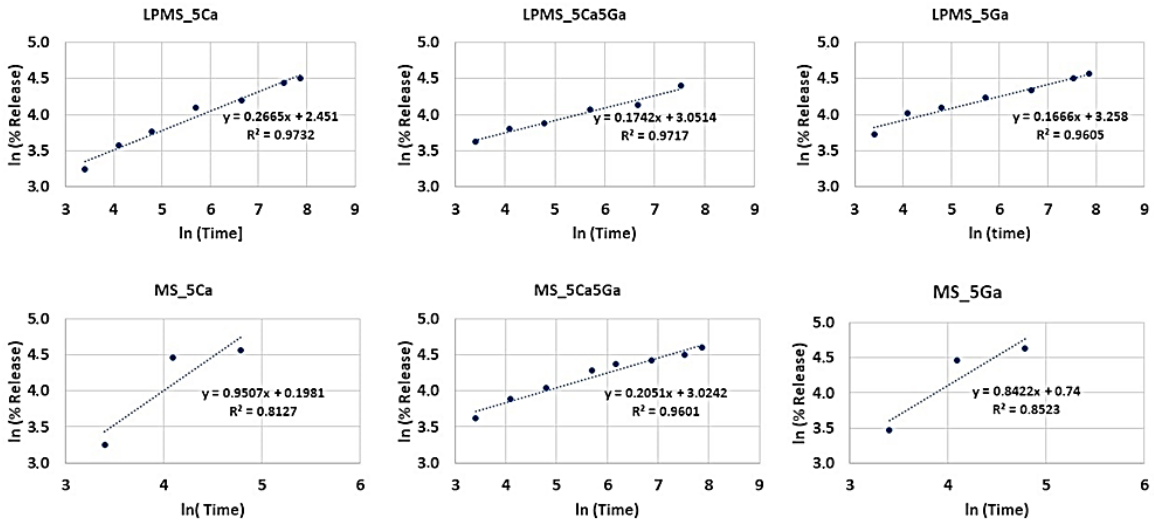

Figure 41. Korsmeyer-Peppas model releases kinetics of nisin aspirin obtained for LPMS and MS samples.

Comparing these results with other studies in the literature (237,238), it is evident that LPMS structures achieve a longer release duration (4 days) compared to the 50 hours reported for MS structures. Furthermore, LPMS structures can achieve near-total release, whereas some studies, like that of Hosseinpour et al. (237), report a maximum release of only 60%.

To validate the mechanical integrity of LPMS structures, SEM-FEG images were taken of the samples both before and after the complete release process (Figure 42). These images confirm that the porous structure of the samples remains intact following Nisin release, indicating that

collapse of the porous structure did not occur. This contrasts with findings in other literature (239), where structural collapse during drug release often leads to incomplete drug release. Additionally, CLSM images (Figure 43) were used to confirm the presence of Nisin on the surface of the materials, verifying its complete release.

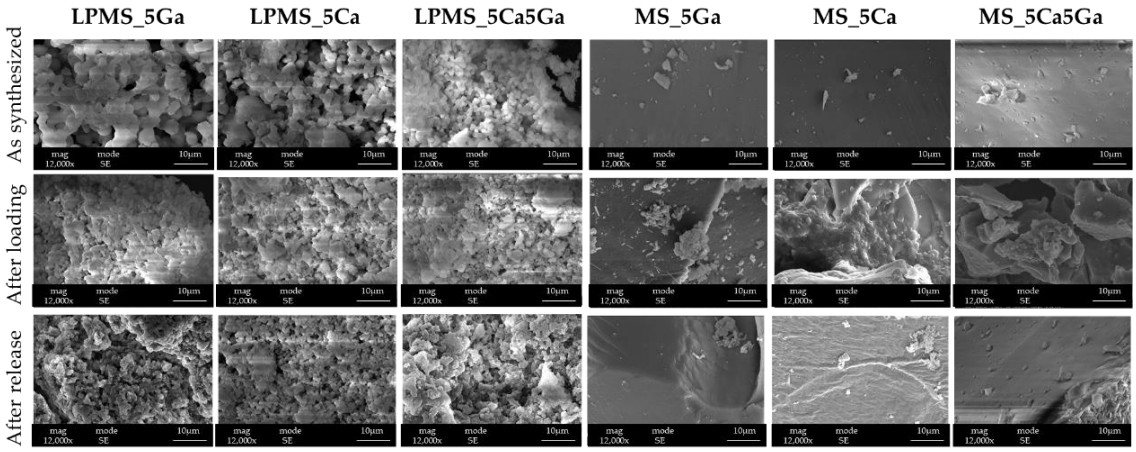

Figure 42. SEM-FEG images of (a) LPMS_5Ga, (b) LPMS_5Ca, (c) LPMS_5Ca5Ga, (d) MS_5Ga, (e) MS_5Ca, (f) MS_5Ca5Ga. In the first row are reported images of as synthesized structures, in the second are reported loaded structures, and in the last row are reported structures after nisin release.

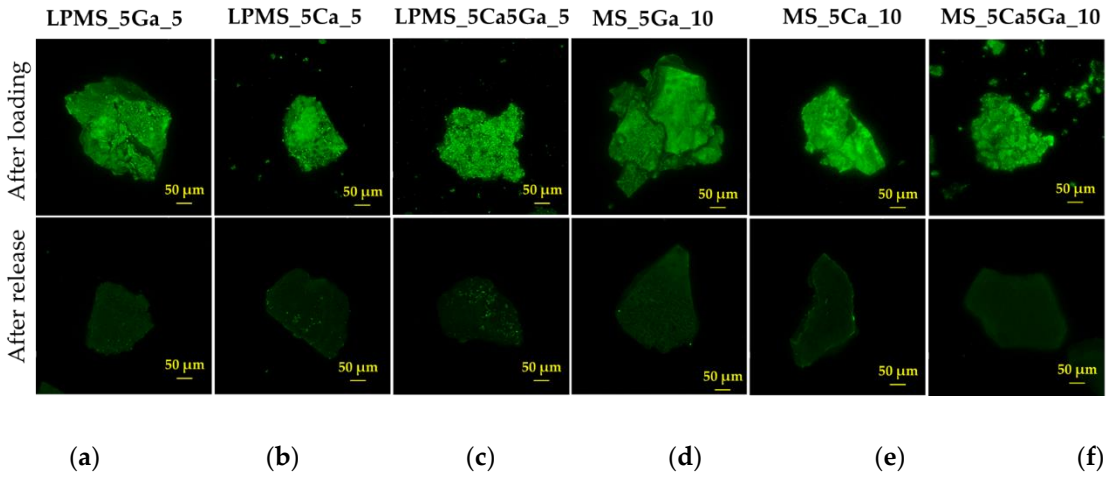

Figure 43. CLSM images of (**a**) LPMS_5Ga_5, (**b**) LPMS_5Ca_5, (**c**) LPMS_5Ca5Ga_5, (**d**) MS_5Ga_10, (**e**) MS_5Ca_10, and (**f**) MS_5Ca5Ga_10. In the first row are reported images of loaded structures, and in the second row are reported structures after release.

Thermogravimetric analysis (TG-DTA)

To investigate how the presence of metals on the silica surface influences interactions with nisin, a TG-DTA was performed, as shown in Figure 44. The DTG curve reveals distinct peaks: the first peak is associated with the pyrolysis (thermal breakdown) of nisin, while the second peak corresponds to the decomposition of nisin's structural components (240).

In the DTG graph, it becomes evident that when Gallium is present on the surface, specific interactions between Gallium and Nisin are enhanced. This is indicated by the shift of the second decomposition peak to a higher temperature, suggesting that the interaction with gallium stabilizes the nisin structure, making it decompose at a higher temperature. Additionally, a third peak appears, further suggesting complex interactions likely promoted by the presence of Gallium.

This behavior is consistent across samples containing only Gallium as well as those with both Calcium and Gallium. The presence of these metals likely contributes to stronger binding or altered interaction dynamics between the Nisin and the silica surface, which can be correlated with the prolonged release times observed in these samples, as depicted in Figure 40. The stabilizing effect of Gallium (and its combination with Calcium) on nisin could be a key factor in the slower, more controlled release of the molecule from these structures.

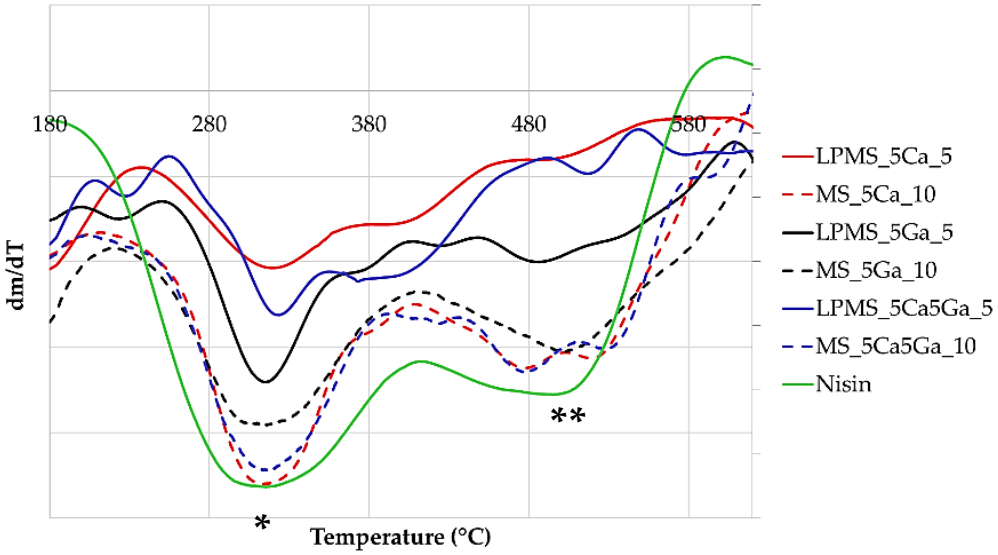

Figure 44. DTG, derivative graph obtained from TG curves of all samples, and a sample of pure Nisin. *, peak relative to pyrolisis of Nisin; **, peak relative to the decomposition of Nisin.

Gallium, Calcium, Silica, and Phosphorous Release in SBF

To evaluate the antitumoral potential of the compound synthesized, gallium release in SBF was examined. Contemporarily, to confirm the formation of a layer of HA on the surface of the powdery compound, control of the amount of Ca and P in SBF was performed (Figure 45).

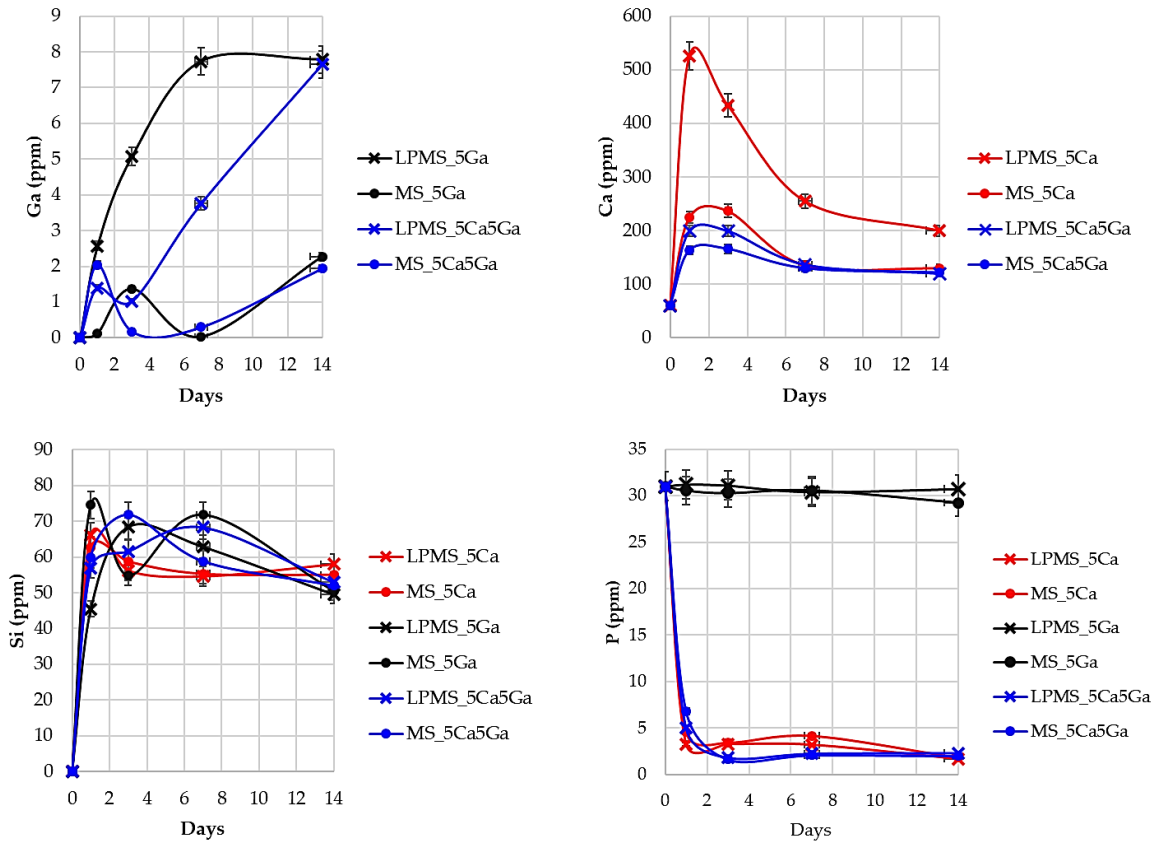

Figure 45. Releases of Ga, Ca, Si and P in SBF, acquired through ICP-OES in a time interval of 14 days.

Regarding the release of Ga^{3+} ions, as detailed in Figure 45, LPMS samples release approximately four times more Ga^{3+} than MS samples over 14 days. Early fluctuations in Ga^{3+} release is likely linked to the formation of several Gallium phosphates. This oscillation is not observed in the LPMS_5Ga sample, which may be due to its notably high release rate of Ga^{3+} ions.

The samples LPMS_5Ga and LPMS_5Ca5Ga demonstrated the highest release of Ga^{3+} ions when immersed in SBF, with peak concentrations around 8 ppm. This concentration is significantly below the toxicity threshold in blood plasma, which is set at 14 ppm (210,241). The release of Ga^{3+} ions at these levels implies potential antibacterial activity. According to S. Pourshahrestani et al. (242), even a release of just 0.3 ppm of Ga^{3+} can inhibit 80% of *E. coli* and 100% of *S. aureus*. Additionally, research by L. Antunes et al. (243) shows that a Ga^{3+} release of 2.5 ppm is sufficient to inhibit approximately 90% of *A. baumannii* growth. Moreover, various studies (244–246) have

identified antitumor activity of Ga^{3+} at concentrations between 100 μM and 1 mM, depending on the type of tumor cells. This suggests that the Ga^{3+} release profile observed in these samples could potentially have therapeutic effects, both antibacterial and antitumoral.

In the case of Ca^{2+} release, the LPMS_5Ca sample exhibited a rapid release of calcium ions, which led to the formation of a small amount of calcite. This Calcite (CA) was detectable through XRDP analysis. The formation of calcite is kinetically favored in the early stages, while the formation of HA, which becomes detectable after 14 days, is thermodynamically more stable.

As the release of calcium increases, the phosphate content in the samples containing calcium decreases, indicating the formation of calcium phosphate compounds. This reduction in phosphate, along with the formation of HA, was confirmed using XRDP and FT-IR spectral analysis.

In addition to these findings, the behavior of Si release from the structures was also monitored. It was observed that its amount always stays near 60 ppm, its solubility in SBF (247,248).

Bioactivity Evaluation after Soaking with SBF

A bioactivity evaluation after soaking with SBF was performed, registering FT-IR spectra of samples taken in contact for a specific time-lapse with SBF (1, 3, 7, or 14 days). All samples containing Calcium presented HA characteristic peaks at 560 cm^{-1} and 605 cm^{-1} (249–251) (in Figure 46 is reported a narrow wavenumber range, for the entire spectra see Figure 47).

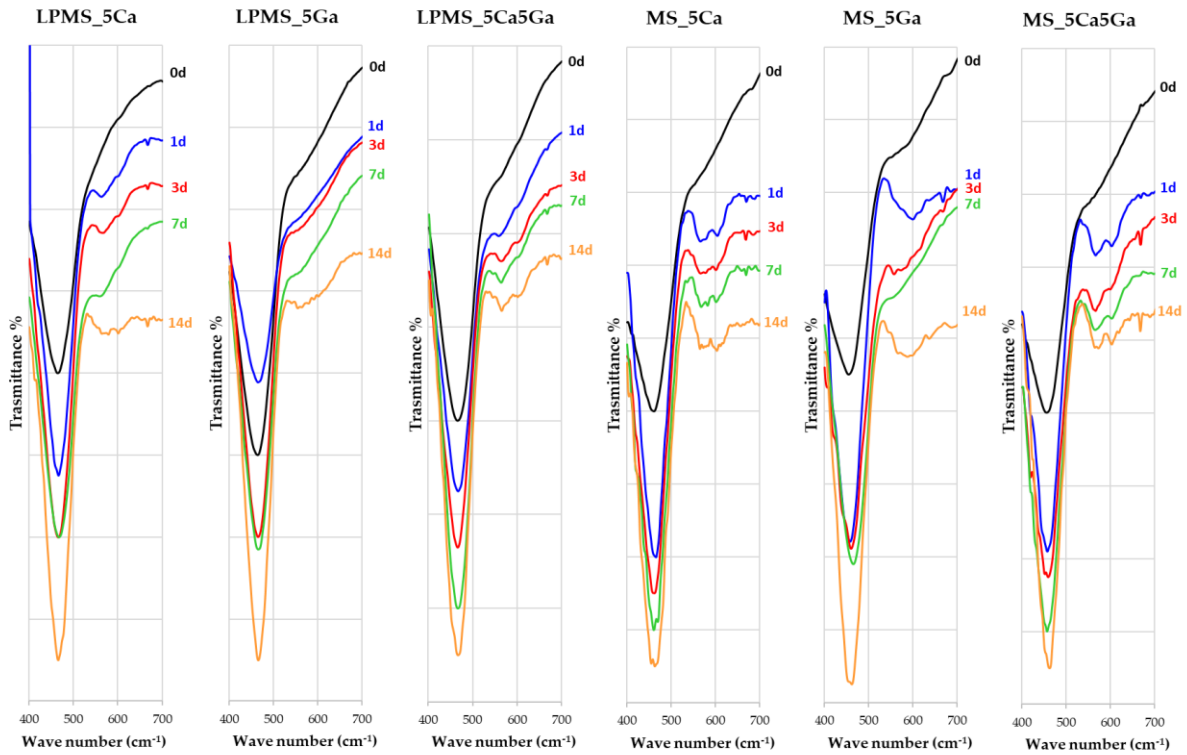

Figure 46. FT-IR spectra of all samples acquired at 1, 3, 7, and 14 days for samples prepared as KBr tablets. In order: (**a**) LPMS_5Ca, (**b**) LPMS_5Ga, (**c**) LPMS_5Ca5Ga, (**d**) MS_5Ca, (**e**) MS_5Ga, and (**f**) MS_5Ca5Ga.

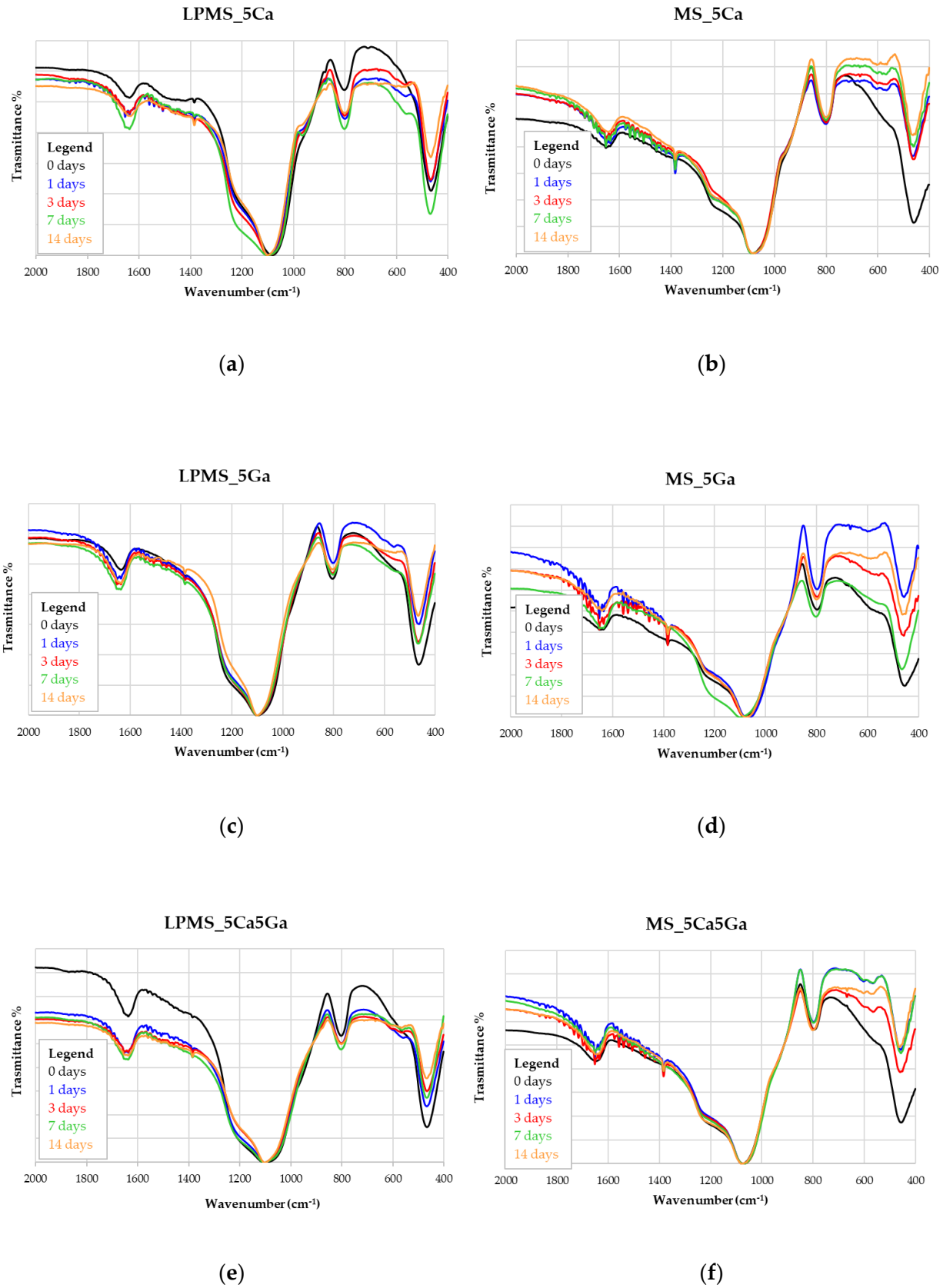

Figure 47. FI-IR spectra of all samples were acquired at 1, 3, 7, and 14 days for samples prepared as KBr pads. In order: a) LPMS_5Ca, b) MS_5Ca, c) LPMS_5Ga, d) MS_5Ga, e) LPMS_5Ca5Ga and f) MS_5Ca5Ga.

To further confirm the presence of HA on the surface of the powder samples after immersion in SBF, XRDP was performed on samples soaked for 14 days. As shown in Figure 48, all samples containing Ca, both LPMSs and MSs, exhibit characteristic HA peaks at 26° and 32° in 2θ (251), indicating HA formation. Additionally, in LPMS samples containing calcium, a peak corresponding to CA formation is observed at 29° in 2θ, likely due to the rapid release of Ca^{2+} ions during the initial hours of soaking. This early formation of calcite is kinetically favored but eventually gives way to HA formation, which is thermodynamically more stable over time.

Surface morphology was also examined to confirm HA presence after SBF soaking. SEM-EDS analysis was conducted on samples soaked for 14 days, with the results shown in Figure 49. A new phase is detectable on the surfaces but with some differences among samples. In the LPMS_5Ca sample, a uniform new layer forms, covering the porous structure, and EDS analysis shows a significant increase in surface calcium and phosphorus. The Ca/P ratio is 1.80, close to the theoretical ratio for HA (1.67), with a slightly higher value likely due to the presence of calcite. For LPMS_5Ca5Ga (Figure 48c), a new layer forms but does not completely cover the surface, while in Figure 48b, only small newly formed particles are observed, with a comparatively lower increase in surface phosphorus and calcium.

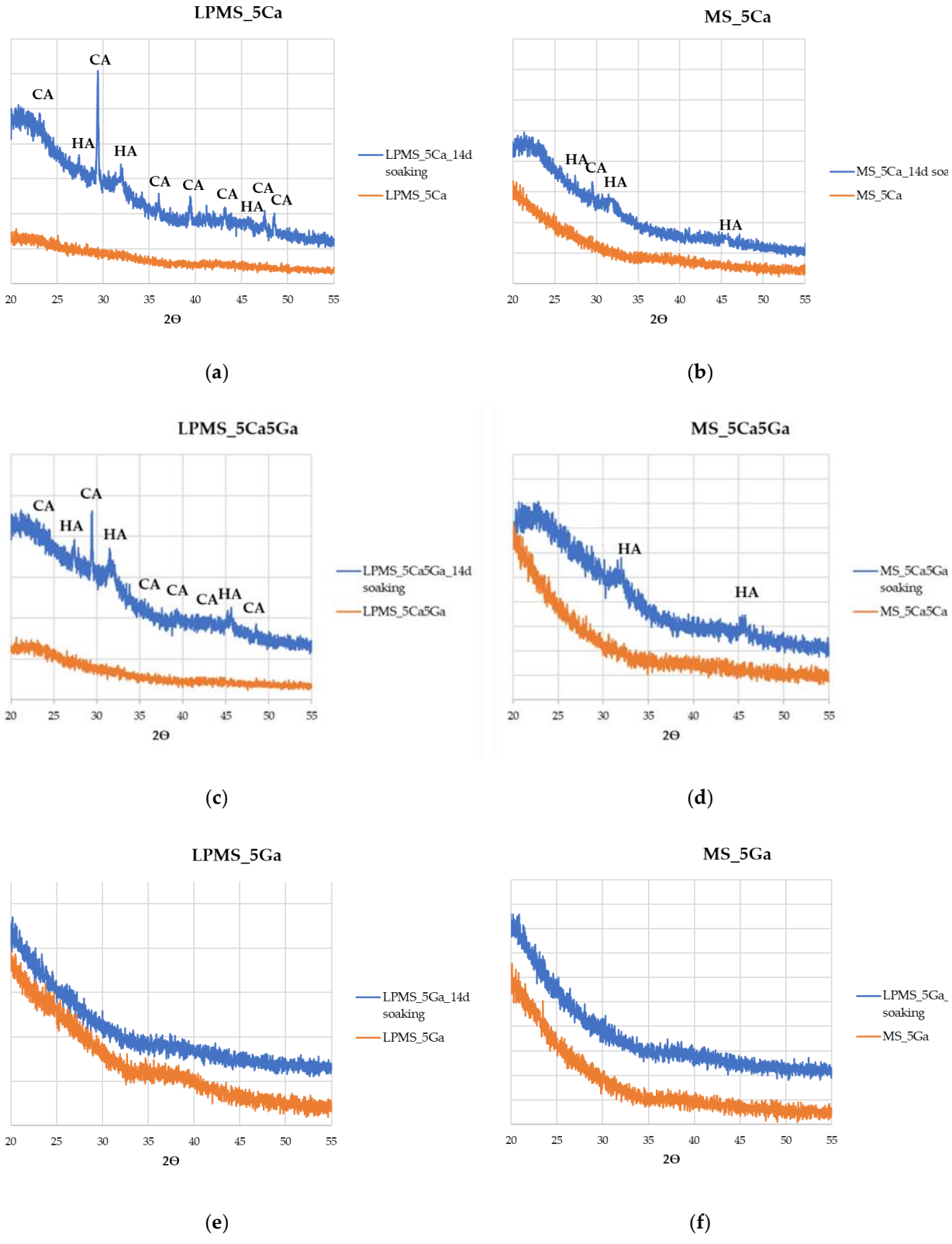

Figure 4. XRPD was recorded for as-synthesized samples (orange) and for samples after 14 days of soaking in SBF. In order: (**a**) LPMS_5Ca, (**b**) M8S_5Ca, (**c**) LPMS_5Ca5Ga, (**d**) MS_5Ca5Ga, (**e**) LPMS_5Ga and (**f**) MS_5Ga

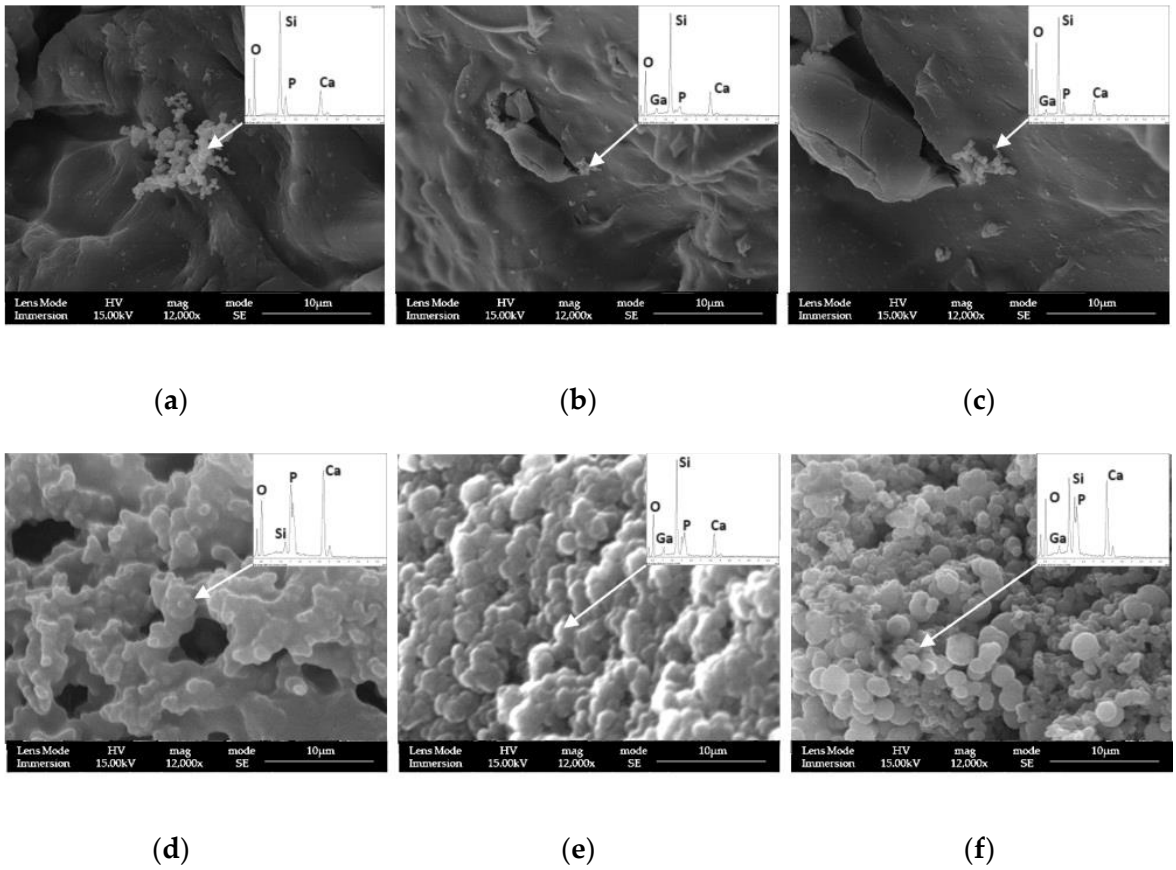

Figure 49. SEM-EDS micrographs for samples after 14 days of soaking in SBF. In order: (**a**) LPMS_5Ca, (**b**) LPMS_5Ga, (**c**) LPMS_5Ca5Ga, (**d**) MS_5Ca, (**e**) MS_5Ga, and (**f**) MS_5Ca5Ga (inset showed the EDS spectra).

For MS samples, it is not possible to see a new layer formed on the glass surface after SBF soaking; however, in the case of MS_5Ca (Figure 49d), clearly evident is the formation of a new phase where Si, Ca, and P are simultaneously present, and the Ca/P ratio is 1.60, very close to the theoretical value for the HA crystal phase.

Chapter 5: Overall discussion - Detailed Comparative Analysis and Discussion of LPMS and Bioactive LPMS.

5.1 Introduction

This chapter provides a comprehensive comparative analysis of LPMS and Functionalized LPMS, synthesizing the findings from Chapter 3 and Chapter 4.

The focus is on understanding how modifications in synthesis, morphology, textural properties, and bioactivity influence the performance of these materials in drug delivery and bone regeneration applications.

This obtained results reported in previous Chapters highlights the specific advantages and trade-offs when LPMS are used instead of classical MS:

- Using different synthesis approach and a different surfactant, bigger pores can be obtained; passing from a range of 3-10 μm for MS to 3-10, 10-30 and 500-600 μm for LPMS (see Table 5);
- Higher pores dimensions bring to have different behaviour in terms of Loading Capacity and Releasing time; in fact, LPMS showed at least doubled Loading Capacity and Releasing times fourth time longer if compared to MS synonyms of slow and controlled release;
- Incorporating a bioactive ion (such as Ca) and an antitumoral ion (such as Ga) into LPMS, it emphasizes both quantitative and qualitative differences observed in the studies. A synergic effect can be achieved: LPMS structure bring to have extremely higher LC% and controlled release, and contemporary the ion releases are higher if compared to MS and for LPMS the release of Ga reaches the minimum required to explicate antitumoral effect.

5.2 Comparative Analysis of Synthesis and Morphology

Synthesis Process

For LPMS, the synthesis aimed to produce large pores capable of accommodating large therapeutic molecules (such as antitumoral Peptides). Then, Functionalized LPMS involved incorporating Ca and Ga ions into the silica matrix to impart bioactivity and antitumoral activity.

Both LPMS and Functionalized LPMS were synthesized using a hydrothermal MW-assisted synthesis. The key difference between LPMSs' synthesis approach and Sol-Gel EISA used for classical MS stays in the different solvents, that for LPMS is water and MS is ethanol, and in the different surfactants used, that for LPMS is Pluronic® F127 and for MS is Pluronic® P123. All these differences in conditions bring to have more opened structures and extremely higher dimension distribution of pores (see Table 5).

The synthesis conditions for LPMS included a specific ratio of TEOS:Surfactant, which was optimized to achieve a bigger pore size. Also type of surfactant has been optimized to achieve the intent of an increase of pores dimensions.

After optimization of type and amount of surfactant, it has been fixed the synthesis conditions for LPMSs structure formation.

Then, the subsequent modification in LPMS has been the inclusion of bioactive (Ca^{2+}) and antitumoral (Ga^{3+}) ions in the Silica latter.

For Functionalized LPMS, the introduction of Ca and Ga required adjustments to the precursor mix, particularly the ratios of $Ca(NO_3)_2$ and $Ga_2(NO_3)_3$, as well as the water content during the hydrothermal process. These changes resulted in slightly smaller pore sizes if compared to the unmodified LPMS.

Morphological Characterization, Textural Properties, and Surface Area Comparison

SEM-FEG analysis revealed distinct differences in the morphology of LPMSs and classical MSs. As reported in Figures 17 and 20, it is possible to notice that hydrothermal synthesis of LPMS brings to an extremely open structure and non-homogeneous surface perfect to host big molecules.

These characteristics of LPMS have been revealed crucial for high drug loading efficiency and controlled release.

SSA_{BET} determined for unmodified LPMSs and MSs showed an average value of the surface area around 320 m^2/g and no significant differences between LPMSs and MSs have been registered.

The main differences between LPMSs and MSs have been highlighted using Hg Porosimeter. Regarding unmodified LPMS, a uniform distribution of large pores with a high degree of order

was determined (see Figure 24 and Table 5). For LPMS pores in the range of 3-10, 10-30 and 500-600 μm were measured, instead of MS which shows pores only in the range of 3-10 μm. Additionally, A_P and V_P for LPMS are 1.5 times higher if compared to MS (see Table 4).

For Functionalized LPMSs and MSs, similar considerations can be made.

An overall resume of characteristics listed above is reported in Table 13.

Table 13. Overall comparison between LPMS, Ms and functionalized LPMPs and MSs.

				3–10 nm	10–30 nm	500–600 nm		
Sample	**SSA_{BET} (m^2/g)**	**A_P (m^2/g)**	**V_P (mL/g)**	**Inter-Pore**	**Super-Nanopore**	**Sub-Micropore**	**LE%**	**LE% increment**
LPMS_7_TMB_18h	330 ± 17	499	3.57	+++++	+++	+++	93.1	+427%
MS	323 ± 16	289	1.49	+++	-	-	21.8	-
LPMS_5Ca	323 ± 16	392	1.56	+++++	++	+++	26.4	+326%
LPMS_5Ga	324 ±15	376	1.77	++++	++++	++	27.6	+223%
LPMS_5Ca5Ga	283 ± 13	344	1.56	+++++	++++	++	23.4	+179%
MS_5Ca	306 ± 12	73	0.31	++	-	-	8.1	-
MS_5Ga	417 ± 20	53	0.23	+	-	-	12.4	-
MS_5Ca5Ga	252 ±12	179	0.29	++++	-	-	13.1	-

From SEM-FEG it is evident that the incorporation of Ca and Ga ions led to a more complex surface morphology, with a more non-homogeneous surface. The pores remained well-defined, but their size distribution shifted slightly to the left of the pore size distribution (see Table 9 and Figure 36). SSA_{BET} registered for both LPMS and MS is in line with the one registered for unfunctionalized structures, around 310 m^2/g. also in this case LPMSs show mesopores in the range of 20-60 and 200-600 μm, instead of MSs that show pores in the range of 2-5 μm (see Figure 36 and Table 9).

A slight reduction in pore size and pore volume was measured for both LPMSs and MSs structures, but in this case was registered the ratio between LPMSs and MSs was around 3:1.

The reduction in surface area and pore volume for Functionalized LPMS can be directly correlated with the incorporation of bioactive ions, which partially occupy the mesopores and alter the silica network. This trade-off between textural properties and bioactivity is a critical consideration in the design of these materials for specific applications.

All LPMSs' synthesized structures feature Type IV, V, and VI pores, as classified by the IUPAC (180). They all show the typical isotherm curve of structures that contain Meso- and Macro-pores. Instead, all MSs show Type I shapes, that correspond to microporous structures.

5.3 Drug Loading Efficiency and Release Profiles

Loading Efficiency

The drug loading efficiency of Nisin, the antibacterial peptide used as a model, was evaluated for both LPMS and Functionalized LPMS.

Unmodified LPMS demonstrated a high LE%, with approximately 50-90% of the available Nisin being successfully incorporated into the pores, instead of MSs that can encapsulate around 20-30% of free Nisin.

This high efficiency is attributed to the large pore size and high surface area, which provide ample space for the accommodation of large therapeutic molecules.

In contrast, Functionalized LPMSs showed a slightly reduced loading efficiency of about 25-30%, but to achieve same LE% with MSs a doubled concentred solutions need to be used.

This decrease is consistent with the reduced surface area and pore volume, as the bioactive ions partially occupy the pores, limiting the space available for drug molecules. However, the reduction in loading capacity is relatively modest, suggesting that Functioalized LPMS still retains substantial potential as a drug delivery system.

Release Profiles

The release profiles of Nisin from both LPMS and Bioactive LPMS were monitored over a period of 14 days.

LPMS exhibited a controlled release, with approximately 95-100% of the loaded Nisin being released over this period. LPMS's release followed a near-linear pattern (Figure 31), indicative of diffusion-controlled release from the large, well-structured pores.

For Functionalized LPMSs, the release profile was similarly controlled, but with a slightly slower release rate for some samples (Figure 38). Slower release was registered for all Ga and Ca

containing samples, for the ones containing both of them indicating a synergistic effect of these two metals.

The slower release can be also attributed to the more complex pore structure and the presence of Ca^{2+} and Ga^{3+} ions, which may slightly hinder the diffusion of Nisin. Despite this, the release profile remained favorable, with the sustained release being maintained, a key requirement for many therapeutic applications.

For Functionalized LPMSs and MSs, the release kinetics were studied. For all LPMSs and MS_5Ca5Ga, Nisin release is predominantly controlled by partial diffusion; for the other MSs release is primarily governed by erosion.

5.4 Bioactivity and In Vitro Performance

Ga, Ca, Si and P Release

Ga, Ca, Si and P Release was measured for Functionalized LPMSs. The study highlights significant differences in the release profiles of Ga, Ca, Si and P ions from LPMSs compared to MS over a 14-day period (see Figure 43).

All Ga-containing LPMSs samples release approximately four times more Ga^{3+} ions than Ga-containing MSs samples, with peak concentrations around 8 ppm, which is well below the toxicity threshold in blood plasma. The fluctuations in Ga^{3+} release in the early stages are attributed to the formation of Gallium Phosphates. Notably, the LPMS samples Ga-contaning show the highest Ga^{3+} release, indicating potential antibacterial and antitumor activity, as even low concentrations of Ga^{3+} can inhibit bacterial growth and show antitumoral effects depending on the tumour cell type.

Regarding Ca^{2+} release, the LPMS_5Ca sample exhibits a rapid release, leading to the formation of CA, which is detectable through XRPD. This formation is kinetically favored initially, while the more thermodynamically stable HA forms over time, becoming detectable after 14 days. The decrease in phosphate content in calcium-containing samples suggests the formation of calcium phosphate compounds, which was confirmed by XRPD and FT-IR spectral analysis. Additionally, the release of Si remains consistent at around 60 ppm, aligning with its solubility in SBF.

Hydroxyapatite Formation

The bioactivity of LPMS and Functionalized LPMS was assessed through their ability to induce the formation of an HA layer after soaking in SBF. LPMS, lacking bioactive components, did not show significant HA formation, confirming its primarily passive role as a drug delivery system.

All functionalized LPMSs containing Ca demonstrated significant bioactivity, as evidenced by the formation of a well-defined HA layer after 14 days of soaking in SBF. XRPD analysis showed characteristic HA peaks at 26° and 32° 2θ, confirming the presence of HA on the surface of Bioactive LPMS. Comparing XRPD pattern of LPMSs to their relative MSs, it is evident that CA and HA peaks in LPMSs are well defined and recognisable.

The formation of a secondary CA phase was observed at 29° 2θ, particularly in samples with higher calcium release (see Figures 43 and 46). This suggests that the calcium ions in Bioactive LPMS not only contribute to HA formation but also participate in the initial formation of CA (the more stable phase), which is subsequently replaced by HA over the time.

All samples containing only Ga as active ion do not demonstrate bioactivity.

The presence of HA in all Ca-containing samples was established also collecting FT-IR spectra (see Figure 44), in which are noticeable the characteristics HA peaks at 560 cm^{-1} and 605 cm^{-1}.

5.5 Surface Morphology After Soaking

SEM-EDS analysis of Bioactive LPMS after soaking in SBF revealed the formation of a uniform HA layer on the surface of samples containing Ca. The Ca/P ratio of the formed layer was approximately 1.80, close to the theoretical value of 1.67 for pure HA, with the slight deviation likely due to the presence of CA.

In samples containing both Ca and Ga, the HA layer was less uniform, with EDS analysis showing lower Ca and P content on the surface compared to the samples containing only Ca (see Figure 47). This suggests that the presence of Ga may influence the formation and uniformity of the HA layer, potentially through interactions with Ca ions or by altering the local pH during the soaking process.

Structural Integrity and Stability Post-Soaking

The structural integrity of both LPMS and Functionalized LPMS was evaluated after soaking in SBF. LPMS maintained its structural integrity well, with no significant degradation observed, consistent with its role as a stable drug delivery platform.

Functioalized LPMS, however, showed signs of surface modification and new phase formation due to the bioactive interactions with SBF. These changes, while indicative of the material's bioactivity, suggest that Functionalized LPMS undergoes more significant structural alterations in biological environments. This could have implications for the long-term stability of the material, particularly in applications where prolonged structural integrity is required.

Chapter 6: Conclusions. Limitations and Future Perspectives.

Based on the results obtained, it can be concluded that a novel synthesis pathway for producing LPMS has been successfully established. This new approach, which involves adjustments in surfactant use, reaction time, temperature, and overall reaction conditions, offers a significant improvement over previous methodologies. In particular, the LPMSs demonstrated enhanced performance in loading and release tests, exhibiting higher LE% and LC%, as well as controlled and prolonged release times compared to older structures. These improvements also extend to their mechanical resilience – related to the structural integrity and stability after soaking in SBF confirmed through SEM-FEG and CSLM analyses – in physiological environments, which is crucial for potential biomedical applications.

Notably, LPMSs, especially the LPMS_7_TMB_18h variant, have shown great promise as candidates for high loading and controlled release of large pharmaceutical molecules. This is attributed to their well-structured pore system and robust mechanical properties. These characteristics make them suitable for studying the mobility of large organic molecules in confined states. Additionally, with this new structure, the potential limitation linked to the risk of superficial pore blockage that can occur in classical MS due to substances found in vivo, (such as cells) is avoided.

Furthermore, the synthesis pathway has been effectively applied to produce Ca and Ga containing LPMSs, maintaining consistent pore distribution and demonstrating enhanced features compared to classical MS. The LPMSs exhibited a doubled release time and loading efficiency, with controlled and sustained release for up to 48 hours. Additionally, the bioactivity of Ca-containing LPMSs was comparable to that of MS, while the Ga-containing LPMSs released four times more Ga ions (8 ppm), a concentration known to provide antibacterial and antitumoral effects.

The comparative analysis of LPMS and Functionalized LPMS reveals distinct advantages and trade-offs between the two materials. LPMSs offer higher surface area, pore volume, and drug loading capacity, making them well-suited for applications requiring maximum loading efficiency and controlled release.

Functionalized LPMSs, while exhibiting slightly reduced textural properties, compensates with significant bioactivity, as evidenced by its ability to induce HA formation and support bone tissue

regeneration. Incorporating bioactive ions such as Ca^{2+} and Ga^{3+} introduces a level of functionality that makes Functionalized LPMS (LPMS_5Ca, LPMS_5Ga and LMS_5Ca5Ga) particularly suitable for applications in bone tissue engineering, achieving both the bioactive and antitumoral effect, where drug delivery and material bioactivity are critical.

Future research should focus on optimizing the balance between textural properties and bioactivity in Functionalized LPMS, potentially through fine-tuning the composition and synthesis parameters. Additionally, exploring the long-term stability and in vivo performance of Functionalized LPMSs will be essential in advancing its application in clinical settings.

In summary, LPMSs stand out as promising candidates for the high loading and controlled release of large pharmaceutical molecules, thanks to their structured pore system and mechanical durability. Their potential application in exploring the behavior of large organic molecules in confined states is noteworthy. Additionally, the inclusion of phosphorous could be considered to enhance the bioactivity of Ga only LPMSs. Future research should explore new pharmaceutical molecules and address the challenge of potential pore obstruction by in vivo substances.

Chapter 7: Other pubblications.

7.1 Curcumin

Curcumin, the primary bioactive compound found in the rhizome of Curcuma longa (commonly known as turmeric), has long been valued for its extensive medicinal uses. Historically, it has been used not only as a spice and dye but also for its medicinal properties, particularly in traditional Ayurvedic and Chinese medicine. The health benefits of curcumin are linked to its polyphenolic structure, which grants it antioxidant, anti-inflammatory, anticancer, antidiabetic, and antiparasitic properties. These pharmacological effects are mainly attributed to curcuminoids (252).

Chemically, curcumin structure includes two aryl rings with ortho-methoxy phenolic groups, symmetrically connected by a β-diketone moiety (Figure 50). The molecule exists in equilibrium between two tautomeric forms: the diketone form, which dominates in acidic and neutral conditions, and the keto-enol form, prevalent in basic environments. This tautomerism plays a critical role in curcumin's biological behavior. In its diketone form, curcumin acts as a Michael acceptor, while the keto-enol form enhances its antioxidant capabilities. The molecule's methoxy groups are crucial for its antioxidant properties, and the hydroxyl groups are necessary for its anti-inflammatory activity. However, curcumin's poor water solubility and rapid degradation, especially in neutral pH environments, limit its therapeutic applications. It degrades by 90% within 30 minutes at pH 7.2, posing a significant challenge for clinical use.

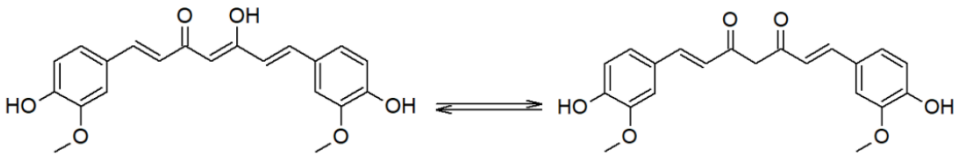

Figure 50. Tautomeric equilibrium of curcumin.

One of the major limitations of curcumin is its poor bioavailability, despite its proven safety profile (253). Studies on curcumin's pharmacokinetics reveal poor absorption, rapid metabolism in the liver, and swift elimination from the body. Curcumin undergoes both phase I metabolic reactions, where structural modifications increase its polarity, and phase II conjugation reactions, which facilitate the elimination of metabolites. To improve its bioavailability, researchers have explored various strategies such as co-administration with piperine and the development of micro and nanoparticle-based delivery systems (254,255).

Curcumin's diverse biological activities include potent anti-inflammatory effects, largely due to its ability to inhibit nuclear factor-kappa B (NF-kB), which reduces the expression of pro-inflammatory enzymes like COX-2 and limits the production of pro-inflammatory molecules (256). Additionally, curcumin's antioxidant activity is linked to its capacity to neutralize Reactive Oxygen Species (ROS) and protect cellular structures. The β-diketone moiety, particularly in its keto-enol form, plays a central role in scavenging free radicals (257).

Curcumin has also demonstrated significant anticancer potential. It can intervene at various stages of carcinogenesis, from initiation to tumor progression (258). Curcumin's ability to inhibit NF-kB and COX-2 helps prevent the chronic inflammation that often triggers cancer development. Furthermore, curcumin induces apoptosis in cancer cells and interferes with metastasis by targeting pathways involved in cell adhesion and migration. These effects make curcumin a promising agent in cancer prevention and treatment (259).

Curcumin has shown neuroprotective activity as well, particularly in the context of neurodegenerative diseases like Alzheimer's (260). Research suggests that curcumin inhibits the aggregation of β-amyloid plaques in the brain, which are characteristic of Alzheimer's disease. It also reduces the phosphorylation of tau proteins, another key factor in neurodegeneration. These effects are believed to stem from curcumin's antioxidant and anti-inflammatory properties, along with its ability to enhance the clearance of β-amyloid by immune cells.

7.2 Ce-containing Glasses

Cerium ions, acting as network modifiers in glass structures, primarily exist in two oxidation states: Ce^{3+} and Ce^{4+}. Cerium enhances the density of glasses, particularly phosphate-based ones, and has multiple industrial applications, including radiation protection, photosensitivity, and glass polishing. Cerium does not significantly alter the short-range order of other cations like silicon, phosphorus, calcium, and sodium in the glass network. However, the local environment of cerium varies depending on its oxidation state, with Ce^{3+} having longer bond lengths than Ce^{4+}. Notably, Ce^{3+} and Ce^{4+} ions are coordinated by different numbers of oxygen atoms depending on the glass composition, especially in the presence of phosphate.

In addition to its glass-modifying properties, Ce has notable biological activities. Studies have shown Cerium Oxalate has antiemetic effects, Cerium Nitrate aids in treating burns due to its antiseptic properties, and Cerium Chloride inhibits cancer cell proliferation (261). Cerium compounds have low cytotoxicity, but their accumulation in tissues—particularly the eyes, bones, and testis—has been observed in animal studies. Nanoparticles of Cerium Oxide (nanoceria) have garnered attention for their biomedical potential, particularly their antioxidant properties, which are linked to cerium's ability to switch between oxidation states (262). These nanoparticles show promise in protecting tissues from radiation-induced damage, making them a potential tool in radioprotection during cancer treatments.

7.3 Mn-containing Glasses

Manganese is a vital transition metal that plays a significant role in various biological processes within the human body, acting as a cofactor for several enzymes essential for metabolism. It is crucial for the activity of enzymes like Manganese Superoxide Dismutase (SOD), which helps protect cells from oxidative stress by converting superoxide radicals into less harmful molecules (263). Additionally, manganese mediates interactions between cells and their environment, influencing cell proliferation, differentiation, and apoptosis. Its incorporation into bioactive glasses is of particular interest due to its potential therapeutic benefits, such as promoting osteoblast growth and enhancing osteogenic differentiation, which makes these glasses promising for applications in bone regeneration (264). Manganese's ability to exist in multiple oxidation states (Mn^{2+}, Mn^{3+}, and Mn^{4+}) allows it to affect the properties of the glass network; for instance, Mn^{2+} can act as a network modifier while Mn^{3+} may serve as a network former under certain conditions. However, excessive manganese intake can lead to toxicity, resulting in neurotoxic effects similar to Parkinson's disease. Therefore, understanding the appropriate dosage is crucial, as small amounts can enhance bioactivity while higher concentrations (generally above 1% mol) may adversely affect it. Existing literature shows that Mn can be incorporated into bioactive glasses through methods like melt-quench and sol-gel techniques, with positive effects on osteoblast growth and osteogenic activity. Overall, Mn is an important element in the development of bioactive glasses, with significant implications for bone health and cellular processes, making it a valuable addition to regenerative medicine applications (265).

7.4 Oxidative stress

Ce and Mn have been shown to possess effective antioxidant properties ROS generated in the human body. ROS, which include free radicals and their precursors, are responsible for cellular aging and death; common examples include hydrogen peroxide (H_2O_2), superoxide ($O_2\cdot-$), and hydroxyl radicals (·OH). The implantation of biomedical devices typically involves surgery, which can lead to tissue damage and subsequent inflammation. This inflammatory response is associated with an increase in ROS production, resulting in oxidative stress—a condition characterized by an imbalance between free radicals and the body's antioxidant enzymes, such as catalase, superoxide dismutase, and glutathione peroxidase, that neutralize these harmful species. As reported in Figure 51, elevated oxidative stress can exacerbate inflammation, leading to further ROS generation.

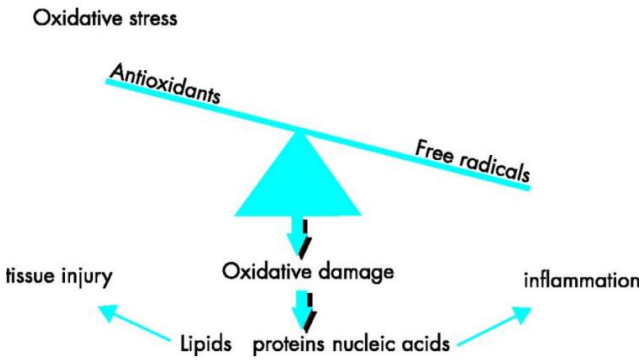

Figure 51. Scheme of the oxidative stress situation that occurs in the site of the surgery. (266)

This imbalance can prolong recovery following surgery. In this context, the ability of Ce and Mn to convert ROS into non-harmful species is particularly significant.

When nanoceria is applied at the inflammation site, it may facilitate the neutralization of excess free radicals, potentially accelerating postoperative recovery. Research by Celardo et al. (267) has demonstrated that cerium oxide nanoparticles (CeONPs) can convert hydrogen peroxide into harmless products through a catalytic process akin to that of the body's catalase enzyme. Furthermore, Korsvic et al. (268) have shown that nanoceria can mimic the activity of SOD, converting superoxide radicals into oxygen and hydrogen peroxide.

Manganese is already known to be a valid choice in the reduction of oxidative stress when incorporated in some complexes (269). Moreover, Mn^{2+} ions have been reported to inhibit lipid peroxidation both in vitro and in vivo (270). However, the manganese release in body fluids should be controlled, because an excessive concentration of Mn^{3+} can produce the opposite

behavior, leading to proliferation of cellular oxidative stress in consequence of its role in causing imbalance of mitochondrial redox activity (271).

pharmaceuticals

MDPI

Article

Curcumin-Based β-Diketo Ligands for Ga^{3+}: Thermodynamic Investigation of Potential Metal-Based Drugs

Matteo Mari [1], Debora Carrozza [1], Gianluca Malavasi [1], Ettore Venturi [1], Giulia Avino [2], Pier Cesare Capponi [3], Michele Iori [3], Sara Rubagotti [3], Silvia Belluti [4], Mattia Asti [3] and Erika Ferrari [1,*]

[1] Department of Chemical and Geological Sciences, University of Modena and Reggio Emilia, Via G. Campi 103, 41125 Modena, Italy; matteo.mari@unimore.it (M.M.); debora.carrozza@unimore.it (D.C.); gianluca.malavasi@unimore.it (G.M.); ettore-venturi@alice.it (E.V.)
[2] Department of Chemical and Pharmaceutical Sciences, University of Trieste, Via L. Giorgieri 1, 34127 Trieste, Italy; gavino@units.it
[3] Radiopharmaceutical Chemistry Section, Nuclear Medicine Unit, Azienda USL-IRCCS Reggio Emilia, Via Amendola 2, 42122 Reggio Emilia, Italy; piercesare.capponi@ausl.re.it (P.C.C.); michele.iori@ausl.re.it (M.I.); sara.rubagotti@ausl.re.it (S.R.); mattia.asti@ausl.re.it (M.A.)
[4] Department of Life Sciences, University of Modena and Reggio Emilia, Via G. Campi 183, 41125 Modena, Italy; silvia.belluti@unimore.it
* Correspondence: erika.ferrari@unimore.it; Tel.: +39-059-205-8631

Abstract: Curcumin is known for its therapeutic properties; among these, antioxidant, anti-inflammatory and anti-cancer ones stand out. Besides, curcumin metal complexes have shown widespread application in medicine and can be exploited as lead structures for developing metal-based drugs. Unfortunately, curcumin is poorly bioavailable, mainly due to its instability in physiological conditions; this weakness is tightly connected to the presence of the β-diketo moiety undergoing tautomeric equilibrium. Stability and metal-chelating ability can be tuned by modulating the electronic effects and steric hindrance close to the β-diketo moiety; in addition, formation of a metal complex shifts the tautomeric equilibrium towards the β-keto–enol form and increases stability in biological media. Among the metals used in clinical therapy, gallium nitrate has shown to have significant antitumor activity against non-Hodgkin lymphoma and bladder cancer, thus indicating that gallium-based drugs have potential for further development as antineoplastic agents with improved therapeutic activity. Curcuminoids have demonstrated high affinity for gallium(III), allowing the formation of stable positively charged M:L 1:2 β-diketonate complexes that benefit from the therapeutic activity of both the metal and the ligand. Seven new curcumin derivatives were synthesized and completely characterized. The new derivatives retain the solvent-dependent keto–enol tautomerism, with the prevalence of the diketo form in aqueous solution. Enhanced stability in simulated physiological conditions was observed in comparison to the lead compound curcumin. The presence of Ga^{3+} anticipates the dissociation of the enolic proton, allowing chelate complex formation, and simultaneously it shifts the tautomeric equilibrium towards the keto–enol form. A complete $^{1}H/^{13}C$ NMR and UV–Vis study was performed to define the metal-to-ligand stoichiometry ratio and the overall stability constants. In addition, we demonstrated that some of the derivatives have increased antiproliferative activity on colon cancer cells compared to curcumin and antioxidant properties. On the whole, the synthesized curcumin-based molecules may act as new gallium(III) chelators with improved stability with respect to curcumin and could open interesting perspectives for the development of novel therapeutic agents for cancer.

Keywords: curcumin; keto–enol equilibrium; β-diketo ligands; gallium(III)-chelating agents; metal-based drugs

Citation: Mari, M.; Carrozza, D.; Malavasi, G.; Venturi, E.; Avino, G.; Capponi, P.C.; Iori, M.; Rubagotti, S.; Belluti, S.; Asti, M.; et al. Curcumin-Based β-Diketo Ligands for Ga^{3+}: Thermodynamic Investigation of Potential Metal-Based Drugs. *Pharmaceuticals* **2022**, *15*, 854. https://doi.org/10.3390/ph15070854

Academic Editors: Angelo Maspero, Luca Nardo and Giovanni Palmisano

Received: 2 June 2022
Accepted: 7 July 2022
Published: 12 July 2022

1. Introduction

Curcumin (CUR) is known for its therapeutic properties; among these, antioxidant, anti-inflammatory and anti-cancer ones stand out [1,2]. Unfortunately, curcumin is poorly

water-soluble and bioavailable [3]; these are the drawbacks that hamper its great therapeutic properties and hold back its use in biomedical applications. This limit could be overcome by designing new methods of administration or synthesizing novel daughter compounds with modified chemical structures. The first strategy allows stabilizing the molecule and increases its bioavailability by reducing its metabolism and increasing the retention time in the bloodstream; recently, many studies have reported on the encapsulation of CUR into nanocarriers (i.e., liposomes, engineered nanoparticles or exosomes, EXOs) with promising preclinical results [4] even for neurological pathologies [5].

The second approach is based on a sort of SWOT analysis that points out particularly the weaknesses in the molecular structure related to the high instability in physiological media and the molecular moieties responsible for therapeutic activities. As the backside of the coin, huge efforts may easily account for failure or terrific success, since in silico investigations have the limit of theoretical models. To date, many SAR (structure–activity–relationship) studies have been performed to design different families of curcuminoids, as lately reviewed by Noureddin et al. [6]. Accordingly, the keto–enol structure is tentatively the main one responsible for fast CUR degradation in physiological conditions and poor bioavailability; this weakness is tightly connected to the presence of the β-diketo moiety undergoing tautomeric equilibrium, although the two tautomeric forms may also account for different biological properties [7].

Due to its C2V symmetry, CUR is characterized by only two tautomers: the keto–enol one (the average of the two equivalent keto–enol forms) and the diketo one. A more intricate situation is instead observed for asymmetric curcuminoids in which the two keto–enol tautomers are not equivalent and are entangled in complex equilibria [8,9]. The keto–enol tautomerism of CUR was investigated in depth, pointing out the prevalence of the keto–enol form in the solid state [10] and in apolar aprotic solvents, while the diketo form is more favored in polar/protic media, particularly in water [11]. Investigations of CUR in aqueous media are further complicated by its extremely low water solubility and by the fact that if spectroscopic techniques are employed, it is challenging to discriminate between the diketo form and the keto–enol form. In fact, mother CUR solutions are commonly prepared in a suitable organic solvent, typically methanol, ethanol or DMSO, that provides a solvation sphere around CUR enabling its dissolution in water but the organic solvation layer stabilizes the keto–enol form despite the polar/protic surrounding environment. Additionally, the structural modification of the keto–enol group by the insertion of a branching arm in the middle of it affects strongly the tautomeric equilibrium; typically, the equilibrium is shifted in favor of the diketo form as the bulkiness of the substituent is increased. In addition to thermodynamic features, recently, it was observed that the rate for reaching the tautomeric equilibrium is highly temperature-dependent, ranging from 700 s at 294 K to 200 s at 314 K [12].

CUR behaves as a weak triprotic acid due to the presence of the keto–enol moiety and the two phenol groups [13], hence, in a solution, proton dissociation equilibria occur. Particularly, the β-keto–enol moiety, due to its weak acid character and the presence of two oxygen atoms, can bind hard metal ions through the formation of a six-membered chelate ring. CUR has been demonstrated to form thermodynamically stable complexes with copper(II) [14–16], iron(III) and gallium(III), and other hard Lewis acids, as summarized by Wanninger et al. [13]. Formation of CUR metal complexes shifts the tautomeric equilibrium towards the β-keto–enol form and increases stability in biological media [14]. Furthermore, the stability in physiological conditions and the metal-chelating ability can be tuned by modulating the electronic effects and steric hindrance close to the β-diketo moiety.

Besides, CUR metal complexes have shown widespread application in medicine [13,17] and can be exploited as lead structures for developing metal-based drugs. Among the metals used in clinical therapy, gallium nitrate has been shown to have significant antitumor activity against non-Hodgkin lymphoma and bladder cancer [18], thus indicating that gallium-based drugs have potential for further development as antineoplastic agents

with improved therapeutic activity [19–24]. Curcuminoids demonstrated high affinity for gallium(III), allowing the formation of stable positively charged M:L 1:2 β-diketonate complexes that benefit from the therapeutic activities of both the metal and the ligand [25].

In this landscape, seven new curcumin derivatives were synthesized (Figure 1) and completely characterized. Two of them, compounds **1** and **2**, are asymmetric low-molecular-weight hemi-curcuminoids.

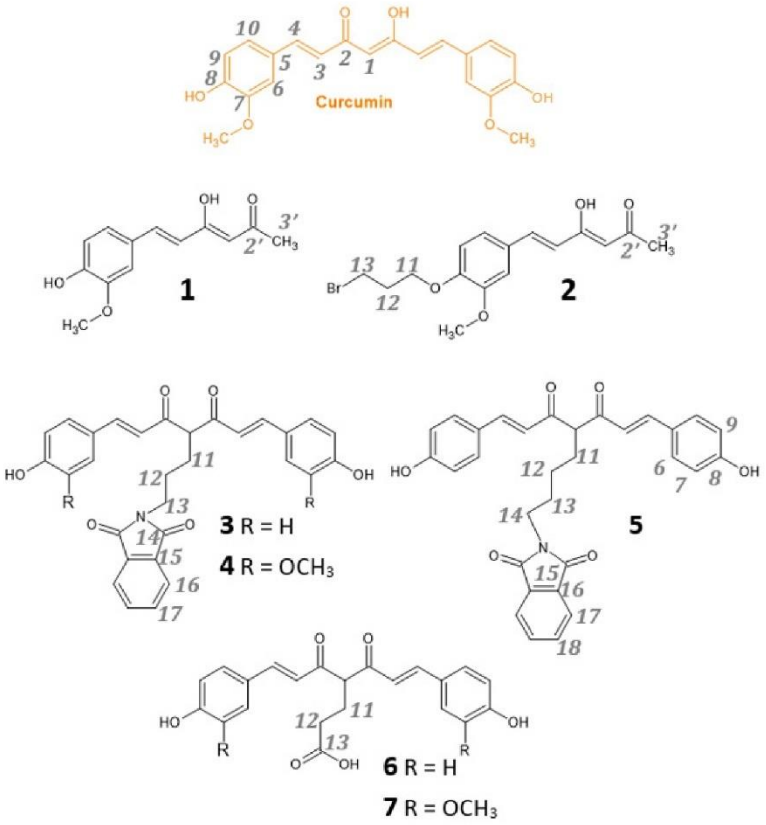

Figure 1. Chemical structures of curcuminoids and atom numbering for NMR signals' assignment.

The addition of a substituent in the center of the keto–enol moiety strongly affects the tautomeric equilibrium as well as acidity, stability and polarity, features woven with bioavailability and the related biological properties that can be tuned accordingly. Compounds **3**, **4** and **5** are symmetric substituted curcuminoids with an alkyl chain ending with a phthalimide group attached in the center of the keto–enol group. Phthalimide derivatives have recently shown similar activity to CUR in the inhibition of prostate cancer (PC) cell growth and migration, as well as in the modulation of the key molecular pathways involved in tumor progression and survival, opening the opportunity to develop new therapeutic drugs in aggressive PC tumors [26].

Finally, the carboxylic group in compounds **6** and **7** increases the solubility in aqueous media and provides an additional metal-binding group, as previously observed for K2A series [27].

The keto–enol tautomerism is hereafter investigated for all the new derivatives by means of UV–Vis and NMR spectroscopy, and stability in simulated physiological condi-

tions in comparison to the lead compound CUR is estimated as well. The different ligands were compared for their gallium(III)-chelating ability to suggest a potential candidate for further in vitro investigations.

2. Results and Discussion

2.1. Synthesis

Syntheses of all the CUR derivatives were performed using a modified procedure of the Pabon reaction [28]. Differently from the condition applied according to Pabon, DMF was used as a solvent instead of ethyl acetate because the higher reaction temperature, 120 °C vs. 80 °C, increases the reactants' and products' solubility. The use of DMF increases the reaction yield and facilitates the work-up.

The insertion of the chain in the keto–enol moiety was directly carried out in acetylacetone, the methylene group was activated in slightly basic conditions allowing the nucleophilic substitution to the Br derivative. All the curcuminoids were obtained with an average yield of around 50% except for compounds **2** and **5** that were obtained with 35% yield.

2.2. Stability in Physiological Conditions

All the investigated compounds showed greater stability than the lead compound curcumin in physiological conditions [29], although ligands **1**, **2**, **6** and **7** are more stable than **3**, **4** and **5** (Figure 2). The reduction in conjugation for **1** and **2** and particularly the protection of the phenol group provides an improvement in stability of the physiological condition, a pillar feature for clinical applications. Carboxylic ligands **6** and **7** are found in their mono-dissociated negatively charged form at pH 7.4, able to form strong interactions with water molecules that probably prevent degradation equilibria. Considering the residual compound's percentage after 4 h, the order of stability is as follows:

2 > 7 > 1 > 6 > 5 > 3 > 4

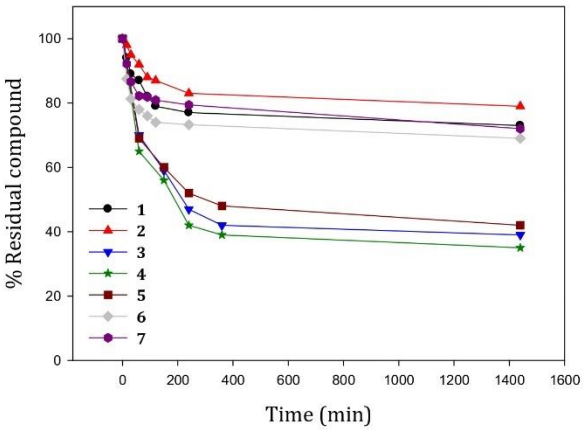

Figure 2. Stability profiles of the curcumin derivatives in simulated physiological conditions (PBS, 0.01 M; NaCl, 0.1 M; pH = 7.4; 37 °C in darkness). Residual percentage was calculated as $A_t \times 100/A_0$, where A_t and A_0 stand for absorbance at λ_{max} at time *t* and time zero, respectively.

2.3. Tautomeric Equilibria in a Solution and Acid–Base Behavior of Ligands

Nuclear magnetic resonance provides valuable information on keto–enol tautomerism, although the main issue of this technique is the required concentration that should be around the mM range to gain quantitative data. All the investigated curcuminoids

showed poor water solubility; hence, NMR analysis was performed in MeOD-d_4 or DMSO-d_6 solutions.

Bearing in mind the chemical structure of curcuminoids, two keto–enol forms (KE and EK) are in equilibrium with each other and with the diketo form (KK), as reported in Figure 3. Although the equilibrium between the two keto–enol forms (KE and EK) is too fast to be detected by NMR, in symmetrical structures ($R_1 = R_2$), such as curcumin, the two forms KE and EK are equivalent, and it is not possible to distinguish one from the other. In fact, the populations of the two tautomers (KE and EK) are equal, so the ^{13}C chemical shift of C-2/C-2′ (~180 ppm) is an average of the carbonyl (~190 ppm) and enol (~170 ppm) carbons. For asymmetrical derivatives ($R_1 \neq R_2$, $R_2 = CH_3$, i.e., compounds **1** and **2**, Figure 1), the KE and EK forms are not equally populated and the equilibrium shifts strongly in favor of the EK form. ^{13}C chemical shits of carbon 2 and 2′ are still an average of the chemical shifts of the two forms (KE and EK) in fast exchange with respect to the NMR timescale. However, in this situation, since the EK form is the prevailing species, the chemical shift of C-2 will be close to that of an enolic carbon while the chemical shift of C-2′ has a value typical of a carbonyl group. This hypothesis is verified by ^1H,^{13}C HMBC NMR experiments; in fact, the terminal methyl protons show long-range coupling with carbon C-2′ (~197 ppm) but not with C-2 (~178 ppm).

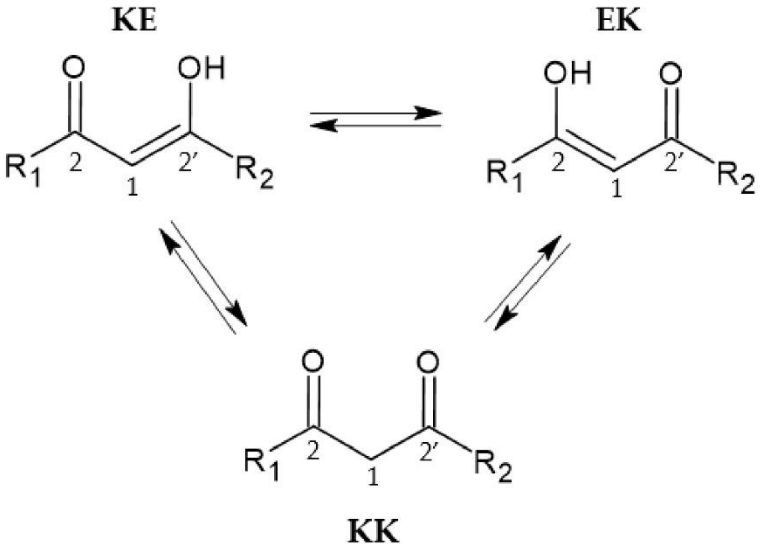

Figure 3. Schematic representation of tautomeric equilibria.

In a solution, with respect to the diketo moiety, the keto–enolic forms are usually stabilized by a strong intramolecular hydrogen bond (ΔE, ~4 kcal/mol), this energy barrier diminishes as long as the *s-trans* diketo form interacts with a protic environment as an H-bond acceptor. In MeOD-d_4 and DMSO-d_6, the predominant form for CUR is the keto–enol one [30]; differently, all the new derivatives in methanol show the presence of both the KE and KK forms, with a high prevalence of the KE form according to the degree of π-conjugation and the bulkiness of the substituent in the middle of the keto–enol group, as summarized in Table 1. The addition of a bulky substituent within the keto–enol moiety accounts for an increase in the KK species, especially for compounds **6** and **7** that are mainly in the KK form.

Table 1. Amount (molar percentage, %) of the keto–enol (KE) and diketo (KK) forms estimated based on the ^{1}H NMR data acquired in MeOD-d_4 at 298 K as reported in Experimental Section 3.5. * Percentage of KE includes the KE form of the Z isomer (6%).

Compound	KE (%)	KK (%)
1	96	4
2	88 *	12
3	45	55
4	47	53
5	70	30
6	25	75
7	25	75

The most informative NMR signal to investigate the keto–enol tautomerism should be the enol vinyl one, as reported in Figure 4 for compound 1. However, for highly conjugated structures such as curcuminoids, this proton undergoes fast exchange with deuterium of MeOD-d_4; as a consequence, a disappearance of the enol vinyl proton is observed after little time from the sample preparation. It is possible to detect the presence of the tautomers through the protons on the double bond that are strongly affected by the tautomeric equilibrium. The integrated areas of this spin system were used to estimate the relative percentage of the tautomeric forms as reported in Table 1 and described in Experimental Section 3.5.

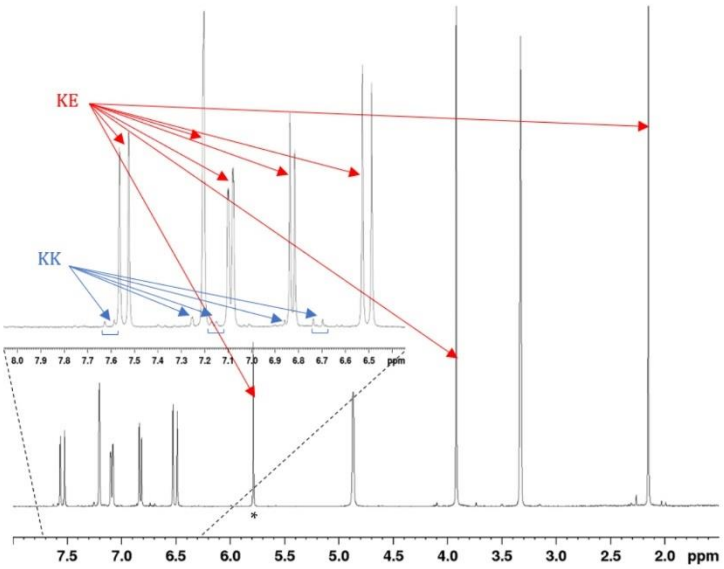

Figure 4. ^{1}H NMR spectrum of compound **1** in MeOD-d_4 at 298 K (at 600 MHz). Blue and red arrows highlight the KK end KE tautomeric forms, respectively. * Enol vinyl signal.

For asymmetrical curcumin derivatives, in addition to the enol equilibria, it is also possible to observe in a solution the equilibrium between two structural isomers with respect to the double bond: E and Z isomers [31]. The energy gap between the E and Z forms is quite small (4/6 kcal/mol), and isomerization is possible. Although the E/Z equilibrium is shifted in favor of the E isomer, these two isomeric forms can easily be discriminated by ^{1}H NMR on the basis of the scalar coupling constant $^3J_{HH}$ between the two vinyl protons: 16 Hz for the E isomer and 12 Hz for the Z one. Since the two structural

isomers exchange slowly in comparison to the NMR timescale, it is possible to observe two separate species corresponding to the E and Z forms, not an average of the two.

UV–Vis spectroscopy can be particularly suitable to overcome NMR limitations caused by poor water solubility of CUR. In fact, curcuminoids, due to their extremely high molar extinction coefficient (ε_0), can be analyzed in aqueous media (methanol <2%) despite their low solubility. CUR being a weak triprotic acid characterized by a keto–enol group, its spectroscopic properties are particularly dependent on the solvent and the pH conditions [32]. The enolic form is predominant in most of the solvents if CUR powder is dissolved in alcohol or DMSO before dilution in water. This species is the main one responsible for strong absorption with the maximum wavelength (λ_{max}) ranging from 410 to 430 nm and weak absorption between 260 and 280 nm due to $\pi \rightarrow \pi^*$ transitions [33]. Additionally, CUR presents a weaker transition n-π^* (at ca. 375 nm) due to the KK form that increases when CUR is directly suspended in water. Keto–enol tautomerism is strongly affected by the presence of water molecules due to the different hydrogen bond interactions the keto and enol group can form as pointed out by Manolova et al. [8]. Compounds **1** and **2** show an intense absorption peak at 360 nm corresponding to the KE form; the blue shift compared to CUR is due to the reduced π-π conjugation. Derivatives **3**–**5** are characterized by a mixture of the KE (350–370 nm) and KK (420–450 nm) forms while **6** and **7** are mostly found in their KK form (330–350 nm) (Figure S1).

Spectrophotometric pH titrations were performed to evaluate the pH effect on the ligands for all the investigated compounds. According to the number of acid sites it is possible to group the ligands as HL (**2**), H_2L (**1**), H_3L (**3**,**4**,**5**) and H_4L (**6**,**7**). As long as the pH is increased, a new absorption band is observed in the 450–500 nm range, as shown in Figure 5 for **7**, due to the dissociated form.

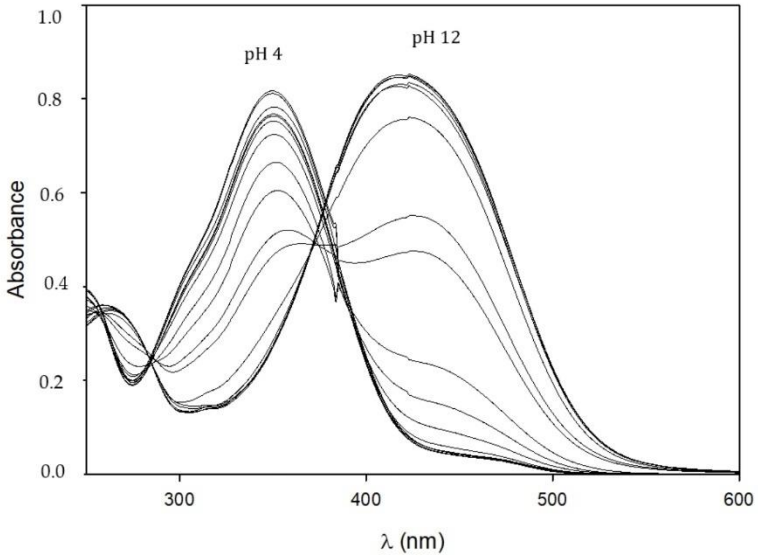

Figure 5. UV–Vis spectra of **7** at 25 °C in an aqueous solution (L = 50 μM) with increasing pH.

Many equilibria occur as pointed out by the woven structure close to the isosbestic point, particularly dissociation reactions. Elaboration of the data allows estimating the overall protonation constants ($\log\beta_{MLH}$) and pK_a values for all the compounds, as reported in Table 2.

Table 2. Overall protonation constants calculated from spectrophotometric data at 298 K using HypSpec software [34]; pK_a values were calculated from logβ values as follows: (HL) $pK_{a1} = \log\beta_{011}$; ($H_2L$) $pK_{a1} = \log\beta_{012} - \log\beta_{011}$, $pK_{a2} = \log\beta_{011}$; ($H_3L$) $pK_{a1} = \log\beta_{013} - \log\beta_{12}$; $pK_{a2} = \log\beta_{012} - \log\beta_{011}$, $pK_{a3} = \log\beta_{011}$; ($H_4L$) $pK_{a1} = \log\beta_{14} - \log\beta_{13}$, $pK_{a2} = \log\beta_{13} - \log\beta_{12}$, $pK_{a3} = \log\beta_{12} - \log\beta_{12}$, $pK_{a4} = \log\beta_{11}$. * Refers to the keto–enol moiety dissociation.

$\log\beta_{MLH}$	***1***	***2***	***3***	***4***	***5***	***6***	***7***
$\log\beta_{011}$	10.212 (2)	10.903 (8)	10.88 (2)	10.78 (4)	10.44 (3)	11.42 (2)	12.22 (2)
$\log\beta_{012}$	18.509 (3)		20.29 (2)	20.44 (6)	20.45 (2)	21.12 (6)	21.61 (5)
$\log\beta_{013}$			28.84 (4)	29.44 (6)	29.58 (4)	29.76 (7)	29.98 (4)
$\log\beta_{014}$						34.62 (5)	34.92 (9)
pK_{a1}	8.297 (5)	10.903 (8) *	8.55 (4)	9.00 (10)	9.13 (6)	4.86 (12)	4.92 (13)
pK_{a2}	10.212 (2) *		9.41 (4) *	9.66 (12) *	10.01 (5)	8.64 (13)	8.37 (9)
pK_{a3}			10.88 (2)	10.78 (4)	10.44 (3)	9.70 (8) *	9.39 (7) *
pK_{a4}						11.42 (2)	12.22 (2)

Spectrophotometric titrations confirm, as recently suggested [29], that the phenol group in *para* position to the aliphatic chain is more acidic than the keto–enol moiety. Compound **2** is a monoprotic weak acid with a pK_a value of 10.903; likewise, compound **1** shows a similar value for the second dissociation (pK_{a2}) that can only be attributed to the keto–enol group. For all the compounds, the proton dissociation of the first phenol group responsible for the main UV–Vis absorption around 450 nm, occurs within the pK_a range of 8.3–9.1. The pK_a values for keto–enol group are all in the range of 9.4–10.9 (Table 2), consistently with the previously reported keto–enol derivatives [29,35]. The second phenol group dissociates at extremely high pH; in fact, pK_a values range from 10.4 to 12.2. Compounds **6** and **7** have an additional acid group, the carboxylic one, that undergoes proton dissociation with a pK_a value close to 5. The species distribution curves for **1**, **4** and **7** are reported in Figure 6. All the compounds are mainly in their neutral form at physiological pH (7.4), except for **6** and **7** which are negatively charged as carboxylate anions.

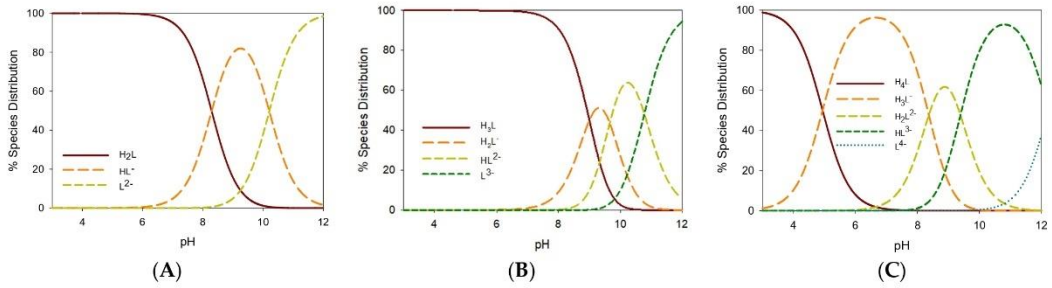

Figure 6. Species distribution curves for **1** (panel **A**), **4** (panel **B**) and **7** (panel **C**) at 25 °C ($[L]_{total} = 10^{-4}$ mol L^{-1}). The data were calculated on the basis of the $log\beta_{MLH}$ values reported in Table 2.

2.4. Gallium Complexing Ability

NMR can shed light on the metal–ligand interactions; particularly, these data allow not only defining the binding site and the metal-to-ligand molar ratio, but also investigating the actual equilibria in a solution, given that they are compatible with the NMR timescale. For all the free ligands, the enol proton of the keto–enol form was confirmed by the presence of a broad signal at 15–17 ppm (DMSO-d_6/MeOD-d_4) that disappears when the metal ion (Ga^{3+})

is added to the solution. Apparently, this could be a proof of the proton dissociation of the ligand; indeed, the enol proton is extremely mobile and exchanges with the deuterated solvent after little time from sample preparation even in the absence of the metal ion. Hence, these data cannot be used as a solid proof of proton dissociation. Indeed, NMR titrations with Ga^{3+} quite clearly support the removal of the proton in favor of a trivalent metal ion; in fact, a downfield shift is observed for the protons close to the keto–enol moiety. However, for all the examined curcuminoids, the addition of Ga^{3+} at acidic pH (~5) instantly turns into the formation of a new set of downfield-shifted signals in a slow chemical exchange with respect to the NMR timescale. The high affinity of the keto–enol moiety for hard Lewis acid gallium(III) triggers an anticipated proton dissociation that enables the formation of an M:L 1:2 complex of the KE tautomer, the only one capable of binding the metal ion, as confirmed by the downfield shift of both allyl protons (H-3 and H-4, Figure 2) and ^{13}C chemical shifts of the keto–enol group. The keto–enol group is an *O*,*O* bidentate chelator that allows the formation of a highly stable six-membered ring with the metal ion. The reaction is fast, and the formation of the metal complex is observed immediately after the addition of the metal ion. As long as the KE form reacts with the metal, the tautomeric equilibrium is shifted towards the depletion of the KK form in favor of the KE one. The complete disappearance of KK is observed within 24 h for all the ligands. An increase in Ga^{3+} concentration till the 1:1 M:L molar ratio allows the formation of a complex species with metal-to-ligand molar ratio 1:1 as suggested by new downfield-shifted signals and the concurrent disappearance of the 1:2 M:L complex. Figure 7 reports the titration with Ga^{3+} in MeOD-d_4 for compound **1** (compound **7** is reported in Figure S2).

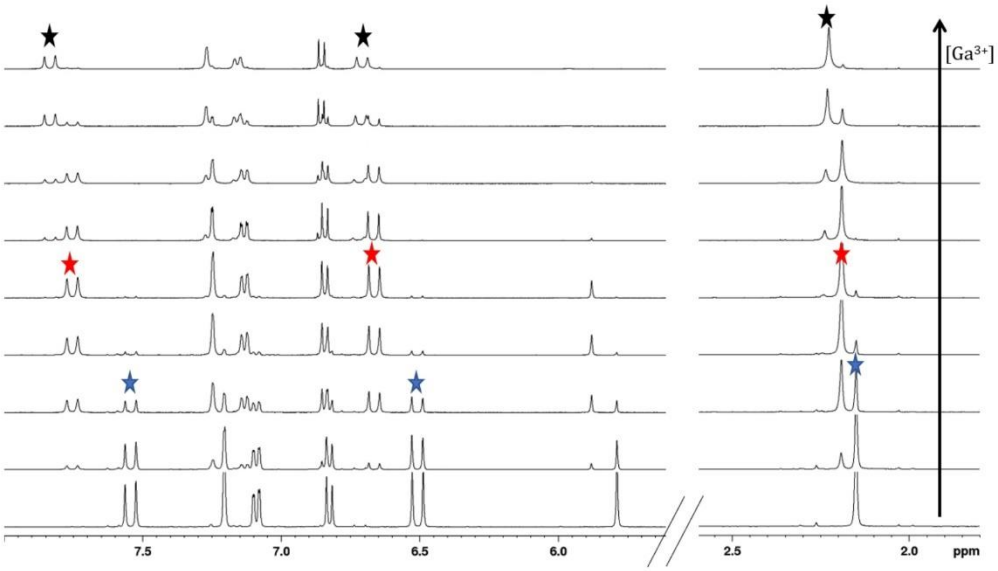

Figure 7. ^{1}H NMR spectra of compound **1** in MeOD-d_4 at 298 K (at 600 MHz) at increasing addition of a Ga^{3+} MeOD-d_4 solution up to the metal-to-ligand 1:1.5 molar ratio. The stars highlight resonances of protons H-1, H-3 and H-4 in the free ligand (blue), M:L 1:2 complex (red) and M:L 1:1 complex (black).

The downfield shifts for protons H-3 and H-4 in the M:L 1:1 complex range between 0.15 and 0.3 ppm (90–180 Hz at 600 MHz) for all ligands, C-3 and C-4 are downfield-shifted (around 3–4 ppm). The shift observed for C-2 is close to 1 ppm for all the compounds except for **1** and **2**. In these compounds, carbons C-2 and C-2′ are not chemical shift-equivalent since only one of the two keto–enol forms is observed in the solution, the EK form, in which the keto group is in the α position to the methyl one, as confirmed by ^{1}H,^{13}C HMBC

spectra (Figure 8—left). The EK tautomer is favored by higher π–π conjugation that is gained when the enol group is directly attached to the vinyl chain. When Ga^{3+} is bound to the keto–enol group (Figure 8—right), C-2 is upfield-shifted by the exchange of the proton with the metal ion, $\Delta\delta(^{13}C) = 6.9$ ppm from 177.8 to 184.7 ppm and $\Delta\delta(^{13}C) = 7.7$ from 177.0 to 184.7 ppm for compounds **1** and **2**, respectively. C-2′ is less affected by the insertion of the metal ion, and it results in downfield shifting, $\Delta\delta(^{13}C) = -2.6$ ppm from 197.9 to 195.3 ppm and $\Delta\delta(^{13}C) = -2.1$ ppm from 197.9 to 195.8 ppm for **1** and **2**, respectively.

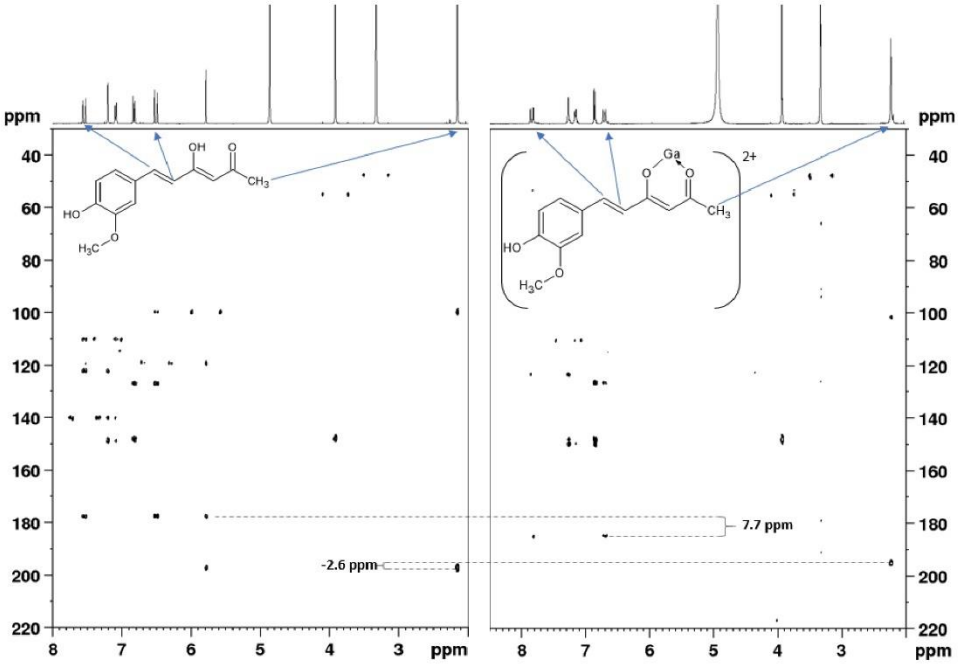

Figure 8. $^{1}H,^{13}C$ HMBC NMR spectra in MeOD-d_4 at 298 K (at 600 MHz) of compound **1** (**left**) and its gallium(III) complex with the metal-to-ligand 1:1 molar ratio (**right**).

Finally, NMR data suggest that the carboxylic group of **6** and **7** is probably not involved in metal coordination; in fact, we observed a higher downfield shift for the proton closer to the KE group (H-11) than the farther one (H-12), $\Delta\delta(^{1}H) = 24$ Hz and 50 Hz vs. 11 Hz and 38 Hz for M:L 1:2 and M:L 1:1, respectively (Figure S2). The weak interaction of the carboxylic group with the metal ion could be explained by the absence of a beneficial chelate effect connected to the long length of the aliphatic chain itself.

As reported above, curcuminoids have characteristic UV–Vis absorption spectra; hence, formation of metal complexes can be investigated using this technique. When Ga^{3+} is added to the ligand aqueous solution under acidic conditions (pH ~5), the absorbance decreases and a red shift of the KE maximum is observed, suggesting the formation of the metal complex (Figure 9). By plotting the absorbance vs. the metal-to-ligand molar ratio, the formation of M:L 1:2 and 1:1 complexes can be suggested, confirming the outcomes of NMR titrations. The so-formed metal complexes are extremely stable (residual compound's percentage (8 h) >90% for all the ligands), suggesting that fixing the keto–enol moiety into the KE form in the formation of coordination bonds highly enhances the kinetic stability of the ligand itself.

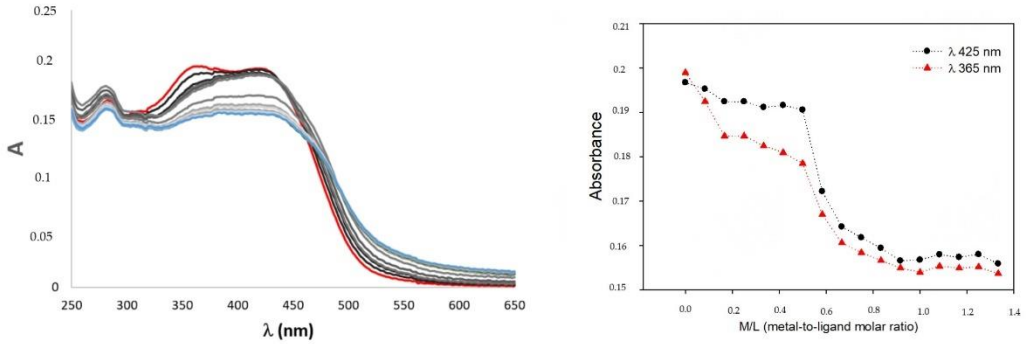

Figure 9. Spectrophotometric titration of **4** with a Ga^{3+} solution in acidic conditions (pH ~5) up until the M/L 1:1.3 is reached (**left**) and plots of absorbance at different λ_{max} vs. M/L (**right**) at 25 °C ([L] = 50 μM).

In order to assess the metal-to-ligand molar ratio, LC/MS experiments were carried out supporting the formation of M:L 1:2 complexes for compounds **1**–**5** and of M:L 1:1 species for compounds **6** and **7** (Table S1).

A complete investigation of the thermodynamic stability of metal complexes in an aqueous medium was then carried out through pH-metric UV–Vis titrations.

The increase in pH in M:L 1:1 systems causes an initial decrease in the intensity of the maximum band, followed by the appearance of a new intense absorption of deprotonated systems around 420–430 nm (Figure S3). The presence of the metal ion in the solution anticipates the dissociation of the keto–enol group of 3–4 pK_a units, as suggested by the plot of absorbance at λ_{max} vs. pH for compound **6** as an example (Figure 10). On increasing pH starting from extremely acidic conditions (pH 3), a decrease in absorbance at 405 nm is observed until pH reaches a value around 8 (Figure 10A). In this pH interval, the spectral profile remains unchanged, with the coexistence of both KE and KK forms suggesting that the conversion of the KK form into the KE form, due to metal chelation, is slow and probably hampered by the formation of a strong network of hydrogen bonds between keto groups and water molecules. When pH is raised above 8 (Figure 10B), the absorbance band of dissociated phenol appears at 420 nm and increases in intensity until pH 12. It is possible to observe a slight blue shift of λ_{max} within this pH range.

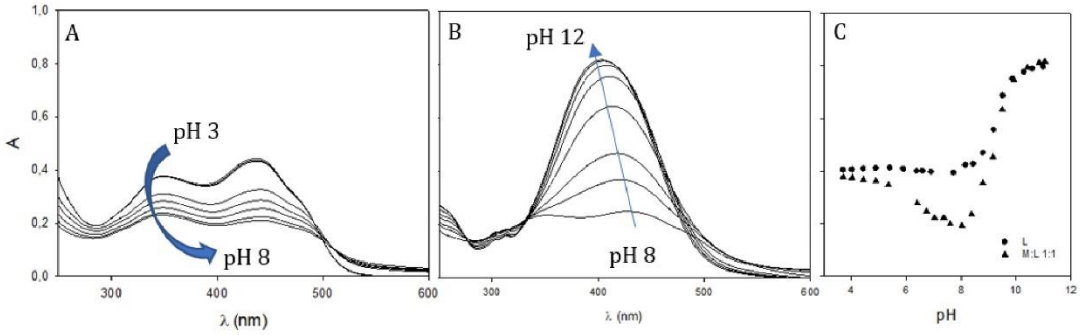

Figure 10. UV–Vis spectra of the Ga^{3+}: **6** 1:1 molar ratio at 25 °C (L = 50 μM) on increasing pH. Panel (**A**)—pH range of 3–8; panel (**B**)—pH range of 8–12; panel (**C**)—plot of absorbance at 405 nm vs. pH for the free ligand (circles) and the metal-ligand system (triangles).

The stability constants of the complexes were calculated taking into account the possible complexes at the M:L 1:1, 1:2 and 1:3 molar ratios, but only for compounds **1** and **2** the refinements converged completely. For bulky ligands (**3**,**4**,**5**,**6**,**7**), it was necessary to exclude M:L 1:3 to reach convergence due to their steric hindrance that prevents the rearrangement of three ligands in the octahedral coordination sphere of Ga^{3+}.

To compare ligands with different proticity, $logK_{11}$, $logK_{12}$ and $logK_{13}$ were calculated according to the equations reported in the caption of Table 3.

Table 3. Overall stability constants (β) and apparent formation constants (K) calculated from spectrophotometric data at 298 K using HypSpec software [36]. LogK values were estimated starting from the $log\beta_{MLH}$ ones according to the different number of acid groups as follows: (HL) $logK_{11} = log\beta_{110}$, $logK_{12} = log\beta_{120}$, $logK_{13} = log\beta_{130}$; ($H_2L$) $logK_{11} = log\beta_{111} - log\beta_{11}$, $logK_{12} = log\beta_{122} - 2log\beta_{11}$, $logK_{13} = log\beta_{133} - 3log\beta_{11}$; ($H_3L$) $logK_{11} = log\beta_{112} - log\beta_{12}$, $logK_{12} = log\beta_{124} - 2log\beta_{12}$; ($H_4L$) $logK_{11} = log\beta_{112} - log\beta_{12}$; *pGa* ($-log[Ga^{3+}]_{free}$) was calculated at specific conditions ($[Ga^{3+}]_{total}$ = 1 μM, $[L]_{total}$ = 10 μM, pH 7.4 at 25 °C).

	1	**2**	**3**	**4**	**5**	**6**	**7**
$\mathbf{H_xL}$	H_2L	HL	H_3L	H_3L	H_3L	H_4L	H_4L
$\mathbf{log\beta_{110}}$	11.78 (4)	8.129 (9)					
$\mathbf{log\beta_{111}}$	17.59 (3)						
$\mathbf{log\beta_{112}}$			28.28 (3)	28.48 (5)	28.54 (3)	27.79 (5)	28.29 (5)
$\mathbf{log\beta_{113}}$						34.09 (5)	36.51 (6)
$\mathbf{log\beta_{120}}$	20.30 (5)	15.185 (4)					
$\mathbf{log\beta_{122}}$	34.77(3)						
$\mathbf{log\beta_{124}}$			54.63 (5)	55.33 (5)	57.00 (1)		
$\mathbf{log\beta_{130}}$	28.37 (7)	20.45 (3)					
$\mathbf{log\beta_{133}}$	49.7 (4)						
$\mathbf{logK_{11}}$	7.38 (3)	8.129 (9)	7.99	8.04	8.09	6.67	6.68
$\mathbf{logK_{12}}$	14.35 (3)	15.185	14.05	14.45	16.1		
$\mathbf{logK_{13}}$	19.1 (4)	20.45					
pGa	19.0	13.1	20.8	21.5	23.2	14.0	15.3

The species distribution curves for **1**, **4** and **7** are reported in Figure 11.

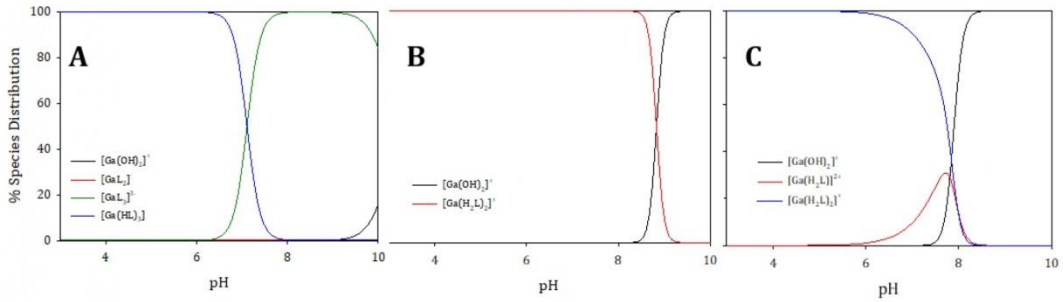

Figure 11. Species distribution curves for **1** (panel **A**), **4** (panel **B**) and **7** (panel **C**) at 25 °C (L_{total} = 10 μM; $Ga^{3+}{}_{total}$ = 1 μM). The data were calculated based on the logβ values reported in Table 3.

Compounds **1–5** have similar logK values, while ligands **6** and **7,** probably due to their steric hindrance, are unable to form metal complexes with a smaller M:L molar ratio and show lower K values. This decreased affinity for the metal ion is highlighted by the species distribution curves (Figure 11C); indeed, formation of Ga(III) hydroxide species is observed slightly above the physiological pH (>7.5).

To consistently compare the chelating abilities for Ga(III), *pGa* values (Table 3) were calculated as $-\log[Ga^{3+}]_{free}$. The use of pM dates back to the paper of Harris et al. [37], in which it was used for the first time to express and relate the iron(III)-sequestering ability of siderophores. Among the investigated chelators, only the phthalimide derivatives (**3**, **4** and **5**) showed interesting *pGa* values, quite close to those of renowned gallium chelators such as DFOB (*pGa* = 21.6) [38] or the recently developed PrP9, a triazacyclononane-based phosphinate ligand (*pGa* = 23.1) [39], and the hydroxamate chelators lately reported by Toporivska et al. [40] (*pGa* 21.9 (min)–25.4 (max)). The difference of two orders of magnitude between compounds **3**/**4** and **5** reflects the steric hindrance provided by the phthalimide group. In fact, when this bulky moiety is separated from the keto–enol moiety by a longer spacer (butyl vs. propyl chain), metal chelation is more effective and $\log K_{12}$ is greatly increased (16.1 vs. 14.05/14.45), suggesting the formation of a more stable M:L 1:2 complex species.

Finally, the kinetic stability of metal complexes at the M:L 1:1 molar ratio were investigated by UV–Vis spectroscopy in physiological conditions (PBS pH 7.4). Formation of coordination bonds to the metal strongly stabilizes the ligand, and for all the metal complexes, the percentage of the residual compound was greater than 85% within 8 h (data not shown).

2.5. Transmetalation Reactions of Selected Curcumin Derivatives **4** *and* **5**

Compounds **4** and **5** were selected to evaluate iron-chelating ability by spectrophotometric analysis in the same conditions as the ones applied to carry out investigations on Ga^{3+} systems. The calculated $\log\beta_{124(Fe)}$ values were 56.2 (2) and 58.6 (4) for **4** and **5**, respectively. From the difference between the logβ values of the complexes with two metal ions, it is possible to calculate the apparent stability constant K ($\log K = \log\beta_{124(Fe)} - \log\beta_{124(Ga)}$) associated with the transmetalation reaction (Equation (1)).

$$Fe^{3+} + [Ga(H_2L)_2]^+ \leftrightarrows Ca^{3+} + [Fe(H_2L)_2]^+ \quad (1)$$

LogK values are small for **4** and **5** (0.9(3) and 1.2(7), respectively), confirming a similar sequestering ability towards Ga^{3+} and Fe^{3+}.

2.6. Antioxidant Activity and Cell Viability Assays

Compounds **4** and **5** are characterized by the presence of two phenolic groups that could be responsible for additional antioxidant properties, so the DPPH radical-scavenging assay was carried out for the free ligands **4** and **5** and their Ga^{3+} complexes (Figure S4). Both compounds showed similar IC_{50} values (20 μM and 32 μM for **4** and **5**, respectively) and close to that reported for curcumin (13 μM [14]).

To establish the potential antitumor activity of compounds **3**, **4** and **5**, we evaluated their effects on the proliferation of HCT116 colon carcinoma cells, a cellular tumor model previously used for the characterization of curcumin derivatives [41]. We performed dose response experiments (Figure 12A) and calculated GI_{50} values as the concentration of molecules that induces 50% growth inhibition after 48 h of treatment (Figure 12B). Curcumin and compound **4** were used as reference drugs since we had previously reported their antiproliferative activity in HCT116 cells [26]. Comparing curcumin with the synthesized derivatives revealed that the conjugation of phthalimide significantly increases their antiproliferative activity in HCT116 cells (Figure 12). Besides, **5** showed a major efficacy in terms of growth inhibitory activity (GI_{50}) compared to curcumin.

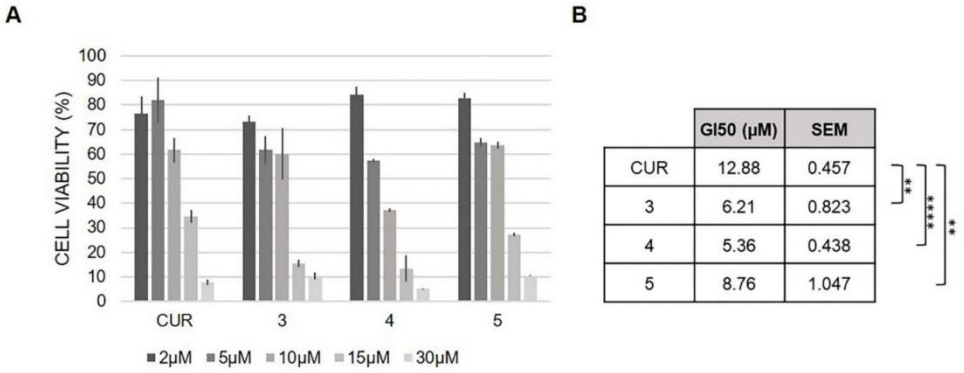

Figure 12. Biological activity of the selected curcumin derivatives on human colorectal HCT116 cancer cells. Panel (**A**): dose-dependent effect of curcumin derivatives administration for 48 h on the cell growth of HCT116 cancer cells as assessed by the MTT assay. Panel (**B**): GI_{50} values and statistical significance compared to curcumin are indicated as the means ± SEM (unpaired *t*-test: ** $p < 0.01$, **** $p < 0.0001$).

3. Materials and Methods

3.1. General Procedures

All the chemicals and solvents were purchased with the highest purity grade available and used without further purification unless otherwise specified; pH measurements were carried out using a calibrated pH-meter (Mettler-Toledo). Liquid chromatography/mass spectrometry (LC/MS) was performed on an Agilent 6300 Ion Trap LC/MS System equipped with an electrospray ionization (ESI) interface. Elemental analysis was performed on a Thermo Scientific™ FLASH 2000 CHNS Analyzer.

All the reaction intermediates were purified as specified in the following procedures and their purity (≥95%) was checked by a combination of LC/MS, NMR and elemental analysis.

Atom numbering of the NMR data refers to Figure 1.

3.2. Synthesis

4-(3-bromopropyl)-3-methoxybenzaldehyde

1,3-dibromopropane (3 mL) is slowly added to a suspension of vanillin (1.5 g) and K_2CO_3 (1.9 g) in 15 mL of dimethylformamide (DMF). The mixture is kept under stirring at 75 °C overnight, then the temperature is cooled down, the solid is filtered off and the solution is neutralized by adding 10% CH_3COOH aqueous solution. The product is extracted in ethyl acetate (EtOAc), the organic phases are then collected, washed with $NaHCO_3$ and brine and finally dried over Na_2SO_4. After filtering off the salts, the solvent is removed under reduced pressure. The raw product is purified by flash column chromatography (silica, gradient (*v*/*v*) petroleum ether (EtPet): ethyl acetate (EtOAc) 100:0→70:30). Light yellow solid, 27% yield. Elemental analysis for $C_{11}H_{13}O_3Br$ (267.08 g/mol): calc. C, 50.19%; H, 5.27%; exp. C, 50.02%, H, 5.49%. LC/MS (ESI): *m*/*z* 287.0 $[M + H]^+$. ^1H NMR (δ (ppm), $CDCl_3$): 9.87 (1H), 7.43 (d, 1H), 6.99 (d, 1H), 7.46 (dd, 1H), 4.16 (t, 2H), 2.10 (m, 2H), 3.53 (t, 2H), 3.94 (OCH_3, s, 3H).

*(3Z,5E)-4-hydroxy-6-(3-methoxy-4-methylphenyl)hexa-3,5-dien-2-one (***1***)*

The procedure was adapted from Pabon's CUR synthesis [28]; actually, boron acetylacetonate is obtained by reacting B_2O_3 (0.72 g) and 1.1 mL of acetylacetone (acac) in DMF (11 mL). The mixture is kept under reflux at 80 °C for 30 min, then 11 mL tributyl borate is added, and the mixture is kept under stirring at 80 °C overnight. After 16 h, the suspension turns orange–red and becomes dark red when vanillin is added (0.265 g). *n*-butylamine

(145 µL in 0.5 mL of DMF) is slowly dropped over 1 h. The reaction batch is maintained under heating and stirring for 6 more hours, then the system is cooled down to r.t., acidified by adding 40 mL of 0.5 M HCl and kept under stirring for 1 h. The aqueous phase is extracted with EtOAc three times, the organic phases are collected, washed with $NaHCO_3$, brine and eventually dried under Na_2SO_4. After filtering off the salts, the solvent is removed under reduced pressure. The raw product is purified by flash column chromatography (silica, gradient (*v*/*v*) EtPet: EtOAc 100:0→70:30). Yellow powder, 45% yield. Elemental analysis for $C_{13}H_{14}O_4$ (234.25 g/mol): calc. C, 66.66%, H, 6.02%; exp. C, 66.52%, H, 6.18. LC/MS (ESI): *m*/*z* 235.1 $[M + H]^+$. ^1H NMR (δ (ppm), MeOD-d_4): 7.55 (H-4, d, 1H), 7.20 (H-6, d, 1H), 7.09 (H-10, dd, 1H), 6.82 (H-9, dd, 1H), 6.51 (H-3, d, 1H), 5.79 (H-1, s, 1H), 3.92 (OCH3, s, 3H), 2.15 (H-3′, s, 3H).

(3Z,5E)-6-[4-(3-bromopropoxy)-3-methoxyphenyl]-4-hydroxyhexa-3,5-dien-2-one (**2**)

Compound **2** was obtained similarly to **1**, but 4-(3-bromopropyl)-3-methoxybenzaldehyde was used instead of vanillin. Yellow powder, 35% yield. Elemental analysis for $C_{16}H_{19}BrO_4$ (355.22 g/mol): calc. C, 54.10%, H, 5.39%; exp. C, 53.89%, H, 5.48%. LC/MS (ESI): *m*/*z* 355.1 $[M + H]^+$. ^1H NMR (δ (ppm), MeOD-d_4): 2.16 (H-3′, s, 3H), 5.81 (H-1, s, 1H), 6.56 (H-3, d, 1H), 7.56 (H-4, d, 1H), 7.25 (H-7, dd, 1H), 7.00 (H-9, dd, 1H), 7.17 (H-10, dd, 1H), 4.18 (H-11, t, 2H), 2.34 (H-12, m, 2H), 3.67 (H-13, t, 2H), 3.91 (OCH_3, s, 3H).

(2-((4Z,6E)-5-hydroxy-7-(4-hydroxyphenyl)-4-((E)-3-(4-hydroxy-3-ethoxyphenyl) acryloyl) hepta-4,6-dien-1-yl)isoindoline-1,3-dione (**3**)

Compound **3** was synthesized as previously reported [21]. Orange powder, 40% yield. Elemental analysis for $C_{30}H_{25}NO_6$: calc. C, 72.72%, H, 5.09%, N, 2.83%; exp. C, 73.06%, H, 5.21%, N, 2.75%. LC/MS-IT: *m*/*z* 496.6 $(M + H)^+$. ^1H NMR (DMSO-d_6): 7.00 (H-3, d, 2H), 7.58 (H-4, d, 2H), 7.54 (H-6/H-10, d, 4H), 6.79 (H-7/H-9, d, 4H), 2.65 (H-11, t, 2H), 1.83 (H-12, m, 2H), 3.77 (H-13, t (broad), 2H), 7.88 (H-16, m, 2H), 7.85 (H-17, m, 2H).

(2-((4Z,6E)-5-hydroxy-7-(3-methoxy-4-hydroxyphenyl)-4-((E)-3-(4-hydroxy-3-ethoxyphenyl) acryloyl) hepta-4,6-dien-1-yl)isoindoline-1,3-dione (**4**)

Compound **4** was synthesized as previously reported [26]. Light-orange powder, 50% yield. Elemental analysis for $C_{32}H_{29}NO_8$ (555.57 g/mol): calc. C, 69.18%, H, 5.26%, N, 2.52%; exp. C, 69.02%, H, 5.39%, N, 2.83%. LC/MS-IT: *m*/*z* 556.2 $(M + H)^+$. ^1H NMR (δ (ppm), DMSO-d_6): 7.00 (H-3, d, 2H), 7.58 (H-4, d, 2H), 7.54 (H-6/H-10, d, 4H), 6.79 (H-7/H-9, d, 4H), 2.65 (H-11, t, 2H), 1.83 (H-12, m, 2H), 3.77 (H-13, t (broad), 2H), 7.88 (H-16, m, 2H), 7.85 (H-17, m, 2H).

2-((4Z,6E)-5-hydroxy-7-(4-hydroxyphenyl)-4-((E)-3-(4-hydroxy-3-ethoxyphenyl) acryloyl) hepta-4,6-dien-1-yl)isoindoline-1,3-dione (**5**)

Compound **5** was synthesized following a procedure previously reported [26]. 2,4-pentandione (25 mmol) is added to a suspension of K_2CO_3/KI (50/3 mmol) in dry acetone (15 mL) at 80 °C and kept under stirring for 1 h. Then, a solution of 2-(4-bromobutyl)-1H-isoindole-1,3(2H)-dione (25 mmol) in dry acetone (5 mL) is added dropwise and kept under magnetic stirring overnight at 80 °C. The solution is then cooled down to *r.t.*, diluted with aqueous NH_4Cl and extracted twice with DCM. The organic phases are washed with brine and dried over Na_2SO_4. After solvent removal under reduced pressure, a yellow sticky product is obtained that requires further purification by flash column chromatography. Orange powder, 34% yield. Elemental analysis for $C_{31}H_{27}NO_6$ (509.55 g/mol): calc. C, 73.07%, H, 5.34%, N, 2.75%; exp. C, 73.25%, H, 5.44%, N, 2.85%. LC/MS-IT: *m*/*z* 510.2 $(M + H)^+$. ^1H NMR (δ (ppm), $CDCl_3$): 7.72 (H-18, m, 2H), 7.81 (H-17, dd, 2H), 3.83 (H-14, m (broad), 2H), 1.92 (H-13, m, 2H), 1.62 (H-12, m, 2H), 2.67 (H-11, t, 2H), 6.98 (H-3, d, 2H), 7.73 (H-4, d, 2H), 7.22 (H-10, dd, 2H), 7.18 (H-9, d, 2H), 6.99 (H-6, d, 2H), 4.03 (OCH_3, s, 6H).

(6E)-7-(4-hydroxyphenyl)-4-[(2E)-3-(4-hydroxyphenyl)prop-2-enoyl]-5-oxohept-6-enoic acid (**6**)

Compound **6** was synthesized following the procedure reported by Ferrari et al. starting from 4-acetyl-5-oxohexanoic acid obtained as previously reported [27]. Light

orange powder, 47% yield. Elemental analysis for $C_{22}H_{20}O_6$ (380.39 g/mol): calc. C, 69.46%, H, 5.30%; exp. C, 69.31%, H, 5.60%. LC/MS-IT: *m/z* 381.1 $(M + H)^+$. ^1H NMR (δ (ppm), MeOD-d_4): 2.35 (H-12, t, 2H), 2.20 (H-11, m, 2H), 6.79 (H-3, d, 2H), 7.69 (H-4, d, 2H), 7.43–760 (H-6/10, m, 4H), 6.60–6.88 (H-7/9, m, 4H).

(6E)-7-(3-methoxy-4-hydroxyphenyl)-4-[(2E)-3-(3-methoxy-4-hydroxyphenyl)prop-2-enoyl]-5-oxohept-6-enoic acid (**7**)

Compound **7** was synthesized following the procedure reported by Ferrari et al. [22] starting from 4-acetyl-5-oxohexanoic acid obtained as previously reported [24]. Orange-red powder, 58% yield. Elemental analysis for $C_{24}H_{24}O_8$ (440.44 g/mol): calc. C, 65.45%, H, 5.49%; exp. C, 65.26%, H, 5.74%. LC/MS-IT: *m/z* 441.2 $(M + H)^+$. ^1H NMR (δ (ppm), $CDCl_3$): 7,72 (H-3, d, 2H), 6.82 (H-4, d, 2H), 7.25 (H-6, dd, 2H), 6.84 (H-9, dd, 2H), 7.16 (H-10, dd, 2H), 2.24 (H-11, t, 2H), 2.38 (H-12, t, 2H), 3.90 (OCH_3, s, 6H).

3.3. Kinetic Stability of Ligands in Physiological Conditions

The chemical stability of ligands and metal complexes at the M:L 1:L molar ratio at 37 °C in darkness was evaluated by UV−Vis spectroscopy as a change in absorbance in the 250−600 nm range over an overall period of 8 h. Solutions (5.0×10^{-5} mol L^{-1}) of the ligands were prepared in 0.1 mol L^{-1} phosphate-buffered solution (PBS) at pH 7.4. Spectra were recorded every 30 min. All profiles were linearized as the hyperbolic function defined by Equation (2), which represents an empirical model that describes drug decomposition or release well [42]:

$$\frac{t}{f_{\%}} = at + b \quad (2)$$

where $f_{\%}$ is the percentage of the residual compound at time t (min) referred to the starting concentration at time zero determined by reading the absorbance at λ_{max}.

3.4. UV–Visible Spectroscopy

UV–visible spectra were recorded with a JASCO V-570 UV/Vis/NIR spectrophotometer at 298 K in the 250–600 nm spectral range employing quartz cells (1 cm optical path). To perform spectrophotometric titrations, ligands (denoted generally as L in the following) were dissolved in methanol to give a mother solution (2.50 mM), that was then diluted in water in order to obtain a final concentration of 50 μM. The metal/ligand (M:L) solutions were obtained by adding appropriate quantities of $Ga(NO_3)_3$ as methanol solutions (5–10 mM) in order to obtain the metal-to-ligand 1:1 molar ratio (L = 50 μM and V = 25 mL). For both L and M:L systems, pH (initial value of about 5) was varied by adding small amounts (<1 μL) of concentrated NaOH (4 M) up to ca. pH 11, thus to consider volume variations negligible. To evaluate the complexation ratio, constant additions of the M solution (10 μL each time, M = 10^{-2} M) were dropped into the ligand solution (V = 25 mL, L = 50 μM) using a micropipette in order to reach different M:L molar ratios. A constant ionic strength ($NaNO_3$, 0.1 M) was maintained in all experiments. Spectrophotometric investigations of iron(III) systems were performed in the same conditions; the Fe^{3+} solution was freshly prepared in methanol starting from $Fe(NO_3)_3 \cdot 9H_2O$. The overall protonation constants ($\log\beta_{qr}$) and the overall stability constants of metal complexes ($\log\beta_{pqr}$) were evaluated from spectrophotometric data. The stability constants (β_{pqr}), defined by the following equations:

$$pM^{m+} + qL^{l-} + rH^+ \rightleftharpoons M_pL_qH_r^{(mp-lq+r)} \quad (3)$$

$$\beta_{pqr} = \frac{\left[M_pL_qH_r^{(mp-lq+r)}\right]}{[M^{m+}]^p \cdot [L^{l-}]^q \cdot [H^+]^r} \quad (4)$$

where L is the ligand in the completely dissociated form and H is proton, were refined using least-squares calculation in HypSpec [36]. The results of least-squares calculation include the standard deviations and correlation coefficients of the refined parameters. The

quantities are obtained by performing error propagation calculation from the experimental errors onto the parameters. The stability constant refinement furnishes least-squares estimates of the standard deviation, σ, of the stability constant β. The error on logβ is calculated as follows: $\sigma(\log\beta) = [\log(\beta + \sigma) - \log(\beta - \sigma)]/2$.

Hydroxide species, such as $[Ga(OH)_2]^+$, were taken into account for calculations. The hydrolysis constants for Ga^{3+} are as follows: $\log\beta_{1,1,0} = -3.93$; $\log\beta_{2,1,0} = -7.73$; $\log\beta_{3,1,0} = -12.38$; $\log\beta_{4,1,0} = -15.96$; $\log\beta_{32,13,0} = -66.3$; $\log\beta_{3,1,0(s)} = -3.54$ [43]; pGa is defined as $(-\log[Ga^{3+}]_{free})$ and is calculated at specific conditions (Ga^{3+}_{total} = 1 μM, L_{total} = 10 μM, pH 7.4, 25 °C). For the calculation of the iron(III) overall stability constants, the presence of $[Fe(OH)]^{2+}$, $[Fe(OH)_2]^+$ and $[Fe(OH)_3]$ species was taken into account [44].

3.5. Nuclear Magnetic Resonance

NMR spectra were recorded by means of a Bruker Biospin FT-NMR AVANCE III HD (600 MHz) spectrometer equipped with a CryoProbe BBO H&F 5 mm in inverse detection. The nominal frequencies were 150.90 MHz for ^{13}C and 600.13 MHz for ^{1}H, respectively. For each sample, 1–5 mg were weighed and diluted up to 0.6 mL with a proper solvent in a 5 mm NMR tube; 90° pulse was calibrated for each sample, and standard NMR parameters were used to achieve quantitative results (relaxation delay, 10 s). Proton and carbon chemical shifts are given in parts per million (ppm) versus external TMS and were determined by reference to the solvent residual signals. Typical 2D homo- and heteronuclear techniques were used for assignment, i.e., ^{1}H,^{1}H COSY, ^{1}H,^{13}C HSQC, ^{1}H,^{13}C HMBC. NMR investigations of Ga^{3+}:L systems were performed in MeOD-d_4 by adding small amounts of a $Ga(NO_3)_3$ solution (10 μL each) to 1 mM ligand solution (0.6 mL) until reaching the desired metal-to-ligand molar ratio. The complexation reaction is fast, and spectra were registered few minutes after the addition. Two-dimensional ^{1}H,^{13}C heteronuclear multiple bond correlation (HMBC) experiments (*hmbcgpndqf* in Bruker library) were performed via heteronuclear zero and double quantum coherence, optimized on long-range couplings ($^{3/4}J_{HC}$ = 8 Hz), with no decoupling during acquisition, and gradient pulses were used for selection. The relative percentages of the isomeric forms were estimated on the basis of the NMR data. Particularly, ^{1}H NMR spectra were acquired in quantitative conditions being D1 (relaxation delay) at least five times the T1 of the slowest relaxing signal of interest. The raw data were Fourier-transformed, and then the processing was performed by zero filling (SI = TD), line broadening (lb 0.3 Hz), accurate phasing and correcting the baseline. The most isolated signals were selected for integration, i.e., the vinyl protons (H-3 and H-4), and an average of the integrated area (A) of H-3 and H-4 was used for relative quantitation, according to the following equation:

$$\%Tautomer_i = \frac{(A_{(H-3)i} + (A_{(H-4)i})/2}{\sum_i (A_{(H-3)i} + (A_{(H-4)i})/2} \times 100$$

3.6. Antioxidant Activity (DPPH Assay)

The antioxidant activity of compounds **4** and **5** and their Ga^{3+} metal complexes at the M:L 1:1 and 1:2 molar ratio was evaluated in terms of hydrogen-donating or radical scavenging ability using a stable DPPH radical, 1,1-diphenyl-2-picrylhydrazyl radical, following the procedure previously reported [26]. The percentage of inhibition (%In) of the DPPH radical by each sample was calculated according to the following formula:

$$\%In = \frac{A_0 - A_t}{A_0} \times 100$$

where A_0 represents the absorbance of the control (DPPH radical) at time 0, while A_t refers to the absorbance of the mixture antioxidant/DPPH at time t (120 min). Values of absorbance were corrected considering volume dilution. All the determinations were performed in duplicate.

3.7. Cell Viability Assay

Human colorectal carcinoma HCT116 cells (#91091005, ECACC) were grown in an IMDM medium (Biowest) supplemented with 2 mM glutamine, 100 IU/mL penicillin, 100 µg/mL streptomycin and 10% FBS (Gibco). The cell lines were grown at 37 °C in a humidified incubator containing 5% CO_2. The cells were verified to be mycoplasma-free and passaged < 3 months. The inhibition of cell proliferation was measured by colorimetric 3-(4,5-dimethylthiazol-2-yl)-2,5-diphenyltetrazolium bromide (MTT) assay [45]. GI_{50} concentrations were determined using the CompuSyn software version 1.0 (ComboSyn, Inc., Paramus, NJ USA) (free download via www.combosyn.com, accessed on 30 May 2022), and statistical analyses were performed using the GraphPad PRISM software (version 6.01 for Windows, GraphPad Software, San Diego, California USA GraphPad Prism) using unpaired *t*-test. Data were considered to be statistically significant if $p < 0.05$ (*), $p < 0.01$ (**), $p < 0.001$(***) and $p < 0.0001$ (****).

4. Conclusions

With the lead compound curcumin, all the investigated ligands were characterized by a β-keto–enol group, suitable to bind hard Lewis acids such as Ga^{3+}. Since one of the main drawbacks of curcumin is its high instability in physiological conditions, tightly related to its poor bioavailability, we synthesized seven new derivatives with improved stability in physiological environment (PBS pH 7.4, 37 °C). Estimating the stability under cell culture conditions would be remarkable to also predict potential therapeutic applications of the gallium complexes. In previous studies, the stability of gallium complexes with the lead compound curcumin was investigated in plasma and cellular cultures, demonstrating an increased stability of the metal complexes over the free ligand in these media and their ability to enter into the cells in vitro, as supported by confocal microscopy and ICP-MS analysis [46,47]. As it concerns the stability in a slightly acidic environment (pH 5–6) such as inside tumor cells [48], all gallium complexes are formed in acidic conditions (pH 4–6) and demonstrated to be stable in acid media, as suggested by the species distribution curves. However, it is not possible to exclude transchelation reactions; indeed, Ga^{3+} could be bound to the two metal-binding domains of transferrin with binding constants almost comparable to those of Fe^{3+} (log K_1 = 20.3 (Ga^{3+}), 22.8 (Fe^{3+}) and log K_2 = 19.3 (Ga^{3+}), 21.7 (Fe^{3+})) at the normal plasma bicarbonate concentrations [21].

Additional issues in predicting the chemical stability and behavior in vivo are trans-metalation reactions with endogenous metal ions. The high affinity of oxygen for strong Lewis acids such as Ga^{3+} reduces the incidence of transmetalation with bivalent metal ions such as Ca^{2+}, Mg^{2+}, Zn^{2+}, while the exchange with Fe^{3+} cannot be excluded and should be estimated. Interestingly, iron is an essential nutrient the demand wherefore highly increases in cancer cells; consequently, limiting its availability can reduce cell proliferation, so iron chelators seem to have a high potential in cancer treatment [49,50]. The affinity for iron(III) of compounds **4** and **5** was comparable to that for gallium(III). Although we may not exclude transmetalation reactions with Fe(III), Ga^{3+} complexes of compounds **4** and **5** appear to be stable, given that iron homeostasis is finely regulated and the labile iron pool is negligible [51].

The main chemical features of the investigated ligands and their Ga^{3+} complexes are outlined in Table 4. The outcomes suggest that compounds **5** and, to a minor extent, **4** stand out as the most promising ones for potential therapeutic applications. In fact, the free ligand is more stable than curcumin, and a further increased stability is gained when Ga^{3+} complexes are formed. Compounds **4** and **5** are the strongest Ga^{3+}-chelating agents, with pGa values similar to those of clinically established chelators (i.e., DFOA). In addition, the prevailing metal complex species are positively charged and remain unchanged with the switch in pH from physiological conditions (pH 7.4) to pathological ones, such as in tumor cells (pH 5–6), possibly favoring cellular uptake. Furthermore, upon the DPPH assay, compounds **4** and **5** and their Ga^{3+} complexes showed interesting antioxidant properties, with the IC_{50} values close to those of curcumin. As for similar compounds, the presence of

a methoxy group in the ortho position to the phenolic one reduces the radical scavenging ability increasing the IC_{50} value [14]. The radical scavenging ability remains unaffected in the formation of Ga^{3+} complexes since the phenolic group remains untouched by metal coordination as previously observed for other derivatives [52].

Table 4. Summary of chemical features. * Percentage of the residual ligand after 4 h (ranking). ** Possible formation of gallium hydroxide species.

Ligand	Prevailing Tautomer (MeOD-d_4)	Stability *	pGa	Prevailing Species (pH 5.5)	Prevailing Species (pH 7.4)
1	KE	77% (3)	19.0	$[Ga(HL)_3]$	$[Ga(L)_3]^{3-}$
2	KE	83% (1)	13.1	$[Ga(L)_3]$	$[Ga(L)_3]$
3	KK	47% (6)	20.8	$[Ga(H_2L)_2]^+$	$[Ga(H_2L)_2]^+$
4	KK	42% (7)	21.5	$[Ga(H_2L)_2]^+$	$[Ga(H_2L)_2]^+$
5	KE	52% (5)	23.4	$[Ga(H_2L)_2]^+$	$[Ga(H_2L)_2]^+$
6	KK	73% (4)	14.0	$[Ga(H_2L)_2]^+$	$[Ga(H_2L)_2]^+$ **
7	KK	79% (2)	15.3	$[Ga(H_2L)_2]^+$	$[Ga(H_2L)_2]^+$ **

According to the chemical characterization of these newly synthesized Ga(III) derivatives, molecules **3**, **4** and **5** were selected for MTT assays. The preliminary results pointed out that the conjugation of phthalimide significantly increases the antiproliferative activity in HCT116 cells, and among all, compound **5** showed major efficacy in terms of growth inhibitory activity (GI_{50}) compared to curcumin. Further investigation would allow better characterizing this molecule as a potential therapeutic anticancer drug and could ascertain if its Ga(III) derivative can inhibit cancer-related cellular processes, such as clonal growth and migration, similarly to what we recently reported for compound **4** [**26**]. It is also conceivable that gallium complexes might exert antimicrobial effects, as suggested by Seoung Choi et al. [53].

Finally, we demonstrated that compounds **6** and **7** can bind Ga^{3+} through the keto–enol moiety while the carboxylic group is not involved due to its spatial distance from the metal ion. The chemical structure of these compounds affects the overall stability constants of gallium complexes, reducing the Ga^{3+}-sequestering ability. Nonetheless, this apparent flaw could be turned into an additional therapeutic property since the free carboxylate moiety could be exploited as a targeting vector for monocarboxylate transporters (MCTs), especially MCT1 that is overexpressed in several cancer cells, for instance, breast, lung and ovarian cancer cells [54,55].

Supplementary Materials: The following supporting information can be downloaded at: https://www.mdpi.com/article/10.3390/ph15070854/s1, Figure S1: UV–Vis spectra of the investigated compounds at 25 °C in an aqueous solution (L = 50 μM). Figure S2: ^{1}H NMR spectra of compound **7** in MeOD-d_4 at 298 K (at 600 MHz) at the increasing addition of Ga^{3+}. Figure S3: pH-metric spectrophotometric titration of the Ga^{3+}:1 1:1 system in an aqueous solution (L = 50 μM; $NaNO_3$ = 0.1 M, 298 K). Figure S4: Radical scavenging ability of derivatives **4** and **5** together with their Ga^{3+} metal complexes. Table S1: Liquid chromatography/mass spectrometry (LC/MS) results (*m*/*z*) for gallium(III) complexes.

Author Contributions: Conceptualization, E.F. and M.A.; Methodology, D.C. and M.M.; Investigation, M.M., G.A., E.V. and S.B.; Resources, E.F. and G.M.; Data curation, E.F.; Writing—original draft preparation, E.F. and M.M.; Writing—review and editing, E.F., M.M., P.C.C., M.I. and S.R.; Visualization, D.C.; Supervision, E.F.; Project administration, E.F.; Funding acquisition, E.F. All authors have read and agreed to the published version of the manuscript.

Funding: This research received no external funding.

Institutional Review Board Statement: Not applicable.

Informed Consent Statement: Not applicable.

Data Availability Statement: Data is contained within the article and supplementary material.

Acknowledgments: The authors want to thank the C.I.G.S. (Centro Interdipartimentale Grandi Strumenti) of UNIMORE for technical support and the Network for Equilibria and Chemical Thermodynamics Advanced Research (NECTAR) COST ACTION CA18202.

Conflicts of Interest: The authors declare no conflict of interest.

References

1. Razavi, B.M.; Ghasemzadeh Rahbardar, M.; Hosseinzadeh, H. A review of therapeutic potentials of turmeric (*Curcuma longa*) and its active constituent, curcumin, on inflammatory disorders, pain, and their related patents. *Phyther. Res.* **2021**, *35*, 6489–6513. [CrossRef] [PubMed]
2. Ojo, O.A.; Adeyemo, T.R.; Rotimi, D.; Batiha, G.E.-S.; Mostafa-Hedeab, G.; Iyobhebhe, M.E.; Elebiyo, T.C.; Atunwa, B.; Ojo, A.B.; Lima, C.M.G.; et al. Anticancer Properties of Curcumin Against Colorectal Cancer: A Review. *Front. Oncol.* **2022**, *12*, 1–13. [CrossRef] [PubMed]
3. Kharat, M.; Du, Z.; Zhang, G.; McClements, D.J. Physical and Chemical Stability of Curcumin in Aqueous Solutions and Emulsions: Impact of pH, Temperature, and Molecular Environment. *J. Agric. Food Chem.* **2017**, *65*, 1525–1532. [CrossRef] [PubMed]
4. Ramesh, G.; Kaviyil, J.E.; Paul, W.; Sasi, R.; Joseph, R. Gallium-Curcumin Nanoparticle Conjugates as an Antibacterial Agent against Pseudomonas aeruginosa: Synthesis and Characterization. *ACS Omega* **2022**, *7*, 6795–6809. [CrossRef] [PubMed]
5. Panzarini, E.; Mariano, S.; Tacconi, S.; Carata, E.; Tata, A.M.; Dini, L. Novel therapeutic delivery of nanocurcumin in central nervous system related disorders. *Nanomaterials* **2021**, *11*, 2. [CrossRef]
6. Noureddin, S.A.; El-Shishtawy, R.M.; Al-Footy, K.O. Curcumin analogues and their hybrid molecules as multifunctional drugs. *Eur. J. Med. Chem.* **2019**, *182*, 111631. [CrossRef]
7. Yanagisawa, D.; Kato, T.; Taguchi, H.; Shirai, N.; Hirao, K.; Sogabe, T.; Tomiyama, T.; Gamo, K.; Hirahara, Y.; Kitada, M.; et al. Keto form of curcumin derivatives strongly binds to Aβ oligomers but not fibrils. *Biomaterials* **2021**, *270*, 120686. [CrossRef]
8. Manolova, Y.; Deneva, V.; Antonov, L.; Drakalska, E.; Momekova, D.; Lambov, N. The effect of the water on the curcumin tautomerism: A quantitative approach. *Spectrochim. Acta Part A Mol. Biomol. Spectrosc.* **2014**, *132*, 815–820. [CrossRef]
9. Puglisi, A.; Giovannini, T.; Antonov, L.; Cappelli, C. Interplay between conformational and solvent effects in UV-visible absorption spectra: Curcumin tautomers as a case study. *Phys. Chem. Chem. Phys.* **2019**, *21*, 15504–15514. [CrossRef]
10. Parimita, S.P.; Ramshankar, Y.V.; Suresh, S.; Row, T.N.G. Redetermination of curcumin: (1E,4Z,6E)-5-hydroxy-1,7-bis(4-hydroxy-3-methoxy-phenyl)hepta-1,4,6-trien-3-one. *Acta Crystallogr. Sect. E Struct. Rep. Online* **2007**, *63*, 860–862. [CrossRef]
11. Prasad, D.; Praveen, A.; Mahapatra, S.; Mogurampelly, S.; Chaudhari, S.R. Existence of β-diketone form of curcuminoids revealed by NMR spectroscopy. *Food Chem.* **2021**, *360*, 130000. [CrossRef] [PubMed]
12. Enumo, A.; Irineu, C.; Pereira, D.; Parize, A.L. Temperature Evaluation of Curcumin Keto−Enolic Kinetics and Its Interaction with Two Pluronic Copolymers. *J. Phys. Chem. B* **2019**, *123*, 5641–5650. [CrossRef] [PubMed]
13. Wanninger, S.; Lorenz, V.; Subhan, A.; Edelmann, F.T. Metal complexes of curcumin—Synthetic strategies, structures and medicinal applications. *Chem. Soc. Rev.* **2015**, *44*, 4986–5002. [CrossRef] [PubMed]
14. Ferrari, E.; Benassi, R.; Saladini, M.; Orteca, G.; Gazova, Z.; Siposova, K. In vitro study on potential pharmacological activity of curcumin analogues and their copper complexes. *Chem. Biol. Drug Des.* **2017**, *89*, 411–419. [CrossRef]
15. Balasubramanian, K. Quantum chemical insights into Alzheimer's disease: Curcumin's chelation with Cu(II), Zn(II), and Pd(II) as a mechanism for its prevention. *Int. J. Quantum Chem.* **2016**, *116*, 1107–1119. [CrossRef]
16. Halevas, E.; Pekou, A.; Papi, R.; Mavroidi, B.; Hatzidimitriou, A.G.; Zahariou, G.; Litsardakis, G.; Sagnou, M.; Pelecanou, M.; Pantazaki, A.A. Synthesis, physicochemical characterization and biological properties of two novel Cu(II) complexes based on natural products curcumin and quercetin. *J. Inorg. Biochem.* **2020**, *208*, 111083. [CrossRef]
17. Prasad, S.; Dubourdieu, D.; Srivastava, A.; Kumar, P.; Lall, R.; Bachmeier, E. Molecular Sciences Metal-Curcumin Complexes in Therapeutics: An Approach to Enhance Pharmacological Effects of Curcumin. *Int. J. Mole. Sci.* **2021**, *22*, 7094. [CrossRef]
18. dos, S.S.; Firmino, G.; André, S.C.; Hastenreiter, Z.; Campos, V.K.; Abdel-Salam, M.A.L.; de Souza-Fagundes, E.M.; Lessa, J.A. In vitro assessment of the cytotoxicity of gallium(III) complexes with Isoniazid-Derived Hydrazones: Effects on clonogenic survival of HCT-116 cells. *Inorg. Chim. Acta* **2019**, *497*, 119079. [CrossRef]
19. Qi, J.; Liu, T.; Zhao, W.; Zheng, X.; Wang, Y. Synthesis, crystal structure and antiproliferative mechanisms of gallium(III) complexes with benzoylpyridine thiosemicarbazones. *RSC Adv.* **2020**, *10*, 18553–18559. [CrossRef]
20. Chitambar, C.R.; Purpi, D.P.; Woodliff, J.; Yang, M.; Wereley, J.P. Development of Gallium Compounds for Treatment of Lymphoma: Gallium Maltolate, a Novel Hydroxypyrone Gallium Compound, Induces Apoptosis and Circumvents Lymphoma Cell Resistance to Gallium Nitrate. *J. Pharmacol. Exp. Ther.* **2007**, *322*, 1228–1236. [CrossRef]
21. Chitambar, C.R. Gallium-containing anticancer compounds. *Future Med. Chem.* **2012**, *4*, 1257–1272. [CrossRef] [PubMed]
22. Ellahioui, Y.; Prashar, S.; Gómez-Ruiz, S. Anticancer applications and recent investigations of metallodrugs based on gallium, tin and titanium. *Inorganics* **2017**, *5*, 4. [CrossRef]
23. Lessa, J.A.; Parrilha, G.L.; Beraldo, H. Gallium complexes as new promising metallodrug candidates. *Inorg. Chim. Acta* **2012**, *393*, 53–63. [CrossRef]

24. Collery, P.; Keppler, B.; Madoulet, C.; Desoize, B. Gallium in cancer treatment. *Crit. Rev. Oncol. Hematol.* **2002**, *42*, 283–296. [CrossRef]
25. Jahangoshaei, P.; Hassani, L.; Mohammadi, F.; Hamidi, A.; Mohammadi, K. Investigating the effect of gallium curcumin and gallium diacetylcurcumin complexes on the structure, function and oxidative stability of the peroxidase enzyme and their anticancer and antibacterial activities. *J. Biol. Inorg. Chem.* **2015**, *20*, 1135–1146. [CrossRef]
26. Belluti, S.; Orteca, G.; Semeghini, V.; Rigillo, G.; Parenti, F.; Ferrari, E.; Imbriano, C. Potent anti-cancer properties of phthalimide-based curcumin derivatives on prostate tumor cells. *Int. J. Mol. Sci.* **2019**, *20*, 28. [CrossRef]
27. Ferrari, E.; Pignedoli, F.; Imbriano, C.; Marverti, G.; Basile, V.; Venturi, E.; Saladini, M. Newly synthesized curcumin derivatives: Crosstalk between chemico-physical properties and biological activity. *J. Med. Chem.* **2011**, *54*, 8066–8077. [CrossRef]
28. Pabon, H.J.J. A synthesis of curcumin and related compounds. *Recl. Trav. Chim. Pays Bas* **2010**, *83*, 379–386. [CrossRef]
29. Ferrari, E.; Benassi, R.; Sacchi, S.; Pignedoli, F.; Asti, M.; Saladini, M. Curcumin derivatives as metal-chelating agents with potential multifunctional activity for pharmaceutical applications. *J. Inorg. Biochem.* **2014**, *139*, 38–48. [CrossRef]
30. Payton, F.; Sandusky, P.; Alworth, W.L. NMR study of the solution structure of curcumin. *J. Nat. Prod.* **2007**, *70*, 143–146. [CrossRef]
31. Benassi, R.; Ferrari, E.; Grandi, R.; Lazzari, S.; Saladini, M. Synthesis and characterization of new β-diketo derivatives with iron chelating ability. *J. Inorg. Biochem.* **2007**, *101*, 203–213. [CrossRef] [PubMed]
32. Rapalli, V.K.; Kaul, V.; Gorantla, S.; Waghule, T.; Dubey, S.K.; Pandey, M.M.; Singhvi, G. UV Spectrophotometric method for characterization of curcumin loaded nanostructured lipid nanocarriers in simulated conditions: Method development, in-vitro and ex-vivo applications in topical delivery. *Spectrochim. Acta Part A Mol. Biomol. Spectrosc.* **2020**, *224*, 117392. [CrossRef] [PubMed]
33. Dias Pereira, C.I.; Fabiano de Freitas, C.; Braga, T.L.; Braga, G.; Gonçalves, R.S.; Tessaro, A.L.; Graton Mikcha, J.M.; Hioka, N.; Caetano, W. Concise behavior of Curcumin in water-ethanol: Critical Water Aggregation Percentage and multivariate analysis of protolytic equilibria. *Dyes Pigment.* **2022**, *197*, 143–7208. [CrossRef]
34. Gans, P.; Sabatini, A.; Vacca, A. To improve accuracy of the calculated pKa values. *Ann. Chim.* **1999**, *89*, 45–49.
35. Rigamonti, L.; Orteca, G.; Asti, M.; Basile, V.; Imbriano, C.; Saladini, M.; Ferrari, E. New curcumin-derived ligands and their affinity towards Ga^{3+}, Fe^{3+} and Cu^{2+}: Spectroscopic studies on complex formation and stability in solution. *New J. Chem.* **2018**, *42*, 7680–7690. [CrossRef]
36. Gans, P.; Sabatini, A.; Vacca, A. Investigation of equilibria in solution. Determination of equilibrium constants with the HYPERQUAD suite of programs. *Talanta* **1996**, *43*, 1739–1753. [CrossRef]
37. Harris, W.R.; Carrano, C.J.; Raymond, K.N. Coordination Chemistry of Microbial Iron Transport Compounds. 16. Isolation, Characterization, and Formation Constants of Ferric Aerobactin. *J. Am. Chem. Soc.* **1979**, *101*, 2722–2727. [CrossRef]
38. Borgias, B.; Hugi, A.D.; Raymond, K.N. Isomerization and Solution Structures of Desferrioxamine B Complexes of Al^{3+} and Ga^{3+}. *Inorg. Chem.* **1989**, *28*, 3538–3545. [CrossRef]
39. Notni, J.; Hermann, P.; Havlíčková, J.; Kotek, J.; Kubíček, V.; Plutnar, J.; Loktionova, N.; Riss, P.J.; Rösch, F.; Lukeš, I. A triazacyclononane-based bifunctional phosphinate ligand for the preparation of multimeric 68Ga tracers for positron emission tomography. *Chemistry* **2010**, *16*, 7174–7185. [CrossRef]
40. Toporivska, Y.; Mular, A.; Piasta, K.; Ostrowska, M.; Illuminati, D.; Baldi, A.; Albanese, V.; Pacifico, S.; Fritsky, I.O.; Remelli, M.; et al. Thermodynamic Stability and Speciation of Ga(III) and Zr(IV) Complexes with High-Denticity Hydroxamate Chelators. *Inorg. Chem.* **2021**, *60*, 13332–13347. [CrossRef]
41. Asti, M.; Ferrari, E.; Croci, S.; Atti, G.; Rubagotti, S.; Iori, M.; Capponi, P.C.; Zerbini, A.; Saladini, M.; Versari, A. Synthesis and Characterization of ^{68} Ga-Labeled Curcumin and Curcuminoid Complexes as Potential Radiotracers for Imaging of Cancer and Alzheimer's Disease. *Inorg. Chem.* **2014**, *53*, 4922–4933. [CrossRef] [PubMed]
42. Rubagotti, S.; Croci, S.; Ferrari, E.; Orteca, G.; Iori, M.; Capponi, P.C.; Versari, A.; Asti, M. Uptake of Ga-curcumin derivatives in different cancer cell lines: Toward the development of new potential 68Ga-labelled curcuminoids-based radiotracers for tumour imaging. *J. Inorg. Biochem.* **2017**, *173*, 113–119. [CrossRef] [PubMed]
43. El Deeb, S.; Ma, B.N.; Baecker, D.; Gust, R. Studies on the stability of the anticancer-active [N,N′-bis(salicylidene)-1,2-phenylenediamine]chloridoiron(III) complex under pharmacological-like conditions. *Inorg. Chim. Acta* **2019**, *487*, 76–80. [CrossRef]
44. Zacchi, P.; Schioppa, T.; Stein, J.; Farrag, K.; Aksan, A.; Aksan, S.; Schroeder, O. Flipside of the Coin: Iron Deficiency and Colorectal Cancer. *Front. Immunol.* **2021**, *12*, 635899. [CrossRef]
45. Pandrangi, S.L.; Chittineedi, P.; Chikati, R.; Lingareddy, J.R.; Nagoor, M.; Ponnada, S.K. Role of dietary iron revisited: In metabolism, ferroptosis and pathophysiology of cancer. *Am. J. Cancer Res.* **2022**, *12*, 974.
46. Anderson, G.J.; Frazer, D.M. Current understanding of iron homeostasis. *Am. J. Clin. Nutr.* **2017**, *106*, 1559S–1566S. [CrossRef]
47. Ferrari, E.; Asti, M.; Benassi, R.; Pignedoli, F.; Saladini, M. Metal binding ability of curcumin derivatives: A theoretical vs. experimental approach. *Dalt. Trans.* **2013**, *42*, 5304–5313. [CrossRef]
48. Belluti, S.; Basile, V.; Benatti, P.; Ferrari, E.; Marverti, G.; Imbriano, C. Concurrent inhibition of enzymatic activity and NF-Y-mediated transcription of Topoisomerase-IIa by bis-DemethoxyCurcumin in cancer cells. *Cell Death Dis.* **2013**, *4*, e756-11. [CrossRef]

49. Choi, S.R.; Britigan, B.E.; Narayanasamy, P. Dual Inhibition of Klebsiella pneumoniae and Pseudomonas aeruginosa Iron Metabolism Using Gallium Porphyrin and Gallium Nitrate. *ACS Infect. Dis.* **2019**, *5*, 1559–1569. [CrossRef]
50. Payen, V.L.; Mina, E.; Van Hée, V.F.; Porporato, P.E.; Sonveaux, P. Monocarboxylate transporters in cancer. *Mol. Metab.* **2020**, *33*, 48–66. [CrossRef]
51. Lee, J.Y.; Lee, I.K.; Chang, W.J.; Ahn, S.M.; Lim, S.H.; Kim, H.S.; Yoo, K.H.; Jung, K.S.; Song, H.N.; Cho, J.H.; et al. MCT4 as a potential therapeutic target for metastatic gastric cancer with peritoneal carcinomatosis. *Oncotarget* **2016**, *7*, 43492–43503. [CrossRef] [PubMed]
52. Paolino, D.; Tudose, A.; Celia, C.; Di Marzio, L.; Cilurzo, F.; Mircioiu, C. Mathematical Models as Tools to Predict the Release Kinetic of Fluorescein from Lyotropic Colloidal Liquid Crystals. *Material* **2019**, *12*, 693. [CrossRef] [PubMed]
53. Hakobyan, S.; Boily, J.F.; Ramstedt, M. Proton and gallium(III) binding properties of a biologically active salicylidene acylhydrazide. *J. Inorg. Biochem.* **2014**, *138*, 9–15. [CrossRef] [PubMed]
54. Gama, S.; Frontauria, M.; Ueberschaar, N.; Brancato, G.; Milea, D.; Sammartano, S.; Plass, W. Cite this. *New J. Chem.* **2018**, *42*, 8062. [CrossRef]
55. Belluti, S.; Semeghini, V.; Rigillo, G.; Ronzio, M.; Benati, D.; Torricelli, F.; Reggiani Bonetti, L.; Carnevale, G.; Grisendi, G.; Ciarrocchi, A.; et al. Alternative splicing of NF-YA promotes prostate cancer aggressiveness and represents a new molecular marker for clinical stratification of patients. *J. Exp. Clin. Cancer Res.* **2021**, *40*, 362. [CrossRef]

International Journal of
Molecular Sciences

MDPI

Article

Alginate Beads Containing Cerium-Doped Mesoporous Glass and Curcumin: Delivery and Stabilization of Therapeutics

Debora Carrozza, Gianluca Malavasi *, Erika Ferrari and Maria Cristina Menziani

Department of Chemical and Geological Sciences, University of Modena and Reggio Emilia, Via G. Campi 103, 41125 Modena, Italy
* Correspondence: gianluca.malavasi@unimore.it

Abstract: Cancer is a leading cause of death worldwide, its genesis and progression are caused by homeostatic errors, and reactive oxygen species play a major role in promoting aberrant cancer homeostasis. In this scenario, curcumin could be an interesting candidate due to its versatile antioxidant, anti-inflammatory, anti-tumor, anti-HIV, and anti-infection properties. Nonetheless, the major problem related to its use is its poor oral bioavailability, which can be overcome by encapsulating it into small particles, such as hydrogel beads containing mesoporous silica. In this work, various systems have been synthesized: starting from mesoporous silica glasses (MGs), cerium-containing MGs have been produced; then, these systems have been loaded with 4 to 6% of curcumin. Finally, various MGs at different compositions have been included in alginate beads. In vitro studies showed that these hybrid materials enable the stabilization and effective delivery of curcumin and that a synergic effect can be achieved if Ce^{3+}/Ce^{4+} and curcumin are both part of the beads. From swelling tests, it is possible to confirm a controlled curcumin release compartmentalized into the gastrointestinal tract. For all beads obtained, a curcumin release sufficient to achieve the antioxidant threshold has been reached, and a synergic effect of cerium and curcumin is observed. Moreover, from catalase mimetic activity tests, we confirm the well-known catalytic activity of the couple Ce^{3+}/Ce^{4+}. In addition, an extremely good radical scavenging effect of curcumin has been demonstrated. In conclusion, these systems, able to promote an enzymatic-like activity, can be used as drug delivery systems for curcumin-targeted dosing.

Keywords: antioxidant properties; composite biomaterials; alginate beads; hydrogels

Citation: Carrozza, D.; Malavasi, G.; Ferrari, E.; Menziani, M.C. Alginate Beads Containing Cerium-Doped Mesoporous Glass and Curcumin: Delivery and Stabilization of Therapeutics. *Int. J. Mol. Sci.* **2023**, *24*, 880. https://doi.org/10.3390/ijms24010880

Academic Editors: Narsimha Mamidi and Murali Mohan Yallapu

Received: 9 December 2022
Revised: 28 December 2022
Accepted: 30 December 2022
Published: 3 January 2023

1. Introduction

Cancer genesis and progression is caused by homeostatic errors occurring within the tumor microenvironment [1], related or not to genetic mutations, addressing all components of the cancer tissue [2], and implying many alterations, including increased oxidative status. Reactive oxygen species (ROS) play a major role in promoting the aberrant cancer homeostasis, favoring vicious communications between cancer cells and stroma, endothelium, and matrix, thus favoring tumor neo-angiogenesis, matrix degradation, and improper immune infiltrations [3]. Hence, antioxidant therapy is considered as a means to prevent and revert the alteration of the tumor microenvironment.

Curcumin is widely used as a pharmaceutical or nutraceutical in functional foods, food supplements, and medicine [4,5] due to its versatile antioxidant, anti-inflammatory, anti-tumor, anti-HIV, and anti-infection properties [2–4]. However, the formulation of curcumin as a therapeutic agent is a difficult task due to its low aqueous solubility and chemical and metabolic instability, resulting in poor oral bioavailability [5,6].

Curcumin is rapidly metabolized within the gastrointestinal tract (GIT), which limits its potential beneficial biological effects [7–9]. To overcome these limitations, several techniques have been proposed, including encapsulation in a delivery system [10] that consists of small particles (typically comprising lipids, phospholipids, surfactants, and/or

biopolymers) [11]; these delivery systems can be designed to improve curcumin's chemical/biochemical stability and to control its fate within the gastrointestinal tract.

Previous studies [12] have demonstrated the potential of improving the bioavailability of curcumin by using emulsion-based carriers. In particular, the lipid phase in emulsions can be designed to rapidly digest within the small intestine and form mixed micelles capable of solubilizing and transporting lipophilic bioactive components [12,13]. One of the main limitations of conventional oil-in-water emulsions as drug carriers is that they have only a limited scope in controlling the stability and release of encapsulated bioactive agents since the lipid droplets are coated by a thin layer of emulsifier molecules. Furthermore, lipids droplets can present some limitations concerning the stability of drug encapsulation, whereby important drug leakage can be observed because, at times, a phase demixing and drug expulsion can be induced [14]. These limitations can be overcome by trapping the lipid droplets inside hydrogel beads [15].

Hydrogel beads are usually fabricated from food-grade biopolymers, such as proteins and/or polysaccharides [16–18]. Among the wide number of different approaches [19] that can be used for encapsulation, protection, and delivery of food-grade bioactive components, the injection–gelation method is one of the simplest and most widely utilized. In this method, a biopolymer solution (typically alginate or κ-carrageenan) containing the bioactive component is injected into another "hardening" solution under conditions that promote the gelation of the injected biopolymer. This procedure results in the formation of a hydrogel bead with the bioactive components trapped inside [20]. The nature of the hydrogel matrix can be designed to improve its physical and chemical stability, control its gastrointestinal track fate, and synergize the beneficial properties by adding other antioxidant agents. It has recently been reported [21] that ionic cross-linking of alginate and mesoporous bio-glasses (MGs) containing various amounts of cerium oxides (Ce^{3+}/Ce^{4+}) produces excellent candidates for oxidative stress control.

The encapsulation of MGs inside beads [22] allows not only the development of antioxidant properties but also the improvement of physical and mechanical properties of the beads [23], which became more resistant to dissolution, and, thus, rehydration can be easily performed [24]. The introduction of small amounts of CeO_2 into silicate glasses (for example in mesoporous glasses, MG) confers antioxidant properties, such as catalase mimetic activity [25]. Catalase is an enzyme that catalyzes the decomposition of hydrogen peroxide (H_2O_2) into water and oxygen. Its role is very important because it protects cells from oxidative stress by ROS, of which hydrogen peroxide is part. We recently [26] showed that the ability of these glasses to present catalase mimetic activity is strictly related to the simultaneous presence of Ce^{3+} and Ce^{4+} on the glass [27] surface, and we developed biocompatible Ce-MG/alginate beads able to promote a fast degradation of H_2O_2 to reduce the oxidative stress.

The aim of this work is to develop a composite material on the basis of Ce-MG/alginate beads (B-MG) acting as carriers for curcumin. Two mesoporous glasses were synthesized, one with a standard composition (MG) and a second one doped with cerium (MG_5.0Ce), and both were investigated as powders (P). The MG powdery forms were uploaded with curcumin (P-MG_curc5 and P-MG_5.0Ce_curc5) and used to prepare the hydrogel beads (B-MG_curc5 and B-MG_5.0Ce_curc5). We will demonstrate that this delivery system is able to promote an enzymatic-like activity (catalase), thus reducing the concentration of H_2O_2, a potent ROS, and potentiate the beneficial effects of curcumin by protecting it through the gastrointestinal tract with a subsequent drug release in the intestinal environment.

2. Results

2.1. P-MGs and B-MGs Characterization

The compositions of P-MGs and B-MGs were determined using two different methods: alginate and glass content were determined by TG-thermogravimetric analysis and elemental analysis, and curcumin content was determined through UV-Vis quantification.

Table 1 reports the amount of each component for all the samples studied: P-MGs and all the diff B-MGs obtained containing only the bioactive glass (B-MG and B-MG_5.0Ce), both bioactive glass and curcumin (B-MG_curc5, B-MG_5.0Ce_curc5), only curcumin (B-curc), and only the sodium alginate (B).

Table 1. Theoretical and experimental compositions of the samples synthesized *.

Sample	%m/m Alginate		%m/m Glass		%m/m Curcumin	
	Theoretical	Experimental	Theoretical	Experimental	Theoretical	Experimental
P-MG_curc5	-	-	83.3	98.2	16.7	1.8
P-MG_5.0Ce_curc5	-	-	83.3	98.4	16.7	1.6
B	100.0	99.1	-	-	-	-
B-curc	95.0	93.8	-	-	5.0	6.2
B-MG	28.6	36.6	71.4	63.4	-	-
B-MG_curc5	26.7	27.4	66.7	68.4	6.6	4.2
B-MG_5.0Ce	28.6	39.3	71.4	60.7	-	-
B-MG_5.0Ce_curc5	26.7	26.8	66.7	67.1	6.6	6.1

* The experimental %m/m Glass was determined by TG-thermogravimetry, while %m/m Curcumin was determined by extraction, as reported in Section 4.3.

Figure 1 shows the SEM images of beads containing MBGs powders. The micrographs show that the surface is characterized by a partially homogeneous distribution of the glass powders incorporated and held together in a polymeric matrix of alginate. The presence of volume defects, such as fractures, have been likely formed during the drying process at 60 °C.

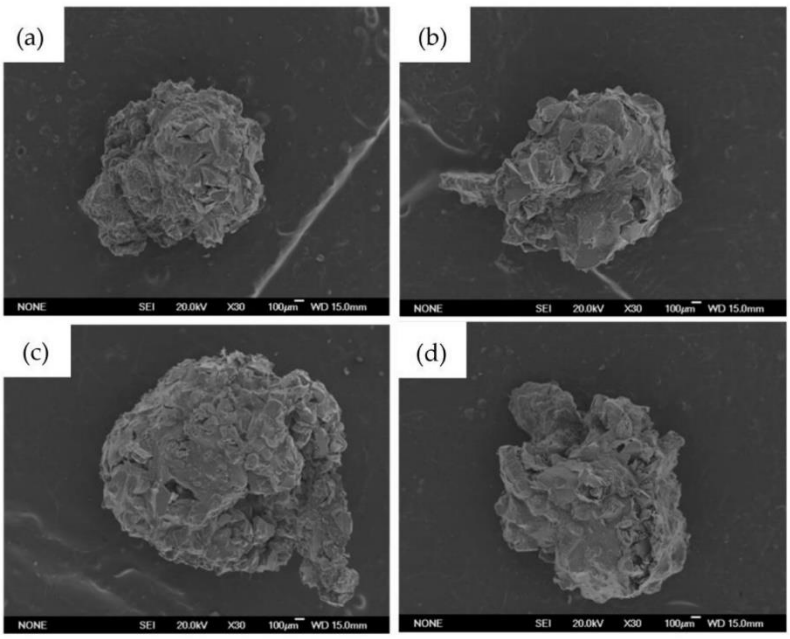

Figure 1. Bead images obtained with scanning electron microscope (SEM). In order: (**a**) B-MG; (**b**) B-MG_5.0Ce; (**c**) B-MG_curc5; and (**d**) B-MG_5.0Ce_curc5.

To evaluate B-MGs dimensions, images with optical microscope have been acquired (Figure 2), and through an image analysis program (ImageJ®-win64), dimensions of the beads have been determined using the average of 24 measures for each sample (Table 2).

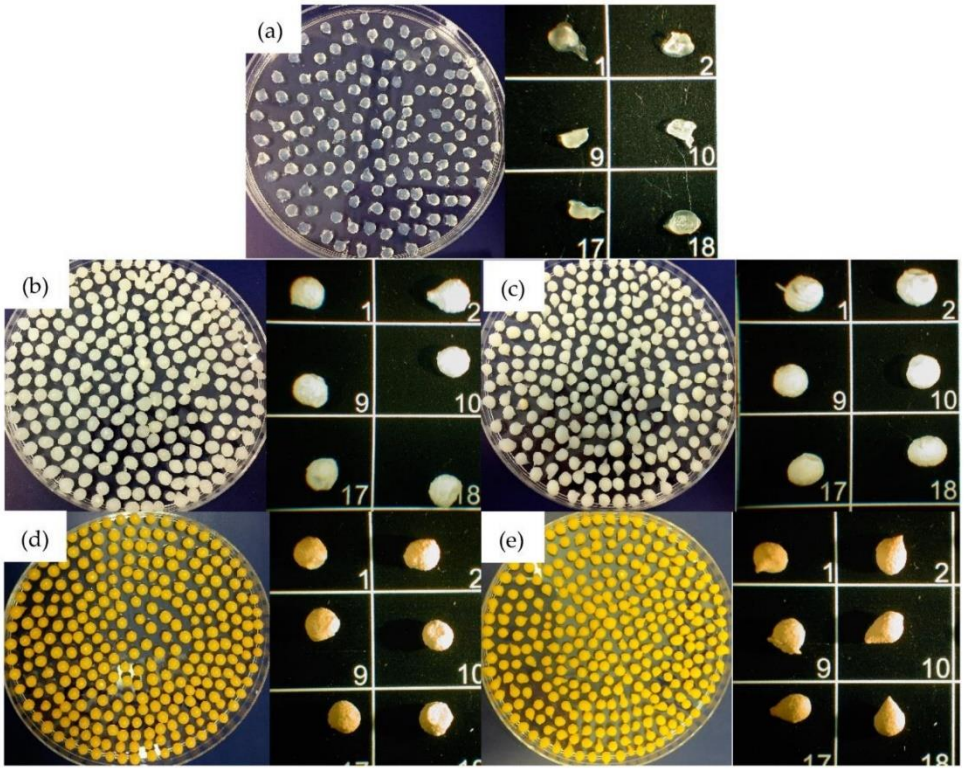

Figure 2. Beads images obtained with optic microscope. In order: (**a**) B; (**b**) B-MG; (**c**) B-MG_5.0Ce; (**d**) B-MG_curc5; and (**e**) B-MG_5.0Ce_curc5. The numbers identify different beads of the same sample.

Table 2. Average dimensions of synthesized beads.

Sample	Average Diameter (mm)
B	1.4 ± 0.2
B-MG	1.8 ± 0.1
B-MG_curc5	2.3 ± 0.1
B-MBG_5.0Ce	2.0 ± 0.1
B-MBG_5.0Ce_curc5	2.4 ± 0.1

As it is possible to notice from the data reported in Table 2, beads containing curcumin are slightly larger than those containing only MGs; this evidence could be explained by considering the surface layer made by deposition of curcumin formed during the loading process into MGs.

FTIR−ATR spectra (Figure 3) were acquired for all beads and for pure alginate and curcumin to highlight the presence of signals of all components inside the beads.

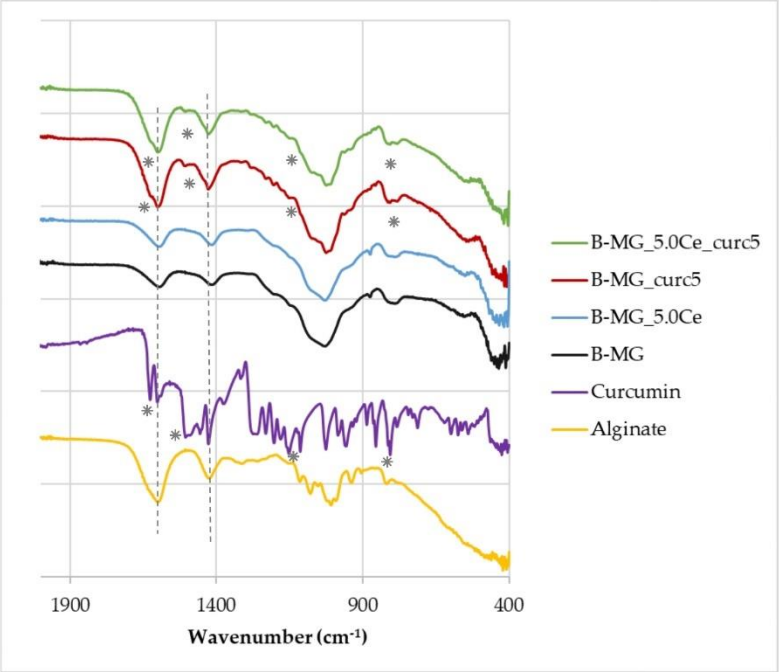

Figure 3. FTIR−ATR spectra of beads, pure alginate, and curcumin. Characteristic peaks of alginate and curcumin are highlighted by dashed lines and asterisks, respectively.

The FTIR−ATR spectra show that the characteristic peaks of alginate (dashed lines) at 1419 cm^{-1} and 1601 cm^{-1} [28] are present in all samples, whereas the characteristic peaks of curcumin (asterisks) at 1630 cm^{-1}, 1516 cm^{-1}, 1093 cm^{-1}, and 798 cm^{-1} [29] are present only in B-MG_curc5 and B-MG_5.0Ce_curc5, providing further evidence of the success of curcumin uploaded.

2.2. Swelling Test

The rehydration rate [30] (Figure 4) was obtained using gravimetric analysis from the difference between initial mass and the mass calculated after specific time intervals.

Figure 4 shows the rate of rehydration (%W) as a function of time in different media: H_2O, simulated body fluid (SBF), Dulbecco's Modified Eagle Medium (D-MEM), and simulated gastric fluid (SGF) and simulated intestinal fluid (SIF) with various buffers.

Swelling in H_2O MilliQ—In these cases, there is no evidence of a high rehydration rate because no values greater than 40% were reached. During the first 6 h, swelling takes place, then a small decline in rehydration rates occurs. This indicates a partial solubilization.

Swelling in D-MEM—In these cases, rehydration rates are extremely high. At 24 h, it was not possible to evaluate the beads' mass because of their disruption. The maximum time reached was 15 h. In this medium, the rehydration is gradual; the systems rehydrate gradually and become very fragile. In the presence of MGs, inside the structure, the beads show more compactness.

Swelling in SBF—Initially, a large swelling was registered, then a plateau was reached. The highest swelling is observed for samples with lower MGs concentrations. This phenomenon is caused by the formation of a hydroxyapatite (HA) layer on the surface of the beads as a direct function of the MGs concentration formed at physiological conditions.

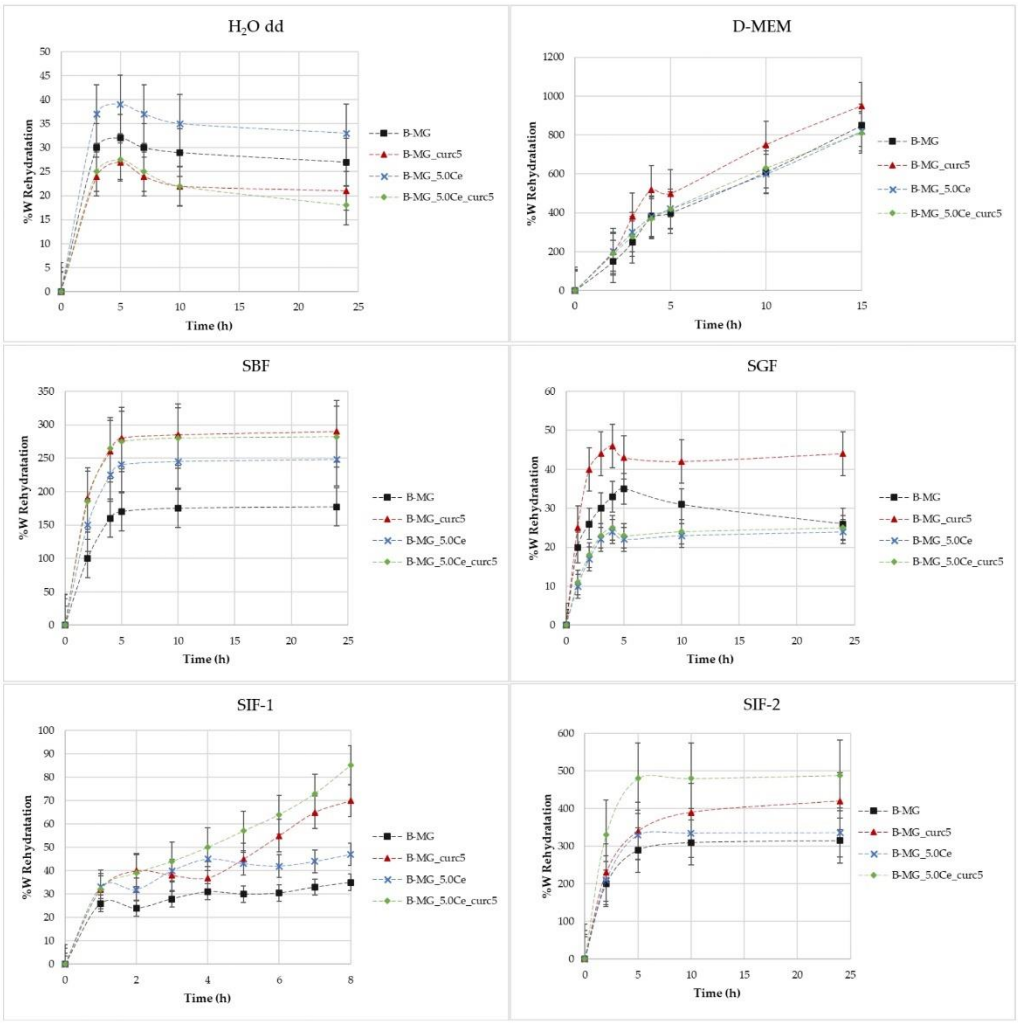

Figure 4. Rate of rehydration (%W) as a function of time in different media.

Swelling in SGF—It was demonstrated that the rehydration rate is proportional to the pH value [4]. In this medium, rehydration rates greater than 40% were not observed.

Swelling in SIF—For these tests, two different types of intestinal fluids were employed: SIF-1 (phosphate buffer 0.01 M at pH of 6.8) and SIF-2 (TRIS buffer 1 M at pH 6.8). In SIF-1, no high values were reached, whereas SIF-2 caused elevated swelling. It is probable that this phenomenon is caused by the interaction between TRIS and alginic residuals of alginate chains.

2.3. Curcumin Release

Both MGs and beads were studied. For all the samples, the same mathematical model, Higuchi's model [31], can be applied (Equation (1)). The release has been detected for 24 h,

but models must be applied only in the time interval in which the release has significant values; under this condition, the equation is linear.

$$Q = k \cdot t^{\frac{1}{2}} \quad (1)$$

in which Q is the quantity of drug release, t is the time, and k is the diffusion constant.

The generalization of this model leads to Peppas' equation [32] (Equation (2)).

$$Q = k \cdot t^{n} \quad (2)$$

If n, obtained from the linearization of the plot of % curcumin release vs time, is 0.5, the release is under diffusion control; if it is 1, the release is controlled by the erosion of the system and the swelling of the polymer.

2.4. MGs' Curcumin Release

The studies were performed in SBF (pH 7.2–7.4). At different timing, curcumin concentration was determined by spectrophotometric analysis (Figure 5a), and the SBF solution was replaced with a new one every time. In addition, after 24 h, a slight release was registered. Both models are applied to perform data linearization (Figure 5b,c); Higuchi's model confirms the diffusion control, while Peppas' model (n = 1) confirms the erosion/dissolution of the glass matrix.

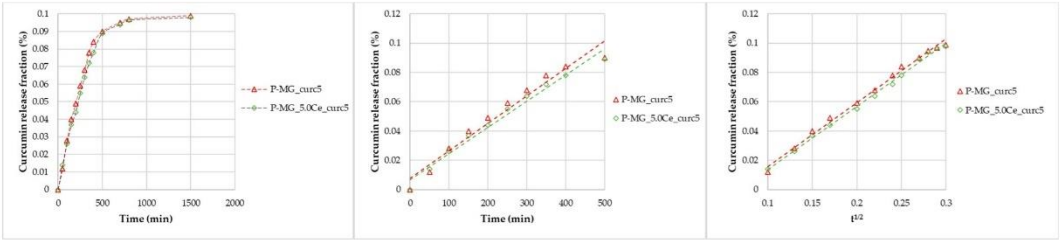

(**a**) (**b**) (**c**)

Figure 5. Curcumin release kinetics from P-MGs; (**a**) graph of the curcumin fraction released in the first 24 h compared with the amount contained in 50 mg; (**b**) linearization according to Peppas' model (n = 1); and (**c**) linearization according to Higuchi's model.

After 24 h, from 50 mg of P-MGs, a release of approximately 1 µg of curcumin in 5 mL of biological medium was achieved; this amount is comparable to that detected in serum (curcumin level of 0.36 µg/mL) after an intravenous injection of 10 mg/kg given in rats [6].

2.5. Beads' Curcumin Release

The studies were performed in three different biological fluids: SBF, SGF, and SIF (SIF-1 and SIF-2). To confirm the diffusive nature of curcumin release, the same mathematical models described above were applied.

2.6. Release in Simulatd Body Fluid (SBF)

These studies were performed for 24 h (Figure 6a). The same trend seen for MGs was registered, and by applying the two mathematical models, good regressions were obtained (Figure 6b,c). Concerning beads, diffusion and swelling/desegregation occur simultaneously.

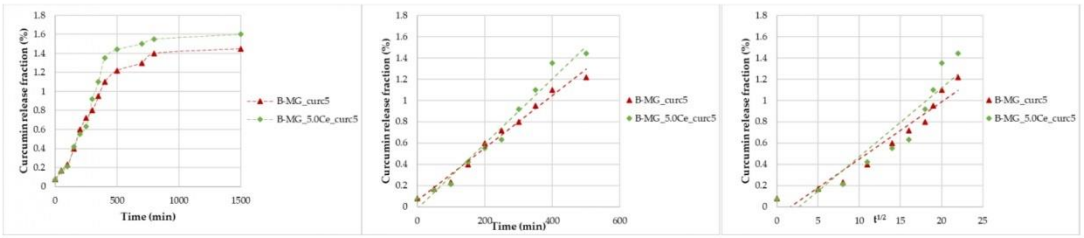

(**a**) (**b**) (**c**)

Figure 6. Curcumin release kinetics from B-MGs in SBF; (**a**) curcumin fraction released in the first 24 h for the two samples B-MG_curc5 and B-MG_5.0Ce_curc5; (**b**) linearization according to Peppas' model (n = 1); and (**c**) linearization according to Higuchi's model (n = 0.5).

From the collected data, a release of 3.0–3.1 µmol of curcumin per 100 mg of beads was recorded, a higher quantity than the minimum necessary to have a pharmaceutical effect [5,6].

2.7. Release in Simulated Gastric Fluid (SGF)

Simulated gastric fluid (pH = 1.2) allows for the study of the beads' behavior in an acid environment. Beads were tested for 4 h. All beads showed acid resistance, no significant swelling occurred, and, consequently, no high percentage of curcumin was released (Figure 7).

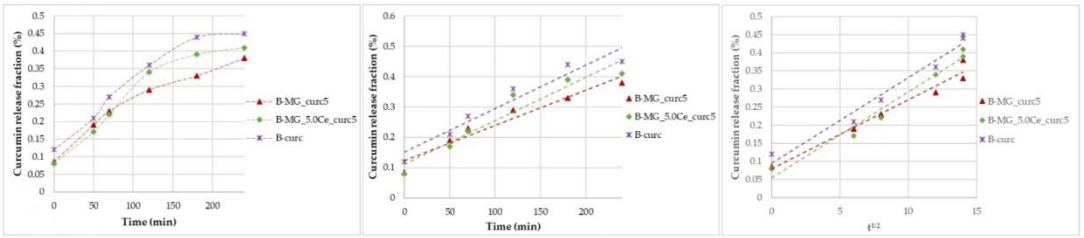

(**a**) (**b**) (**c**)

Figure 7. Curcumin release kinetics from B-MGs in SGF; (**a**) curcumin fraction released in the first 24 h for the samples B-MG_curc5 and B-MG_5.0Ce_curc5, and B-curc; (**b**) linearization according to Peppas' model (n = 1); and (**c**) linearization according to Higuchi's model.

2.8. Release in Simulated Intestinal Fluid (SIF)

Studies in SIF were conducted after the incubation in SGF. Comparing the percentage release of curcumin in both simulated fluids, a more gradual release for beads in SIF-1 than in SIF-2 (Figure 8a,a′) was noticeable; thus, a different swelling behavior in different media is observed (Figure 8b,b′,c,c′). During the first 30 min, the release is higher due to the adaptation of the beads to the new environment.

Linearizing the data collected in SIF-1 highlighted the prevalence of diffusive phenomena. For beads containing MGs, a diffusive release is still prevalent after 4 h. Release in SIF-2 is more gradual: during the first 30 min, no release is registered, but release takes place between 30 and 60 min. The release in this interval is not controlled; in fact, no good results have been obtained, either with Higuchi's linearization or with Peppas' model.

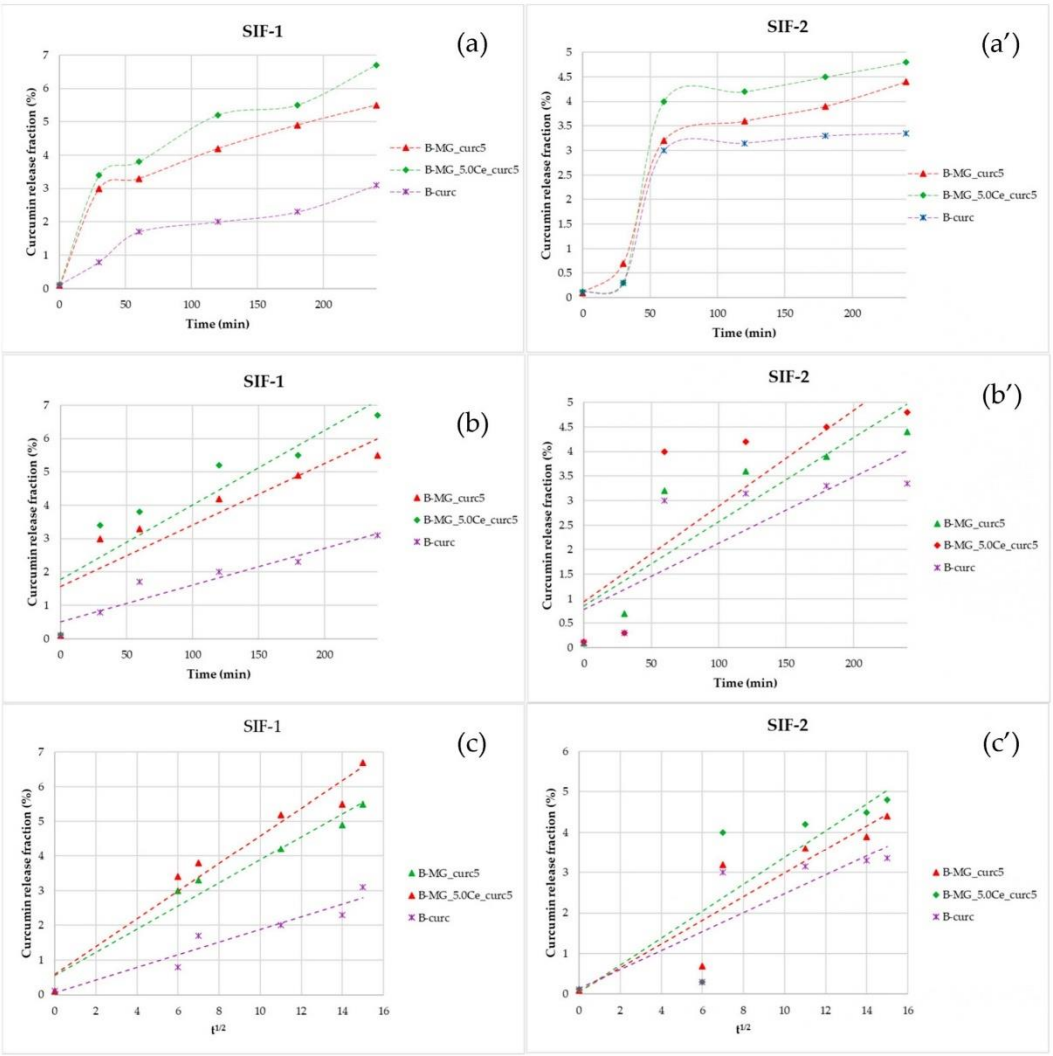

Figure 8. Representations of the kinetics release of the beads in SIF. (**a**,**a′**) Percentage fraction of time-released curcumin; (**b**,**b′**) linearization according to Peppas' model; and (**c**,**c′**) linearization according to Higuchi's model.

2.9. SEM Characterization after Soaking in SGF and SIF

To control the external aspect of beads after soaking in SGF and SIF, SEM characterization was performed. As is possible to notice in Figure 9, and as was confirmed by curcumin release, in SGF, the structure of the beads is maintained and only a few cracks are evident. Furthermore, after soaking in SIF, the surface appears damaged, and as was confirmed by curcumin release, the alginate dissolution allows curcumin release in intestinal fluids.

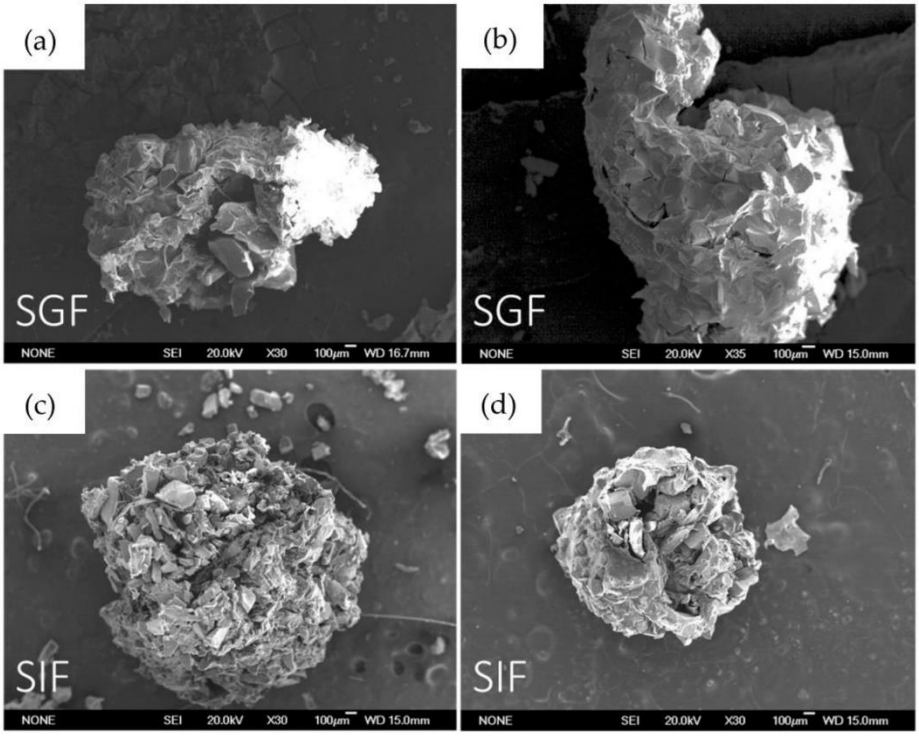

Figure 9. SEM images in order: (**a**) B-MG_curc5 after 4 h soaking in SGF; (**b**) B-MG_5.0_curc5 after 4 h soaking in SGF; (**c**) B-MG_curc5 after 4 h soaking in SIF; and (**d**) B-MG_5.0Ce_curc5 after 4 h soaking in SIF.

2.10. Catalase Mimetic Activity (CMA) Tests

CMA Tests of Powders

The enzymatic-like activity of MG_5.0Ce glasses has been demonstrated previously [1]; therefore, we focused on the curcumin effect on the degradation process of peroxide.

As shown in Figure 10, where the variation of H_2O_2 concentration vs. time is plotted for the samples at different pH values, the degradation registered for the curcumin-loaded samples is the spontaneous degradation of a H_2O_2 solution. The slight increase of CMA for the P-MG_5.0Ce_curc5 sample could be explained by considering the presence of phosphate groups that could influence the activity. Phosphate groups present in MGs stabilize Ce^{3+} ions, forming an insoluble phase of $CePO_4$ that blocks the interconversion between Ce^{3+} and Ce^{4+}.

Samples containing cerium degrade approximately 90% of H_2O_2, whereas samples without cerium, in 7 days, degrade only 10–15% of H_2O_2.

The kinetic degradation of each sample was studied by applying mathematical models for first- and second-order reactions (Table 3).

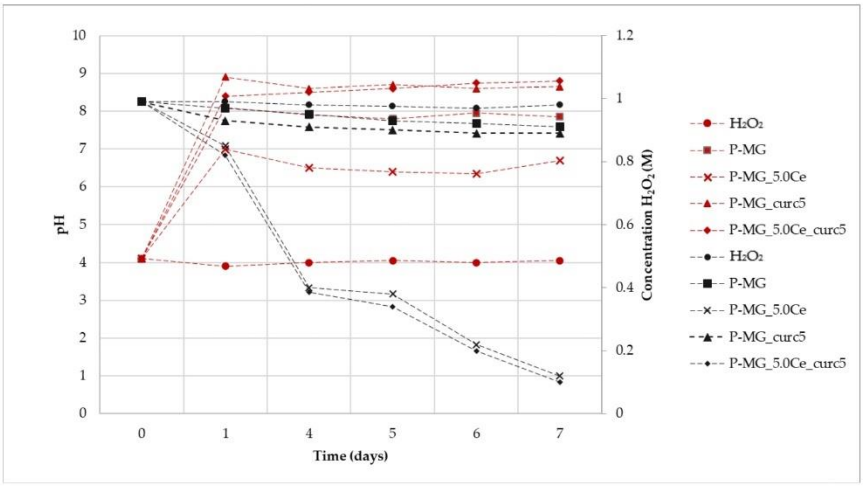

Figure 10. Variation of H_2O_2 concentration mediated by samples (black) and variation of pH (red) during the assay time.

Table 3. Linear equations and kinetic order of degradation in for each sample.

	2° Order			1° Order	
H_2O_2	y = 0.0041x + 1.0065	R^2 = 0.846	**H_2O_2**	y = 0.0052x	R^2 = 0.743
P-MG	y = 0.0174x + 1.0042	R^2 = 0.960	**P-MG**	y = 0.0172x	R^2 = 0.9577
P-MG_curc5	y = 0.0210x + 1.0247	R^2 = 0.922	**P-MG_curc5**	y = 0.0238x	R^2 = 0.8425
P-MG_5.0Ce	y = 0.8123x + 0.2239	R^2 = 0.7301	**P-MG_5.0Ce**	y = 0.2564x	R^2 = 0.944
P-MG_5.0Ce_curc5	y = 0.9437x + 0.0679	R^2 = 0.7154	**P-MG_5.0Ce_curc5**	y = 0.2741x	R^2 = 0.948

* Kinetic orders (2° or 1°) equations with higher R^2 are highlighted in grey.

Samples containing cerium show a first-order degradation constant. The presence of Ce^{3+} causes faster degradation of H_2O_2; moreover, the degradation depends only on its presence, as shown by the poor R^2 for H_2O_2 due to a very limited degradation.

For all samples, an increase of pH is registered during the first 24 h due to the release of Ca^{2+} in solution (Figure 9). This effect does not affect the Ce^{3+} catalytic activity, which occurs both at physiological and slightly basic pH (pH of approximately 7 for P-MG_5.0Ce and 8 for P-MG_5.0Ce_curc5).

To demonstrate that the catalytic system Ce^{3+}/Ce^{4+} persists over time, samples containing Ce^{3+}, which had already been in an incubator for 7 days, were kept in contact with fresh H_2O_2 1 M solution. At the end of the additional 7 days, the titration of H_2O_2 was performed, and a degradation rate of 90–95% was registered.

These systems act as antioxidants (CMA) with a time-dependent activity due to the solubilization of the systems in physiological ambient environments.

2.11. CMA Tests of Beads

The synergic effect on the beads caused by the presence of alginate and curcumin was examined (Figure 11). In general, a trend similar to that which was previously reported in Figure 8 is observed; therefore, the degradation process of peroxide is not affected by the presence of both alginate and curcumin.

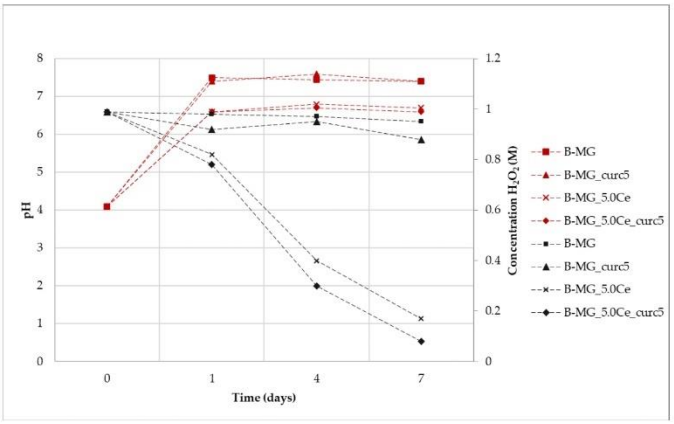

Figure 11. Variation of H_2O_2 concentration mediated by samples (black) and variation of pH (red) during the assay time.

Kinetic degradation was studied by applying mathematical models for first- and second-order reactions. Accordingly, to results collected for P-MGs, beads samples containing cerium with or without curcumin follow a first-order kinetic, while beads containing only MG with or without curcumin follow a second-order kinetic (Table 4).

Table 4. Linear equations and kinetic order of degradation in each sample.

	1° Order			2° Order	
B-MG	y = 0.0119x	R^2 = 0.9195	**B-MG**	y = 0.0138x + 0.9925	R^2 = 0.9296
B-MG_curc5	y = 0.0226x	R^2 = 0.7887	**B-MG_curc5**	y = 0.0228x + 1.0086	R^2 = 0.7994
B-MG_5.0Ce	y = 0.278x	R^2 = 0.9858	**B-MG_5.0Ce**	y = 0.9324x + 0.3377	R^2 = 0.8911
B-MG_5.0Ce_curc5	y = 0.361x	R^2 = 0.9838	**B-MG_5.0Ce_curc5**	y = 1.8335x − 0.4935	R^2 = 0.852

* Kinetic orders (2° or 1°) equations with higher R^2 are highlighted in grey.

For all the suspensions, the pH values during the time were recorded (Figure 10). An increase of pH was registered for all samples due to the presence of Ca^{2+} in the solution, according to previous results. It is worth noticing that the pH value of samples without cerium is higher in comparison with the samples containing it. This can be explained by the interactions among MG, alginate, and curcumin, which are enforced by the presence of cerium. This phenomenon causes a reduction in the exchange between Ca^{2+} and protons, thus exhibiting a lower pH value. After 24 h, the pH value stabilizes at basic pH, but Ce^{3+} activity persists. Therefore, as was the case for the beads, the catalytic activity also occurs at physiological pH.

2.12. Antioxidant Activity, DPPH Test

The antioxidant activity of curcumin has been evaluated by analyzing the decrease in the UV-Vis adsorption of DPPH in correspondence with the maximum. The spectra in Figure 12 show that degradation occurs only for samples containing curcumin, in which the adsorption of radicals is extinguished. In particular, the higher the curcumin concentration, the higher the depletion.

Curcumin expresses activity as a radical scavenger [2]. For this region, this work also investigated the concentration at which curcumin does not cause the complete degradation of DPPH (Figure 13). Different concentrations were studied: 5·10–3 mg/L, 3.3·10–3 mg/L, and 1.7·10–3 mg/L. None of these solutions brought about the complete degradation of DPPH in 2 h time.

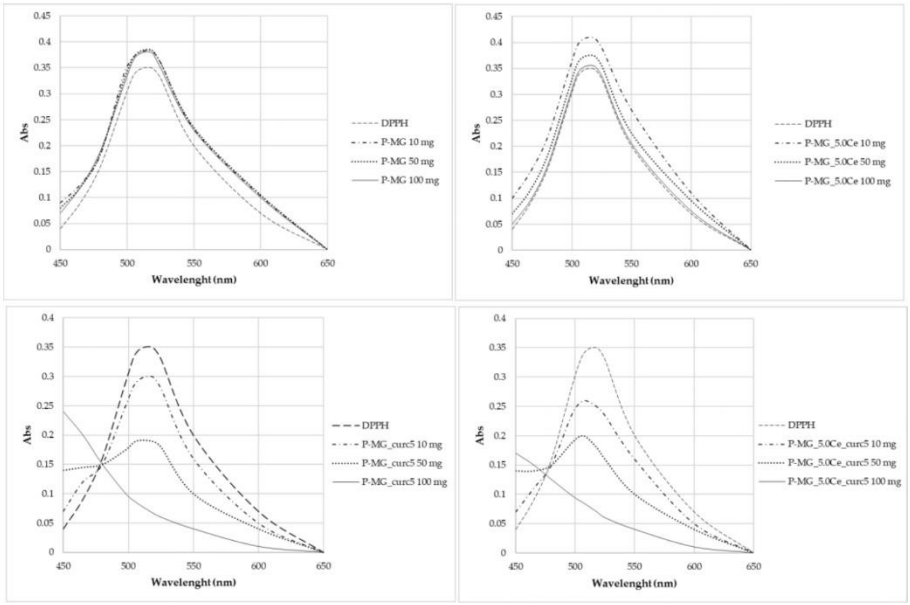

Figure 12. UV-Vis absorption spectra after 2 h contact with DPPH.

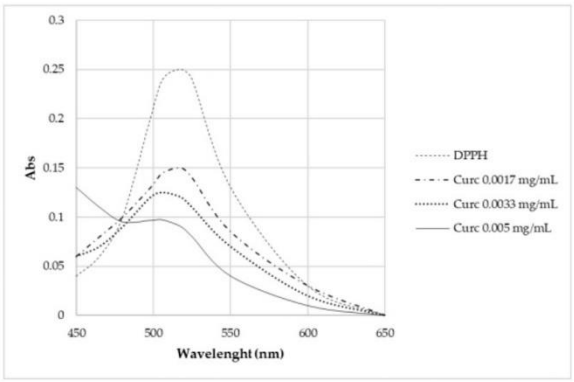

Figure 13. UV-Vis absorption spectra of samples kept in contact for 2 h with DPPH.

Samples antioxidant activity was calculated using a formula proposed by Gulcin (Equation (3)) [3,29]:

$$Radical\ Scavenging\ Effect\ (RSE)\ \% = \left(1 - \frac{A\ sample}{A\ reference}\right) \cdot 100 \quad (3)$$

From the *radical scavenging effect* (*RSE*%) calculation (Table 5), the significant action of curcumin on the depletion of radicals can be highlighted, whereas no activity is observed for P-MGs. Moreover, the action against radicals is attenuated in P-MG_5.0Ce_curc5 with respect to P-MG_curc due to the controlled release of curcumin when cerium is present.

Table 5. Radical scavenging effect of some samples tested to evaluate the antioxidant power against the radical DPPH.

Concentration mg/mL	RSE%	Concentration mg/mL	RSE%	Concentration mg/mL	RSE%
P-MG 1 mg/mL	8	P-MG_5.0Ce 1 mg/mL	0	Curc $5{\cdot}10^{-3}$ mg/mL	78
P-MG 5 mg/mL	8	P-MG_5.0Ce 5 mg/mL	7	Curc $3.3{\cdot}10^{-3}$ mg/mL	64
P-MG 10 mg/mL	7	P-MG_5.0Ce 10 mg/mL	14	Curc $1.7{\cdot}10^{-3}$ mg/mL	41
P-MG_curc5 1 mg/mL	15	P-MG_5.0Ce_curc5 1 mg/mL	25		
P-MG_curc5 5 mg/mL	50	P-MG_5.0Ce_curc5 5 mg/mL	44		
P-MG_curc5 10 mg/mL	100	P-MG_5.0Ce_curc5 10 mg/mL	100		

2.13. DPPH Degradation Kinetic

Table 6 lists the linear equations and related parameters for the kinetic study of antioxidant power in the DPPH test.

Table 6. Linear equations and related parameters for the kinetic study of antioxidant power in the DPPH test.

Sample	Linear Equations	
DPPH $6{\cdot}10^{-5}$ M	y = 0.0705x + 3.981	R^2 = 0.9929
P-MG	y = 0.078x + 4.0149	R^2 = 0.9875
P-MG_5.0Ce	y = 0.0791x + 4.051	R^2 = 0.9591
P-MG_curc5	y = 0.0962x + 3.3147	R^2 = 0.9315
P-MG_5.0Ce_curc5	y = 0.165x + 3.3016	R^2 = 0.9633
Curc	y = 0.7276x + 5.0969	R^2 = 0.7704

All samples show a second-order kinetic; for samples with no curcumin, this depends strictly on depleting agents present on the surface of the solids.

Through percentage degradation analysis of DPPH radicals (Figure 14a), it was possible to observe that samples containing curcumin depleted a higher quantity of radicals in comparison with the parallel samples without curcumin. Moreover, the synergic effect of the couple cerium–curcumin is also demonstrated. The degradation activity of curcumin is higher during the first hour (Figure 14b); after this time, the action slows down.

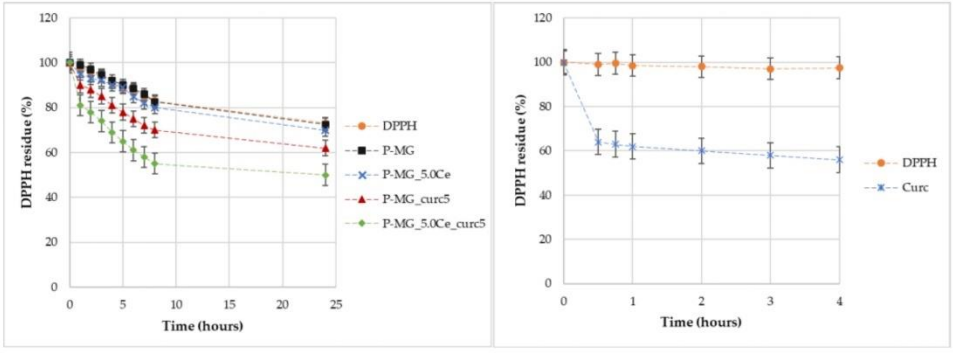

Figure 14. Graphic representation of the percentage of DPPH remaining over time for samples (**a**) and for curcumin effect (**b**).

3. Discussion

The synergistic application of various experimental techniques applied in this study demonstrates that the composite material based on Ce-MG/alginate beads (B-MG) is a suitable drug delivery system for curcumin.

The curcumin molecule, after the loading, shows the characteristic adsorbing peak in the UV-Vis spectrum performed on solid-state, indicating that its integrity is maintained in the composite. An efficiency of 4–6% on curcumin loading inside MGs is expected by both the elemental and TG analyses, which confirm the same results.

Concerning the releases, different behaviors have been registered as a function of the medium: in SIF, the swelling is gradual, so it permits a controlled release that persists over time; tests conducted in SGF demonstrated that beads do not swell if they are put in contact with an extremely acidic environment (pH 1.2 of SGF), but the rehydration process takes place only in a slightly acid environment (pH 6.8 of SIF). Thanks to this phenomenon, we can assume a selective release at the intestinal level and not at the gastric one. These trends suggest a very interesting result: a specific release of curcumin (3 mg released in 4 h) in the intestinal tract and not in the gastric tract. Moreover, an increment of stability in the simulated gastrointestinal tract in shown by the triphasic systems (alginate, MGs, and curcumin) with respect to the MGs systems.

CMA tests confirm the well-known catalytic activity of the couple Ce^{3+}/Ce^{4+} and the absence of catalytic behavior made by the contribution of curcumin.

Curcumin is very active in scavenging the DPPH radicals, and only very low concentrations prevent the complete radical reduction. Anti-radical action is practically absent when only MG is present. Analyzing the radical degradation during 24 h, a noticeable reducing action was also observed for cerium-containing samples. This suggests an independent effect of the metal ion, although it was lower than curcumin.

The amount of curcumin released varies from 0.8–1 μmol/g for MGs in 8 h to 3.0–3.1 μmol/100 mg for beads. For both systems, the release is sufficient to reach the antioxidant activity threshold. The results suggest that in MGs, the release follows a diffusive and erosive mechanism of the glass matrix, whereas, in the beads, initially curcumin is released on the surface, and then the release became diffusive and ruled by swelling of the polymeric lattice.

4. Material and Methods

4.1. General Procedures

All the chemicals and solvents were purchased with the highest purity grade available and used without further purification unless otherwise specified; pH measurements were carried out using a calibrated pH-meter (Hach).

UV–visible spectra were recorded using a JASKO V-570 UV/Vis/NIR spectrophotometer at 298 K in the 250–600 nm spectral range employing quartz cells (1 cm optical path). Elemental analysis was performed on a Thermo Scientific™ FLASH 2000 CHNS Analyzer. TG analyses were performed using a Seiko SSC 5200 in a temperature range between 25 °C and 1000 °C, with a heating rate of 1 °C/min. The morphology of the beads before and after soaking was examined by SEM using a JSM-6335F (JEOL) microscope operating at 20 kV. IR spectra were recorded in the 4000–400 cm^{-1} spectral range, using a FT-IR Jasco 4700 equipped with the ATR proONE.

4.2. Synthesis

In this work, MGs were synthesized following the sol–gel method by using the evaporation-induced self-assembly process (EISA) [1,2]. All the syntheses require a symmetric triblock copolymer comprising poly(ethylene oxide) (PEO) and poly(propylene oxide) (PPO), in an alternating linear fashion, and a non-ionic surfactant used as a structural agent, Pluronic® P123 [3].

For this study, two different MGs were studied: starting from the composition of 80%SiO_2–20%CaO (MG) and adding, to one sample, 5% of CeO_2 (MG_5.0Ce). Each sample

was prepared starting from the precursor of SiO_2, CaO, and CeO_2: tetraethyl orthosilicate (TEOS) (98%, Sigma Aldrich, Milan, Italy), calcium nitrate tetrahydrate $Ca(NO_3)_2{\cdot}4H_2O$ (99.5%, Sigma Aldrich), and cerium nitrate hexahydrate $Ce(NO_3)_3{\cdot}6H_2O$ (99%, Sigma Aldrich, Milan, Italy).

The theoretical molar compositions of the samples are reported in Table 7.

Table 7. Theoretical molar composition of bioactive glasses.

Glass	SiO_2 (mol%)	CaO (mol%)	CeO_2 (mol%)
MG	80	20	-
MG_5.0Ce	80	15	5

To conduct the syntheses [28,29], 2 g of Pluronic® P123 was added to a solution composed of 80 mL of ethanol and 1 mL of hydrochloric acid 10%m/m. The solution was stirred at room temperature (RT) until complete dissolution. Then, for the synthesis of MG, 10 mL of TEOS and 1.99 g of $Ca(NO_3)_2{\cdot}4H_2O$ were added at RT in sequence, under continuous stirring, for approximately 3 h. For the synthesis of MG_5.0Ce, the amount of 1.38 g of $Ce(NO_3)_3{\cdot}6H_2O$ was also added.

These solutions were stirred overnight to allow for the formation of a gel phase. Following that, they were transferred to Petri dishes for 48 h to undergo the EISA process. Successively, the dried gels were removed as homogeneous and transparent membranes and heated at 700 °C for 3 h under an air atmosphere to remove the surfactant and nitrate groups and to stabilize the resultant mesoporous glasses. The powders were obtained by grinding the mesoporous glass pieces with an agate pestle. The powders were sieved to a particle size < 125 µm and stored in a desiccator until further use.

The in vitro bioactivity of B-MG and powdery MGs (P-MG) was confirmed in previous papers [4,5,32]. To evaluate drug release both in pure distilled water and physiological environment, a simulated body fluid (SBF) buffered at a pH of 7.4 according to Kokubo was prepared [6,33]. Table 8 shows the comparison between plasma and SBF ion concentrations (expressed as mM).

Table 8. Comparison between the composition (mM) of human plasma and simulated body fluid (SBF).

	Na^+	K^+	Mg^{2+}	Ca^{2+}	Cl^-	HCO_3^-	HPO_4^{2-}	SO_4^{2-}	pH
SBF	142.0	5.0	1.5	2.5	147.8	4.2	1.0	0.5	7.4
Plasma	142.0	5.0	1.5	2.5	103.0	27.0	1.0	0.5	7.20/7.40

4.3. Curcumin Loading onto P-MGs

For the two bioactive glass samples prepared in the previous paragraph, curcumin loadings were performed by using the impregnation method: an ethanol solution of curcumin (98%, Sigma Aldrich; 40 mL, 5 mg/mL) was kept in contact with 1 g of sample (grain size < 125 µm) at RT for 48 h to obtain 1–2% m/m of curcumin for each glass (P-MG_curc5) [34,35]. Loadings were performed on different MGs: the unaltered MG (P-MG_curc5) and the cerium-doped one (P_MG_5.0Ce_curc5). A blank sample was also prepared in identical conditions using only ethanol as a contact solution.

The final solutions were then filtered, and the solids were dried for 24 h at 70 °C.

4.4. P-MGs Curcumin Content Determination

Curcumin content was determined through solvent extraction followed by a UV-Vis determination. The data were reported in Table 1.

Then, 250 mg of the solid was put in contact with 25 mL of ethyl acetate for 3 h, and the curcumin released from the solid was determined spectrophotometrically at 420 nm using a calibration curve of curcumin in ethyl acetate in the range of $5{\cdot}10^{-6}$–$2{\cdot}10^{-5}$ M [35,36].

4.5. Beads' Synthesis

Alginate beads were synthesized following the cross-linking ionic method: starting from sodium alginate solution, through an ion exchange between sodium and calcium present in a second solution, a calcium alginate lattice was formed [37].

Under continuous stirring, 0.5 g of the unloaded glass powder samples (P-MG and P-MG_5.0Ce, grain size < 125 µm) were added to 20 mL of sodium alginate solution 1%m/m until the formation of a homogeneous suspension. The suspension was added dropwise into the solution of calcium chloride 0.1 M. The formed beads (B-MG and B-MG_5.0Ce) were kept under continuous stirring overnight to allow for the complete digestion and the formation of a resistant lattice of calcium alginate. Under continuous stirring, 0.5 g of the loaded glass powder samples (P-MG_curc5 and P-MG_5.0Ce_curc5) were added to 40 mL of ethanol solution of curcumin (5 mg/mL) and 20 mL of sodium alginate solution 1%m/m until the formation of a homogeneous suspension. The suspension was added dropwise into the solution of calcium chloride 0.1 M. The formed beads (B-MG_curc5 and B-MG_5.0Ce_curc5) were kept under continuous stirring overnight to allow for the complete digestion and the formation of a resistant lattice of calcium alginate.

For comparison purposes, 20 mL of sodium alginate solution 1%m/m was added dropwise into the solution of calcium chloride 0.1 M. The formed beads (B) were kept under continuous stirring overnight to allow for the complete digestion and the formation of a resistant lattice of calcium alginate. Moreover, a mix of 20 mL of sodium alginate solution 1%m/m and 40 mL of ethanol solution of curcumin (5 mg/mL) was added dropwise into the solution of calcium chloride 0.1 M. The formed beads (B-curc) were kept under continuous stirring overnight to allow for the complete digestion and the formation of a resistant lattice of calcium alginate.

After that, the beads were filtered under vacuum and washed with ethanol. Thermal treatment at 60 °C for removing water was then performed.

4.6. Catalase Mimetic Activity (CMA) Tests

The catalase mimetic activity tests (CMA) were performed to evaluate enzymatic-like activity of samples.

To conduct the test, a solution 1 M of H_2O_2 was added to the powder glass sample using a ratio MG/H_2O_2 of 5 mg/mL. In addition, the blank reference, i.e., only the solution of H_2O_2, was prepared. Each sample was incubated at 37 °C and 120 rpm for five different time periods: 1 day, 4 days, 5 days, 6 days, and 7 days. At the end of incubation, the solutions were filtered, and the filtrates were collected. To perform CMA, 10 mL of filtrate was diluted 1:10, and 10 mL of the diluted solution was added to 20 mL of deionized water and 20 mL of sulfuric acid 1:4. The titration was performed using $KMnO_4$ 0.1 N, previously standardized.

4.7. 2,2-Diphenyl-1-Picrylhydrazyl (DPPH) Test

This test allows for the evaluation of the antioxidant activity through a spectrophotometric method by using a DPPH (99.9% Sigma Aldrich) solution. DPPH presents a characteristic adsorption peak at 517 nm, but when an oxidant agent is present in the solution, a decrease of the adsorption is registered.

A solution $1.2 \cdot 10^{-2}$ M of DPPH in methanol was prepared and then diluted 1: 200.

Different amounts of samples were used: 10 mg, 20 mg, 30 mg, 50 mg, 70 mg, and 100 mg. All samples were added to 10 mL of DPPH 6×10^{-5} M and incubated at 37 °C, 120 rpm, in the dark for 2 h. Simultaneously, a blank solution of only DPPH was prepared and incubated. After incubation, the solutions were centrifuged, and the supernatants were collected and analyzed spectrophotometrically. At the same time, to evaluate the antioxidant activity of curcumin, assuming a loading of 15% of curcumin inside MG and a complete release of it in solution, an analogous solution (10^{-2} M in methanol) was prepared.

4.8. DPPH Degradation Kinetic

To determine the DPPH degradation kinetic constant, a solution with the same concentration as the previous one was prepared (0.33 g of P-MG in 1 mL) but different timing was studied: 1 h, 2 h, 3 h, 4 h, 5 h, 6 h, 7 h, 8 h, and 24 h. In addition, a reference solution of curcumin was prepared (0.50 mg of curcumin in 10 mL of a DPPH solution $6{\cdot}10^{-5}$ M).

Determining the radical scavenging effect (RSE%), following the Gulcin equation [3], it is possible to evaluate the action against radicals.

4.9. Swelling Test

The swelling test was used to evaluate the beads' rehydration rate and degradation. The rehydration test is performed in different mediums: H_2O dd, SBF, D-MEM (Dulbecco's Modified Eagle Medium), SGF (simulated gastric fluid), and SIF (simulated intestinal fluid).

In a multi-well plate, an appropriate amount of the beads was added together with 2 mL of the biological fluid. The plate was incubated at 37 °C and 120 rpm. At different timing, according to the biological fluid, beads were collected, dried, weighed, and re-immersed into the swelling medium. The weight variation was used to evaluate the rehydration rate, according to Equation (4) [38,39].

$$\%\ W\ rehydration = 100 * \frac{W_t - W_d}{W_d} \quad (4)$$

where W_t is rehydrated bead weight, t is the time, and W_d is the initial weight.

4.10. Curcumin Release

For these tests, 50 mg of the sample was put in contact with 5 mL of the appropriate medium (SBF, SGF, or SIF) for different time periods: 0 min, 30 min, 1 h, 2 h, 3 h, 4 h, 5 h, 6 h, 7 h, 8 h, and 24 h. For the analysis, a limpid released solution of curcumin is mandatory; therefore, the suspension was centrifuged, and the supernatant was collected, then the solid sample was re-suspended in a new amount of medium. After centrifugation, 3 mL of the supernatant was extracted with the mixture ethylacetate: methanol 95:5 V:V. The amount of curcumin released was determined after its extraction from the medium by using UV-Vis spectroscopy (concentration of calibration solutions: 2 μM–50 μM).

Samples treated in SGF for 4 h were washed with deionized water and then used for release in SIF [7].

5. Conclusions

In light of the results obtained, it can be concluded that the investigated scaffolds represent multifunctional systems potentially useful in drug delivery. One of the main achievements is the improvement in curcumin stabilization and bioavailability, especially in the intestine, where it can exert its therapeutic action, mainly against colorectal cancer. The fundamental release behavior of hybrid materials has been shown and demonstrated.

In conclusion, all scaffolds take advantage of the synergic effect of cerium and curcumin, and they can be used as drug delivery systems for curcumin, with high release.

Author Contributions: Conceptualization, G.M.; investigation, D.C.; resources, G.M. and E.F.; supervision, M.C.M., G.M. and E.F.; writing—original draft, D.C.; writing—review and editing, M.C.M., G.M. and E.F. All authors have read and agreed to the published version of the manuscript.

Funding: This research received no external funding.

Institutional Review Board Statement: Not applicable.

Informed Consent Statement: Not applicable.

Data Availability Statement: Additional data that support the findings of this study are available from the corresponding author.

Conflicts of Interest: The authors declare no conflict of interest.

References

1. Huang, A.; Cao, S.; Tang, L. The tumor microenvironment and inflammatory breast cancer. *Cancer. J.* **2017**, *8*, 1884–1891. [CrossRef] [PubMed]
2. De Wever, O.; Mareel, M. Role of tissue stroma in cancer cell invasion: Stroma; cancer invasion. *Pathol. J.* **2003**, *200*, 429–447. [CrossRef] [PubMed]
3. Jozkowicz, A.; Dulak, J. Oxidative Stress in Tumor Angiogenesis—Therapeutic Targets. *Curr. Pharm. Des.* **2010**, *16*, 3877–3894. [CrossRef]
4. Kalman, S. Curcumin: A Review of Its Effects on Human Health. *Foods* **2017**, *6*, 92.
5. Kotha, R.R.; Luthria, D.L. Curcumin: Biological, Pharmaceutical, Nutraceutical, and Analytical Aspects, Molecules. *Molecules* **2019**, *24*, 2930. [CrossRef] [PubMed]
6. Moghadamtousi, S.Z.; Kadir, H.A.; Hassandarvish, P.; Tajik, H.; Abubakar, S.; Zandi, K. A Review on Antibacterial, Antiviral, and Antifungal Activity of Curcumin. *BioMed Res. Int.* **2014**, *2014*, 186864. [CrossRef]
7. Anand, P.; Kunnumakkara, A.B.; Newman, R.A.; Aggarwal, B.B. Bioavailability of curcumin: Problems and promises. *Mol. Pharm.* **2007**, *4*, 807–818. [CrossRef]
8. Sharma, R.A.; Steward, W.P.; Gescher, A.J. Pharmacokinetics And Pharmacodynamics Of Curcumin. In *The Molecular Targets and Therapeutic Uses of Curcumin in Health and Disease*; Aggarwal, B.B., Surh, Y.-J., Shishodia, S., Eds.; Springer: Boston, MA, USA, 2007; Volume 595, pp. 453–470.
9. Basile, V.; Ferrari, E.; Lazzari, S.; Belluti, S.; Pignedoli, F.; Imbriano, C. Curcumin derivatives: Molecular basis of their anti-cancer activity. *Biochem. Pharmacol.* **2009**, *78*, 1305–1315. [CrossRef]
10. Feng, T.; Hu, Z.; Wang, K.; Zhu, X.; Chen, D.; Zhuang, H.; Yao, L.; Song, S.; Wang, H.; Sun, M. Emulsion-based delivery systems for curcumin: Encapsulation and interaction mechanism between debranched starch and curcumin. *Int. J. Biol. Macromol.* **2020**, *161*, 746–754. [CrossRef]
11. Zheng, B.; Peng, S.; Zhang, X.; McClements, D.J. Impact of Delivery System Type on Curcumin Bioaccessibility: Compari-son of Curcumin-Loaded Nanoemulsions with Commercial Curcumin Supplements. *J. Agric. Food Chem.* **2018**, *66*, 10816–10826. [CrossRef]
12. Yu, H.; Huang, Q. Improving the Oral Bioavailability of Curcumin Using Novel Organogel-Based Nanoemulsions. *J. Agric. Food Chem.* **2012**, *60*, 5373–5379. [CrossRef]
13. Porter, C.J.; Trevaskis, N.L.; Charman, W.N. Lipids and lipid-based formulations: Optimizing the oral delivery of lipophilic drugs. Nat. Rev. *Drug Discov.* **2007**, *6*, 231–248. [CrossRef]
14. Yao, E.C.; Xue, L. Therapeutic Effects of Curcumin on Alzheimer's Disease. Adv. *Alzheimer's Dis.* **2014**, *3*, 145–159. [CrossRef]
15. Desfrançois, C.; Auzély, R.; Texier, I. Lipid Nanoparticles and Their Hydrogel Composites for Drug Delivery: A Review. *Pharmaceuticals* **2018**, *11*, 118. [CrossRef]
16. Li, Y.; McClements, D.J. Controlling lipid digestion by encapsulation of protein-stabilized lipid droplets within alginate–chitosan complex coacervates. *Food Hydrocoll.* **2011**, *25*, 1025–1033. [CrossRef]
17. Shewan, H.M.; Stokes, J.R. Review of techniques to manufacture micro-hydrogel particles for the food industry and their applications. *J. Food Eng.* **2013**, *119*, 781–792. [CrossRef]
18. McClements, D.J. Recent progress in hydrogel delivery systems for improving nutraceutical bioavailability. *Food Hydrocoll.* **2017**, *68*, 238–245. [CrossRef]
19. Matalanis, A.; Jones, O.G.; McClements, D.J. Structured biopolymer-based delivery systems for encapsulation, protection, and release of lipophilic compounds. *Food Hydrocoll.* **2011**, *25*, 1865–1880. [CrossRef]
20. Lee, K.Y.; Mooney, D.J. Alginate: Properties and biomedical applications. *Prog. Polym. Sci.* **2012**, *37*, 106–126. [CrossRef]
21. Varini, E.; Sánchez-Salcedo, S.; Malavasi, G.; Lusvardi, G.; Vallet-Regí, M.; Salinas, A.J. Cerium (III) and (IV) containing mesoporous glasses/alginate beads for bone regeneration: Bioactivity, biocompatibility and reactive oxygen species activity. *Mater. Sci. Eng. C* **2019**, *105*, 109971. [CrossRef]
22. Manzano, M.; Vallet-Regí, M. New developments in ordered mesoporous materials for drug delivery. *J. Mater. Chem.* **2010**, *20*, 5593–5604. [CrossRef]
23. Wu, K.; Liao, Y.-T.; Liu, C.-H.; Yu, J. Liver cancer cells: Targeting; prolonged-release drug carriers consisting of mesoporous silica nanoparticles; alginate microspheres. *Nanomedicine* **2014**, *9*, 2767. [CrossRef] [PubMed]
24. Wang, F.; Zhao, J.; Pan, F.; Zhou, H.; Yang, X.; Li, W.; Liu, H. Adsorption Properties toward Trivalent Rare Earths by Alginate Beads Doping with Silica. *Ind. Eng. Chem. Res.* **2013**, *52*, 3453–3461. [CrossRef]
25. Nicolini, V.; Malavasi, G.; Menabue, L.; Lusvardi, G.; Benedetti, F.; Valeri, S.; Luches, P. Luches Cerium-doped bioactive 45S5 glasses: Spectroscopic, redox, bioactivity and biocatalytic properties. *J. Mater. Sci.* **2017**, *52*, 8845–8857. [CrossRef]
26. Nicolini, V.; Nicolini, V.; Gambuzzi, E.; Malavasi, G.; Menabue, L.; Menziani, M.C.; Lusvardi, G.; Pedone, A.; Benedetti, F.; Luches, P.; et al. Evidence of Catalase Mimetic Activity in Ce^{3+}/Ce^{4+} Doped Bioactive Glasses. *J. Phys. Chem. B* **2015**, *119*, 4009–4019. [CrossRef] [PubMed]
27. Shruti, S.; Salinas, A.J.; Malavasi, G.; Lusvardi, G.; Menabue, L.; Ferrara, C.; Mustarelli, P.; Vallet-Regì, M. Structural and in vitro study of cerium, gallium and zinc containing sol–gel bioactive glasses. *J. Mater. Chem.* **2012**, *22*, 13698. [CrossRef]
28. Narra, K.; Dhanalekshmi, U.; Rangaraj, G.; Raja, D.; Kumar, C.S.; Reddy, P.N.; Mandal, A.B. Effect of Formulation Variables on Rifampicin Loaded Alginate Beads. *Iran. J. of Pharm. Res.* **2012**, *11*, 715–721. [CrossRef]

29. Gangwar, R.K.; Tomar, G.B.; Dhumale, V.A.; Zinjarde, S.; Sharma, R.B.; Datar, S. Curcumin Conjugated Silica Nanoparti-cles for Improving Bioavailability and Its Anticancer Applications. *J. Agric. Food Chem.* **2013**, *61*, 9632–9637.
30. Wu, I.Y.; Bala, S.; Škalko-Basnet, N.; di Cagno, M.P. Interpreting non-linear drug diffusion data: Utilizing Korsmeyer-Peppas model to study drug release from liposomes. *Eur. J. Pharm. Sci.* **2019**, *138*, 105026. [CrossRef]
31. Gülçin, İ. Comparison of in vitro antioxidant and antiradical activities of L-tyrosine and L-Dopa. *Amino Acids* **2007**, *32*, 431–438. [CrossRef]
32. Lei, Q.; Guo, J.; Noureddine, A.; Wang, A.; Wuttke, S.; Brinker, C.J.; Zhu, W. Sol–Gel-Based Advanced Porous Silica Materials for Biomedical Applications. *Adv. Funct. Mater.* **2020**, *30*, 1909539. [CrossRef]
33. Kokubo, T.; Kushitani, H.; Sakka, S.; Kitsugi, T.; Yamamuro, T. Solutions able to reproduce in vivo surface-structure changes in bioactive glass-ceramic A-W3. *J. Biomed. Mater. Res.* **1990**, *24*, 721–734. [CrossRef] [PubMed]
34. Arcos, D.; Vallet-Regí, M. Sol–gel silica-based biomaterials and bone tissue regeneration. *Acta Biomater.* **2010**, *6*, 2874–2888. [CrossRef] [PubMed]
35. Gianluca, M.; Erika, F.; Gigliola, L.; Valentina, A.; Francesca, F.; Claudio, M.; Ledi, M. The role of coordination chemistry in the development of innovative gallium-based bioceramics: The case of curcumin. *J. Mater. Chem.* **2011**, *21*, 5027. [CrossRef]
36. Shruti, S.; Salinas, A.J.; Ferrari, E.; Malavasi, G.; Lusvardi, G.; Doadrio, A.L.; Menabue, L.; Vallet-Regi, M. Curcumin release from cerium, gallium and zinc containing mesoporous bioactive glasses. *Microporous Mesoporous Mater.* **2013**, *180*, 92–101. [CrossRef]
37. Mandal, S.; Kumar, S.S.; Krishnamoorthy, B.; Basu, S.K. Development and evaluation of calcium alginate beads prepared by sequential and simultaneous methods. *Braz. J. Pharm. Sci.* **2010**, *46*, 785–793. [CrossRef]
38. Jin, L.; Hong, Y.C.; Pyo, J.W.; Song, H.; Kang, J.Y.; Lee, S.W.; No, K. Monitoring of Swelling and Degrading Behavior of Alginate Beads using Optical Tweezers. *Biochip J.* **2009**, *3*, 213–218.
39. Singhvi, G.; Singh, M. REVIEW: In-Vitro Drug Release Characterization Models. *Int. J. Pharm. Stud. Res.* **2011**, *2*, 77–84.

Ceramics International 50 (2024) 2574–2587

Contents lists available at ScienceDirect

Ceramics International

journal homepage: www.elsevier.com/locate/ceramint

Assessing Mn as an antioxidant agent in bioactive glasses by quantification of catalase and superoxide dismutase enzymatic mimetic activities

Matteo Abati [a,c], Altair T. Contreras Jaimes [b,c], Luca Rigamonti [a], Debora Carrozza [a], Gigliola Lusvardi [a], Delia S. Brauer [c,**], Gianluca Malavasi [a,*]

[a] Department of Chemical and Geological Sciences, Università degli Studi di Modena e Reggio Emilia, via G. Campi 103, 41125, Modena, Italy
[b] Fraunhofer-Institut für Silicatforschung (ISC), Neunerplatz 2, 97082, Würzburg, Germany
[c] Otto Schott Institute of Materials Research, Friedrich Schiller University Jena, Fraunhoferstr. 6, 07743, Jena, Germany

ARTICLE INFO

Handling Editor: Dr P. Vincenzini

Keywords:
Catalase mimetic activity
Bioactive glasses
Manganese
Superoxide dismutase
Apatite

ABSTRACT

The antioxidant activity of Mn as additive in a 45S5 type glass system with and without P_2O_5 was studied by mimicking the activity of catalase (CMA) and superoxide dismutase (SOD) enzymes. Glasses were melted either under oxidizing or reducing atmosphere (N_2/H_2) to compare the processing influence on the Mn oxidation state. Thermal (DTA) and optical (UV–Vis) characterizations of the glass powders were carried out to obtain further insight into the structural role of Mn. A correlation of *in vitro* apatite formation between Tris buffer solution and Simulated Body Fluid (SBF) was performed to optimise Mn substitution, where a decrease in apatite formation was observed by increasing Mn content. Despite this, glasses with up to 1.0 mol% MnO did not show any delay in apatite formation and maintained their CMA and SOD activity. The antioxidant effect of Mn can be attributed to the interconversion $Mn^{2+} \leftrightarrow Mn^{3+}$ occurring on the glass surface through a heterogeneous catalysis. P_2O_5 plays an important role in the antioxidant effect of the glass, possibly by charge balancing Mn ions and forming more stable units compared to those formed with Ca and Na. The amount of Mn^{2+} is predominant in the glass network with respect to Mn^{3+} in all synthetized glasses. Moreover, glass melting in a reducing atmosphere further avoided Mn oxidation.

1. Introduction

The implantation of biomaterials to treat and repair tissues has inherent inflammatory and repair mechanisms. During these processes, redox reactions occur and cells such as platelets and macrophages release reactive oxygen species (ROS). With this regard, the effect of oxidative stress in biomaterials has been overlooked despite the influence of the chemical composition, surface properties and by-products being of importance in the production of oxidant molecules. Furthermore, low levels of oxidative stress can lead to a low immunological response and infections while high levels are associated with implant rejection [1].

It has been investigated that an *in vitro* decrease in superoxide-dismutase (SOD) enzymes after exposure to Ti6Al4V implants, with high ROS levels such as superoxide anion (O_2^-), was associated with pathological events after implantation of coronary artery stents. Additionally, pre-existing inflammation in the host tissue was reported to be an affecting factor of the redox balance and tissue repair [1].

As the first biomaterial to be considered bioactive, Bioglass® 45S5 [2,3] has extensive potential applications owing to the multiple options in which its glass network can be modified, by means of doping with alkaline, alkaline earth and transition metal ions [4,5]. It has been proved that one of the main factors controlling the composition-degradation relationship is the silicate network connectivity (NC) given by its chemical composition [6,7]. Consequently, the glass dissolution mechanism plays a key role in its bioactivity, allowing for tissue regrowth and actively stimulating cells to produce new tissue. During the first few hours of contact in a biological environment, a complex mechanism of alkaline ions release occurs. The exchange of these ions with H^+ from the surrounding aqueous solution leads to the formation of the initial reaction film, which evolves into a silica-gel layer and consecutively into a mineralized hydroxyapatite layer [2].

The incorporation of functional ions in the glass structure has shown to improve their physical and therapeutic properties by adapting their

* Corresponding author.
** Corresponding author.
E-mail addresses: delia.brauer@uni-jena.de (D.S. Brauer), gmalavasi@unimore.it (G. Malavasi).

https://doi.org/10.1016/j.ceramint.2023.10.091
Received 12 June 2023; Received in revised form 18 September 2023; Accepted 10 October 2023
Available online 11 October 2023

chemistry depending on the final application. These effects are associated with antibacterial activity (Ag [8–11] and Ga [12,13]), stimulation of bone development and maintenance (Mg [14], Sr [15], Zn [16,17], and Co [18]), fluorapatite precipitation (F [19–21]), mechanical properties (K [22,23]), reduction of local oxidative stress (Ce [24], Sr [25]), and in magnetic localised hyperthermia for tumours treatment (Fe [26]).

Amongst the different ions with therapeutic properties, Mn has attracted attention in recent years for incorporation in different bioceramics [27–29]. Recent works highlight advantages of glasses doped with Mn compared to other materials doped, for example, with Mg [30], Sr[29], Ag [31], Te [32] or Se [33]. The incorporation of Mn into bioactive glasses synthesized by melt [34,35] or sol-gel [36–39] routes, were done because Mn has an important role in relevant biological processes. As a redox-active metal, Mn is important in the oxygen chemistry within the body by acting as a catalytic cofactor for SOD metalloenzymes, which remove toxic products from O_2 metabolism such as superoxide (O_2^-) and hydrogen peroxide [40]. Mn also acts as a mediator of interactions between cells and the surrounding environment, and as an activator of integrins and glycoproteins of the cellular membrane [41].

Concerning the clinical applications of bioactive glasses, it is known that Mn plays an essential role in key cellular processes involved in the metabolism of hard tissues [4,42], such as: extracellular matrix remodelling (ECM) [43], improvement of bone mineralization [37,44], cell adhesion, proliferation [45] and bone mass maintenance [46]. Therefore, further research dealing with its potential use in clinical applications in bone regeneration is of great interest. For example, incorporation of small amounts of Mn in bioactive silicate glasses showed positive effects such as *in vitro* osteoblast growth and osteogenic activity [39,47]. A previous study on CMA activity of a series of doping ions [48] showed that Mn had the highest decomposition rate (k) after Co, with other tested ions being Cu > Ce > Fe > V > Ti > Zr. Similarly, Kapoor et al. [39] found that a 1 mol% MnO doping in a bioactive type glass showed the best outcome when tested under oxidative stress conditions among other ions (Co, Cu, Fe) [39]. The antioxidant activity was also described to be dose-dependant [39] with its effect being gradually reduced up to a 5 mol% content in a bioactive type glass. In view of these results, a more detailed to study on Mn-containing potential bioactive glasses is very important to find the best compositions for obtaining glasses with bioactivity and CMA.

The significance of adjusting Mn concentration is also fundamental since more than 1 mol% of MnO_2 was reported to have a negative effect on bioactivity for 45S5 containing glasses [35]. However, the confirmation for this trend should be further investigated, since this study by Srivastava et al. [35] substituted MnO by CaO on a weight basis instead of a molar basis. While Ca and Mn have comparable charge/size ratio, leading to the hypothesis that Mn^{2+} acts also as a modifier ion [34,36,49], substitution in wt.% was reported to lead to significant changes in the glass dissolution because of structural modifications [50].

The substitution of Ca^{2+} with Mn^{2+} was previously reported to maintain the glass NC, since both are divalent ions [51] and therefore should have a comparable effect on the bioactivity [36]. Moreover, during the melting process, a portion of the Mn^{2+} ions can be oxidized to Mn^{3+} [52–54], and the coexistence of Mn in two oxidation states, as Mn^{2+} [34,37] or as Mn^{3+} [55], can lead to variation in properties such as coordination number, ligand field strength and optical absorption.

Therefore, the aim of this work is to substitute Ca^{2+} by Mn^{2+} in increasing quantities up to 4 mol% MnO. The glass systems are based on the 45S5 glass (46.1 SiO_2 - 24.4 Na_2O - 26.9 CaO - 2.6 P_2O_5 mol% [5]) and its phosphate free counterpart (called N25C25S50 glass), as described by Kokubo and co-workers (50 SiO_2 - 25 Na_2O - 25 CaO mol%) [56]. In addition, the influence of glass synthesis in a reducing atmosphere is evaluated with particular emphasis given to the structural role of Mn^{2+}/Mn^{3+} and the correlation between glass composition and *in vitro* bioactivity. The antioxidant activity is assessed by quantification of CMA and SOD enzymes.

2. Materials and methods

2.1. Glass synthesis

Table 1 shows the melt-derived bioactive glass series modified by molar substitution of CaO for MnO (0.5, 1.0, 2.0 and 4.0 mol%) produced in oxidizing (air) and reducing (N_2/H_2) atmospheres. Glasses were prepared by mixing SiO_2 (>99.0%), Na_2CO_3 (>99.0%), $CaCO_3$ (>99.0%), $NaPO_3$ (pure grade) and $MnCO_3$ (>99.5) all from Carl Roth, Germany. 45S5 based glasses are labelled as "H xMn" while the phosphate free series are labelled as "K xMn", where x is the MnO content in mol%. For each composition, raw materials were weighed and mixed with the aid of alumina balls before being transferred into a Pt crucible and covered with a Pt lid. A preheating step at 600 °C for 30 min was carried out to avoid foaming, after which the glass was melted at 1340 °C for 1 h. The melt was then water-quenched to obtain a frit and dried in an oven at 100 °C overnight. Glass powders were obtained by grinding the frit with an agate pestle. The powders were sieved to a particle size range between 125 and 250 μm and stored in a desiccator until further use.

In addition, a selection of Mn-containing bioactive glasses based on compositions 45S5 (0.5 or 1.0 mol% MnO) and N25C25S50 (1.0 mol% MnO) were prepared by melting in a reducing atmosphere (N_2/H_2 90:10) within an electric furnace to avoid oxidation of Mn^{2+} to Mn^{3+} at 1340 °C for 1 h. Melts were quenched onto a block using a graphite stamp to obtain samples. The samples are named as "H xMn_red" or "K xMn_red". Samples with 1 mol% MnO (H 1.0Mn_red and K 1.0Mn_red) were not visually homogeneous, probably owing to partial crystallization during the melting process, as confirmed by XRD. Hence, these were not processed further.

2.2. Chemical characterization

Compositional analysis of the glass powders (125–250 μm size range) was performed by X-ray fluorescence (XRF) spectroscopy with a PW 1480 instrument (Philips, Netherlands). Argon methane mix was used as the inert gas. An error of <0.7% was calculated after quantitative analysis obtained from calibration with silicate references containing Mn.

Thermal analysis was performed by differential scanning calorimetry (DSC) with a PT-1600 instrument (Linseis, Germany). Glass powders (90 mg/125–250 μm) were heated at 10 °C/min in a platinum crucible in two steps: from RT to 580 °C, cooling down to 150 °C, followed by heating up to 1000 °C. All measurements were corrected with a background analysis carried out with an empty platinum crucible.

Temperature-Programmed Reduction (TPR) is a characterization technique widely used to determine the reduction properties of bulk and/or supported metal oxides as temperature is linearly increased in a

Table 1
Experimental composition (mol%) of the synthesized samples obtained by XRF analysis and nominal values (in parenthesis). An error <0.7% was calculated from calibration curves.

Glass	SiO_2	Na_2O	CaO	P_2O_5	MnO
H	46.3 (46.1)	24.1 (24.4)	27.1 (26.9)	2.5 (2.6)	–
H 0.5Mn	46.3 (46.1)	24.1 (24.4)	26.5 (26.4)	2.6 (2.6)	0.5 (0.5)
H 1.0Mn	46.3 (46.1)	24.1 (24.4)	26.1 (25.9)	2.5 (2.6)	1.0 (1.0)
H 2.0Mn	46.2 (46.1)	24.0 (24.4)	25.2 (24.9)	2.6 (2.6)	2.0 (2.0)
H 4.0Mn	45.6 (46.1)	24.5 (24.4)	23.3 (22.9)	2.6 (2.6)	4.0 (4.0)
K	50.0 (50.0)	25.6 (25.0)	24.4 (25.0)	–	–
K 0.5Mn	49.9 (50.0)	25.4 (25.0)	24.2 (24.5)	–	0.5 (0.5)
K 1.0Mn	49.9 (50.0)	25.4 (25.0)	23.8 (24.0)	–	0.9 (1.0)
K 2.0Mn	49.9 (50.0)	25.2 (25.0)	22.9 (23.0)	–	2.0 (2.0)
K 4.0Mn	49.8 (50.0)	24.9 (25.0)	21.3 (21.0)	–	4.0 (4.0)
H 0.5Mn_red	46.5 (46.1)	24.2 (24.4)	26.1 (26.4)	2.7 (2.6)	0.5 (0.5)
H 1.0Mn_red	45.4 (46.1)	24.6 (24.4)	26.1 (25.9)	2.8 (2.6)	1.1 (1.0)
K 1.0Mn_red	48.5 (50.0)	25.9 (25.0)	24.5 (24.0)	–	1.1 (1.0)

reducing flow. TPR analyses are usually carried out using a standardized experimental protocol and conditions such as solid mass, flow rate, reducing/oxidizing concentration and heating rate [57]. In particular, this technique was reported to successfully investigate the $MnO_2 \rightarrow MnO$ reduction on bulk manganese oxide catalysts [58].

In this study H_2-TPR was conducted in a ChemiSorb 2750 (Micromeritics, USA) equipped with a thermal conductivity detector (TCD). The glass powder (250 mg, 125–250 μm) was placed in a quartz reactor, degassed at 200 °C under a 20 mL/min N_2 flow and reduced under a 20 mL/min H_2/N_2 (10% *v/v*) flow at a heating rate of 10 °C/min from RT up to 900 °C. The TCD signal was then converted to concentration of active gas (H_2) using a level calibration. The H_2 consumption was calibrated using TPR of Ag_2O at the same experimental conditions. The fraction of Mn^{3+} is calculated according to (1):

$$Mn^{3+}/Mn_{total}(\%) = (H_2(mmol/g)*2/(Mn_{total}(mmol/g))*100 \quad (1)$$

While the occurring, chemical reaction is represented by:

$$2\ Mn^{3+} + H_2 \rightarrow 2\ Mn^{2+} + 2H^+$$

X-ray diffraction (XRD) analyses were performed on crystallized glass samples obtained performing a thermal treatment (2 h) at crystallization temperature (T_c) on glass sample powders. The measures were done using a Panalytical X'Pert Pro XRD (Malvern Panalytical, Netherlands), with Ni-filtered Cu Kα radiation (λ = 1.54060 Å). A generator voltage of 40 kV and a tube current of 40 mA was employed. The conditions for data collections were $20 < 2\theta < 60°$ range and step size 0.033°. X-ray diffraction patterns of the glasses before and after immersion in Tris buffer solution and SBF were collected using the same instrument. Diffraction patterns were collected at RT in the 15–55° 2θ range, with a step size of 0.033°.

Infrared spectra of all glasses were collected using attenuated total reflection (ATR) Fourier transform infrared spectroscopy (FT-IR; Agilent Cary 630 ATR FT-IR Spectrometer, Agilent Technologies GmbH, Germany), to qualitatively characterize the glass structure before and after immersion in Tris buffer solution and SBF to detect apatite formation. The spectra were collected from 4000 to 400 cm^{-1} with a 2 cm^{-1} resolution and 32 scans per measurement.

Optical absorption spectra of all glasses were recorded in the 250–650 nm range (JASCO V-570 double-beam UV–Vis–NIR spectrophotometer, JASCO, USA) with the implementation of a 60 mm integrating sphere element (JASCO, USA) required for analysis on glass powders. This technique was used to qualitatively characterize the Mn oxidation state when incorporated in the glasses and to analyse its redox behaviour during glass immersion in H_2O_2 for catalase mimetic activity (CMA).

2.3. Immersion studies

In vitro bioactivity was evaluated in SBF and Tris buffer solutions, with both being prepared following a protocol described in the literature [59]. The immersion tests were carried out by soaking 75 mg of glass powders (125–250 μm, 3 independent replicates) in 50 mL of SBF solution or 0.062 mol/L tris(hydroxymethyl)aminomethane-HCl buffer solution (Tris buffer) for 1, 4, 7, 14 and 28 d. Samples were maintained in a shaking incubator at 37 °C at 60 rpm before filtering [60]. Blank samples consisting of 50 mL of either of these solutions were used as controls. The elemental concentration of the ions released into Tris buffer solution at each time-point was obtained by inductively coupled plasma optical emission spectroscopy (ICP-OES Varian Liberty 150, Agilent Technologies, Germany). XRD and ATR FT-IR spectroscopy were used to identify the presence of apatite on the glass surface after immersion.

pH measurements were performed using a portable pH-meter SevenGo Starter-Kit SG2-ELK (Mettler-Toledo, USA) calibrated before each set of measurements using pH 7.01 and 10.01 standard solutions (Hanna Instruments, Germany).

2.4. Antioxidant activity

The antioxidant activity of the glasses was measured by their CMA and SOD mimetic activity. The CMA method has been previously described in detail [25], and was performed by soaking 100 mg of glass powder (125–250 μm, n = 3) in 20 mL of H_2O_2 1 mol/L and maintained on a shaking plate at 37 °C and 60 rpm. H_2O_2 1 mol/L blank solutions were measured at each time-point (1, 4 and 7 d) to normalise results considering the spontaneous degradation of H_2O_2. The antioxidant activity for each glass was determined by quantification of the peroxide residue in solution through permanganatometric titration (n = 2).

Conversely, the SOD method is not standardized for bioactive glasses, and therefore a previously reported procedure developed by Ukeda et al. [61] was adapted in two different protocols to understand whether the catalytic decomposition of $O_2^{\bullet}$ anions occurs homogeneously in solution or heterogeneously on the glass surface. The first procedure is referred as "homogeneous" because the potential enzymatic activity originates from the species released from the glass into deionized water during the incubation step. This protocol consists of placing 100 mg of glass powder (125–250 μm) into a 15 mL PP centrifuge tube (Sigma-Aldrich, Italy) with 5 mL of deionized water. The centrifuge tube was kept in a shaking incubator at 37 °C and 120 rpm for 1 h. Afterwards, the tube was centrifuged at 1000 rpm for 10 min and the supernatant was filtered using a 0.45 μm Acrodisc® syringe filter (Sigma-Aldrich, Italy), and then used for the SOD test as proposed by the measurement kit (19160 SOD determination kit, Sigma Aldrich). The second protocol is referred as "heterogeneous" because the potential enzymatic activity originates directly from the glass bulk. The test was carried out by placing 50 mg of glass powder (125–250 μm) and using it directly with the measurement kit as per manufacturer instructions. After each procedure, optical absorption was measured using UV–Vis spectrophotometry (JASCO V-570, USA) and the inhibition rate % (I.R. %) was calculated to quantify SOD activity [62].

Statistical analysis was performed using OriginPro2019 Statistics App. One-way analysis of variance (ANOVA) and Bonferroni multiple comparisons was used with $p < 0.05$ defined as the level of statistical significance.

3. Results

Glassy materials were obtained for both series (H *x*Mn and the K *x*Mn), and substitution of Ca by Mn gave a purple-like tone to the glasses, with colour intensity increasing with Mn content. This was associated with the presence of Mn^{3+} ions [63], owing to the $MnCO_3$ decomposition. The thermal process occurs via various steps [64], with Mn^{2+} being the stable redox state above 1030 °C. However, an incomplete decomposition of Mn_3O_4 to MnO may explain the presence of Mn^{3+} ions. In contrast, a yellow tone was observed for one of the glasses melted in reducing atmosphere (H 0.5Mn_red), supporting the avoided oxidation of Mn^{2+}. Samples with higher Mn content (H 1.0Mn_red and K 1.0Mn_red) were not completely transparent and visually not homogeneously in colour when melted in a N_2/H_2 atmosphere. This was associated with the partial crystallization of the glasses, which was later confirmed by XRD.

The experimental compositions of all synthesized glasses analysed by XRF agree with the nominal ones (Table 1).

The effect of Mn^{2+} ions on the glass colour was analysed by UV–Vis spectroscopy (Fig. 1). As reported in the literature for other silicate glasses [65,66], Mn^{2+} has a weak absorption band at around 415–430 nm corresponding to the spin-forbidden $^6A_1 \rightarrow {}^4A_1$ transition that confers the pale-yellow colour. By contrast, Mn^{3+} presents an absorption band at around 470–500 nm, corresponding to the $^5Eg \rightarrow {}^5T_{2g}$ transition, which is about one-hundred times more intense than the Mn^{2+} band and confers the purple colour. Fig. 1 shows the UV–Vis spectra for all the

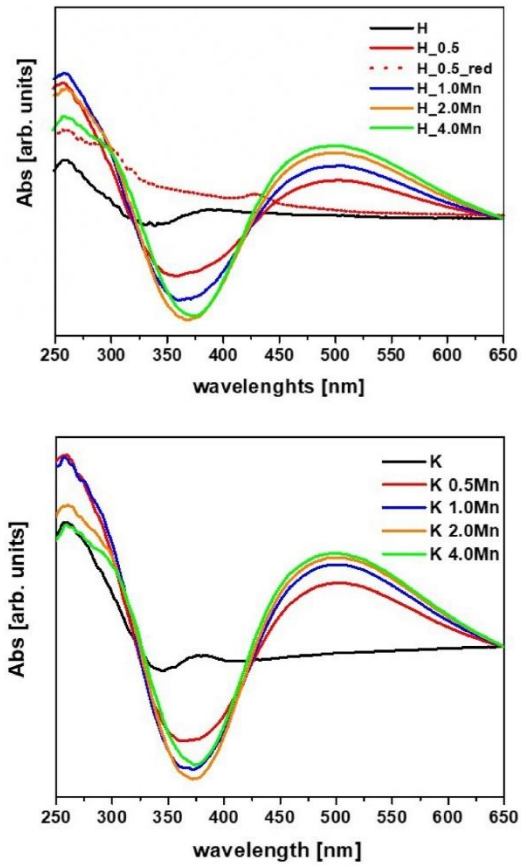

Fig. 1. Total reflectance UV–Vis spectra of glass powders with increasing Mn content upper panel: H *x*Mn; bottom panel: K *x*Mn.

glasses, where the main band in the visible region is positioned at 500 nm and it is assigned to Mn^{3+}. However, the weak band positioned at 430 nm, corresponding to Mn^{2+}, was detected for the 45S5 glass with 0.5 Mn mol% produced in a reducing atmosphere. Therefore, we could consider that in both glass series the Mn^{3+} band, by having a higher absorption coefficient, overlaps and disguises the Mn^{2+} signal [66].

In this study, the H_2-TPR technique was implemented to characterize the oxidation state of Mn [67]. For this, XPS was used to provide surface related information, while H_2-TPR also provided bulk related information. A study on Ce containing bioactive glasses pointed out that XPS characterization only showed evidence of a surface occurring reaction between the powder and the H_2O_2 solution [24].

Hence, in this study we have chosen to characterize by H_2-TPR the glasses with the higher Mn content (H 4.0Mn and K 4.0Mn) and their Mn free versions. Fig. 2a shows the H_2-TPR profile for H4.0Mn and K4.0Mn glasses. The final H_2-consumption (mmol/g) was determined as the difference between the redox behaviour of the glasses with and without MnO. Therefore, it was possible to obtain the value that exclusively corresponds to the effect of MnO in the glass composition. This analysis showed that the change in oxidation state occurs between 200 and 700 °C. H_Mn showed the highest H_2 consumption with two peaks at 270 and 350 °C, suggesting that the presence of P_2O_5 in the glass composition induces a higher fraction of Mn^{3+} when compared with K_4.0Mn.

The temperature range of Mn^{3+} reduction (200–700 °C) is slightly higher with respect to that found for Mn_2O_3 in the literature [68]. This was associated with the amorphous character of the studied materials. The calculated fraction of Mn^{3+} was 10% for H 4.0Mn and 5% for K 4.0Mn, assuming that the H_2-consuption is due to the complete reduction of Mn^{3+} to Mn^{2+}. This result was confirmed by the UV–Vis analysis performed after H_2-TPR (Fig. 2b). Here, an intensity reduction of the 500 nm Mn^{3+} absorption band was observed. Moreover, the Mn^{2+} spin-forbidden transition band at 430 nm also appears to be a weak band.

Figure S1a, S1b and Fig. 3a show the XRD patterns of the glasses, confirming their amorphous character (H *x*Mn and K *x*Mn), and therefore that Mn was successfully incorporated in the glass network. Conversely, the samples melted in a reducing atmosphere (H 1.0Mn_red and K 1.0Mn_red) were partially crystallized to $Na_2CaSi_2O_6$[69] (Fig. 3a–b). Since it was not possible to obtain glassy samples for these compositions, no further characterization was carried out owing to the differences in ion release that result from partially crystallized samples when compared with their glass counterpart [70,71].

Fig. 4 shows the DSC curves for the H *x*Mn and K *x*Mn glasses. The general trend of decreasing T_g with increasing Mn content was observed for both series. Nonetheless, this effect was not considered within the K

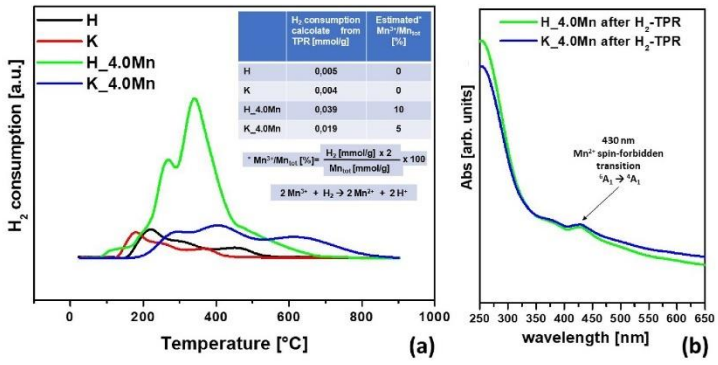

Fig. 2. (a) H_2-TPR profile measured between 25 and 900 °C for H and K glass series with and without Mn (4 mol%). (b) Total reflectance UV–Vis spectra after H_2-TPR analysis of Mn containing glasses H 4.0Mn and K 4.0Mn.

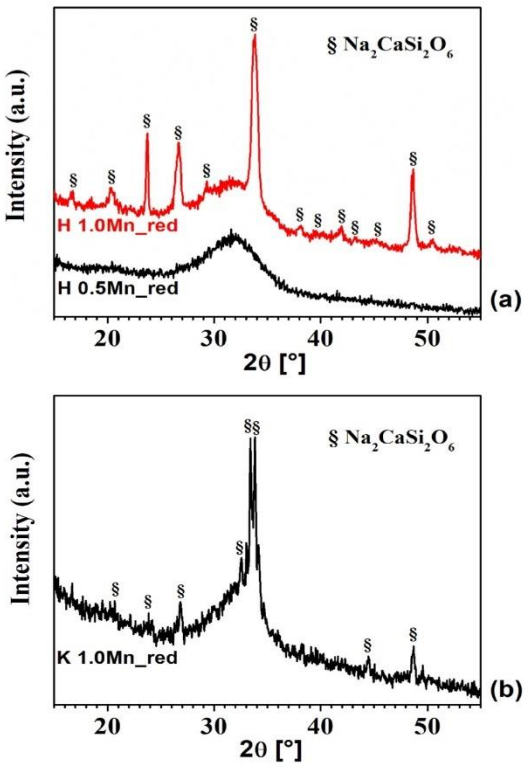

Fig. 3. (a) XRD powder patterns of H 0.5Mn_red and H 1.0Mn_red glasses, and (b) K 1.0Mn_red glass; (§) = $Na_2CaSi_2O_6$. (For interpretation of the references to colour in this figure legend, the reader is referred to the Web version of this article.)

series varying up to 1.0 Mn mol% since differences would fall within the instrumental error. Even if both Mn^{2+} and Mn^{3+} act as modifier ions [34,37,49], but with differ effect on glass network. The substitution of Ca^{2+} with Mn^{3+} leads to lower network connectivity, because of the formation of larger numbers of non-bridging oxygens (NBOs), which can be expected to cause a decrease of T_g. However, Mn^{3+} can also be expected to form stronger bonds to oxygen compared to Ca^{2+} or Mn^{2+} (bond strength z/a, Mn^{3+} (coord. 6) = 1.50 *vs* Mn^{2+} (coord. 6) = 0.92 and Ca^{2+} (coord. 6) = 0.85 [72]), and this can be expected to increase T_g. In average, this value was higher for P_2O_5 free glasses with Mn content up to 1 mol%. This difference was associated to its NC (2.00 vs. 2.12) leading to a less cross-linked structure. The addition of P_2O_5 re-polymerises the silicate network as Ca and Na have a higher affinity with the phosphate groups [73].

For both the H *x*Mn and K *x*Mn glass series, crystallization temperature (T_c) did not significantly change with Mn content, except for H 4.0Mn, which showed a lower T_c. One possible explanation could be that glasses with up to 2 mol% of MnO crystallise to comparable phases, whereas the decrease of T_c at 4 mol% MnO in the H xMn glass series may indicate that a different crystalline phase is formed, or that an interaction with the phosphate phase occurs. In general, the T_c of the H *x*Mn series is higher than T_c of the K *x*Mn series, owing to the presence of the phosphate phase that increases the disorder in the network and, thus, hinders the mobility of ions to form crystals. This observation was confirmed by XRD analysis performed on H 2.0Mn, H 4.0Mn and

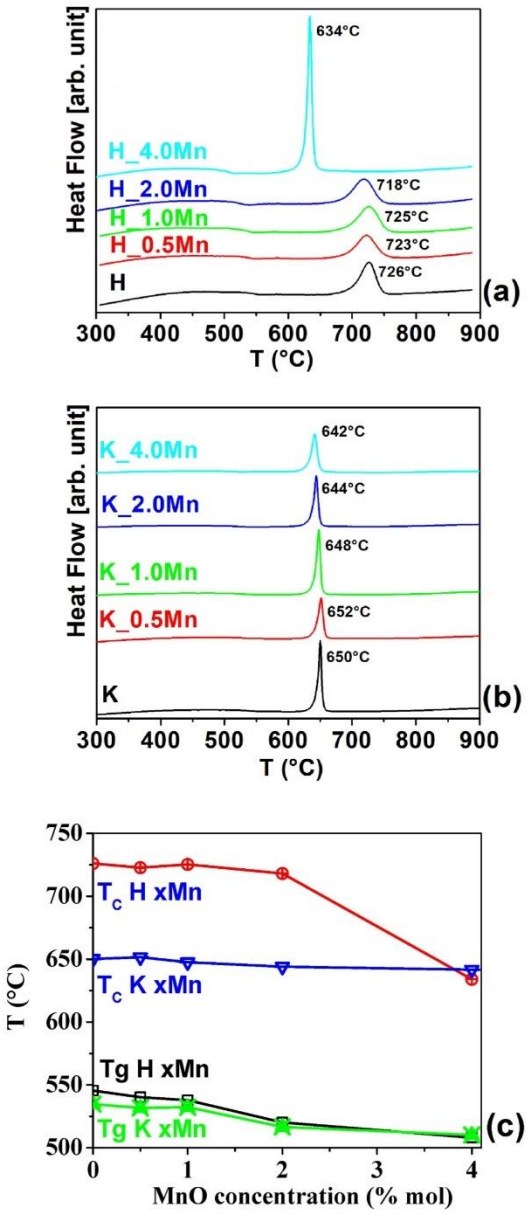

Fig. 4. DSC curves showing crystallization temperature (T_c) of glasses (a) H *x*Mn and (b) K *x*Mn glass series. (c) Glass transition (T_g) and crystallization temperatures (T_c) as a function of MnO concentration.

K4.0Mn glassy powder after thermal treatment at T_c, respectively, for 2 h. The introduction of 4.0% of MnO in the H system promoted the formation of the crystal phase β-$NaCaPO_4$ (Fig. 5).

The processing window (T_c–T_g) is larger for the phosphate containing glasses (H *x*Mn) resulting in reduced tendency to crystallise when compared with the K *x*Mn series, making synthesis and further glass

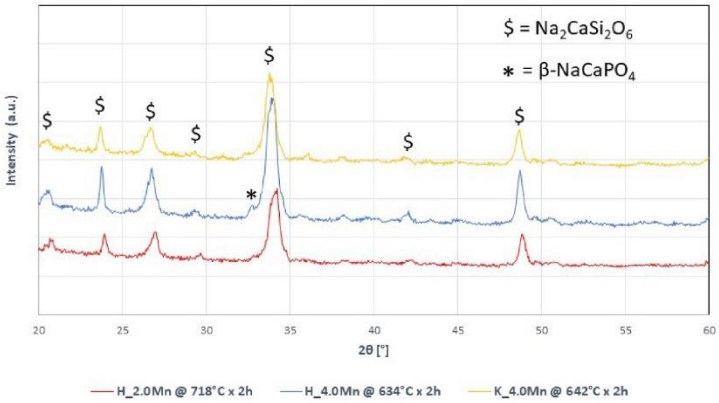

Fig. 5. XRD powder patterns of H 2.0Mn, H 4.0Mn and K 4.0Mn samples after 2 h of thermal treatment at T_c crystallization temperature.

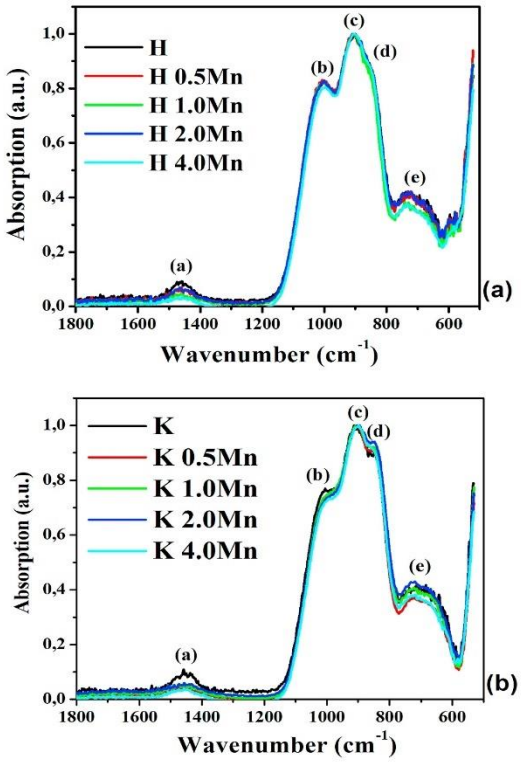

Fig. 6. Normalized ATR FT-IR absorption spectra of (a) H *x*Mn and (b) K *x*Mn glass series. The assignment of bands labelled (a), (b), (c), (d) and (e) to vibration modes is shown in Supplementary Table S1.

processing more difficult for the latter [74].

Fig. 6 shows the normalized ATR FT-IR spectra of the glasses (Fig. 6a and b). The weak band at 1450 cm^{-1} (CO_3^{2-} asymmetric stretching, Table S1) is caused by a surface aging process that leads to carbonatation [75]. The band positioned at 850 cm^{-1}, associated with Si–O–2NBOs, has a higher intensity in the K *x*Mn series compared to the H xMn series, as a consequence of the latter having a higher BOs/NBOs ratio (Table 2) due to the higher content of network modifiers. This was explained by the presence of phosphate in the 45S5 type compositions, because, despite these glasses having a higher molar quantity of modifier ions compared to the SiO_2 content than the P_2O_5 free composition, some of these are associated to the phosphate phase, leading to a lower number of SiO_4 tetrahedra with two NBOs. In the H *x*Mn series the BO/NBO ratio is larger than in the K *x*Mn series (Table 2), which is reflected in the calculated network connectivity [76] value of glass H, this being 2.12 [77] respect to a value of 2.00 for the phosphate free glass (K).

The structural role of Mn in the H *x*Mn and K *x*Mn glass series was qualitatively studied by calculating the ratio between the absorption intensity of the Si–O–Si band and the NBO bands (Si-O-NBO and Si–O–2NBO bands) and analysing changes with the amount of MnO (Fig. 6). For further discussion, both ratios $Abs_{Si\text{-}O\text{-}Si}/Abs_{Si\text{-}O\text{-}NBO}$ and $Abs_{Si\ O\ Si}/Abs_{Si\ O\ 2NBO}$ will be labelled as "$Abs_{BO/NBO}$ ratio" since a similar trend was observed (Table 2).

It is well known that Ca^{2+} acts as a modifier ion in the glass structure. Assuming that both Mn^{2+} and Mn^{3+} act as modifier ions by replacing Ca^{2+}, the BO/NBO molar ratio would not be expected to change in the presence of Mn^{2+}, as both metal ions have the same charge leading to the formation of two NBOs for charge-balancing. On the other hand, molar substitution of Ca^{2+} with Mn^{3+} could be expected to increase the number of NBOs needed to charge balance, and the BO/NBO ratio would then be expected to decrease. According to the results presented in Table 2, the $Abs_{BO/NBO}$ ratio slightly decreased within the K *x*Mn series with increasing Mn content. This trend can be explained by the presence of small amounts of Mn^{3+} ions, as detected by H_2-TPR analysis, acting as modifiers. On the other hand, the $Abs_{BO/NBO}$ ratio did not vary significantly with Mn content in the H *x*Mn series. A noticeable decrease of the $Abs_{BO/NBO}$ ratio is detected only for H 4.0Mn glass compared to Mn-free glass, which could be explained with the effect previously described for the K *x*Mn series.

The influence of Mn in both glass series with respect to *in vitro* apatite formation was tested after immersion in Tris buffer or SBF solution, in combination with pH measurement and ionic concentration with immersion time.

Fig. 7a–e show the ATR FT-IR spectra of the H *x*Mn glasses before and after immersion in Tris buffer solution. The release of modifier ions (Na^+ and Ca^{2+}) and the formation of an amorphous silica gel layer on the glass surface are related to the bands positioned between 1140 and 1270 and 800 cm^{-1}, which are associated to Si–O–Si stretching and Si–O–Si

Table 2
Normalized FTIR absorbance attributed to Si–O–Si, Si-O-NBO and Si–O–2NBO bands and their ratio relative of spectra reported in Fig. 5.

Glass	$Abs_{Si\text{-}O\text{-}Si}$	$Abs_{Si\text{-}O\text{-}NBO}$	$Abs_{Si\text{-}O\text{-}2NBO}$	$Abs_{Si\text{-}O\text{-}Si}/Abs_{Si\text{-}O\text{-}NBO}$	$Abs_{Si\text{-}O\text{-}Si}/Abs_{Si\text{-}O\text{-}2NBO}$
H	0.82	0.99	0.89	0.83	0.92
H 0.5Mn	0.82	0.99	0.88	0.83	0.94
H 1.0Mn	0.82	0.99	0.86	0.83	0.95
H 2.0Mn	0.83	1.00	0.89	0.83	0.93
H 4.0Mn	0.80	1.00	0.89	0.80	0.90
K	0.76	1.00	0.89	0.76	0.85
K 0.5Mn	0.74	1.00	0.91	0.74	0.82
K 1.0Mn	0.75	1.00	0.92	0.75	0.81
K 2.0Mn	0.74	1.00	0.94	0.74	0.78
K 4.0Mn	0.73	1.00	0.92	0.73	0.79

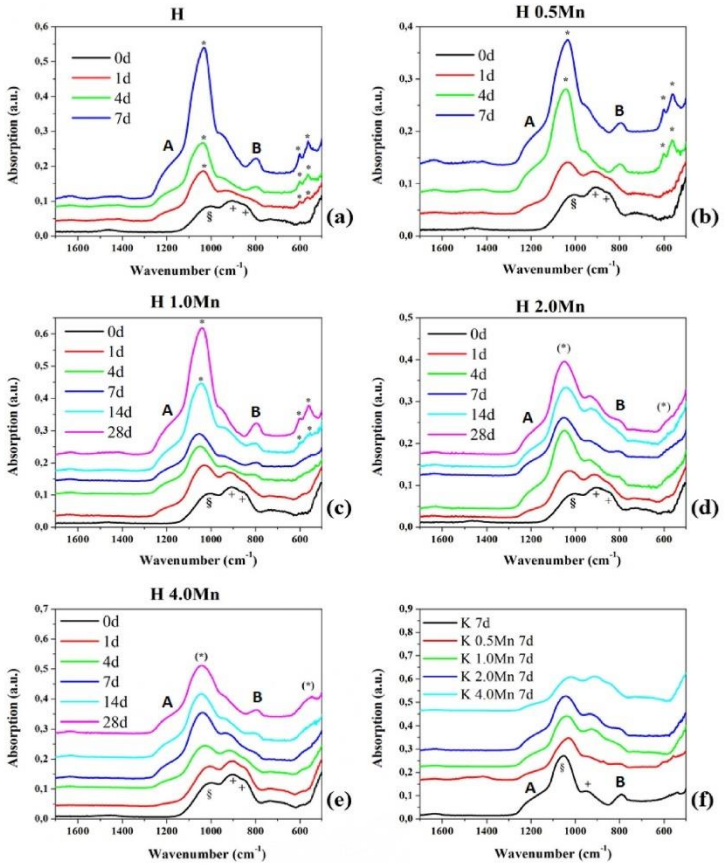

Fig. 7. (a–e) ATR FT-IR absorption spectra of H *x*Mn glass series before and after immersion in Tris buffer solution. (f) ATR FT-IR absorption spectra of K *x*Mn glass series after 7 d of immersion in Tris buffer solution. The assignment of bands labelled Λ, B, §, +, (*) and * to vibration modes is shown in Supplementary Table S2 [75, 94,95].

bending modes, respectively. The ion release occurrence is then confirmed by an increase in the intensity of the BO band with a simultaneous decrease of the NBO band (Table S2). These changes can be observed for the H series with Mn content up to 2.0 mol% after 1 d of immersion, while this change was observed later (4 d) for the H 4.0Mn glass. The formation of the apatite layer is considered as an indication of *in vitro* bioactivity, which was confirmed with the split band at 560–565 and 600-605 cm^{-1} together with a sharp band positioned between 1035 and 1050 cm^{-1} (Table S2). Apatite formation was detected for glass H (45S5) after 1 d of immersion, while 0.5 and 1.0 mol% Mn contents increased the onset to 4 and 14 d respectively. For samples with higher MnO content (2.0 and 4.0 mol% MnO), the formation of the amorphous calcium phosphate layer was detected only after 28 d.

Fig. 7f shows the ATR FT-IR spectra of the K *x*Mn glasses after

immersion in Tris buffer solution for 7 d. Here, apatite formation is not feasible, as neither the glass nor the immersion medium contains phosphate. The spectra only show the characteristic bands related to cation (Na^+ and Ca^{2+}) release and the formation of an amorphous silica gel layer on the surface. For the glass with the maximum Mn content (K 4.0Mn), these two steps appeared to be delayed.

Fig. 8 shows the relative ion concentrations in Tris buffer solution after immersion for up to 28 d. The concentration of Si, Na, Ca, P and Mn ions in the Tris buffer solution before glass immersion was lower than the limit of quantification of the ICP-OES instrument, meaning that this solution did not contribute to the ion concentration measured at later time points. For this reason, no normalization with respect to initial values detected in the blank samples was necessary. Na concentration was considered to indicate the glass degradability in solution since other ions like Si, Ca and P are involved in the silica gel formation and apatite precipitation.

Similarly, such ion release was clearly seen by ICP analysis (Fig. 8) with a variation of relative Na % in solution varying from 80% to approximately 55% with increasing Mn content. This suggests that the incorporation of Mn increases the glass durability, probably caused by the replacement of Ca^{2+}-O bonds with stronger Mn^{2+}-O or Mn^{3+}-O bonds. Na^+ and Ca^{2+} release in Tris buffer solution was lower for H *x*Mn series when compared with K *x*Mn after 7 d of immersion. This is probably due to the lower NC (or lower BO/NBO ratio, Table 2) of the K *x*Mn glasses in comparison with H *x*Mn glasses [71] According to this, Mn release was higher for the K *x*Mn series with respect to H *x*Mn series, with a maximum of nearly 20 and 10% MnO relative ion concentration, respectively.

Fig. 8 shows the ATR FT-IR spectra and XRD patterns of H *x*Mn and K *x*Mn glasses at different immersion times in SBF solution. Results suggested that the incorporation of Mn into the glasses lowered their ability to induce apatite precipitation [35]. Individual peaks in the XRD pattern were not detected, which is typical for bioactive glasses owing to the high degree of substitution in the apatite lattice and to the nanometre-size of the crystals [78]. The shape of the XRD patterns of samples with low or no Mn content in the H *x*Mn series are typical for apatite formation on bioactive glass surfaces. This agrees with the appearance of the characteristic split band in ATR FT-IR for these compositions. Combined results showed that H *x*Mn glasses with MnO up to 1 mol% induced apatite formation within 7 d. Conversely, glasses with higher MnO content, such as H 2.0Mn glass, induced apatite formation within 28 d, and H 4.0Mn glass did not form apatite within the duration of the experiment. Regarding the K *x*Mn series, K and K 0.5Mn glasses formed apatite within 7 d. Apatite formation was observed on K 1.0Mn glass surface within 14 d, while higher MnO content appeared to inhibit its formation within the duration of the experiment. Fig. 9 shows that the apatite formation, denoted by the presence of the CaP associated stretching band, is faster for the H *x*Mn glass series, suggesting the fundamental role of phosphate in the glass for the precipitation of this phase. The ATR FT-IR bands attributed to carbonate (CO_3^{2-}) incorporation into apatite (1500-1400 and 870 cm^{-1}) were not intense. Therefore, it was not possible to neither confirm nor exclude the formation of carbonated apatite. However, calcite ($CaCO_3$) formation [69] was detected by XRD on the K glass series with up to 2.0 MnO mol%, which could explain the formation of carbonated apatite or calcite precipitation.

Table 3 shows the CMA results with the molar H_2O_2 concentration before and after immersion at various time points. During CMA experiments, gas formation at the glass powder surface was observed, which was most likely related to O_2 decomposition from H_2O_2. The data reported in Table 3 highlight that increasing Mn content in the glass has a beneficial effect on the H_2O_2 decomposition rate. These results showed that there is a positive correlation between the Mn and the CMA of both H *x*Mn and K *x*Mn glass series, conferring them an increase of antioxidant activity properties.

At earlier time points (1 and 4 d) significant differences between the H_2O_2 decomposition activities were observed between the glass series. For example, there was a H_2O_2 concentration difference of slightly over 30% after 1 d between the best performing glass in the H series (H 4.0 Mn) and the composition with the highest H_2O_2 concentration from the K series (K_0.5 Mn). Interestingly, K *x*Mn glass series showed total H_2O_2 decomposition after 4 d of immersion, while a comparable result was only obtained after 7 d for the H *x*Mn glasses.

The glass melted in a reduced atmosphere (H 0.5Mn_red) seemed to

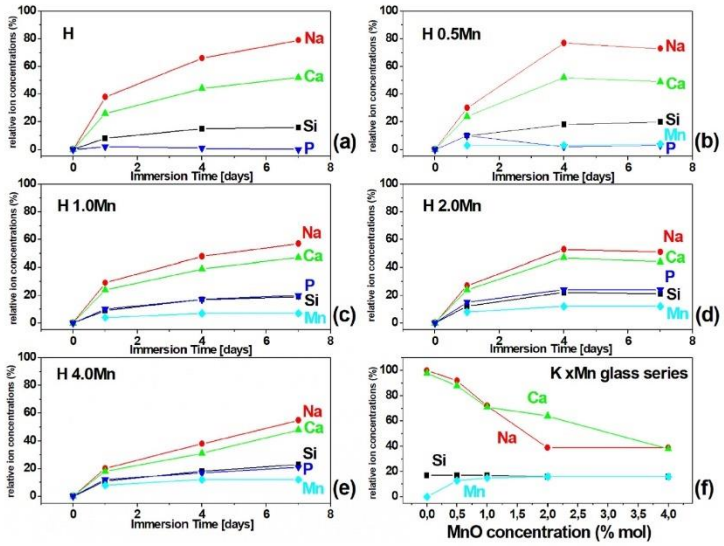

Fig. 8. Relative concentrations (percentage of the ions present in the untreated glass; in %) present in Tris buffer solution for the H (a), H 0.5Mn (b), H 1.0Mn (c), H 2.0Mn (d) and H 4.0Mn (e) glasses after 1, 4, or 7 d of immersion and for the K *x*Mn glass series (f) after 7 d of immersion.

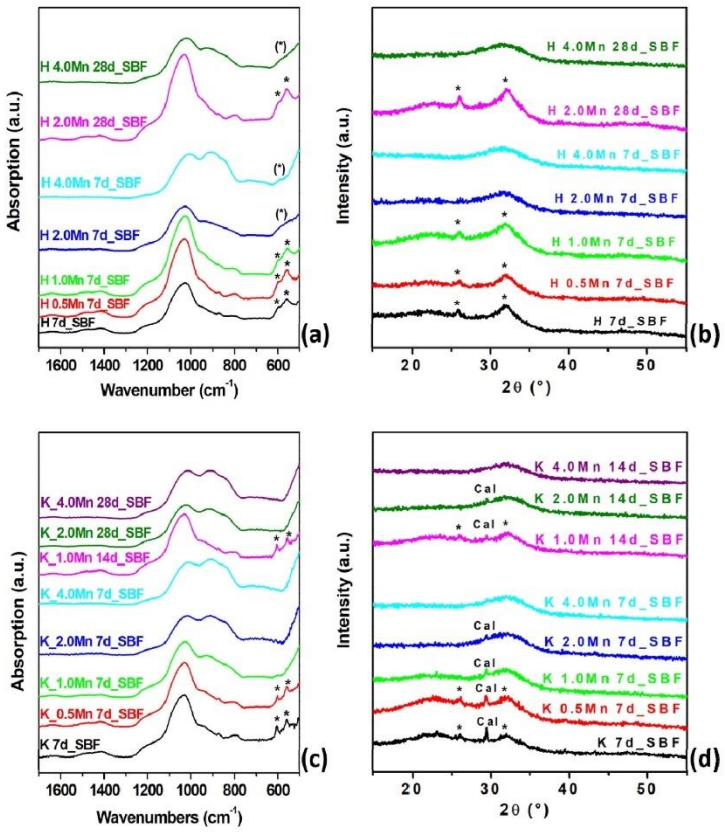

Fig. 9. ATR FT-IR absorption spectra (left, section (a) and (c)) and XRD patterns (right, section (b) and (d)) of glasses in the H *x*Mn and K *x*Mn series at different times of immersion in SBF. Band and reflection labels: * HA/HCA, (*) amorphous CaP layer and Cal Calcite ($CaCO_3$). Curves were stacked to facilitate observing the features without overlapping.

Table 3
Molar H_2O_2 concentration (mol/L) and ratios between the UV–Vis absorption intensity of the Mn^{3+} (500 nm) and Mn^{2+} bands (406 nm) ($AbsMn^{3+}/AbsMn^{2+}$) before (0 d) and after (at 1, 4 or 7 d) immersion in 1.00 mol/L H_2O_2 solution (± standard deviation, n = 3).

	0d		1d		4d		7d	
	H_2O_2 conc. [mol/L]	$AbsMn^{3+}/AbsMn^{2+}$	H_2O_2 conc. [mol/L]	$AbsMn^{3+}/AbsMn^{2+}$	H_2O_2 conc. [mol/L]	$AbsMn^{3+}/AbsMn^{2+}$	H_2O_2 conc. [mol/L]	$AbsMn^{3+}/AbsMn^{2+}$
Blank (H_2O_2)	1.00 ± 0.00	–	1.00 ± 0.00	–	1.00 ± 0.00	–	0.99 ± 0.01	–
H	1.00 ± 0.00	0.96	0.97 ± 0.02	1.06	0.87 ± 0.00	1.07	0.86 ± 0.02	1.07
H 0.5Mn	1.00 ± 0.00	1.81	0.81 ± 0.01	1.78	0.15 ± 0.01	1.51	0.07 ± 0.00	1.55
H 0.5Mn_red	1.00 ± 0.00	0.79	0.74 ± 0.02	0.88	0.23 ± 0.02	0.90	0.09 ± 0.00	0.90
H 1.0Mn	1.00 ± 0.00	2.26	0.69 ± 0.01	1.98	0.09 ± 0.02	1.59	0.02 ± 0.00	1.65
H 2.0Mn	1.00 ± 0.00	2.69	0.70 ± 0.01	2.28	0.07 ± 0.00	1.77	0.02 ± 0.00	1.75
H 4.0Mn	1.00 ± 0.00	2.70	0.64 ± 0.01	2.37	0.08 ± 0.00	1.98	0.02 ± 0.01	1.85
K	1.00 ± 0.00	1.06	0.97 ± 0.02	1.07	0.95 ± 0.02	1.06	0.90 ± 0.04	1.07
K 0.5Mn	1.00 ± 0.00	2.27	0.42 ± 0.01	1.87	0.03 ± 0.00	1.83	0.00 ± 0.00	1.73
K 1.0Mn	1.00 ± 0.00	2.77	0.20 ± 0.01	2.20	0.00 ± 0.00	2.10	0.00 ± 0.00	1.98
K 2.0Mn	1.00 ± 0.00	2.99	0.08 ± 0.00	2.44	0.00 ± 0.00	2.28	0.00 ± 0.00	2.30
K 4.0Mn	1.00 ± 0.00	2.72	0.11 ± 0.00	2.38	0.00 ± 0.00	2.18	0.00 ± 0.00	2.12

catalyse H_2O_2 decomposition better than their air-melt counterpart for early time points (1 d); however, this trend changed at the fourth day of the measurement. Moreover, when comparing the base glasses, no significant CMA was observed up to day 7, which further confirms that for these glass systems there is an association between Mn and an early-stage antioxidant effect. Therefore, it is possible that such approach

would be useful for the tissue regenerative process occurring after a biomaterial is implanted.

pH changes during CMA experiments were measured since it is known that an alkaline pH also enhances the H_2O_2 decomposition rate [79] (Supplementary Table S3). pH increased from 4.20 (1.00 mol/L H_2O_2) to 8–9 after 1 d, stabilizing to 8.5–9 after 4 d. In bioactive type glasses, the pH increase is caused by ion exchange (Na^+) from the glass for protons in solution. Moreover, pH change is also caused by H_2O_2 decomposition since it is a weak acid in solution. However, the effect of pH increase on the H_2O_2 decomposition rate seems negligible at least up to pH 9, as glass K reaches this value at 7 d after immersion while the H_2O_2 concentration is comparably high (0.90 mol/L). Supplementary Figs. S2 and S3 and **S4** show the UV–Vis absorption spectra of all glasses before and after CMA tests. The Mn^{3+} band (at 500 nm) and Mn^{2+} band (at 406 nm) intensity ratios were calculated (Table 3) to quantitatively extract information concerning the Mn ion role in H_2O_2 decomposition. This ratio was solely considered as a qualitative parameter that could aid to identify a trend in Mn^{3+}/Mn^{2+} molar ratio changes. The $AbsMn^{3+}/AbsMn^{2+}$ ratios of the glasses without Mn (H glass and K glass) do not significantly change over time. Nonetheless, for Mn containing glasses (Table 3), this value decreased over time, reaching a stable value when H_2O_2 was completely decomposed at 4 d (K *x*Mn) and 7 d (H *x*Mn glass). Conversely, for glasses melted under a reducing atmosphere, this ratio did not significantly change with immersion time.

I.R. % obtained with the "homogeneous" protocol were negligible, meaning that in these conditions there was no evidence of SOD mimetic activity for any of the glasses (see Table 4). In contrast, I.R. % values obtained with the "heterogeneous" protocol showed significant differences between samples ($p < 0.05$). Substitution of Mn by Ca produced an increase of SOD mimetic activity ranging between approximately 25% (K 4.0Mn) and 40% (H 1.0Mn). No significant difference in SOD mimetic activity was detected between Mn content ranging between 0.5 and 2.0 mol% for the H *x*Mn series. However, a significant decrease of at least 8% occurred between this group and the highest Mn content sample (H 4.0 Mn). A similar trend was observed for the K *x*Mn series, where significant differences were only observed between K - K 4.0Mn and the group corresponding to Mn content between 0.5 and 2.0 Mn.

4. Discussion

When incorporated into silicate glass systems, Mn exists either as Mn^{3+} or Mn^{2+} since higher oxidation states such as 4+ and 7+ are possible but very unlikely [66]. In the studied glass systems, Mn appears to be incorporated as Mn^{2+} and Mn^{3+}, as shown by UV–Vis spectra (Fig. 1). Owing to the significantly larger extinction coefficient of Mn^{3+} (25–100 L cm^{-1} mol^{-1}) compared to Mn^{2+} (0.2–0.5 L cm^{-1} mol^{-1}) [80], the Mn^{3+} band at 500 nm is approximately one-hundred times more intense when compared to that attributed to Mn^{2+} (at 406 nm) if equimolar quantities of the two oxidation states are present. The presence of Mn^{2+} is confirmed by the slight changes in the BO/NBO ratio measured by ATR FT-IR (Fig. 6) and H_2-TPR (Fig. 2), suggesting that only a small Mn fraction is present as Mn^{3+}, and that most of Mn is present as Mn^{2+}, which structural role is very similar to that of Ca^{2+}. If the MnO content in the glass structure is low (0.5 mol %) and the melting is performed in a reducing atmosphere (N_2/H_2 90:10), it is possible to avoid its oxidation and obtain a glass with only Mn^{+2} ions.

Replacing Ca^{2+} with Mn^{2+}/Mn^{3+} ions decreases the possibility of the glass surface to be carbonated, and this result follows the logical progression of phase stability in oxygenated aqueous systems predicted from Eh—pH diagrams for the Mn system [81], where Mn carbonate is unstable compared to hausmannite (Mn_3O_4) and manganite (MnO(OH)) [82].

The substitution of Ca^{2+} with Mn^{2+} in both glass systems leads to the introduction of stronger oxygen bonds, which increase the network compactness. This was confirmed by the higher durability in Tris buffer solution (Table 2) with increasing Mn content. On the other hand, the presence of a small quantity of Mn^{3+} that replaced Ca^{2+} slightly decreases the network connectivity. This was confirmed by a lowering in the glass transition temperature (T_g, Fig. 4) and the slight decrease of the BO/NBO molar ratio shown by FT-IR measurements (Fig. 6) with increasing Mn content. The T_g trend was opposite to the one detected by Gaddam et al. [83], where the introduction of Mn increased T_g. The Authors concluded that Mn ions were mainly present as Mn^{3+}interstitial ions located in the glass network, thus avoiding the silicate network depolymerization. This would therefore suggest that Mn ions (Mn^{2+} and Mn^{3+}) entered the network as modifier ions in our glass system [84].

The role of Mn ions also affected the degradation behaviour. Replacing Ca by Mn in the glass leads to a decrease of Ca^{2+} ions available at the surface, and as both Mn^{2+} and Mn^{3+} ions form stronger bonds with oxygen compared to Ca^{2+} ions, the tendency to react with water decreases. It has also been described by a computational approach that Mn increases the chemical durability of the glass due to its affinity to orthophosphate units, leading to insoluble metal-phosphate segregated areas [85]. Similarly, this was experimentally observed by FTIR: as Mn content increased, the P–O band intensity decreased, correlated to Mn charge balancing the phosphate groups. It would be also possible that Mn^{+3}, when it is present, could readily balance the phosphate unit, leaving Ca and Na ions to depolimerise the silicate network.

The obtained results agree with a lower rate of Ca^{2+} release into Tris buffer solution (52% *vs* 44% of Ca for H and H 4.0Mn, respectively, as well as 98% *vs* 38% of Ca for K and K 4.0Mn, respectively, Fig. 8). The substitution of Mn delayed the apatite inducing ability of the glasses, as formation of an amorphous calcium phosphate and apatite requires the release of Ca^{2+} ions. In Tris buffer and SBF solutions, glasses with 0.5 mol% of MnO formed apatite within 7 d, which was comparable to the base glasses (H and K), while for higher MnO contents apatite formation was delayed. This result agrees with those by Miola et al. [34] that showed how Mn incorporation slightly delayed bioactivity in SBF. These results are also in agreement with those by Srivastava et al., [35] where a content of MnO_2 higher than 1% resulted in a decrease of HCA formation, while the bioactivity was maintained for lower substitutions. However, the substitution in the study was carried out in wt% instead of mol%, which has been reported to have an important effect in structural changes of the glass [50].

The onset of apatite formation also differs between the two series, with glasses in the H *x*Mn series forming apatite slightly faster (7 d) than glasses in the K *x*Mn (14 d) one. Similar trends were observed in a previous study [24,86] where H and K bioactive glasses were modified by the incorporation of CeO_2. The substitution of cerium ions (Ce^{3+} and Ce^{4+}) caused a delay in apatite formation, but this was attributed to cerium ions forming a very low soluble $CePO_4$ phase, which inhibits apatite formation for glasses with more than 3.6 mol% CeO_2.

Relative calcium concentrations in Tris buffer solution were lower for the H *x*Mn series than for the K *x*Mn series. This may be explained

Table 4
Inhibition rate (I.R. %) values with relative standard deviations for the H *x*Mn and K *x*Mn glass series and glasses H 0.5Mn_red. I.R.% is an index of the SOD mimetic activity of a glass following a homogeneous and heterogeneous protocol.

Glass	"homogeneous"	"heterogeneous"
H	−2.3 ± 2.4	52.7 ± 4.1
H 0.5Mn	−0.8 ± 3.5	90.7 ± 0.4
H 0.5Mn_red	−4.3 ± 4.4	91.2 ± 0.8
H 1.0Mn	−1.3 ± 4.9	92.7 ± 0.9
H 2.0Mn	−2.0 ± 1.8	90.7 ± 1.6
H 4.0Mn	−0.4 ± 4.7	81.1 ± 0.1
K	3.6 ± 2.3	41.2 ± 2.9
K 0.5Mn	−2.3 ± 2.7	88.5 ± 0.3
K 1.0Mn	1.2 ± 3.8	89.2 ± 0.1
K 2.0Mn	0.5 ± 1.6	83.8 ± 1.5
K 4.0Mn	2.6 ± 2.2	68.6 ± 5.2

with the interaction between orthophosphate (PO_4^{3-}) and calcium ions in glasses of the H *x*Mn series, possibly delaying calcium release compared to phosphate-free glasses in the K *x*Mn series. In sol-gel glasses a similar effect has been related to non-homogeneous Ca ions distribution in phosphate-containing compositions [87,88]. These studies showed that although the glasses were amorphous, a certain level of intermediate distance order was detected, which greatly influenced the *in vitro* and *in vivo* reactivities. In the ternary Si–Ca–P sol-gel glasses, the Ca^{2+} ions were mainly out of the silicate network and bonded to phosphate. However, these structural considerations differ for melt-derived phospho-silicate glasses and the lower calcium concentrations for H *x*Mn compared to K *x*Mn glasses may be related to the higher NC of the H *x*Mn glasses, slowing down interaction with water [89]. The main factor is here probably apatite precipitation. Ion concentrations in solution are not only affected by ion release from the glass, which increases ion concentrations, but also by precipitation of low solubility phases such as apatite, which decreases the concentrations of the involved ions. During immersion in simulated physiological solutions, availability of phosphate is typically the limiting factor for apatite precipitation [78,90]. Consequently, in K *x*Mn series, calcium does not precipitate as apatite, increasing its concentration in solution, whereas, in the H *x*Mn series, calcium, phosphate and ions such as hydroxyl or carbonates are consumed during apatite formation.

During immersion of H *x*Mn and K *x*Mn glasses in SBF, K *x*Mn glasses showed formation of calcite while this phase was not detected for H *x*Mn glasses (Fig. 9). From a thermodynamic viewpoint, apatite precipitation is favoured compared to calcite precipitation, because of its lower solubility ($Ksp_{HA} = 1{\bullet}10^{-58}$; $Ksp_{Calcite} = 3.8{\bullet}10^{-9}$) [91,92]. However, calcite precipitation is kinetically faster than HA/HCA deposit formation, due to a more favourable combination of one Ca^{2+} ion with one CO_3^{2-} ion to form calcite ($CaCO_3$) in comparison to five Ca^{2+} ions, three PO_4^{3-} ions and one hydroxyl ion to form hydroxyapatite $Ca_5(PO_4)_3(OH)$. Thus, the fast release of Ca^{2+} ions from K *x*Mn glasses owing to the lower network connectivity compared to H *x*Mn glasses, and the absence of phosphate phase in K *x*Mn glasses, caused the solubility product of calcite to be reached when K *x*Mn glasses were soaked in SBF, and therefore its presence as a precipitate. Additionally, the delay in apatite formation for K *x*Mn glasses (Fig. 9) is related to the absence of phosphate ions in their composition, making the SBF solution the only phosphate source for formation of either apatite or an amorphous calcium phosphate layer.

The enzyme-mimicking activity of the glasses derives from replacing Ca^{2+} with Mn, which can interconvert between two oxidation states (Mn^{2+} and Mn^{3+}). This redox behaviour can catalyse the decomposition of H_2O_2 through both a reduction reaction (production of H_2O) and an oxidation reaction (production of O_2) (Tables 3 and 4). During CMA experiments, the $AbsMn^{3+}/AbsMn^{2+}$ ratio decreased and reached comparable values at 7 d of immersion in H_2O_2 for all H *x*Mn and K *x*Mn glasses. Therefore, a comparable Mn^{3+}/Mn^{2+} molar ratios would be expected. This tendency to reach an optimum molar ratio of the redox couple involved in the decomposition of H_2O_2 was already shown in our previous study on the CMA of Ce-containing silicate and phospho-silicate bioactive glasses [86]. Once the optimum Ce^{4+}/Ce^{3+} molar ratio was reached, the maximum rate of H_2O_2 decomposition was observed. The existence of an optimum Mn^{3+}/Mn^{2+} molar ratio of the redox couple involved in the decomposition of H_2O_2 was supported by the CMA results for glasses melted in a reducing atmosphere, as the H_2O_2 decomposition rate for these systems seemed higher than those of the glasses melted in air. We can therefore conclude that the best Mn^{3+}/Mn^{2+} molar ratio is lower than that obtained during synthesis of H *x*Mn and K *x*Mn glasses in air. H 0.5Mn_red glass, which contains almost exclusively Mn^{2+}, showed a better CMA performance compared to H 0.5Mn glass, and we can thus conclude that the presence of Mn^{2+} is essential for the enzymatic activity. Regarding the SOD mimetic activity, the Mn-containing glasses showed a very high enzymatic-like activity, without significant difference between the H 0.5Mn_red and H 0.5Mn glass systems. We have confirmed that for the SOD activity, presence of Mn ions on the glass surface are of importance (Mn^{2+} and Mn^{3+}, see Table 4), because of the heterogeneous catalytic mechanism that involves these ions in the superoxide radical decomposition.

For the Mn free glasses (H and K), the mechanism of the heterogeneous catalysis of H_2O_2 decomposition is still unclear, but it is known that it occurs through catalysis by surface defects and the formation of radical species, such as the hydroxyl (•OH) or hydroperoxyl radical (•OOH) [93]. For silica-based materials, Si–O• radicals present on the material surface can disrupt H_2O_2 molecules, forming •OH and •OOH radicals. Therefore, the higher the surface area of the material is the higher the rate of H_2O_2 decomposition, for which particle size might also have an important influence in this process. Nonetheless, particle size was reported as an important factor in the oxidative stress process, since smaller particles with increased surface area were described to produce higher quantities of ROS [1].

This pathway is less effective than decomposition of H_2O_2 by interconversion of multivalent cations such as Mn, but it becomes relevant for Mn free glasses at later time points (7 d), when the glass surface area is higher after exchange reactions with the solution, leading to depolymerization of the silica network and formation of silanol (Si–OH) groups. However, surface defects in soda-lime-silicate glasses could react with other species before acting as active sites for H_2O_2 decomposition. Consequently, introduction of Mn in the glass structure improves H_2O_2 decomposition by a different mechanism.

The correlation between the antioxidant activity and the phosphate content is interesting because of the clear differences encountered between the glass series. A similar effect was found for Ce-containing bioactive glasses [86], suggesting that the presence of phosphate inhibits the enzyme-like activity of inorganic materials. A possible explanation could be attributed to an increased stability of Mn ions charge balancing phosphate units, which takes them from the Mn^{2+}/Mn^{3+} redox equilibrium, an essential step for CMA to occur. This effect was also reflected on the Mn relative ion concentration for both series.

5. Conclusions

Manganese as MnO was successfully incorporated into soda lime silicate glasses with (H) and without phosphate (K) by molar substitution of CaO (≤4 mol%). Characterization by ATR FT-IR and UV–Vis spectroscopies suggested that Mn^{2+}/Mn^{3+} ions have a comparable structural role as modifiers in the glass silicate network similarly to Ca^{2+} ions. Manganese was mainly present as Mn^{2+}; however, a fraction of Mn^{2+} ions oxidized to Mn^{3+} ions by melting oxidizing conditions (air). By contrast, Mn oxidation to a +3 state was avoided when melting under a reducing atmosphere (N_2/H_2 90:10) for the 45S5 type glass with 0.5 mol% MnO content. Replacing Ca^{2+} ions with Mn^{2+}/Mn^{3+} ions leads to the introduction of stronger bonds with oxygen, resulting in increased network compactness. This structural change results in the increased stability in Tris buffer solution with increasing Mn content. As a result, the onset of apatite formation was delayed with increasing Mn content during *in vitro* testing. Interestingly, this trend was reversed for the antioxidant activity of the glasses, with their CMA and SOD mimetic activity improved by Mn content. This was associated with the interconversion between Mn^{2+} and Mn^{3+} oxidation states, which can decompose both hydrogen peroxide and superoxide anion through heterogeneous redox reactions. A distinct improvement in this effect was obtained for the phosphate free glass series (K), for which an early-stage oxidative stress effect reduction was observed for glass with more than 1 mol% MnO, showing the important role of P_2O_5 on the ability of Mn to undergo this interconversion. Further studies will then be required to understand the associated structural mechanisms. Consequently, a balance between the optimum phosphate and Mn content is of importance as to maximise the antioxidant potential of the glass while maintaining its bioactivity expressed as the onset of apatite formation. The results

here presented can be then used as a basis to further explore the benefits of incorporating Mn as an antioxidant ion when developing bioactive glasses for bone replacement applications.

Funding

This study was funded by the German Research Foundation (DFG; grant BR 4608/7-1).

Declaration of competing interest

The authors declare that they have no known competing financial interests or personal relationships that could have appeared to influence the work reported in this paper.

Acknowledgements

The authors would like to thank Steffi Ebbinghaus for dilatometry measurements and Steffen Müller for DSC measurements. MA acknowledges Erasmus+ funding, which made his research stay in Germany possible. DSB and ATCJ acknowledge funding by the German Research Foundation (DFG; grant BR 4608/7-1).

Appendix A. Supplementary data

Supplementary data to this article can be found online at https://doi.org/10.1016/j.ceramint.2023.10.091.

References

[1] P.-A. Mouthuy, S.J.B. Snelling, S.G. Dakin, L. Milković, A.Č. Gašparović, A.J. Carr, N. Žarković, Biocompatibility of implantable materials: an oxidative stress viewpoint, Biomaterials 109 (2016) 55–68, https://doi.org/10.1016/j.biomaterials.2016.09.010.

[2] L.L. Hench, R.J. Splinter, W.C. Allen, T.K. Greenlee, Bonding mechanisms at the interface of ceramic prosthetic materials, J. Biomed. Mater. Res. 5 (6) (1971) 117–141, https://doi.org/10.1002/jbm.820050611.

[3] L.L. Hench, The story of Bioglass, J. Mater. Sci. Mater. Med. 17 (11) (2006) 967–978, https://doi.org/10.1007/s10856-006-0432-z.

[4] V. Mourino, J.P. Cattalini, A.R. Boccaccini, Metallic ions as therapeutic agents in tissue engineering scaffolds: an overview of their biological applications and strategies for new developments, J. R. Soc. Interface 9 (68) (2012) 401–419, https://doi.org/10.1098/rsif.2011.0611.

[5] D.S. Brauer, Bioactive glasses-structure and properties, Angew. Chem. Int. Ed. 54 (14) (2015) 4160–4181, https://doi.org/10.1002/anie.201405310.

[6] R. Hill, An alternative view of the degradation of Bioglass, J. Mater. Sci. Lett. 15 (13) (1996) 1122–1125, https://doi.org/10.1007/BF00539955.

[7] R.G. Hill, D.S. Brauer, Predicting the bioactivity of glasses using the network connectivity or split network models, J. Non-Cryst. Solids 357 (24) (2011) 3884–3887, https://doi.org/10.1016/j.jnoncrysol.2011.07.025.

[8] M. Bellantone, H.D. Williams, L.L. Hench, Broad-spectrum bactericidal activity of Ag2O-doped bioactive glass, Antimicrob. Agents Chemother. 46 (6) (2002) 1940–1945, https://doi.org/10.1128/AAC.46.6.1940-1945.2002.

[9] M. Bellantone, N.J. Coleman, L.L. Hench, Bacteriostatic action of a novel four-component bioactive glass, J. Biomed. Mater. Res. 51 (3) (2000) 484–490, https://doi.org/10.1002/1097-4636(20000905)51:3<484::AID-JBM24>3.0.CO;2-4.

[10] M. Yazdimamaghani, D. Vashaee, S. Assefa, K.J. Walker, S.V. Madihally, G. A. Köhler, L. Tayebi, Hybrid macroporous gelatin/bioactive-glass/nanosilver scaffolds with controlled degradation behavior and antimicrobial activity for bone tissue engineering, J. Biomed. Nanotechnol. 10 (6) (2014) 911–931, https://doi.org/10.1166/jbn.2014.1783.

[11] J.J. Blaker, S.N. Nazhat, A.R. Boccaccini, Development and characterisation of silver-doped bioactive glass-coated sutures for tissue engineering and wound healing applications, Biomaterials 25 (7–8) (2004) 1319–1329, https://doi.org/10.1016/j.biomaterials.2003.08.007.

[12] S.P. Valappil, D. Ready, E.A.A. Neel, D.M. Pickup, W. Chrzanowski, L.A. O'Dell, R. J. Newport, M.E. Smith, M. Wilson, J.C. Knowles, Antimicrobial gallium-doped phosphate-based glasses, Adv. Funct. Mater. 18 (5) (2008) 732–741, https://doi.org/10.1002/adfm.200700931.

[13] S.P. Valappil, D. Ready, E.A. Abou Neel, D.M. Pickup, L.A. O'Dell, W. Chrzanowski, J. Pratten, R.J. Newport, M.E. Smith, M. Wilson, J.C. Knowles, Controlled delivery of antimicrobial gallium ions from phosphate-based glasses, Acta Biomater. 5 (4) (2009) 1198–1210, https://doi.org/10.1016/j.actbio.2008.09.019.

[14] E. Dietrich, H. Oudadesse, A. Lucas-Girot, M. Mami, In *vitro* bioactivity of melt-derived glass 46S6 doped with magnesium, J. Biomed. Mater. Res. A 88A (4) (2009) 1087–1096, https://doi.org/10.1002/jbm.a.31901.

[15] P.J. Meunier, C. Roux, E. Seeman, S. Ortolani, J.E. Badurski, T.D. Spector, J. Cannata, A. Balogh, E.-M. Lemmel, S. Pors-Nielsen, R. Rizzoli, H.K. Genant, J.-Y. Reginster, The effects of strontium ranelate on the risk of vertebral fracture in women with postmenopausal osteoporosis, N. Engl. J. Med. 350 (5) (2004) 459–468, https://doi.org/10.1056/NEJMoa022436.

[16] V. Aina, G. Malavasi, A. Fiorio Pla, L. Munaron, C. Morterra, Zinc-containing bioactive glasses: surface reactivity and behaviour towards endothelial cells, Acta Biomater. 5 (4) (2009) 1211–1222, https://doi.org/10.1016/j.actbio.2008.10.020.

[17] L. Courthéoux, J. Lao, J.-M. Nedelec, E. Jallot, Controlled bioactivity in zinc-doped Sol–Gel-derived binary bioactive glasses, J. Phys. Chem. C 112 (35) (2008) 13663–13667, https://doi.org/10.1021/jp8044498.

[18] W. Fan, R. Crawford, Y. Xiao, Enhancing in vivo vascularized bone formation by cobalt chloride-treated bone marrow stromal cells in a tissue engineered periosteum model, Biomaterials 31 (13) (2010) 3580–3589, https://doi.org/10.1016/j.biomaterials.2010.01.083.

[19] D.S. Brauer, N. Karpukhina, M.D. O'Donnell, R.V. Law, R.G. Hill, Fluoride containing bioactive glasses: effect of glass design and structure on degradation, PH and apatite formation in simulated body Fluid, Acta Biomater. 6 (8) (2010) 3275–3282, https://doi.org/10.1016/j.actbio.2010.01.043.

[20] E. Lynch, D.S. Brauer, N. Karpukhina, D.G. Gillam, R.G. Hill, Multi-component bioactive glasses of varying fluoride content for treating dentin hypersensitivity, Dent. Mater. 28 (2) (2012) 168–178, https://doi.org/10.1016/j.dental.2011.11.021.

[21] J.P. Pessan, N.S. Al-Ibrahim, M.A.R. Buzalaf, K.J. Toumba, Slow-release fluoride devices: a literature review, J. Appl. Oral Sci. 16 (4) (2008) 238–244, https://doi.org/10.1590/S1678-77572008000400003.

[22] P. Christel, A. Meunier, J.-M. Dorlot, J.-M. Crolet, J. Witvoet, L. Sedel, P. Boutin, Biomechanical compatibility and design of ceramic implants for orthopedic surgery, Ann. N. Y. Acad. Sci. 523 (1 Bioceramics) (1988) 234–256, https://doi.org/10.1111/j.1749-6632.1988.tb38516.x.

[23] V. Cannillo, A. Sola, Potassium-based composition for a bioactive glass, Ceram. Int. 35 (8) (2009) 3389–3393, https://doi.org/10.1016/j.ceramint.2009.06.011.

[24] V. Nicolini, E. Gambuzzi, G. Malavasi, L. Menabue, M.C. Menziani, G. Lusvardi, A. Pedone, F. Benedetti, P. Luches, S. D'Addato, S. Valeri, Evidence of catalase mimetic activity in Ce^{3+}/Ce^{4+} doped bioactive glasses, J. Phys. Chem. B 119 (10) (2015) 4009–4019, https://doi.org/10.1021/jp511737b.

[25] S. Jebahi, H. Oudadesse, H. el Feki, T. Rebai, H. Keskes, P. Pellen, A. el Feki, Antioxidative/oxidative effects of strontium doped bioactive glass as bone graft. In vivo assays in ovariectomised rats, J. Appl. Biomed. 10 (4) (2012) 195–209, https://doi.org/10.2478/v10136-012-0009-8.

[26] C. Wu, W. Fan, Y. Zhu, M. Gelinsky, J. Chang, G. Cuniberti, V. Albrecht, T. Friis, Y. Xiao, Multifunctional magnetic mesoporous bioactive glass scaffolds with a hierarchical pore structure, Acta Biomater. 7 (10) (2011) 3563–3572, https://doi.org/10.1016/j.actbio.2011.06.028.

[27] B.R. Barrioni, E. Norris, S. Li, P. Naruphontjirakul, J.R. Jones, M. de M. Pereira, Osteogenic potential of sol–gel bioactive glasses containing manganese, J. Mater. Sci. Mater. Med. 30 (7) (2019) 86, https://doi.org/10.1007/s10856-019-6288-9.

[28] U. Pantulap, M. Arango-Ospina, A.R. Boccaccini, Bioactive glasses incorporating less-common ions to improve biological and physical properties, J. Mater. Sci. Mater. Med. 33 (1) (2021) 3, https://doi.org/10.1007/s10856-021-06626-3.

[29] J.V. Rau, A. De Stefanis, K. Barbaro, M. Fosca, V.G. Yankova, R. Matassa, S. A. Nottola, Q. Nawaz, M.S. Ali, W. Peukert, A.R. Boccaccini, Adipogenic, chondrogenic, osteogenic, and antimicrobial features of glass ceramic material supplemented with manganese, J. Non-Cryst. Solids 559 (2021), 120709, https://doi.org/10.1016/j.jnoncrysol.2021.120709.

[30] M. Miola, C.V. Brovarone, G. Maina, F. Rossi, L. Bergandi, D. Ghigo, S. Saracino, M. Maggiora, R.A. Canuto, G. Muzio, E. Vernè, In vitro study of manganese-doped bioactive glasses for bone regeneration, Mater. Sci. Eng. C 38 (2014) 107–118, https://doi.org/10.1016/j.msec.2014.01.045.

[31] M. Miola, J. Massera, A. Cochis, A. Kumar, L. Rimondini, E. Vernè, Tellurium: a new active element for innovative multifunctional bioactive glasses, Mater. Sci. Eng. C 123 (2021), 111957, https://doi.org/10.1016/j.msec.2021.111957.

[32] G. El-Damraw, H. Doweidar, H. Kamal, Characterization of new categories of bioactive based tellurite and silicate glasses, Silicon 9 (2017) 503–509, https://doi.org/10.1007/s12633-014-9248-5.

[33] B. Karakuzu-İkizler, P. Terzioğlu, B.S. Oduncu-Tekerek, S. Yücel, Effect of selenium incorporation on the structure and in vitro bioactivity of 45S5 Bioglass, J. Australas. Ceram. Soc. 56 (2) (2020) 697–709, https://doi.org/10.1007/s41779-019-00388-6.

[34] M. Miola, C.V. Brovarone, G. Maina, F. Rossi, L. Bergandi, D. Ghigo, S. Saracino, M. Maggiora, R.A. Canuto, G. Muzio, E. Vernè, In vitro study of manganese-doped bioactive glasses for bone regeneration, Mater. Sci. Eng. C 38 (2014) 107–118, https://doi.org/10.1016/j.msec.2014.01.045.

[35] A.K. Srivastava, R. Pyare, S.P. Singh, *In vitro* bioactivity and physical–mechanical properties of MnO_2 substituted 45S5 bioactive glasses and glass-ceramics, J. Biomater. Tissue Eng. 2 (3) (2012) 249–258, https://doi.org/10.1166/jbt.2012.1043.

[36] B.R. Barrioni, A.C. Oliveira, M. de Fátima Leite, M. de Magalhães Pereira, Sol–gel-derived manganese-releasing bioactive glass as a therapeutic approach for bone tissue engineering, J. Mater. Sci. 52 (15) (2017) 8904–8927, https://doi.org/10.1007/s10853-017-0944-6.

[37] B.R. Barrioni, P. Naruphontjirakul, E. Norris, S. Li, N.L. Kelly, J.V. Hanna, M. M. Stevens, J.R. Jones, M. de M. Pereira, Effects of manganese incorporation on the morphology, structure and cytotoxicity of spherical bioactive glass nanoparticles, J. Colloid Interface Sci. 547 (2019) 382–392, https://doi.org/10.1016/j.jcis.2019.04.016.

[38] Q. Nawaz, M.A.U. Rehman, A. Burkovski, J. Schmidt, A.M. Beltrán, A. Shahid, N. K. Alber, W. Peukert, A.R. Boccaccini, Synthesis and characterization of manganese containing mesoporous bioactive glass nanoparticles for biomedical applications, J. Mater. Sci. Mater. Med. 29 (5) (2018) 64, https://doi.org/10.1007/s10856-018-6070-4.

[39] S. Kapoor, D. Brazete, I.C. Pereira, G. Bhatia, M. Kaur, L.F. Santos, D. Banerjee, A. Goel, J.M.F. Ferreira, Impact of transition metal ions on the structure and bioactivity of alkali-free bioactive glasses, J. Non-Cryst. Solids 506 (2019) 98–108, https://doi.org/10.1016/j.jnoncrysol.2018.12.003.

[40] J.D. Aguirre, V.C. Culotta, Battles with iron: manganese in oxidative stress protection, J. Biol. Chem. 287 (17) (2012) 13541–13548, https://doi.org/10.1074/jbc.R111.312181.

[41] N.A. Law, M.T. Caudle, V.L. Pecoraro, Manganese redox enzymes and model systems: properties, structures, and reactivity, Adv. Inorg. Chem. 46 (1998) 305–440, https://doi.org/10.1016/S0898-8838(08)60152-X. Elsevier.

[42] J.H. Beattie, A. Avenell, Trace element nutrition and bone metabolism, Nutr. Res. Rev. 5 (1) (1992) 167–188, https://doi.org/10.1079/NRR19920013.

[43] F. Lüthen, U. Bulnheim, P.D. Müller, J. Rychly, H. Jesswein, J.G.B. Nebe, Influence of manganese ions on cellular behavior of human osteoblasts in vitro, Biomol. Eng. 24 (5) (2007) 531–536, https://doi.org/10.1016/j.bioeng.2007.08.003.

[44] P.M.C. Torres, S.I. Vieira, A.R. Cerqueira, S. Pina, O.A.B. da Cruz Silva, J.C. C. Abrantes, J.M.F. Ferreira, Effects of Mn-doping on the structure and biological properties of β-tricalcium phosphate, J. Inorg. Biochem. 136 (2014) 57–66, https://doi.org/10.1016/j.jinorgbio.2014.03.013.

[45] W. Fujitani, Y. Hamada, N. Kawaguchi, S. Mori, K. Daito, A. Uchinaka, T. Matsumoto, Y. Kojima, M. Daito, T. Nakano, N. Matsuura, Synthesis of Hydroxyapatite Contining Manganese and its Evaluation of Biocompatibility, 2010, https://doi.org/10.11344/nano.2.37. (Accessed 4 July 2019).

[46] Y.-J. Bae, M.-H. Kim, Manganese supplementation improves mineral density of the spine and femur and serum osteocalcin in rats, Biol. Trace Elem. Res. 124 (1) (2008) 28–34, https://doi.org/10.1007/s12011-008-8119-6.

[47] S. Fujibayashi, A comparative study between in vivo bone ingrowth and in vitro apatite formation on Na2O–CaO–SiO2 glasses, Biomaterials 24 (8) (2003) 1349–1356, https://doi.org/10.1016/S0142-9612(02)00511-2.

[48] G. Malavasi, G. Lusvardi, Composition and morphology effects on catalase mimetic activity of potential bioactive glasses, Ceram. Int. 46 (16) (2020) 25854–25864, https://doi.org/10.1016/j.ceramint.2020.07.067.

[49] P. Pascuta, G. Borodi, N. Jumate, I. Vida-Simiti, D. Viorel, E. Culea, The structural role of manganese ions in some zinc phosphate glasses and glass ceramics, J. Alloys Compd. 504 (2) (2010) 479–483, https://doi.org/10.1016/j.jallcom.2010.05.147.

[50] M.D. O'Donnell, R.G. Hill, Influence of strontium and the importance of glass chemistry and structure when designing bioactive glasses for bone regeneration, Acta Biomater. 6 (7) (2010) 2382–2385, https://doi.org/10.1016/j.actbio.2010.01.006.

[51] N.N. Greenwood, A. Earnshaw, Chemistry of the Elements, second ed., Butterworth-Heinemann, Oxford ; Boston, 1997.

[52] I. Bratu, I. Ardelean, A. Barbu, V. Mih, D. Maniu, G. Botezan, Spectroscopic investigation of some lead phosphate oxide glasses containing manganese ions, J. Mol. Struct. 482–483 (1999) 689–692, https://doi.org/10.1016/S0022-2860(98)00940-5.

[53] D.K. Durga, N. Veeraiah, Role of manganese ions on the stability of ZnF2–P2O5–TeO2 glass system by the study of dielectric dispersion and some other physical properties, J. Phys. Chem. Solid. 64 (1) (2003) 133–146, https://doi.org/10.1016/S0022-3697(02)00273-1.

[54] N.K. Mohan, M.R. Reddy, C.K. Jayasankar, N. Veeraiah, Spectroscopic and dielectric studies on MnO doped PbO–Nb2O5–P2O5 glass system, J. Alloys Compd. 458 (1–2) (2008) 66–76, https://doi.org/10.1016/j.jallcom.2007.04.143.

[55] I. Konidakis, C.-P.E. Varsamis, E.I. Kamitsos, D. Möncke, D. Ehrt, Structure and properties of mixed Strontium–Manganese metaphosphate glasses, J. Phys. Chem. C 114 (19) (2010) 9125–9138, https://doi.org/10.1021/jp101750t.

[56] H. M. Kim, F. Miyaji, T. Kokubo, C. Ohtsuki, T. Nakamura, Bioactivity of Na2O-CaO-SiO2 glasses, J. Am. Ceram. Soc. 78 (9) (1995) 2405–2411, https://doi.org/10.1111/j.1151-2916.1995.tb08677.x.

[57] N.W. Hurst, S.J. Gentry, A. Jones, B.D. McNicol, Temperature programmed reduction, Catal. Rev. 24 (2) (1982) 233–309, https://doi.org/10.1080/03602458208079654.

[58] F. Kapteijn, L. Singoredjo, A. Andreini, J.A. Moulijn, Activity and selectivity of pure manganese oxides in the selective catalytic reduction of nitric oxide with ammonia, Appl. Catal. B Environ. 3 (2–3) (1994) 173–189, https://doi.org/10.1016/0926-3373(93)E0034-9.

[59] L. Müller, F.A. Müller, Preparation of SBF with different HCO3- content and its influence on the composition of biomimetic apatites, Acta Biomater. 2 (2) (2006) 181–189, https://doi.org/10.1016/j.actbio.2005.11.001.

[60] A.L.B. Maçon, T.B. Kim, E.M. Valliant, K. Goetschius, R.K. Brow, D.E. Day, A. Hoppe, A.R. Boccaccini, I.Y. Kim, C. Ohtsuki, T. Kokubo, A. Osaka, M. Vallet-Regí, D. Arcos, L. Fraile, A.J. Salinas, A.V. Teixeira, Y. Vueva, R.M. Almeida, M. Miola, C. Vitale-Brovarone, E. Verné, W. Höland, J.R. Jones, A unified in vitro evaluation for apatite-forming ability of bioactive glasses and their variants, J. Mater. Sci. Mater. Med. 26 (2) (2015) 115, https://doi.org/10.1007/s10856-015-5403-9.

[61] H. Ukeda, D. Kawana, S. Maeda, M. Sawamura, Spectrophotometric assay for superoxide dismutase based on the reduction of highly water soluble tetrazolium salts by xanthine-xanthine oxidase, Biosci. Biotechnol. Biochem. 63 (3) (1999) 485–488, https://doi.org/10.1271/bbb.63.485.

[62] Y. Sheng, I.A. Abreu, D.E. Cabelli, M.J. Maroney, A.-F. Miller, M. Teixeira, J. S. Valentine, Superoxide dismutases and superoxide reductases, Chem. Rev. 114 (7) (2014) 3854–3918, https://doi.org/10.1021/cr4005296.

[63] H. Kappler, Crystal field spectra and geochemistry of transition metal ions in silicate melts and glasses, Am. Mineral. 77 (1992) 62–75.

[64] L. Biernacki, S. Pokrzywnicki, The thermal decomposition of manganese carbonate thermogravimetry and exoemission of electrons, J. Therm. Anal. Calorim. 55 (1) (1999) 227–232, https://doi.org/10.1023/A:1010165029080.

[65] A. Terczynska-Madej, K. Cholewa-Kowalska, M. Laczka, The effect of silicate network modifiers on colour and electron spectra of transition metal ions, Opt. Mater. 32 (11) (2010) 1456–1462, https://doi.org/10.1016/j.optmat.2010.05.024.

[66] A.J. Werner, in: C.R. Bamford (Ed.), Colour Generation and Control in Glass, Elsevier Scientific Publishing Co., Amsterdam and New York, 1977, p. 224, https://doi.org/10.1002/col.5080030317. Price, $34.95. Color Res. Appl. 1978, 3 (3), 156–156.

[67] S.M. Lee, K.H. Park, S.S. Kim, D.W. Kwon, S.C. Hong, Effect of the Mn oxidation state and lattice oxygen in Mn-based TiO_2 catalysts on the low-temperature selective catalytic reduction of NO by NH_3, J. Air Waste Manag. Assoc. 62 (9) (2012) 1085–1092, https://doi.org/10.1080/10962247.2012.696532.

[68] X. Niu, H. Wei, K. Tang, W. Liu, G. Zhao, Y. Yang, Solvothermal synthesis of 1D nanostructured Mn_2O_3 : effect of Ni^{2+} and Co^{2+} substitution on the catalytic activity of nanowires, RSC Adv. 5 (81) (2015) 66271–66277, https://doi.org/10.1039/C5RA14618F.

[69] PCPFWIN, JCPDS International Center for Diffraction Data, Swarthmore, PA, USA, 2002.

[70] K. Hurrell-Gillingham, I.M. Reaney, C.A. Miller, A. Crawford, P.V. Hatton, Devitrification of ionomer glass and its effect on the in vitro biocompatibility of glass-ionomer cements, Biomaterials 24 (18) (2003) 3153–3160, https://doi.org/10.1016/S0142-9612(03)00124-8.

[71] M. Plewinski, K. Schickle, M. Lindner, A. Kirsten, M. Weber, H. Fischer, The effect of crystallization of bioactive Bioglass 45S5 on apatite formation and degradation, Dent. Mater. 29 (12) (2013) 1256–1264, https://doi.org/10.1016/j.dental.2013.09.016.

[72] M.B. Volf, *Chemical Approach to Glass*; Glass Science and Technology, Elsevier, Amsterdam ; New York, 1984.

[73] A. Tilocca, A.N. Cormack, Structural effects of phosphorus inclusion in bioactive silicate glasses, J. Phys. Chem. B 111 (51) (2007) 14256–14264, https://doi.org/10.1021/jp075677o.

[74] J.R. Jones, Review of bioactive glass: from hench to hybrids, Acta Biomater. 9 (1) (2013) 4457–4486, https://doi.org/10.1016/j.actbio.2012.08.023.

[75] M. Cerruti, C. Morterra, Carbonate Formation on bioactive glasses, Langmuir 20 (15) (2004) 6382–6388, https://doi.org/10.1021/la049723c.

[76] J.E. Shelby, Introduction to Glass Science and Technology, second ed., Royal Society of Chemistry, Cambridge, 2005.

[77] D. Sriranganathan, N. Kanwal, K.A. Hing, R.G. Hill, Strontium substituted bioactive glasses for tissue engineered scaffolds: the importance of octacalcium phosphate, J. Mater. Sci. Mater. Med. 27 (2) (2016) 39, https://doi.org/10.1007/s10856-015-5653-6.

[78] M.D. O'Donnell, S.J. Watts, R.G. Hill, R.V. Law, The effect of phosphate content on the bioactivity of soda-lime-phosphosilicate glasses, J. Mater. Sci. Mater. Med. 20 (8) (2009) 1611–1618, https://doi.org/10.1007/s10856-009-3732-2.

[79] W.D. Nicoll, A.F. Smith, Stability of dilute alkaline solutions of hydrogen peroxide, Ind. Eng. Chem. 47 (12) (1955) 2548–2554, https://doi.org/10.1021/ie50552a051.

[80] D. Möncke, M. Papageorgiou, A. Winterstein-Beckmann, N. Zacharias, Roman glasses coloured by dissolved transition metal ions: redox-reactions, optical spectroscopy and ligand field theory, J. Archaeol. Sci. 46 (2014) 23–36, https://doi.org/10.1016/j.jas.2014.03.007.

[81] M. Pourbaix, Atlas of Electrochemical Equilibria in Aqueous Solutions Retrieved, Electronic Books database, 1974.

[82] J.L. Hager, Sorption of manganese and silica by clay and carbonate, Mar. Chem. 9 (3) (1980) 199–209, https://doi.org/10.1016/0304-4203(80)90039-0.

[83] A. Gaddam, H.R. Fernandes, D.U. Tulyaganov, M.J. Pascual, J.M.F. Ferreira, Role of manganese on the structure, crystallization and sintering of non-stoichiometric lithium disilicate glasses, RSC Adv. 4 (26) (2014), 13581, https://doi.org/10.1039/c3ra46393a.

[84] A.K. Varshneya, Chemical strengthening of glass: lessons learned and yet to Be learned: chemical strengthening of glass, Int. J. Appl. Glass Sci. 1 (2) (2010) 131–142, https://doi.org/10.1111/j.2041-1294.2010.00010.x.

[85] G. Malavasi, A. Pedone, The effect of the incorporation of catalase mimetic activity cations on the structural, thermal and chemical durability properties of the 45S5 Bioglass, Acta Mater. 229 (2022), 117801, https://doi.org/10.1016/j.actamat.2022.117801.

[86] V. Nicolini, G. Malavasi, L. Menabue, G. Lusvardi, F. Benedetti, S. Valeri, P. Luches, Cerium-doped bioactive 45S5 glasses: spectroscopic, redox, bioactivity and biocatalytic properties, J. Mater. Sci. 52 (15) (2017) 8845–8857, https://doi.org/10.1007/s10853-017-0867-2.

[87] M. Vallet-Regi, A. Salinas, Role of the short distance order in glass reactivity, Materials 11 (3) (2018) 415, https://doi.org/10.3390/ma11030415.

[88] M. Vallet-Regí, A.J. Salinas, J. Ramírez-Castellanos, J.M. González-Calbet, Nanostructure of bioactive Sol–Gel glasses and Organic–Inorganic hybrids, Chem. Mater. 17 (7) (2005) 1874–1879, https://doi.org/10.1021/cm047956j.

[89] A. Tilocca, A.N. Cormack, Surface signatures of bioactivity: MD simulations of 45S and 65S silicate glasses, Langmuir 26 (1) (2010) 545–551, https://doi.org/10.1021/la902548f.

[90] M. Mneimne, R.G. Hill, A.J. Bushby, D.S. Brauer, High phosphate content significantly increases apatite formation of fluoride-containing bioactive glasses, Acta Biomater. 7 (4) (2011) 1827–1834, https://doi.org/10.1016/j.actbio.2010.11.037.

[91] Y. Zhu, B. Huang, Z. Zhu, H. Liu, Y. Huang, X. Zhao, M. Liang, Characterization, dissolution and solubility of the hydroxypyromorphite–hydroxyapatite solid solution [(PbxCa1−x)5(PO4)3OH] at 25 °C and PH 2–9, Geochem. Trans. 17 (1) (2016) 2, https://doi.org/10.1186/s12932-016-0034-8.

[92] J.W. Morse, A. Mucci, F.J. Millero, The solubility of calcite and aragonite in seawater of 35%. Salinity at 25°C and atmospheric pressure, Geochem. Cosmochim. Acta 44 (1) (1980) 85–94, https://doi.org/10.1016/0016-7037(80)90178-7.

[93] C.M. Miller, R.L. Valentine, Mechanistic studies of surface catalyzed H2O2 decomposition and contaminant degradation in the presence of sand, Water Res. 33 (12) (1999) 2805–2816, https://doi.org/10.1016/S0043-1354(98)00500-4.

[94] H. Aguiar, J. Serra, P. González, B. León, Structural study of sol–gel silicate glasses by IR and Raman spectroscopies, J. Non-Cryst. Solids 355 (8) (2009) 475–480, https://doi.org/10.1016/j.jnoncrysol.2009.01.010.

[95] I. Notingher, J.R. Jones, S. Verrier, I. Bisson, P. Embanga, P. Edwards, J.M. Polak, L.L. Hench, Application of FTIR and Raman spectroscopy to characterisation of bioactive materials and living cells, Spectroscopy 17 (2–3) (2003) 275–288, https://doi.org/10.1155/2003/893584.

Bibliography

1. Hench LL, Ethridge EC. Biomaterials: An Interfacial Approach. Academic Press. 1982. 408 p.

2. Bruck SD. Properties Of Biomaterials In The Physiological Environment. Boca Raton: CRC Press. 2019. 154 p.

3. Ratner BD, curator. Biomaterials science: an introduction to materials in medicine. San Diego: Academic Press. 1996. 484 p.

4. Aggarwal D, Kumar V, Sharma S. Drug-loaded biomaterials for orthopedic applications: A review. Journal of Controlled Release. 2022. 344:113–33 p.

5. Bhardwaj A, Pandey LM. Biomaterials: Types and Applications. Nanoscale Engineering of Biomaterials: Properties and Applications. Springer Nature. 2022. 89–114 p.

6. Meckstroth KR, Darney PD. Implant contraception. Semin Reprod Med. 2001. 19(4):339–54 p.

7. Hench LL, Polak JM. Third-generation biomedical materials. Science. 2002. 295(5557):1014–7 p.

8. Chengyun N, Zhengnan Z, Guoxin T, Ye Z, Chuanbin M. Electroactive polymers for tissue regeneration: Developments and perspectives. Progress in Polymer Science. 2018. 144-162 p.

9. Ning C, Zhou L, Tan G. Fourth-generation biomedical materials. Materials Today. 2015. 19 p.

10. Hench LL. Bioceramics: From Concept to Clinic. Journal of the American Ceramic Society. 1991. 74(7):1487–510 p.

11. Lemons JE. Ceramics: Past, present, and future. Bone. 1996. 19(1, Supplement 1):S121–8 p.

12. Black J. Systemic effects of biomaterials. The biomaterials: silver jubilee compendium. 1984. 27–34 p.

13. Morscher E. The Cementless Fixation of Hip Endoprostheses. Springer Science & Business Media; 2012. 604 p.

14. Hench LL. Bioceramics. Journal of the American Ceramic Society. 1998. 81(7):1705–28 p.

15. Hench LL, Splinter RJ, Allen WC, Greenlee TK. Bonding mechanisms at the interface of ceramic prosthetic materials. Journal of Biomedical Materials Research. 1971. 5(6):117–41 p.

16. Hench LL. The future of bioactive ceramics. J Mater Sci: Mater Med. 2015. 26(2):86 p.

17. De Groot K. Effect of porosity and physicochemical properties on the stability, resorption, and strength of calcium phosphate ceramics. Ann N Y Acad Sci. 1988. 523:227–33 p.

18. Groot K de. Bioceramics Calcium Phosphate. Boca Raton: CRC Press. 2017. 152 p.

19. Wolke JGC, de Blieck-Hogervorst JMA, Dhert WJA, Klein CPAT, de Groot K. Studies on the thermal spraying of apatite bioceramics. JTST. 1992. 1(1):75–82 p.

20. Weiner S, Traub W. Bone structure: from angstroms to microns. FASEB J. 1 febbraio 1992;6(3):879–85.

21. M. M. Stevens and J. H. George. Exploring and Engineering the Cell Surface Interface. Science. 2005. 310 (5751). 1135-1138.

22. Wegst UGK, Bai H, Saiz E, Tomsia AP, Ritchie RO. Bioinspired structural materials. Nat Mater. gennaio 2015;14(1):23–36.

23. Bullough PG. Orthopaedic Pathology. Elsevier Health Sciences. 2009. 600 p.

24. Marotti G. A new theory of bone lamellation. Calcif Tissue Int. 1993. 53 Suppl 1:S47-55; discussion S56.

25. Rho JY, Kuhn-Spearing L, Zioupos P. Mechanical properties and the hierarchical structure of bone. Medical Engineering & Physics. 1998. 20(2):92–102.

26. Florencio-Silva R, Sasso GR, Sasso-Cerri E, Simões MJ, Cerri PS. Basics of Bone Biology. Biomed Res Int. 2015.

27. Forwood MR, Turner CH. The response of rat tibiae to incremental bouts of mechanical loading: A quantum concept for bone formation. Bone. 1994. 15(6):603–9.

28. Salter RB. Textbook of Disorders and Injuries of the Musculoskeletal System: An Introduction to Orthopaedics, Fractures, and Joint Injuries, Rheumatology, Metabolic Bone Disease, and Rehabilitation. Lippincott Williams & Wilkins. 1999. 750 p.

29. Hill PA, Murphy G, Docherty AJ, Hembry RM, Millican TA, Reynolds JJ, et al. The effects of selective inhibitors of matrix metalloproteinases (MMPs) on bone resorption and the identification of MMPs and TIMP-1 in isolated osteoclasts. J Cell Sci. 1994. 107 (Pt 11):3055–64.

30. Halleen JM, Räisänen S, Salo JJ, Reddy SV, Roodman GD, Hentunen TA, et al. Intracellular fragmentation of bone resorption products by reactive oxygen species generated by osteoclastic tartrate-resistant acid phosphatase. J Biol Chem. 1999. 274(33):22907–10.

31. Palumbo C, Palazzini S, Zaffe D, Marotti G. Osteocyte differentiation in the tibia of newborn rabbit: an ultrastructural study of the formation of cytoplasmic processes. Acta Anat (Basel). 1990. 137(4):350–8.

32. Frost HM. In vivo osteocyte death. J Bone Joint Surg Am. 1960. 42-A:138–43.

33. Tatsumi S, Ishii K, Amizuka N, Li M, Kobayashi T, Kohno K, et al. Targeted ablation of osteocytes induces osteoporosis with defective mechanotransduction. Cell Metab. 2007. 5(6):464–75.

34. Aarden EM, Burger EH, Nijweide PJ. Function of osteocytes in bone. J Cell Biochem. 1994. 55(3):287–99.

35. Shimizu H, Sakamoto M, Sakamoto S. Bone resorption by isolated osteoclasts in living versus devitalized bone: differences in mode and extent and the effects of human recombinant tissue inhibitor of metalloproteinases. J Bone Miner Res. 1990. 5(4):411–8.

36. Brezulier D, Chaigneau L, Jeanne S, Lebullenger R. The Challenge of 3D Bioprinting of Composite Natural Polymers PLA/Bioglass: Trends and Benefits in Cleft Palate Surgery. Biomedicines. 2021. 9:1553 p.

37. Hench LL, Wilson J. An Introduction To Bioceramics. World Scientific. 1993. 399 p.

38. Edén M. Structure and Formation of Amorphous Calcium Phosphate and its Role as Surface Layer of Nanocrystalline Apatite: Implications for Bone Mineralization. Materialia.. 2021. 17:101107.

39. Hench LL, Splinter RJ, Allen WC, Greenlee TK. Bonding mechanisms at the interface of ceramic prosthetic materials. Journal of Biomedical Materials Research. 1971. 117-141 p.

40. Kokubo T, Takadama H. How useful is SBF in predicting in vivo bone bioactivity? Biomaterials. 2006. 27(15):2907–15 p.

41. Izquierdo-Barba I, Salinas AJ, Vallet-RegI M. Effect of the continuous solution exchange on the in vitro reactivity of a CaO-SiO(2) sol-gel glass. J Biomed Mater Res. 2000. 51(2):191–9 p.

42. Salinas AJ, Vallet-Regi M, Izquierdo-Barba I. Biomimetic Apatite Deposition on Calcium Silicate Gel Glasses. Journal of Sol-Gel Science and Technology. 2001. 21(1):13–25 p.

43. Kokubo T, Kushitani H, Sakka S, Kitsugi T, Yamamuro T. Solutions able to reproduce in vivo surface-structure changes in bioactive glass-ceramic A-W. J Biomed Mater Res. 1990;24(6):721–34 p.

44. Izquierdo-Barba I, Arcos D, Sakamoto Y, Terasaki O, López-Noriega A, Vallet-Regí M. High-Performance Mesoporous Bioceramics Mimicking Bone Mineralization. Chem Mater. 2008. 20(9):3191–8 p.

45. Pérez-Pariente J, Balas F, Román J, Salinas AJ, Vallet-Regí M. Influence of composition and surface characteristics on the in vitro bioactivity of SiO2−CaO−P2O5−MgO sol-gel glasses. Journal of Biomedical Materials Research. 1999. 47(2):170–5 p.

46. Fredholm YC, Karpukhina N, Brauer DS, Jones JR, Law RV, Hill RG. Influence of strontium for calcium substitution in bioactive glasses on degradation, ion release and apatite formation. J R Soc Interface. 2012. 9(70):880–9.

47. Bejarano J, Detsch R, Boccaccini AR, Palza H. PDLLA scaffolds with Cu- and Zn-doped bioactive glasses having multifunctional properties for bone regeneration. J Biomed Mater Res A. 2017. 105(3):746–56 p.

48. Beck JS, Vartuli JC, Roth WJ, Leonowicz ME, Kresge CT, Schmitt KD, Chu CTW, Olson DH, Sheppard EW, McCullen SB, Higgins JB, Schlenker JL. A new family of mesoporous molecular sieves prepared with liquid crystal templates. Journal of the American Chemical Society. 1992. 10834-10843 p.

49. Roth WJ. A method of modifying a crystalline molecular sieve material. EP1054732A1, 2000.

50. Kresge CT, Leonowicz ME, Roth WJ, Vartuli JC, Beck JS. Ordered mesoporous molecular sieves synthesized by a liquid-crystal template mechanism. Nature. 1992. 359(6397):710–2 p.

51. Brinker CJ, Lu Y, Sellinger A, Fan H. Evaporation-Induced Self-Assembly: Nanostructures Made Easy. Advanced Materials. 1999. 579-585 p.

52. Qisheng Huo, Chapter 16 - Synthetic Chemistry of the Inorganic Ordered Porous Materials. Modern Inorganic Synthetic Chemistry. 2011. 339-373.

53. Galarneau A, Iapichella J, Bonhomme K, Di Renzo F, Kooyman P, Terasaki O, Fajula F. Controlling the Morphology of Mesostructured Silicas by Pseudomorphic Transformation: a Route Towards. Advanced Functional Materials. 2006. 1657-1667 p.

54. Soler-Illia GJAA, SanchezBénédicte C, Patarin L. Chemical Strategies To Design Textured Materials: from Microporous and Mesoporous Oxides to Nanonetworks and Hierarchical Structures. Chemical Reviews. 4093-4138 p.

55. Wan Y, Shi Y, Zhao D. Supramolecular Aggregates as Templates: Ordered Mesoporous Polymers and Carbons. Chemistry of Materials. 2007. 932-945 p.

56. López-Noriega A, D Arcos, Izquierdo-Barba I, Sakamoto Y,Terasaki O,Vallet-Regí M. Ordered Mesoporous Bioactive Glasses for Bone Tissue Regeneration. Chemistry of Materials. 2006. 3137–3144 p.

57. Cicuendez M, Arcos D. Essential Role of Calcium Phosphate Heterogeneities in 2D-Hexagonal and 3D-Cubic SiO 2 −CaO−P 2 O 5 Mesoporous Bioactive Glasses. Chemistry of Materials. 2009. 5474–5484 p.

58. Li Z, Chen D, Tu B, Zhao D. Synthesis and phase behaviors of bicontinuous cubic mesoporous silica from triblock copolymer mixed anionic surfactant. Microporous and Mesoporous Materials. 2007. 34-40 p59.

59. Akunna C, Cerruti M. Structural connectivity and bioactivity in sol–gel silicate glass design. Acta Biomaterialia. 2004. 1-23 p.

60. Kurtuldu F, Mutlu N, Boccaccini AR, Galusek D. Gallium containing bioactive materials: A review of anticancer, antibacterial, and osteogenic properties. Bioact Mater. 2022. 17:125–46 p.

61. Liao W, Guo Y, Lu Y, Liu C. Crystallization of sodium calcium silicate glass for highly transparent glass-ceramics. Journal of the European Ceramic Society. 2024. 44(5):3218–25 p.

62. Brinker CJ and Scherer GW, curators. Sol–gel science, the physics and chemistry of sol–gel processing. Academic Press, Boston 1990, 908 p.

63. Li R, Clark AE, Hench LL. An investigation of bioactive glass powders by sol-gel processing. Journal of Applied Biomaterials. 1991. 2(4):231–9 p.

64. Mahony O, Jones JR. Porous Bioactive Nanostructured Scaffolds for Bone Regeneration: A Sol-Gel Solution. Nanomedicine. 2008. 3(2):233–45 p.

65. Oonishi H, Kushitani S, Yasukawa E, Iwaki H, Hench LL, Wilson J, et al. Particulate bioglass compared with hydroxyapatite as a bone graft substitute. Clin Orthop Relat Res. 1997. (334):316–25 p.

66. Chitambar CR. Gallium-containing anticancer compounds. Future Med Chem. 2012. 4(10):1257–72 p.

67. Bernstein LR. Mechanisms of therapeutic activity for gallium. Pharmacol Rev. 1998. 50(4):665–82 p.

68. Beatty EJ, curator. Ga3+-induced structural changes in human serum transferrin: [1H, 13C] NMR studies of methionine residues in the N-lobe. Magazine. 315-320 p.

69. Harris WR, Pecoraro VL. Thermodynamic binding constants for gallium transferrin. Biochemistry. 1983. 22(2):292–9 p.

70. Foster BJ, Clagett-Carr K, Hoth D, Leyland-Jones B. Gallium nitrate: the second metal with clinical activity. Cancer Treat Rep. 1986. 70(11):1311–9 p.

71. Collery P, Keppler B, Madoulet C, Desoize B. Gallium in cancer treatment. Critical Reviews in Oncology/Hematology. 2002. 42(3):283–96 p.

72. Bernstein LR, Tanner T, Godfrey C, Noll B. Chemistry and pharmacokinetics of gallium maltolate, a compound with high oral gallium bioavailability. Met Based Drugs. 2000. 7(1):33–47 p.

73. Rahimnejad Yazdi A, Towler M. The effect of the addition of gallium on the structure of zinc borate glass with controlled gallium ion release. Materials & Design. 2016. 92:1018–27 p.

74. Franchini M, Lusvardi G, Malavasi G, Menabue L. Gallium-containing phospho-silicate glasses: Synthesis and in vitro bioactivity. Materials Science and Engineering: C. 2012. 32(6):1401–6 p.

75. Serra J, González P, Liste S, Chiussi S, León B, Pérez-Amor M, et al. Influence of the non-bridging oxygen groups on the bioactivity of silicate glasses. J Mater Sci Mater Med. 2002. 13(12):1221–5.

76. Xin R, Leng Y, Chen J, Zhang Q. A comparative study of calcium phosphate formation on bioceramics in vitro and in vivo. Biomaterials. 2005. 26(33):6477–86.

77. Sontakke AD, Kalyandurg A. Network coordination in low germanium alkaline-earth gallate systems: Influence on glass formation. RSC Adv. 2012. 2:13024–31.

78. Beck JS, Vartuli JC, Roth WJ, Leonowicz ME, Kresge CT, Schmitt KD, et al. A new family of mesoporous molecular sieves prepared with liquid crystal templates. J Am Chem Soc. 1992. 114(27):10834–43.

79. McCusker LB, Liebau F, Engelhardt G. Nomenclature of structural and compositional characteristics of ordered microporous and mesoporous materials with inorganic hosts(IUPAC Recommendations 2001). Pure and Applied Chemistry. 2001. 73(2):381–94.

80. Moussaoui R, Elghniji K, ben Mosbah M, Elaloui E, Moussaoui Y. Sol–gel synthesis of highly TiO2 aerogel photocatalyst via high temperature supercritical drying. Journal of Saudi Chemical Society. 2017. 21(6):751–60.

81. Cai G, Zheng X, Zheng Y, Xiao Y, Zheng Y. Synthesis of ordered mesoporous boron-doped gamma-alumina with high surface area and large pore volume. Materials Letters. 2016. 178:248–51.

82. Gupta M, Leong EWW. Microwaves and Metals. John Wiley & Sons. 2008. 242 p.

83. Sun J, Wang W, Yue Q. Review on Microwave-Matter Interaction Fundamentals and Efficient Microwave-Associated Heating Strategies. Materials (Basel). 2016. 231 p.

84. Jian X,Tian W, Li J, Deng L, Zhou Z, Zhang L, Lu H, Yin L, Mahmood N. High-Temperature Oxidation-Resistant ZrN0.4B0.6/SiC Nanohybrid for Enhanced Microwave Absorption. ACS Applied Materials & Interfaces. 2019. 15869–15880 p.

85. Guo Y, Jian X, Zhang L, Mu C, Yin L, Xie J, Mahmood N, Dou S, Che R, Deng L. Plasma-induced FeSiAl@Al2O3@SiO2 core–shell structure for exceptional microwave absorption and anti-oxidation at high temperature. Chemical Engineering Journal. 2020. 123371 p.

86. Schanche JS. Microwave synthesis solutions from Personal Chemistry. Mol Divers. 1 gennaio 2003. 7(2–4):293–300.

87. Kappe CO. Microwave dielectric heating in synthetic organic chemistry. Chemical Society Reviews. 2008. 37(6):1127–39.

88. Sansano M, De los Reyes R, Andrés A, Heredia A. Effect of Microwave Frying on Acrylamide Generation, Mass Transfer, Color, and Texture in French Fries. Food and Bioprocess Technology. 2018. 1934–1939 p.

89. Wei R, Wang P, Zhang G, Wang N, Zheng T. Microwave-responsive catalysts for wastewater treatment: A review. Chemical Engineering Journal. 2020.

90. Rattanadecho P, Makul N. Microwave-Assisted Drying: A Review of the State-of-the-Art. Drying Technology. 2016. 34(1):1–38.

91. Mirzaei A, Neri G. Microwave-assisted synthesis of metal oxide nanostructures for gas sensing application: A review. Sensors and Actuators B: Chemical. 2016. 749-775 p.

92. Kappe CO, Dallinger D. Controlled microwave heating in modern organic synthesis: highlights from the 2004–2008 literature. Mol Divers. 2009. 13(2):71–193.

93. Yang G, Park SJ. Conventional and Microwave Hydrothermal Synthesis and Application of Functional Materials: A Review. Materials. gennaio 2019;12(7):1177.

94. Khan NA, Jhung SH. Synthesis of metal-organic frameworks (MOFs) with microwave or ultrasound: Rapid reaction, phase-selectivity, and size reduction. Coordination Chemistry Reviews. 2015. 11.23 p.

95. Ebner C, Bodner T, Stelzer F, Wiesbrock F. One Decade of Microwave-Assisted Polymerizations: Quo vadis?. Macromolecular Rapid Communications. 2011. 254-288 p.

96. Li JS, Huang H, Zhou YJ, Zhang CY, Li ZT. Research progress of graphene-based microwave absorbing materials in the last decade. Journal of Materials Research. 2017. 32(7):1213–30.

97. Kamarudin KHN, Jalil AA, Triwahyono S, Artika V, Salleh NFM, Karim AK, Jaafar NF, Sazegar MR, Mukti RR, Hameed BH, Johari A. Variation of the crystal growth of mesoporous silica nanoparticles and the evaluation to ibuprofen loading and release. Journal of Colloid and Interface Science. 2014. 6-13 p.

98. Flores-López SL, Villanueva SF, Montes-Morán MA, Cruz G, Garrido JJ, Arenillas A. Advantages of microwave-assisted synthesis of silica gels. Colloids and Surfaces A: Physicochemical and Engineering Aspects. 2020. 604:125248.

99. Neves GM, Lenza RFS, Vasconcelos WL. Evaluation of the Influence of Microwaves in the Structure of Silica Gels. Mat Res. 2002. 5:447–51.

100. Veselov GB, Vedyagin AA. Resorcinol–Formaldehyde-Derived Carbon Xerogels: Preparation, Functionalization, and Application Aspects. Materials (Basel). 2023. 16(19):6566.

101. Díaz de Greñu B, de los Reyes R, Costero AM, Amorós P, Ros-Lis JV. Recent Progress of Microwave-Assisted Synthesis of Silica Materials. Nanomaterials (Basel). 2020. 10(6):1092.

102. Palma V, Barba D, Cortese M, Martino M, Renda S, Meloni E. Microwaves and Heterogeneous Catalysis: A Review on Selected Catalytic Processes. Catalysts. 2020. 10(2):246.

103. Narayan R, Nayak UY, Raichur AM, Garg S. Mesoporous Silica Nanoparticles: A Comprehensive Review on Synthesis and Recent Advances. Pharmaceutics. 2018. 10(3):118.

104. Jafari S, Derakhshankhah H, Alaei L, Fattahi A, Varnamkhasti BS, Saboury AA. Mesoporous silica nanoparticles for therapeutic/diagnostic applications. Biomedicine & Pharmacotherapy. 2019. 109:1100–11.

105. Baig MM, Zulfiqar S, Yousuf MA, Shakir I, Aboud MFA, Warsi MF. DyxMnFe2-xO4 nanoparticles decorated over mesoporous silica for environmental remediation applications. Journal of Hazardous Materials. 2021. 123526 p.

106. Pérez-Botella E, Valencia S, Fernando Rey VF. Zeolites in Adsorption Processes: State of the Art and Future Prospects. Chemical Reviews. 2022. 17647–17695 p.

107. Feijoo J, Gomez-Villalba LS, Fort R, Rabanal ME. Simultaneous desalination and consolidation treatment through the application of electrokinetic techniques. Construction and Building Materials. 2023. 408:133686.

108. Petrovic B, Gorbounov M, Masoudi Soltani S. Impact of Surface Functional Groups and Their Introduction Methods on the Mechanisms of CO2 Adsorption on Porous Carbonaceous Adsorbents. Carbon Capture Science & Technology. 2022. 3:100045.

109. Hao P, Peng B, Shan BQ, Yang TQ, Zhang K. Comprehensive understanding of the synthesis and formation mechanism of dendritic mesoporous silica nanospheres. Nanoscale Adv. 2020. 2(5):1792–810.

110. Barczak M. Template removal from mesoporous silicas by different methods as a tool for adjusting their properties. New Journal of Chemistry. 2018. 42 p.

111. Vallet-Regí M, Schüth F, Lozano D, Colilla M, Manzano M. Engineering mesoporous silica nanoparticles for drug delivery: where are we after two decades? Chem Soc Rev. 2022. 51(13):5365–451.

112. Becit B, Duchstein P, Zahn D. Molecular mechanisms of mesoporous silica formation from colloid solution: Ripening-reactions arrest hollow network structures. PLoS One. 2019. 14(3):e0212731.

113. Gul A, Hruza J, Yalcinkaya F. Fouling and Chemical Cleaning of Microfiltration Membranes: A Mini-Review. Polymers (Basel). 2021. 13(6):846.

114. Chen X, Argandona SM, Melle F, Rampal N, Fairen-Jimenez D. Advances in surface functionalization of next-generation metal-organic frameworks for biomedical applications: Design, strategies, and prospects. Chem. 2024. 10(2):504–43.

115. Taylor BN, curator. The International System of Units (SI). 2001.

116. Mays TJ. A new classification of pore sizes. In: Studies in Surface Science and Catalysis. Studies in Surface Science and Catalysis. 2007. 57-62 p.

117. Rouquerol J, Avnir D, Fairbridge CW, Everett DH, Haynes JM, Pernicone N, et al. Recommendations for the characterization of porous solids (Technical Report). Pure Appl Chem. 1994. 66(8):1739–58.

118. Ijaz A, Yagci MB, Ow-Yang CW, Demirel AL, Mikó A. Formation of mesoporous silica particles with hierarchical morphology. Microporous and Mesoporous Materials. 2020. 303:110240.

119. Khimani M, Patel H, Patel V, Parekh P, Vekariya R. Self-assembly of stimuli-responsive block copolymers in aqueous solutions: an overview. Polymer Bulletin. 2020. 77 p.

120. Carrozza D, Ferrari E, Malavasi G. Very Large Pore Mesoporous Bioactive Silicate Glasses: Comparison of Behavior toward Classical Mesoporous Bioactive Glasses in Terms of Drug Loading/Release and Bioactivity. Materials. 2024. 17(2):373.

121. Carrozza D, Malavasi G, Ferrari E. Very Large Pores Mesoporous Silica as New Candidate for Delivery of Big Therapeutics Molecules, Such as Pharmaceutical Peptides. Materials. 2023. 16(11):4151.

122. Naharros-Molinero A, Caballo-González M, Mata F, García-Gallego S. Direct and Reverse Pluronic Micelles: Design and Characterization of Promising Drug Delivery Nanosystems. Pharmaceutics. 2022. 14:2628.

123. Han Y, Ying JY. Generalized Fluorocarbon-Surfactant-Mediated Synthesis of Nanoparticles with Various Mesoporous Structures. Angewandte Chemie International Edition. 2005. 44(2):288–92.

124. Zhang X, Zeng D, Li N, Jiang X, Liu C, Li Y. Large-pore mesoporous Ca-Si-based bioceramics with high in vitro bioactivity and protein adsorption capability for bone tissue regeneration. J Mater Chem B. 2016. 4(22):3916–24.

125. Bechinger B, Gorr SU. Antimicrobial Peptides: Mechanisms of Action and Resistance. J Dent Res. 2017. 96(3):254–60.

126. Lázár V, Martins A, Spohn R, Daruka L, Grézal G, Fekete G, et al. Antibiotic-resistant bacteria show widespread collateral sensitivity to antimicrobial peptides. Nat Microbiol. 2018. 3(6):718–31.

127. Faya M, Kalhapure RS, Kumalo HM, Waddad AY, Omolo C, Govender T. Conjugates and nano-delivery of antimicrobial peptides for enhancing therapeutic activity. Journal of Drug Delivery Science and Technology. 2018. 44:153–71 p.

128. Mendez-Samperio P. Peptidomimetics as a new generation of antimicrobial agents: current progress. IDR. 2014. 229 p.

129. Marr AK, Gooderham WJ, Hancock RE. Antibacterial peptides for therapeutic use: obstacles and realistic outlook. Curr Opin Pharmacol. 2006. 6(5):468–72 p.

130. Hancock RE, Lehrer R. Cationic peptides: a new source of antibiotics. Trends Biotechnol. febbraio 1998. 16(2):82–8 p.

131. Friedrich CL, Moyles D, Beveridge TJ, Hancock RE. Antibacterial action of structurally diverse cationic peptides on gram-positive bacteria. Antimicrob Agents Chemother. 2000. 44(8):2086–92 p.

132. Wu M, Maier E, Benz R, Hancock RE. Mechanism of interaction of different classes of cationic antimicrobial peptides with planar bilayers and with the cytoplasmic membrane of Escherichia coli. Biochemistry. 1999. 38(22):7235–42 p.

133. Zhang L, Dhillon P, Yan H, Farmer S, Hancock REW. Interactions of Bacterial Cationic Peptide Antibiotics with Outer and Cytoplasmic Membranes of Pseudomonas aeruginosa. Antimicrob Agents Chemother. 2000. 44(12):3317–21 p.

134. Brogden KA. Antimicrobial peptides: pore formers or metabolic inhibitors in bacteria? Nat Rev Microbiol. 2005. 3(3):238–50 p.

135. Zhang QY, Yan ZB, Meng YM, Hong XY, Shao G, Ma JJ, et al. Antimicrobial peptides: mechanism of action, activity and clinical potential. Mil Med Res. 2021. 8:48 p.

136. Bucataru C, Ciobanasu C. Antimicrobial peptides: Opportunities and challenges in overcoming resistance. Microbiological Research. 2024. 286:127822 p.

137. Lin L, Chi J, Yan Y, Luo R, Feng X, Zheng Y, et al. Membrane-disruptive peptides/peptidomimetics-based therapeutics: Promising systems to combat bacteria and cancer in the drug-resistant era. Acta Pharm Sin B. 2021. 11(9):2609–44 p.

138. Bowdish DME, Davidson DJ, Hancock REW. Immunomodulatory Properties of Defensins and Cathelicidins. Antimicrobial Peptides and Human Disease. 2006. 306:27–66 p.

139. Luong HX, Thanh TT, Tran TH. Antimicrobial peptides – Advances in development of therapeutic applications. Life Sci. 2020. 260:118407 p.

140. Domhan C, Uhl P, Meinhardt A, Zimmermann S, Kleist C, Lindner T, et al. A novel tool against multiresistant bacterial pathogens: lipopeptide modification of the natural antimicrobial peptide ranalexin for enhanced antimicrobial activity and improved pharmacokinetics. International Journal of Antimicrobial Agents. 2018. 52(1):52–62 p.

141. Wang C, Liu X, Chen S, Hu F, Sun J, Yuan H. Facile preparation of phospholipid–amorphous calcium carbonate hybrid nanoparticles: toward controllable burst drug release and enhanced tumor penetration. Chem Commun. 2018. 54(93):13080–3 p.

142. Reuther JF, Dees JL, Kolesnichenko IV, Hernandez ET, Ukraintsev DV, Guduru R, et al. Dynamic covalent chemistry enables formation of antimicrobial peptide quaternary assemblies in a completely abiotic manner. Nature Chem. 2018;10(1):45–50 p.

143. Humphrey W, Dalke A, Schulten K. VMD: Visual molecular dynamics. Journal of Molecular Graphics. 1996. 14(1):33–8 p.

144. Hsu ST, Breukink E, Tischenko E, Lutters MA, de Kruijff B, Kaptein R, Bonvin AM, van Nuland NA. The nisin-lipid II complex reveals a pyrophosphate cage that provides a blueprint for novel antibiotics. Nature structural & molecular biology. 2004. 11(10):963-7 p.

145. Lopes BS, Hanafiah A, Nachimuthu R, Muthupandian S, Md Nesran ZN, Patil S. The Role of Antimicrobial Peptides as Antimicrobial and Antibiofilm Agents in Tackling the Silent Pandemic of Antimicrobial Resistance. Molecules. 2022. 27(9):2995 p.

146. Scherer KM, Spille JH, Sahl HG, Grein F, Kubitscheck U. The Lantibiotic Nisin Induces Lipid II Aggregation, Causing Membrane Instability and Vesicle Budding. Biophys J. 2015. 108(5):1114–24 p.

147. Santos R, Ruza D, Cunha E, Tavares L, Oliveira M. Diabetic foot infections: Application of a nisin-biogel to complement the activity of conventional antibiotics and antiseptics against Staphylococcus aureus biofilms. PLoS One. 2019. 14(7):e0220000.

148. Ataide JA, Zanchetta B, Santos ÉM, Fava ALM, Alves TFR, Cefali LC, et al. Nanotechnology-Based Dressings for Wound Management. Pharmaceuticals (Basel). 2022. 15(10):1286.

149. Gao L, Kuraji R, Zhang MJ, Martinez A, Radaic A, Kamarajan P, et al. Nisin probiotic prevents inflammatory bone loss while promoting reparative proliferation and a healthy microbiome. NPJ Biofilms Microbiomes. 2022. 8:45 p.

150. Maaß S, Bartel J, Mücke PA, Schlüter R, Sura T, Zaschke-Kriesche J, et al. Proteomic Adaptation of Clostridioides difficile to Treatment with the Antimicrobial Peptide Nisin. Cells. 2021. 10(2):372 p.

151. Radaic A, Brody H, Contreras F, Hajfathalian M, Lucido L, Kamarajan P, et al. Nisin and Nisin Probiotic Disrupt Oral Pathogenic Biofilms and Restore Their Microbiome Composition towards Healthy Control Levels in a Peri-Implantitis Setting. Microorganisms. 2022. 10(7):1336 p.

152. Meade E, Slattery MA, Garvey M. Bacteriocins, Potent Antimicrobial Peptides and the Fight against Multi Drug Resistant Species: Resistance Is Futile? Antibiotics (Basel). 2020. 9(1):32 p.

153. Ezike TC, Okpala US, Onoja UL, Nwike CP, Ezeako EC, Okpara OJ, et al. Advances in drug delivery systems, challenges and future directions. Heliyon. 2023. 9(6):e17488 p.

154. Mhlongo JT, Waddad AY, Albericio F, de la Torre BG. Antimicrobial Peptide Synergies for Fighting Infectious Diseases. Adv Sci (Weinh). 2023. 10(26):2300472 p.

155. Shin JM, Gwak JW, Kamarajan P, Fenno JC, Rickard AH, Kapila YL. Biomedical Applications of Nisin. J Appl Microbiol. 2016. 120(6):1449–65.

156. Niamah AK, Al-Sahlany STG, Verma DK, Shukla RM, Patel AR, Tripathy S, et al. Emerging lactic acid bacteria bacteriocins as anti-cancer and anti-tumor agents for human health. Heliyon. 2024. 10(17):e37054 p.

157. Zainodini N, Hassanshahi G, Hajizadeh M, Falahati-Pour SK, Mahmoodi M, Mirzaei MR. Nisin Induces Cytotoxicity and Apoptosis in Human Asterocytoma Cell Line (SW1088). Asian Pac J Cancer Prev. 2018. 19(8):2217–22 p.

158. Wang Y, Wang Y, Sun T, Xu J. Bacteriocins in Cancer Treatment: Mechanisms and Clinical Potentials. Biomolecules. 2024. 14(7):831 p.

159. Ma Z, Bai J, Wang Y, Jiang X. Impact of Shape and Pore Size of Mesoporous Silica Nanoparticles on Serum Protein Adsorption and RBCs Hemolysis. ACS Appl Mater Interfaces. 2014. 6(4):2431–8 p.

160. Nicolini V, Malavasi G, Lusvardi G, Zambon A, Benedetti F, Cerrato G, et al. Mesoporous bioactive glasses doped with cerium: Investigation over enzymatic-like mimetic activities and bioactivity. Ceramics International. 2019. 45(16):20910–20 p.

161. Hadipour Moghaddam SP, Yazdimamaghani M, Ghandehari H. Glutathione-sensitive hollow mesoporous silica nanoparticles for controlled drug delivery. Journal of Controlled Release. 2018. 282:62–75.

162. Bansal A, Simon MC. Glutathione metabolism in cancer progression and treatment resistance. Journal of Cell Biology. 2018. 217(7):2291–8 p.

163. Ding B, Shao S, Yu C, Teng B, Wang M, Cheng Z, et al. Large-Pore Mesoporous-Silica-Coated Upconversion Nanoparticles as Multifunctional Immunoadjuvants with Ultrahigh

Photosensitizer and Antigen Loading Efficiency for Improved Cancer Photodynamic Immunotherapy. Advanced Materials. 2018. 30(52):1802479.

164. Florensa M, Llenas M, Medina-Gutiérrez E, Sandoval S, Tobías-Rossell G. Key Parameters for the Rational Design, Synthesis, and Functionalization of Biocompatible Mesoporous Silica Nanoparticles. Pharmaceutics. 2022. 14(12):2703.

165. Sobrino-López A, Martín-Belloso O. Use of nisin and other bacteriocins for preservation of dairy products. International Dairy Journal. 2008. 18(4):329–43 p.

166. Flynn J, Mallen S, Durack E, O'Connor PM, Hudson SP. Mesoporous matrices for the delivery of the broad spectrum bacteriocin, nisin A. Journal of Colloid and Interface Science. 2019. 537:396–406 p.

167. Shin JM, Gwak JW, Kamarajan P, Fenno JC, Rickard AH, Kapila YL. Biomedical applications of nisin. Journal of Applied Microbiology. 2016. 120(6):1449–65 p.

168. Brum LFW, dos Santos C, Zimnoch Santos JH, Brandelli A. Structured silica materials as innovative delivery systems for the bacteriocin nisin. Food Chemistry. 2022. 366:130599 p.

169. Bharatiya B, Ghosh G, Bahadur P, Mata J. The Effects of Salts and Ionic Surfactants on the Micellar Structure of Tri-Block Copolymer PEO-PPO-PEO in Aqueous Solution. Journal of Dispersion Science and Technology. 2008. 29(5):696–701 p.

170. Bharatiya B, Ghosh G, Bahadur P, Mata J. The Effects of Salts and Ionic Surfactants on the Micellar Structure of Tri-Block Copolymer PEO-PPO-PEO in Aqueous Solution. Journal of Dispersion Science and Technology. 2008. 29(5):696–701 p.

171. Poyraz AS, Dag Ö. Role of Organic and Inorganic Additives on the Assembly of CTAB-P123 and the Morphology of Mesoporous Silica Particles. J Phys Chem C. 2009. 113(43):18596–607 p.

172. Pitto-Barry A, Barry NPE. Pluronic® block-copolymers in medicine: from chemical and biological versatility to rationalisation and clinical advances. Polym Chem. 2014. 5(10):3291–7 p.

173. Horvat G, Pantić M, Knez Ž, Novak Z. A Brief Evaluation of Pore Structure Determination for Bioaerogels. Gels. 2022. 8(7):438 p.

174. Varini E, Sánchez-Salcedo S, Malavasi G, Lusvardi G, Vallet-Regí M, Salinas AJ. Cerium (III) and (IV) containing mesoporous glasses/alginate beads for bone regeneration: Bioactivity, biocompatibility and reactive oxygen species activity. Materials Science and Engineering: C. 2019. 105:109971 p.

175. Ganguly A, Ahmad T, Ganguli AK. Silica Mesostructures: Control of Pore Size and Surface Area Using a Surfactant-Templated Hydrothermal Process. Langmuir. 2010. 26(18):14901–8 p.

176. Brown SM, Lard EW. A comparison of nitrogen and mercury pore size distributions of silicas of varying pore volume. Powder Technology. 1974. 9(4):187–90 p.

177. Lei Q, Guo J, Noureddine A, Wang A, Wuttke S, Brinker CJ, et al. Sol–Gel-Based Advanced Porous Silica Materials for Biomedical Applications. Advanced Functional Materials. 2020. 30(41):1909539 p.

178. Sing KSW. Reporting physisorption data for gas/solid systems with special reference to the determination of surface area and porosity (Recommendations 1984). Pure and Applied Chemistry. 1985. 57(4):603–19 p.

179. Mays TJ. A new classification of pore sizes. In: Llewellyn PL, Rodriquez-Reinoso F, Rouqerol J, Seaton N, curatori. Studies in Surface Science and Catalysis. 2007. 57–62 p

180. Mays TJ. A new classification of pore sizes. In: Llewellyn PL, Rodriquez-Reinoso F, Rouqerol J, Seaton N, curatori. Studies in Surface Science and Catalysis. 2007. 57–62 p.

181. Kassem MA, El-Sawy HS, Abd-Allah FI, Abdelghany TM, El-Say KM. Maximizing the Therapeutic Efficacy of Imatinib Mesylate–Loaded Niosomes on Human Colon Adenocarcinoma Using Box-Behnken Design. Journal of Pharmaceutical Sciences. 2017. 106(1):111–22 p.

182. Ibrahim AH, Smått JH, Govardhanam NP, Ibrahim HM, Ismael HR, Afouna MI, et al. Formulation and optimization of drug-loaded mesoporous silica nanoparticle-based tablets to improve the dissolution rate of the poorly water-soluble drug silymarin. European Journal of Pharmaceutical Sciences. 2020. 142:105103 p.

183. Shen S, Wu Y, Liu Y, Wu D. High drug-loading nanomedicines: progress, current status, and prospects. IJN. 2017. 12:4085–109 p.

184. El-Say KM. Maximizing the encapsulation efficiency and the bioavailability of controlled-release cetirizine microspheres using Draper–Lin small composite design. DDDT. 2016. 10:825–39 p.

185. Grünberg B, Emmler T, Gedat E, Shenderovich I, Findenegg GH, Limbach HH, et al. Hydrogen Bonding of Water Confined in Mesoporous Silica MCM-41 and SBA-15 Studied by 1H Solid-State NMR. Chemistry – A European Journal. 2004. 10(22):5689–96 p.

186. Petrisor G, Ficai D, Motelica L, Trusca RD, Bîrcă AC, Vasile BS, et al. Mesoporous Silica Materials Loaded with Gallic Acid with Antimicrobial Potential. Nanomaterials (Basel). 2022. 12(10):1648 p.

187. Badea E, Carşote C, Hadîmbu E, Șendrea C, Lupaș MC. The effect of halloysite nanotubes dispersions on vegetable-tanned leather thermal stability. Heritage Science. 2019. 7(1):68 p.

188. Carrozza D, Malavasi G, Ferrari E, Menziani MC. Alginate Beads Containing Cerium-Doped Mesoporous Glass and Curcumin: Delivery and Stabilization of Therapeutics. International Journal of Molecular Sciences. 2023. 24(1):880 p.

189. Wang L, Wang N, Zhang W, Cheng X, Yan Z, Shao G, et al. Therapeutic peptides: current applications and future directions. Signal Transduct Target Ther. 2022. 7:48 p.

190. Johnell O, Kanis JA. An estimate of the worldwide prevalence and disability associated with osteoporotic fractures. Osteoporos Int. 2006. 17(12):1726–33 p.

191. Kao CT, Chiu YC, Lee AKX, Lin YH, Huang TH, Liu YC, et al. The synergistic effects of Xu Duan combined Sr-contained calcium silicate/poly-ε-caprolactone scaffolds for the promotion of osteogenesis marker expression and the induction of bone regeneration in osteoporosis. Materials Science and Engineering: C. 2021. 119:111629 p.

192. Turnbull G, Clarke J, Picard F, Riches P, Jia L, Han F, et al. 3D bioactive composite scaffolds for bone tissue engineering. Bioactive Materials. 2018. 3(3):278–314 p.

193. Hollister SJ. Scaffold Design and Manufacturing: From Concept to Clinic. Advanced Materials. 2009. 21(32–33):3330–42 p.

194. Gao C, Peng S, Feng P, Shuai C. Bone biomaterials and interactions with stem cells. Bone Res. 2017. 5:17059 p.

195. Vallet-Regi M, Salinas AJ. Mesoporous bioactive glasses for regenerative medicine. Materials Today Bio. 2021. 11:100121 p.

196. Montazerian M, Zanotto ED. A guided walk through Larry Hench's monumental discoveries. J Mater Sci. 2017. 52(15):8695–732 p.

197. Salinas AJ, Vallet-Regi M, Heikkilä J. 12 - Use of bioactive glasses as bone substitutes in orthopedics and traumatology. Bioactive Glasses. 2018. 337–64 p.

198. He F, Qiu C, Lu T, Shi X, Ye J. Conjunction of gallium doping and calcium silicate mediates osteoblastic and osteoclastic performances of tricalcium phosphate bioceramics. Biomed Mater. 2021. 17(1):015012 p.

199. Geng Z, Ji L, Li Z, Wang J, He H, Cui Z, et al. Nano-needle strontium-substituted apatite coating enhances osteoporotic osseointegration through promoting osteogenesis and inhibiting osteoclastogenesis. Bioactive Materials. 2021. 6(4):905–15 p.

200. Zhu H, Zheng K, Boccaccini AR. Multi-functional silica-based mesoporous materials for simultaneous delivery of biologically active ions and therapeutic biomolecules. Acta Bioaterialia. 2021. 129:1–17 p.

201. Ni S, Chang J, Chou L, Zhai W. Comparison of osteoblast-like cell responses to calcium silicate and tricalcium phosphate ceramics in vitro. Journal of Biomedical Materials Research Part B: Applied Biomaterials. 2007. 80B(1):174–83 p..

202. Kurtuldu F, Mutlu N, Boccaccini AR, Galusek D. Gallium containing bioactive materials: A review of anticancer, antibacterial, and osteogenic properties. Bioactive Materials. 2022. 17:125–46 p.

203. Collery P, curator. Metal Ions in Biology and Medicine. 1990.

204. Bernstein LR. Mechanisms of Therapeutic Activity for Gallium. Pharmacol Rev. 1998. 50(4):665–82 p.

205. Petrisor G, Ficai D, Motelica L, Trusca RD, Bîrcă AC, Vasile BS, et al. Mesoporous Silica Materials Loaded with Gallic Acid with Antimicrobial Potential. Nanomaterials (Basel). 2022. 12(10):1648 p.

206. Grnberg B, Emmler T, Gedat, Shenderovich I, Findenegg GH, Limbach HH, Buntkowsky G. Hydrogen Bonding of Water Confined in Mesoporous Silica MCM-41 and SBA-15 Studied by 1H Solid-State NMR. Chem Eur J. 2004. 10:5689–96 p.

207. Siqueira RL, Alves PFS, da Silva Moraes T, Casemiro LA, da Silva SN, Peitl O, et al. Cation-doped bioactive ceramics: *In vitro* bioactivity and effect against bacteria of the oral cavity. Ceramics International. 2019. 45(7, Part A):9231–44 p.

208. Franchini M, Lusvardi G, Malavasi G, Menabue L. Gallium-containing phospho-silicate glasses: Synthesis and in vitro bioactivity. Materials Science and Engineering: C. 2012. 32(6):1401–6 p.

209. Blumenthal NC, Cosma V, Levine S. Effect of gallium on thein vitro formation, growth, and solubility of hydroxyapatite. Calcif Tissue Int. 1989. 45(2):81–7 p.

210. Campoccia D, Montanaro L, Arciola CR. The significance of infection related to orthopedic devices and issues of antibiotic resistance. Biomaterials. 2006. 27(11):2331–9 p.

211. Keenan TJ, Wren AW, Coughlan A, Towler MR, Hall MM. Relating pH and Ion Release from Ga2O3-Na2O-CaO-ZnO-SiO2 Bioactive Glasses. 2013. 98–9 p.

212. Valappil SP, Ready D, Neel EAA, Pickup DM, Chrzanowski W, O'Dell LA, et al. Antimicrobial Gallium-Doped Phosphate-Based Glasses. Advanced Functional Materials. 2008. 18(5):732–41 p.

213. Valappil SP, Higham SM. Antibacterial effect of gallium and silver on Pseudomonas aeruginosa treated with gallium–silver–phosphate-based glasses. Bio-Medical Materials and Engineering. 2014. 24(3):1589–94 p.

214. Kurtuldu F, Mutlu N, Boccaccini AR, Galusek D. Gallium containing bioactive materials: A review of anticancer, antibacterial, and osteogenic properties. Bioactive Materials. 2022. 17:125–46 p.

215. Sahdev R, Ansari TI, Higham SM, Valappil SP. Potential use of gallium-doped phosphate-based glass material for periodontitis treatment. J Biomater Appl. 2015. 30(1):85–92 p.

216. Keenan T j., Placek L m., Hall M m., Wren A w. Antibacterial and antifungal potential of Ga-bioactive glass and Ga-bioactive glass/polymeric hydrogel composites. Journal of Biomedical Materials Research Part B: Applied Biomaterials. 2017. 105(5):1102–13 p.

217. Keenan TJ, Placek LM, Coughlan A, Bowers GM, Hall MM, Wren AW. Structural characterization and anti-cancerous potential of gallium bioactive glass/hydrogel composites. Carbohydrate Polymers. 2016. 153:482–91 p.

218. Keenan T, Placek L, Keenan N, Hall M, Wren A. Synthesis, characterization, and in vitro cytocompatibility of Ga-bioactive glass/polymer hydrogel composites. J Biomater Appl. 2016. 31(4):553–67.

219. Wren AW, Keenan T, Coughlan A, Laffir FR, Boyd D, Towler MR, et al. Characterisation of Ga2O3–Na2O–CaO–ZnO–SiO2 bioactive glasses. J Mater Sci. 2013. 48(11):3999–4007 p.

220. Patil BS, Kulkarni U, Bhavik P. FORMULATION AND EVALUATION OF DICLOFENAC POTASSIUM MATRIX TABLETS. International Journal of Pharmaceutical Sciences and Research. 2010. 88-92 p.

221. Zhai W, He C, Wu L, Zhou Y, Chen H, Chang J, et al. Degradation of hollow mesoporous silica nanoparticles in human umbilical vein endothelial cells. Journal of Biomedical Materials Research Part B: Applied Biomaterials. 2012. 100B(5):1397–403 p.

222. Braun K, Pochert A, Beck M, Fiedler R, Gruber J, Lindén M. Dissolution kinetics of mesoporous silica nanoparticles in different simulated body fluids. J Sol-Gel Sci Technol. 2016. 79(2):319–27 p.

223. Pham ALT, Sedlak DL, Doyle FM. Dissolution of mesoporous silica supports in aqueous solutions: Implications for mesoporous silica-based water treatment processes. Applied Catalysis B: Environmental. 2012. 126:258–64 p.

224. Tarn D, Yu CJ, Lu J, Hartz A, Tamanoi F, Zink JI. In vitro delivery of calcium ions by nanogated mesoporous silica nanoparticles to induce cancer cellular apoptosis. Mol Syst Des Eng. 2017. 2(4):384–92 p.

225. Brunauer S, Emmett PH, Teller E. Adsorption of Gases in Multimolecular Layers. J Am Chem Soc. 1938. 60(2):309–19 p.

226. Barrett EP, Joyner LG, Halenda PP. The Determination of Pore Volume and Area Distributions in Porous Substances. I. Computations from Nitrogen Isotherms. J Am Chem Soc. 1951. 73(1):373–80 p.

227. Collery P. Metal Ions in Biology and Medicine. John Libbey Eurotext. 2000. 852 p.

228. Arcos D, Vallet-Regí M. Sol–gel silica-based biomaterials and bone tissue regeneration. Acta Biomaterialia. 2010. 6(8):2874–88 p.

229. Brown SM, Lard EW. A comparison of nitrogen and mercury pore size distributions of silicas of varying pore volume. Powder Technology. 1974;9(4):187–90 p.

230. Sing KSW. Reporting physisorption data for gas/solid systems with special reference to the determination of surface area and porosity (Recommendations 1984). Pure and Applied Chemistry. 1985. 57(4):603–19 p.

231. ALOthman ZA. A Review: Fundamental Aspects of Silicate Mesoporous Materials. Materials. 2012. 5(12):2874–902 p.

232. Kumar KV, Gadipelli S, Wood B, Ramisetty KA, Stewart AA, Howard CA, et al. Characterization of the adsorption site energies and heterogeneous surfaces of porous materials. J Mater Chem A. 2019. 7(17):10104–37 p.

233. Mazzella A, Tilocca C, Ciccu R. Analisi comparativa delle potenzialità di confinamento della CO2 per via geologica e mineralogica all'interno del bacino minerario del Sulcis. 2011.

234. Lowell S, Shields J, Thomas M, Thommes M. Characterization of Porous Solids and Powders: Surface Area, Pore Size and Density. Vol. 1. 2006.

235. Grünberg B, Emmler T, Gedat E, Shenderovich I, Findenegg GH, Limbach HH, et al. Hydrogen Bonding of Water Confined in Mesoporous Silica MCM-41 and SBA-15 Studied by 1H Solid-State NMR. Chemistry – A European Journal. 2004. 10(22):5689–96 p.

236. Fosca M, Rau J, Uskokovic V. Factors influencing the drug release from calcium phosphate cements. Bioactive Materials. 2022. 7:341–63 p.

237. Hosseinpour S, Gomez-Cerezo MN, Cao Y, Lei C, Dai H, Walsh LJ, et al. A Comparative Study of Mesoporous Silica and Mesoporous Bioactive Glass Nanoparticles as Non-Viral MicroRNA Vectors for Osteogenesis. Pharmaceutics. 2022. 14(11):2302 p.

238. Li X, Zhang L, Dong X, Liang J, Shi J. Preparation of mesoporous calcium doped silica spheres with narrow size dispersion and their drug loading and degradation behavior. Microporous and Mesoporous Materials. 2007. 102(1):151–8 p.

239. Vialpando M, Aerts A, Persoons J, Martens J, Van Den Mooter G. Evaluation of ordered mesoporous silica as a carrier for poorly soluble drugs: Influence of pressure on the structure and drug release. Journal of Pharmaceutical Sciences. 2011. 100(8):3411–20 p.

240. Badea E, Carşote C, Hadîmbu E, Șendrea C, Lupaș MC. The effect of halloysite nanotubes dispersions on vegetable-tanned leather thermal stability. Heritage Science. 2019. 7(1):68 p.

241. Minandri F, Bonchi C, Frangipani E, Imperi F, Visca P. Promises and Failures of Gallium as an Antibacterial Agent. Future Microbiology. 2014. 9(3):379–97 p.

242. Pourshahrestani S, Zeimaran E, Kadri NA, Gargiulo N, Samuel S, Naveen SV, et al. Gallium-containing mesoporous bioactive glass with potent hemostatic activity and antibacterial efficacy. J Mater Chem B. 2015. 4(1):71–86 p.

243. Antunes LCS, Imperi F, Minandri F, Visca P. In Vitro and In Vivo Antimicrobial Activities of Gallium Nitrate against Multidrug-Resistant Acinetobacter baumannii. Antimicrobial Agents and Chemotherapy. 2012. 56(11):5961–70 p.

244. Peng XX, Gao S, Zhang JL. Gallium (III) Complexes in Cancer Chemotherapy. European Journal of Inorganic Chemistry. 2022. 2022(6):e202100953 p.

245. Lessa JA, Parrilha GL, Beraldo H. Gallium complexes as new promising metallodrug candidates. Inorganica Chimica Acta. 2012. 393:53–63 p.

246. Hart MM, Smith CF, Yancey ST, Adamson RH. Toxicity and Antitumor Activity of Gallium Nitrate and Periodically Related Metal Salts22. JNCI: Journal of the National Cancer Institute. 1971. 47(5):1121–8 p.

247. Prokopowicz M, Żegliński J, Gandhi A, Sawicki W, Tofail SAM. Bioactive silica-based drug delivery systems containing doxorubicin hydrochloride: *In vitro* studies. Colloids and Surfaces B: Biointerfaces. 2012. 93:249–59 p.

248. Santos EM, Radin S, Ducheyne P. Sol–gel derived carrier for the controlled release of proteins. Biomaterials. 1999. 20(18):1695–700 p.

249. Shenderovich IG. For Whom a Puddle Is the Sea? Adsorption of Organic Guests on Hydrated MCM-41 Silica. Langmuir. 2020. 36(38):11383–92 p.

250. Saravanapavan P, Hench LL. Low-temperature synthesis, structure, and bioactivity of gel-derived glasses in the binary CaO-SiO2 system. Journal of Biomedical Materials Research. 2001. 54(4):608–18 p.

251. Koutsopoulos S. Synthesis and characterization of hydroxyapatite crystals: A review study on the analytical methods. Journal of Biomedical Materials Research. 2002;62(4):600–12.

252. Urošević M, Nikolić L, Gajić I, Nikolić V, Dinić A, Miljković V. Curcumin: Biological Activities and Modern Pharmaceutical Forms. Antibiotics (Basel). 2022. 11(2):135 p.

253. Agrawal N, Jaiswal M. Bioavailability enhancement of curcumin via esterification processes: A review. European Journal of Medicinal Chemistry Reports. 2022. 6:100081 p.

254. Tabanelli R, Brogi S, Calderone V. Improving Curcumin Bioavailability: Current Strategies and Future Perspectives. Pharmaceutics. 2021. 13(10):1715 p..

255. Arora S, Singh B, Kumar S, Kumar A, Singh A, Singh C. Piperine loaded drug delivery systems for improved biomedical applications: Current status and future directions. Health Sciences Review. 2023. 9:100138 p.

256. Olivera A, Moore TW, Hu F, Brown AP, Sun A, Liotta DC, et al. Inhibition of the NF-κB signaling pathway by the curcumin analog, 3,5-Bis(2-pyridinylmethylidene)-4-piperidone (EF31): anti-inflammatory and anti-cancer properties. Int Immunopharmacol. 2012. 12(2):368–77 p.

257. Lee WH, Loo CY, Bebawy M, Luk F, Mason RS, Rohanizadeh R. Curcumin and its Derivatives: Their Application in Neuropharmacology and Neuroscience in the 21st Century. Curr Neuropharmacol. 2013. 11(4):338–78 p.

258. Aliyari M, Hashemy SI, Hashemi SF, Reihani A, Kesharwani P, Hosseini H, et al. Targeting the Akt signaling pathway: Exploiting curcumin's anticancer potential. Pathology - Research and Practice. 2024. 261:155479 p.

259. Wang M, Jiang S, Zhou L, Yu F, Ding H, Li P, et al. Potential Mechanisms of Action of Curcumin for Cancer Prevention: Focus on Cellular Signaling Pathways and miRNAs. Int J Biol Sci. 2019. 15(6):1200–14 p.

260. Cole GM, Teter B, Frautschy SA. NEUROPROTECTIVE EFFECTS OF CURCUMIN. Adv Exp Med Biol. 2007. 595:197–212 p.

261. Qian LW, Fourcaudot AB, Chen P, Brandenburg KS, Weaver AJ, Leung KP. Cerium nitrate enhances anti-bacterial effects and imparts anti-inflammatory properties to silver dressings in a rat scald burn model. Int J Burns Trauma. 2020. 10(4):91–100 p.

262. Karakoti AS, Monteiro-Riviere NA, Aggarwal R, Davis JP, Narayan RJ, Self WT, et al. Nanoceria as Antioxidant: Synthesis and Biomedical Applications. JOM (1989). 2008. 60(3):33–7 p..

263. Liu M, Sun X, Chen B, Dai R, Xi Z, Xu H. Insights into Manganese Superoxide Dismutase and Human Diseases. Int J Mol Sci. 2022. 23(24):15893 p.

264. Barrioni BR, Norris E, Li S, Naruphontjirakul P, Jones JR, Pereira M de M. Osteogenic potential of sol-gel bioactive glasses containing manganese. J Mater Sci Mater Med. 2019. 30(7):86 p.

265. Gerhardt LC, Boccaccini AR. Bioactive Glass and Glass-Ceramic Scaffolds for Bone Tissue Engineering. Materials (Basel). 2010. 3(7):3867–910 p.

266. Kelly F. Oxidative stress: its role in air pollution and adverse health effects. Occup Environ Med. 2003. 60(8):612–6 p.

267. Celardo I, Pedersen JZ, Traversa E, Ghibelli L. Pharmacological potential of cerium oxide nanoparticles. Nanoscale. 2011. 3(4):1411–20 p.

268. Korsvik C, Patil S, Seal S, Self WT. Superoxide dismutase mimetic properties exhibited by vacancy engineered ceria nanoparticles. Chem Commun. 2007. (10):1056–8 p.

269. Yang JY, Nocera DG. Catalase and epoxidation activity of manganese salen complexes bearing two xanthene scaffolds. J Am Chem Soc. 2007. 129(26):8192–8 p.

270. Coassin M, Ursini F, Bindoli A. Antioxidant effect of manganese. Archives of Biochemistry and Biophysics. 1992. 299(2):330–3 p..

271. Dobson AW, Aschner M. Manganese-induced oxidative stress. In: Oxidative Stress and Neurodegenerative Disorders.2007. 433–50 p.

Acknowledgments

First and foremost, I would like to express my deepest gratitude to my Tutor and co-Tutor, respectively Prof. Gianluca Malavasi and Prof. Erika Ferrari, for their continuous support, guidance, and encouragement throughout my research. Their expertise and insights were invaluable to the completion of this thesis.

A special thank you goes to my colleagues of the DSCG Department, who firstly are friends, who provided academic support, for the countless discussions, encouragement, and friendship during this journey.

On a personal note, I want to thank my family and my partner for their unwavering support and love. To my parents, who have always believed in me and encouraged me to pursue my dreams.

I would like to sincerely thank my Managers from Omya International AG, who hosted me during my period abroad, Antonella De Luca and Eugenio Mattioni. They provided me with the incredible opportunity to be part of their team during the course of my research. Their support, guidance, and willingness to share their expertise were invaluable to me.

Thank you for creating a welcoming and stimulating environment that fostered my professional growth and allowed me to gain practical insights into fertilizer granules production. Your mentorship and advice were crucial in shaping my understanding of the industry and refining my research approach.

I am also grateful to the entire team at Group Operation – Granulation team for their kindness, support, and collaboration throughout my stay.

Finally, to everyone who has contributed to my thesis in any way, whether through guidance, support, or encouragement, thank you. This accomplishment would not have been possible without each and every one of you.